# Radiogenic Background Suppression in a Heavy Water Solar Neutrino Detector

Andrew Peter Ferraris
Magdalen College

February 1992

A thesis submitted in partial fulfillment of the requirements
for the degree of Doctor of Philosophy
in the University of Oxford.

To my parents

*Observation by means of the eyes and ears and all the other senses is entirely deceptive and philosophy urges the soul to refrain from using them unless it is necessary to do so, and encourages it to collect and concentrate itself by itself, trusting nothing but its own independent judgement upon objects considered in themselves, and attributing no truth to anything which it views indirectly as being subject to variation, because such objects are sensible and visible, but what the soul itself sees is intelligible and invisible.*

*Plato. Phaedo.*

# Radiogenic Background Suppression in a Heavy Water Solar Neutrino Detector

Andrew Peter Ferraris
Magdalen College
February 1992

## Abstract

The Sudbury Neutrino Observatory, a heavy water Čerenkov solar neutrino detector under construction in Canada, should afford a high-statistics measurement of the $\nu_e$ component of the solar neutrino flux. It will in addition have neutral current sensitivity and so could resolve the long-standing Solar Neutrino Problem. Backgrounds to both the charged and neutral current reactions arise from trace radioactive contaminants in the materials of the detector. The most stringent purity requirements are those imposed on the central heavy water detecting element: its Thorium and Radium content must not exceed 1 disintegration per day per ton.

The required concentrations are below the levels accessible to direct counting methods, so that pre-concentration onto a solid phase sorbent is necessary. Manganese Dioxide, $MnO_2$, is known to act as a sorbent for a number of radioisotopes, notably Radium, under a wide range of conditions. Measurements were therefore performed which established the performance of packed bed absorbing columns with respect to Thorium and Radium sorption. Limits were also obtained on the equilibrium constant for Radium sorption, which determines the ultimate purity obtainable if $MnO_2$ were used for purification rather than assay of the water. Radium was found to be rapidly extracted at pH>2. A marked transition in the sorption behaviour of Thorium was found near pH4, attributable to its known tendency to hydrolyse in non-acid solutions.

A novel method of measuring adsorbed $^{228}$Th and $^{224}$Ra activity was developed. $^{220}$Rn, emanating from the $MnO_2$ surface, was carried with a gas stream into a large-volume gas proportional counter where its alpha decay was observed in coincidence with that of its short-lived daughter $^{216}$Po, although background levels in the device were too high for use in SNO. The efficiency with which $^{220}$Rn is de-emanated was also determined, together with its variation with gas flow rate through the $MnO_2$ sample.

# Acknowledgements

I would like to express my thanks to some of the many people who offered their help and advice in this enterprise. Neil Tanner, Dave Wark, David Sinclair and Edward Hooper all freely volunteered their valuable time and considerable experience and I must thank them for their efforts in preventing some of the more absurd errors I would otherwise have made (although, needless to say, I claim sole responsibility for those which remain).

Barrie Knox volunteered a great amount of much-appreciated advice, technical help and insight which has undoubtedly shaped the way in which the work evolved. To him are due my thanks, in addition, for many conversations, often late in the evening, when my understanding of the mysteries of Thorium chemistry, such as it is, was shaped.

I am also much indebted to my father for his patient, not to say long-suffering, and generous support, and to Joanna, for being very much better than I deserve.

Finally, and most especially, I must express my gratitude to Peter Trent. Without his patient encouragement, support, good humour and constructive criticism, this work would never have been completed.

I am indebted to the Science and Engineering Research Council for their support over 3 years of this project.

Andrew Ferraris
Magdalen College
February 1992

# Contents

# Chapter 1

# Solar neutrino astronomy

## 1.1 Standard solar models

It has long been accepted that fusion of light nuclei is the only process capable of sustaining the sun's energy output for its known lifetime. According to the models outlined in his section, the sun's energy output derives from 'hydrogen burning' according to the overall reaction:

$$4p \longrightarrow {}^4\mathrm{He} + 2e^+ + 2\nu_e + 26.73\mathrm{MeV} \tag{1.1}$$

This reaction does not occur directly, since the interaction probability of four particles is very small, but rather through a sequence of reactions known as the proton-proton chain. Other mechanisms also exist which achieve the same result, notably the 'CNO' cycle. Rolfs and Rodney [3] give an excellent account of the possible cycles of hydrogen burning — essentially, a set of interlocking cycles exists in which successively higher-Z nuclei act as catalysts for the reaction (1.1): the CNO cycle is simply the lowest in Z of this series. Because of the successively higher Coulomb barriers to be overcome, each cycle 'turns on' at successively higher temperatures and the CNO cycle, according to the 'Standard Solar Model' (SSM — defined below), contributes only about 1.6% of the sun's energy. At much higher densities and temperatures ($T$ =100–200$\times 10^9$K, $\rho = 10^2$–$10^5 g.cm^{-3}$), a massive star can undergo helium burning, an entirely separate method of energy generation to hydrogen burning. For sufficiently massive stars, stable heavy-ion burning phases can occur. However, with the exception of the CNO cycle, methods of energy generation beyond the p-p chain are thought to be unimportant in the sun [4, 5, 6]

The reactions of the p-p chain are summarised in the well-known diagram in Figure 1.1 which shows the reactions, their branching ratios and the origins of solar neutrinos. The branching ratios shown, it should be noted, are those predicted by the solar models outlined in this section, and are dependent on temperature and nuclear abundances within the sun.

The primary reaction in the chain is the $p+p$ reaction, a weak process whose cross-section is calculable. There follows the rapid addition of a proton to the deuteron and, for the most part, the subsequent reaction

$${}^3\mathrm{He} + {}^3\mathrm{He} \longrightarrow {}^4\mathrm{He} + 2p$$

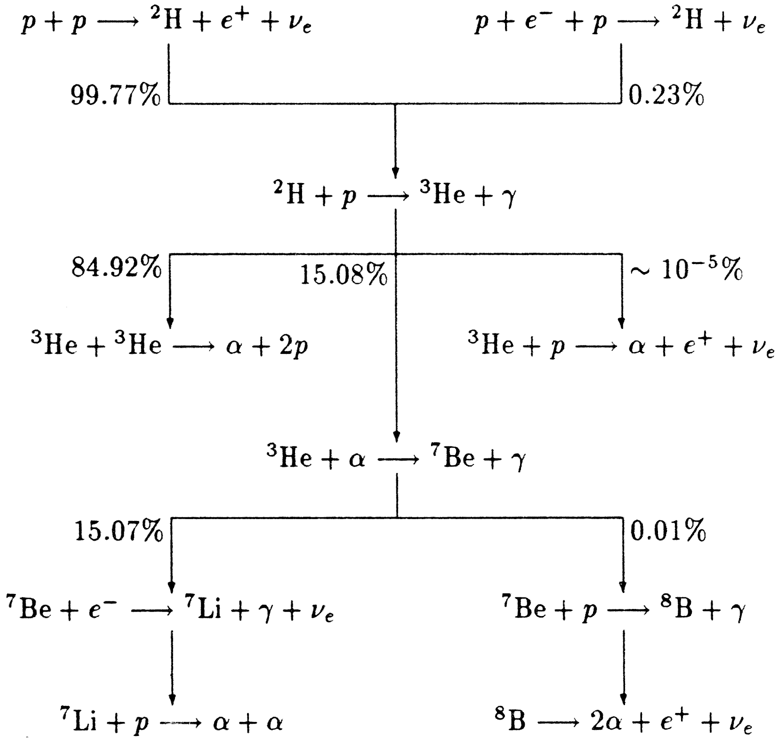

Figure 1.1: The Proton-Proton chain.

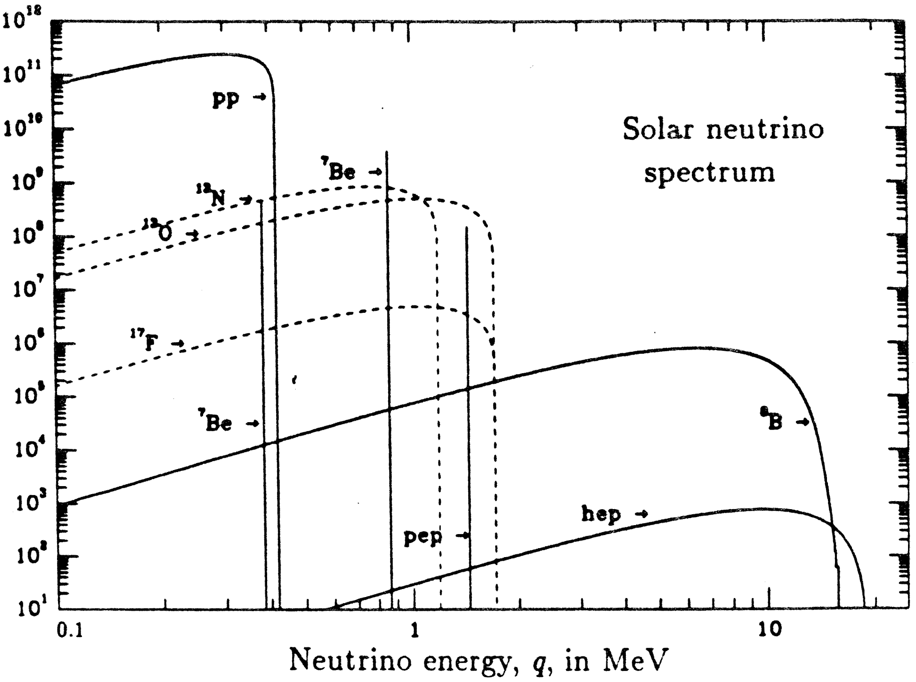

Figure 1.2: Solar neutrino spectrum according to the SSM. Continuum fluxes are in units of $cm^{-2}s^{-1}$MeV$^{-1}$ and line spectra in $cm^{-2}s^{-1}$, both at 1AU.

— the most common termination of the chain. Aside from the minor 'hep' ($^3$He-p) branch, the other possibility leads to the creation of $^7$Be and thence to the important (for existing solar neutrino detectors) $^8$B neutrinos. It may be seen that these neutrinos arise from a very rare branch of the chain.

The predicted neutrino spectrum resulting from SSM's is shown in Figure 1.2 (from Bahcall and Ulrich [8]), which also includes CNO neutrinos. This neutrino spectrum, together with the absolute predicted fluxes, constitute the central prediction of Standard Solar Models of relevance to the present work. Neutrino detectors are intended to obtain information about different aspects of the *true* neutrino spectrum, so that it may be compared with this prediction. It must be noted that the spectrum alone does not predict the rate of neutrino events observable in a given detector: this prediction requires also a knowledge of neutrino interaction cross-sections and is quite a separate problem from stellar modelling.

### 1.1.1 Definition

A solar model consists of a specification, at each point within the sun, of the state variables which describe the solar material. These variables include pressure, temperature, density and composition. The calculation of these parameters is the subject of this section. From such a model may be derived predictions of solar properties such as total luminosity, radius, acoustic oscillation spectrum and neutrino spectrum. A valid solar model is thus constrained by observations of these quantities and by a number of other empirical constraints. A 'Standard Solar Model' (SSM) is defined to be such a model computed using the best available data for its input, without invoking any hitherto unknown physics. However, since the data are known only to limited accuracy, the SSM is not unique: different models can result from different sets of input parameters, each consistent with experiment.

The SSM's to be discussed in this section are those of Bahcall and Ulrich (see [8] and other references below).

### 1.1.2 Input parameters for SSM calculations

The main parameters which are entered into the calculation of a SSM are listed below.

**Nuclear abundances.** The three numbers which characterise the abundances of the various nuclear species present in the sun are the mass fractions of hydrogen, of helium and of all heavier elements, conventionally denoted X, Y and Z respectively. Clearly $X + Y + Z = 1$. The ratio Z/X is an important input parameter to SSM's as it, or rather the individual elemental abundances, determine in large part the radiative opacity of the solar material. The heavy element abundances used by Bahcall and Ulrich [8] are those of Grenvesse [9]. This study and that of Aller [10] are in close agreement.

**Radiative Opacity.** Energy transport within the sun can in principle occur by either of the two mechanisms of photon diffusion (radiation) and bulk convection. Whether a region of the sun is stable or not to convection depends of course on the conditions which prevail in that region. In practice, SSM's assume that the bulk of the sun is quiescent and that the transport mechanism is radiative throughout, apart from a convective envelope comprising a small fraction of the sun's mass. For a plasma in local thermodynamic equilibrium with a radiation spectrum close to that of a black body, the diffusion approximation is appropriate and the material may be characterised by the 'Rosseland mean opacity'. The calculation of opacity is thus critical for the SSM as it determines the temperature and density profile of the sun.

The calculations of the opacity from the composition of the solar material are complex and require large computer codes. They are fully treated by Huebner [13] who details the sequence of calculations necessary for the determination of an opacity. The method is first to establish the structure of the ions (given T), then to calculate the resulting contributions to absorption from bound-bound and bound-free processes and from free-free processes (inverse Bremsstrahlung) and from scattering. The Los Alamos Opacity Library codes were used by Bahcall & Ulrich to evaluate the opacity for the Grenvesse mixture; the results are listed in Table III of Bahcall & Ulrich's paper for the range of temperatures and densities appropriate to SSM's.

**The equation of state** The equation of state (*ie.* relation between P, T and $\rho$) used for the solar plasma (see Rakavy & Shaviv [11] or Schwarzchild [12]) is essentially the ideal gas formula. This is applicable even at densities of order $10^2 g.cm^{-3}$ because at the relevant temperatures, of order $10^7$K, the solar material is fully ionised. Thus the corrections due to the finite volume of gas particles are not significant since the particles are of nuclear, not atomic, dimensions. It is modified by adding the radiation pressure to the dominant thermal pressure and by small corrections due to electron degeneracy and to screening according to the Debye-Hückel formalism [107][1]. The resulting equation is of the form:

$$P = \frac{1}{3}aT^4 + \frac{k\rho T}{\mu M}(1 + D) \tag{1.2}$$

where $\mu$ is the mean molecular weight measured in proton masses, $M$:

$$\frac{1}{\mu} = 2X + \frac{3}{4}Y + \frac{1}{2}Z \tag{1.3}$$

The constant $D$ arises from the above corrections and $a$ is the Stefan-Boltzmann constant.

**Nuclear reaction data** The rate of energy generation in the sun is determined by the reaction rates of the nuclear species present in the sun, *ie.* the cross-sections for the interactions, and by the Q-values for those interactions, less the energy radiated in the form of neutrinos. The energy generation rate is obtained by summing over relevant interactions. While the Q-value is an experimentally accessible quantity, p-p fusion in the sun occurs at thermal energies of a few keV, far below the Coulomb barrier in light elements (but well above kT). Thus the estimation of the low-energy cross-sections is difficult from laboratory data obtained at energies not lower than about 1MeV. An extensive treatment of the experimental techniques and theory needed to arrive at the required cross-sections is given by Rolfs & Rodney [3]. Parker [14] presents an exhaustive treatment of cross-section data and concludes that the relevant cross-sections are sufficiently well understood.

The procedure which allows the extrapolation is to express the cross-section in a form in which the Gamow factor has been separated out:

$$\sigma(E) = \frac{S(E)}{E}e^{-2\pi\eta} \tag{1.4}$$

where

$$\eta = \frac{Z_1 Z_2 e^2}{\hbar v} \tag{1.5}$$

The function S varies slowly with energy as $E \to 0$ below energies of order 1MeV, except in the case of low-energy resonances. The rate of reaction between two given nuclear species is given by an integration over energy of the product $\mathrm{Pr}(v)\sigma(E) \times v$, which contains the product of the Boltzmann and Gamow factors. The result is that a narrow energy window centred about a value $E_0$ (typically between 6 and 10 keV) arises in which the two exponentials are both small but their product is a maximum: this therefore defines the energy range over which the reaction occurs with significant frequency, and thus specifies the energies at which it is necessary to know $S(E)$. This function is determined by extrapolation to energy $E_0$ from laboratory data. Details of

---

[1] Debye-Hückel theory calculates the Coulomb energy density in a gas of charged particles, and from this a 'Coulomb pressure', in the limit that this energy is much less than thermal energies, by calculating the polarising effect on the gas of an individual charge.

how the integration may be performed by expansion of $S$ about $E_0$ in powers of the small quantity $kT/3E_0$ are given by Bahcall [16]. A full discussion of the nuclear data, and uncertainties, may be found in Bahcall *et al.* [15]. Bahcall & Ulrich [8] present an update which collates the best current values for the low energy cross-section factors for the reactions of relevance for the p-p chain. This latter paper also emphasises that the low energy cross-section factor $S(E = 0)$ for the $^7$Be-p reaction is still the largest source of uncertainty in SSM predictions of the high-energy solar neutrino flux.

**Solar age** The age of the sun is presently believed to be about $4.55 \times 10^9 yr$. This estimate derives from known meteoric ages which cluster closely around this value [17]. The time needed for the formation of the sun and of meteorites is not well known, but thought not to be long on this scale.

### Further constraints

1. The sun is in hydrostatic equilibrium. The results of SSM's predict that the sun is in fact expanding very slowly, but the approximation is clearly excellent as the main sequence of stellar evolution is observed to be stable and long-lived for solar-type stars.

2. The surface composition is known. Aller [10] gives an account of how the composition of the solar photosphere is obtained from spectroscopic measurements. An atmosphere model is set up which specifies the effective temperature, gravitational acceleration and composition. Together with laboratory-measured transition probabilities, it allows the calculation of the optical depths appropriate for the observed lines and hence a prediction of their intensity. The composition is varied to obtain agreement with experiment.

### Additional assumptions contained in SSM's

**Uniform composition at zero time** The sun is assumed to have entered the main sequence as a so-called 'zero-age main sequence' star of homogeneous composition. The assumption of homogeneity is an important one as it is equivalent to assuming that the pre-main-sequence sun was convectively mixed. No relevant nuclear transformations are regarded as having taken place during the short pre-main-sequence phase.

The initial homogeneous composition is taken as being identical to the present observed surface composition, the justification being that the convectively mixed surface layers are too cool for nuclear transformations to occur and have not mixed with the convectively stable core. The surface abundances of certain species (Lithium, Beryllium, $^3$He) impose limits on the temperature of solar layers with which the surface is connected by mixing processes (see Schatzman [111]), and eliminate extensive mixing of surface layers with the solar core. It follows that no processes occur to change the surface composition, hence the importance of studying it as a guide to the initial homogeneous composition.

**Convectively mixed envelope** It is assumed that the solar core, stable to convection, is surrounded by an 'envelope' layer where the dominant heat transport mechanism is convective. Schwarzchild [12] derives a condition for a medium to be stable to convection.

### 1.1.3 Calculational Procedure

#### Summary

The calculation of a SSM involves in fact the calculation of an evolutionary sequence of solar models, beginning at $t = 0$ with a sun of known mass $M_\odot$ and known composition, together with the equation of state, nuclear data *etc.* With two other guessed parameters as input to the calculation, the state variables $P$ and $T$ are then uniquely determined for the whole star, and hence the density $\rho$ from the equation of state. This allows the calculation of nuclear reaction rates, and the composition of the next model in the sequence is therefore determined by allowing the reactions to occur for a time step of perhaps $5 \times 10^8 yr$. With the new composition, a new model at the advanced age is computed. This process is repeated until the known age of the sun is attained, and the model luminosity and radius compared with solar values. The two initially guessed parameters are then iterated and the whole procedure repeated until agreement with observation is obtained.

#### Calculation of a solar model

The differential equations which determine the stellar structure for a quasi-static star are (see Schwarzchild [12] for a clear treatment):

$$\frac{dP}{dr} = -\frac{\rho G M}{r^2} \tag{1.6}$$

$$\frac{dM}{dr} = 4\pi r^2 \rho \tag{1.7}$$

$$\frac{dL}{dr} = 4\pi r^2 \rho \epsilon \tag{1.8}$$

$$\frac{dT}{dr} = -\frac{3}{4ac}\frac{\kappa\rho}{T^3}\frac{L}{4\pi r^2} \tag{1.9}$$

where $M$ is the mass included within radius $r$, $\epsilon$ is the energy generation rate per unit mass, $\kappa$ is the opacity and $L$ the luminosity at radius $r$. Equation 1.6 is the equation of hydrostatic equilibrium and 1.9 the equation for radiative energy transport. We also have:

$$P = P(\rho, T, X, Y) \tag{1.10}$$

$$\kappa = \kappa(\rho, T, X, Y) \tag{1.11}$$

$$\epsilon = \epsilon(\rho, T, X, Y) \tag{1.12}$$

for the equation of state, the opacity and the rate of energy generation. Finally we have boundary conditions at two boundaries:

$$r = 0 : \quad M = 0, \ L = 0 \tag{1.13}$$

$$r = R_\odot : \qquad T = 0,\ P = kT^{2.5} \tag{1.14}$$

Substituting the three relations 1.10-1.12 into the differential equations 1.6-1.9 yields four D.E.'s in the variables $T, P, L, M$ as functions of $r$ with four boundary conditions. It is clear that the problem is well-specified and has a unique solution. It follows that a star of given $M_\odot, X, Y$ has exactly one equilibrium configuration. In practice, the approach is to use Equation (1.7) to transform the other three D.E.'s into a form where $M$ is the independent variable. It is thus necessary to integrate from $M = 0$ (centre) to $M = M_\odot$ (surface). The boundary conditions now take the form:

$$M = 0 : \qquad L = 0,\ r = 0 \tag{1.15}$$

$$M = M_\odot : \qquad T = 0,\ P = kT^{2.5} \tag{1.16}$$

However, on integrating from the centre outwards, one encounters an instability due to the appearance of T in the denominator of Equation (1.9), *ie.* a very small change in the central temperature causes a large change in the conditions in the envelope. A similar problem occurs on integrating from the surface inwards, due to the factor $r^{-2}$ in Equation (1.6). The approach used is thus to perform integrations both inwards and outwards and to match the solutions at an appropriate boundary within the star. Bahcall's calculations use fourth order Runge-Kutta integration and match the solutions around $0.2M_\odot$. For the inward integration, the boundary condition provides starting values for $T, P$ but not $L, R$; whereas for the outward integration the converse is true. The trick is, for each integration, to let the unspecified dependent variables at each boundary take trial values, or rather a whole set of trial values, and follow through the integrations for each set. Thus rather than just one solution being followed from the centre outward and from the edge inward, families of trial solutions are evaluated. The true solutions are required to satisfy at the boundary $T_i = T_o$, $P_i = P_o$, $L_i = L_o$, $R_i = R_o$, where the subscripts obviously refer to the inner and outer solutions. This provides four conditions which fix $R$ and $L$ at the surface, $P$ and $T$ at the centre. This completes the solution of a solar model given a set of input parameters as specified above.

### Time evolution

Having calculated the zero-age homogeneous main sequence model (for a given set of input parameters), it is then possible to use the temperature–density profile of the star thus obtained to calculate, in each concentric mass shell, the rates of each nuclear reaction of interest. These are then multiplied by a time step, typically $5 \times 10^8 yr.$ and the new, non-uniform, composition determined. A succession of further models is then calculated using reaction rates interpolated between the previous and new models. The detailed procedure used to integrate the nuclear abundance equations is given by Bahcall [15].

A succession of models is then calculated, the composition of each being determined from the previous model. The parameters $T, P, L$ are determined for each model, as is its radius $R_\odot$. The end-product of the sequence is a model of age equal to the solar age — the radius and luminosity of the model are compared with the accurately-measured astronomical data. The aim is an agreement between calculation and experiment to within 1 part in $10^4$. In order to achieve this, however, it is necessary to have chosen appropriate values of the two parameters which were guessed at the inception of the evolutionary sequence.

These two parameters, mentioned in passing above, are, in Bahcall's models, the initial homogeneous hydrogen mass fraction, $X$, and an entropy-like variable $S$ which determines the constant $k$, which appears in Equation (1.14), and describes the conditions in the solar convective envelope (see [15]). The first of these variables fixes the primordial helium abundance since $Z/X$ is an input parameter and $X + Y + Z = 1$. Equation (1.14) follows from stating that the energy transport is entirely convective in the envelope and thus that the temperature gradient is the adiabatic temperature gradient (see [12]), with $\gamma = C_p/C_v = \frac{5}{3}$ for a completely ionised gas. The relation is thus only applicable to temperatures above about 50,000K where H and He are completely ionised. Bahcall *et. al.* [15] detail the treatment of the cooler solar atmosphere zone, which is taken to comprise $10^{-3}M_\odot$.

With the aid of empirical equations, the parameters $X$ and $S$ are adjusted so as to move the final, fully evolved, model towards the observed solar parameters $R_\odot$ and $L_\odot$. The entire sequence of calculations, commencing with a zero-age main sequence model having the adjusted parameters, is then re-calculated and the procedure iterated until satisfactory agreement is reached, typically after just a few iterations. (Roxburgh, however [18, 19] has pointed out that this procedure amounts to fitting two parameters to two observations, and is thus poorly constrained.) This completes the calculation of a SSM.

## 1.2 Neutrino interaction cross-sections

Before an event rate in a detector can be used to infer a neutrino flux, the interaction cross section for neutrinos in the detecting material must be known at the energy of interest, or the detector calibrated by exposure to neutrino sources such as $^{51}$Cr or $^{65}$Zn. The determination of neutrino interaction cross-sections for all detectors of interest is extensively dealt with by Bahcall [16] and Bahcall & Ulrich [8], and the uncertainties analysed.

Three main classes of interaction are possible:

$$\text{Absorption:} \quad \nu_e + {}^{Z}A \longrightarrow e^- + {}^{(Z+1)}A \tag{1.17}$$

$$\nu - e \text{ scattering:} \quad \nu + e^- \longrightarrow \nu' + e^{-\prime} \tag{1.18}$$

$$\text{Neutral current:} \quad \nu + {}^{Z}A \longrightarrow \nu' + {}^{Z}A' \tag{1.19}$$

The first interaction is the basis of radiochemical detectors such as $^{37}$Cl, $^{71}$Ga and $^{115}$In and includes the inverse beta decay reaction to be used in SNO for determination of the neutrino energy spectrum. The second allows the construction of water Cherenkov detectors: Kamiokande, IMB and SNO. The third interaction, in which a neutral current interaction leaves the nucleus in an excited state, is the general case of the deuteron disintegration reaction to be observed in SNO. (It may be seen, therefore, that SNO is sensitive to all three classes of possible neutrino interaction). The main efforts have been made in the direction of determining the cross section, as a function of energy, for reactions of type Equation (1.17). A fourth class of reaction exists, in which a neutrino undergoes coherent scattering off a nucleus, with the result that a recoiling nucleus of a few keV energy is produced: the cross-section for such an interaction is enhanced over the single-particle case by a factor of order $N^2$, $N$ the number of nucleons. This reaction is only detectable in cryogenic detectors.

The general expression for absorption cross-sections is given by Bahcall as [16]:

$$\sigma \propto (G_v^2\langle 1\rangle^2 + G_a^2\langle\sigma\rangle^2)P_eW_eF(Z,W_e) \tag{1.20}$$

which involves the weak interaction matrix elements — $\langle 1\rangle$, the Fermi matrix element, and $\langle\sigma\rangle$, the Gamow-Teller matrix element. $P_e$ and $W_e$ are respectively the electron's momentum and energy and $F(Z,W_e)$ is the Fermi function appropriate to the daughter nucleus. Bahcall, however, shows that the cross-section can be re-cast in the more convenient form

$$\sigma = (\text{const.}) \times \frac{1}{ft_{1/2}}\frac{2I'+1}{2I+1}\left\langle\frac{w_e p_e F(Z,W_e)}{2\pi\alpha}\right\rangle \tag{1.21}$$

where the $ft_{1/2}$ value contains the weak interaction matrix elements appropriate to a beta decay transition linking the final and initial nuclear states (having spins $I'$ and $I$ respectively) of the neutrino absorption process ($w_e$ and $p_e$ are here the electron's energy and momentum expressed in units of $m_ec^2$ and $m_ec$ respectively). The advantage of using this form is that the phase space factor $f$ is relatively easily calculable and $t_{1/2}$ is a measured parameter of a beta decay. The $ft_{1/2}$ value can thus, in the case of ground-state to ground-state transitions, be determined from beta decay experiments.

For transitions to excited states, this is not possible and the only favourable (*ie.* calculable) case is when the transition rate is dominated (as with $^{37}$Cl and $^{40}$Ar) by a (superallowed) transition to an analogue excited state in the daughter atom. For other cases, often of relevance for the measurement of the high-energy neutrino flux ($^8$B and hep neutrinos), transition probabilities to excited states must be estimated from (p,n) reaction data: there is evidence [31] that the ratio of cross-sections for (p,n) transitions between a pair of states is approximately equal to the ratio of the squared weak interaction matrix elements. Thus one can in principle obtain absolute cross-sections for transitions to excited states by normalising to a well-known analogue state transition or to a transition accessible to beta-decay experiments. However, relatively little data is available and it applies only to low mass nuclei — a large extrapolation is needed to use the method for high-mass isotopes such as $^{71}$Ga, $^{81}$Br, $^{98}$Mo, $^{115}$In, $^{205}$Tl. In view of these complications, Bahcall adopts a factor of 2 uncertainty in matrix elements which must be determined solely from (p,n) data.

### 1.2.1 The electron scattering cross-section

The expression for the cross-section for $\nu - e$ scattering is given by t'Hooft [30] as:

$$\frac{d\sigma}{dT} = \frac{2G_F^2m_e^2}{\pi\hbar^4}\left[G_L^2 + G_R^2(1 - T/q)^2 - G_LG_R(m_eT/q^2)\right] \tag{1.22}$$

where

$$G_L = \pm\frac{1}{2} + \sin^2(\theta_W) \quad (+ \text{ for } \nu_e, - \text{ for } \nu_\mu)$$

and $G_R = \sin^2(\theta_W) = 0.2300 \pm 0.0020$ [33], $T$ is the recoil energy of the electron in electron mass units and $q$ the incoming neutrino energy.

Neutrinos of a given initial energy $q$ are capable of giving rise to recoil electrons of energies from zero to a maximum value $T'_{max}$. Electron scattering experiments invariably detect only electrons above an energy threshold $T_{min}$ and so to obtain the total event rate induced by a neutrino spectrum, it is necessary to integrate the above cross-section, weighted by the anticipated neutrino spectrum, between $T_{min}$ and $T_{max}$. The results of such a calculation for $^8$B neutrinos are tabulated by Bahcall [16] for various values of $T_{min}$.

In the absence of resonant oscillations between neutrino flavours (see Section 1.4.2), the spectral shape will be undistorted and will depend only on the nuclear physics processes occurring in the sun; in this case a comparison of experiment and calculation gives the rate of neutrino production directly. (In the case of SNO, spectral distortion shows up in the absorption, or inverse beta decay, reaction, for which the electron recoil is essentially mono-energetic for a mono-energetic neutrino beam). Since the $\nu - e$ scattering cross-section has an analytic expression, there is little uncertainty in its magnitude. Bahcall & Ulrich [8] give event rates for reasonable thresholds, including absorption and $\nu - e$ scattering for $1kt$ $D_2O$.

One may also determine the differential cross-section for the production of an electron of kinetic energy $T$: this may be obtained by integrating the above expression for $d\sigma/dT$, weighted by the normalised neutrino spectrum, between energies $q_{min}$, the minimum neutrino energy capable of giving rise to a scattered electron of energy T, and $q_{max}$, the end point of the neutrino spectrum. It follows that the observed electrons of energy $T$ 'sample' a band of the neutrino spectrum, rendering $\nu - e$ scattering a less-than-useful tool for determining the spectral shape. $\nu - e$ scattering does, however, afford information not accessible *via* an absorption reaction: the recoil direction of the electron is kinematically constrained to lie within a cone whose axis is the incoming neutrino direction. A measurement of the electron's direction (such as may be performed in water Cherenkov detectors) thus gives an indication of the direction of the neutrino flux.

The electron scattering cross-section for muon neutrinos at the energies of interest to the solar neutrino problem is less by a factor of about 6 to 7, approximately independent of energy. This is due to the presence of a charged current process contributing to $\nu_e - e$ scattering which does not contribute to $\nu_\mu - e$ scattering — the latter process occurs only *via* a neutral current process which is flavour-independent to high accuracy.

## 1.3 Existing solar neutrino detectors

### 1.3.1 The Homestake $^{37}$Cl detector

The $^{37}$Cl experiment consists of 615 tons of tetrachloroethene, $CCl_4$, in a tank 4850ft underground (4100 mwe) in the Homestake Gold Mine in Lead, South Dakota. The active isotope is 24.23% of natural chlorine which captures neutrinos according to the reaction:

$$\nu_e + {}^{37}\mathrm{Cl} \longrightarrow {}^{37}\mathrm{Ar} + e^- \tag{1.23}$$

The capture rate in the detector according to the SSM has been predicted [8] as

$$\begin{aligned} &7.9(1 \pm 0.33)\ \mathrm{SNU} \\ &1.5(1 \pm 0.33)\ {}^{37}\mathrm{Ar}\ \text{atoms per day} \end{aligned} \tag{1.24}$$

where

$$1\ \mathrm{SNU} \equiv 1\ \text{event per } 10^{36}\ \text{target atoms per day}$$

and is a useful unit for intercomparison of neutrino detecting materials, rather than complete detectors, since it includes no consideration of detector size and counting efficiency or detector backgrounds.

Although the threshold for this reaction is 0.814MeV and it is thus sensitive to all solar neutrino sources except p-p, the dominant contribution to this rate comes from $^{8}$B neutrinos, which are energetic enough to excite the analogue state in $^{37}$Ar, with the next largest contribution deriving from $^{7}$Be neutrinos.

The production of radioactive $^{37}$Ar, which has a half-life of 35 days to electron capture, the inverse of the above reaction, is determined by extraction from the tank of the $^{37}$Ar, along with added $^{38}$Ar carrier, by a purge with He gas. The extracted Argon is then isolated and purified of radioactive Krypton, Xenon and Tritium before injection, with a few percent added methane, into a small proportional chamber. The Auger electrons produced after electron capture can be counted over a period of months. The method of identification of $^{37}$Ar decays based on rise time as well as pulse height information is described, which was introduced in 1970 and marks the beginning of the recently-published data sets.

The definitive description of the detector is given by Davis *et al.* [21], including details of the procedure for Argon extraction, tests which demonstrate that the efficiency of the extraction is at least 95%, and investigations of the possible formation of C-Cl-Ar complexes by the free $^{37}\mathrm{Ar}^{+}$ ion before neutralisation: these would trap the $^{37}$Ar in the tank without showing up as an inefficiency in the extraction of carrier $^{38}$Ar. The main test which has not been performed on the $^{37}$Cl detector is direct calibration by exposure to a neutrino source, $^{65}$Zn for example.

Background processes in the chlorine experiment are all initiated by high-energy muons. The principal reaction is $^{37}\mathrm{Cl(p,n)}^{37}\mathrm{Ar}$ where the protons derive from (n,p) reactions on $^{35}$Cl or ($\gamma$,p) reactions on any nuclide. There is also a contribution from cosmic-ray-produced muon- and electron-neutrinos. Backgrounds due to cosmic-ray muons have been assessed by two different methods, using $^{37}$Cl directly and by using $^{39}$K. The first is reported by Wolfendale *et al.* [20] and by Davis *et al.* [21]. Three 6800 litre tanks of tetrachloroethene were exposed at relatively shallow levels in the Homestake mine and the $^{37}$Ar extracted in the normal manner. The production rate was extrapolated to the 4100 mwe level of the solar neutrino detector using a formula which states that any nuclear event rate which derives from fast muons should vary with depth as $N(h)\langle E\rangle^{0.7}$ where $N(h)$ is the flux and $\langle E\rangle$ the mean energy at depth $h$.

An experiment using $^{39}$K to measure the cosmic-ray-muon-induced background is reported by Fireman *et. al.* [24]. $^{37}$Ar production rates were again measured using a helium purge. The much higher event rates per unit mass (by a factor of about 100) in potassium compared to chlorine meant that this experiment could be run at greater depths than the chlorine trials, indeed runs were performed at the 4850ft level of the neutrino detector. Furthermore, solar neutrinos are energetically forbidden from contributing to the rates in the potassium experiment. The processes contributing to $^{37}$Ar production in $^{39}$K are:

$$\begin{aligned} \mu + {}^{39}\mathrm{K} &\longrightarrow \mu + n + p + {}^{37}\mathrm{Ar} \\ n + {}^{39}\mathrm{K} &\longrightarrow 2n + p + {}^{37}\mathrm{Ar} \end{aligned}$$

Any reaction producing secondary neutrons therefore contributes to the event rate. The rates observed at shallow depths with $^{39}$K were normalised to those observed with $^{37}$Cl: the variation with depth was in good agreement with the above formula. The studies with Cl and K lead to the presently-quoted background rates of $0.08 \pm 0.03$ $^{37}$Ar atoms per day.

The average $^{37}$Ar production rate over the period 1970 to 1988 is given by Davis *et al.* [23] as:

$$\begin{aligned} 2.33 \pm 0.25 &\quad \mathrm{SNU}\ (1\sigma\ \mathrm{error}) \\ 0.438 \pm 0.047 &\quad {}^{37}\mathrm{Ar\ atoms\ per\ day} \\ \mathrm{Data/SSM} &= 0.30 \end{aligned}$$

with a production rate approaching twice this value during the period 1986-1988.

### 1.3.2 The Kamiokande II detector

A water Cherenkov detector has been operated in the Kamioka mine in Japan since July 1983. The first phase of operation, Kamiokande I, was as a high-threshold nucleon decay experiment: this phase is not discussed here. The upgraded Kamiokande II experiment is briefly described here: a detailed description of the detector is given by Soo Bong Kim [22].

The detector is 1000$m$ underground (2700mwe) and contains 3000 tons of light water in a cylindrical tank 15.6$m$ in diameter by 16$m$ high. The water is divided into two optically separate parts: an inner cylinder containing 2140 tons monitored by 948 phototubes and a 1$m$ thick outer layer monitored by 123 tubes as a cosmic ray veto. The requirement to shield against backgrounds similar to those of relevance to SNO (see Chapter 2 herein) results in the solar neutrino signal being taken only from a central fiducial volume of 680 tons.

The phototubes are R1449X 20" diameter Hamamatsu tubes which have no single photoelectron response and a transit time spread of 14$ns$. Those monitoring the inner water volume are arranged on the walls of a cylinder 14.4$m$ in diameter by 13.1$m$ high. Pulse height and timing information is recorded for each tube. The detector's trigger threshold has decreased with time as backgrounds have been reduced and is reported by Totsuka [32] to be currently around 5MeV.

Energy calibration of the detector was achieved by exposure to gamma-rays from a Ni(n,$\gamma$) source, and is known to better than 3%. Gamma-rays from the same source were used for evaluating the angular resolution with which it was possible to reconstruct events, and good agreement with Monte-Carlo studies was obtained.

Observation of solar neutrinos by the K-II detector was first reported by Hirata *et al.* [72]. On the basis of low-background data taken from January 1987 to April 1990, 1040 live detector days, the Kamiokande detector has made a measurement of the $^8$B solar neutrino flux. The analysis procedure makes a number of cuts in the data which suppress background sufficiently so that the signal is visible.

1. Large signals in the anticoincidence shield are rejected so that only contained events are studied.
2. Vertex reconstruction is followed by a fiducial cut to the central 680 tons.
3. A 'spallation cut' is imposed to reject events due to cosmic-ray-muon-induced beta emitters with lifetimes from about $20ms$–$5s$ by examining the proximity of the event to a preceding muon.
4. Events in the outer region of the fiducial volume are rejected if they point inward, away from the PMT cylinder.

These cuts imposed, the fitted directions of electron tracks show a pronounced peak, pointing away from the sun, superposed on an isotropic background. The experimental peak is fitted to an a peak of width given by the angular distribution expected of scattered electrons folded with the detector angular resolution; events in the peak then represent the signal. Totsuka reports a flux relative to the SSM of

$$\frac{\mathrm{K-II}}{\mathrm{SSM}} = 0.46 \pm 0.05(\mathrm{stat.}) \pm 0.06(\mathrm{syst.}) \tag{1.25}$$

for electrons of measured energies above 7.5MeV (590 days) and 9.3MeV (450 days). Data analysed using two different threshold energies are rendered comparable by normalising to the appropriate SSM prediction.

### 1.3.3 The SAGE $^{71}$Ga experiment

Of existing neutrino detectors, only experiments using $^{71}$Ga as a neutrino absorber can detect the abundant low-energy pp neutrinos. It will be seen in a later section that information concerning these neutrinos is complementary to that gained by detecting the $^8$B and other high-energy components of the solar neutrino flux.

The reaction

$$\nu_e + {}^{71}\mathrm{Ga} \longrightarrow e^- + {}^{71}\mathrm{Ge} \tag{1.26}$$

has a threshold energy of 0.2332MeV and is thus suitable for detecting the pp neutrinos, whose energies lie below 0.42MeV. The largest single contribution to the predicted capture rate of $132^{+20}_{-17}$ SNU [8], comes from pp neutrinos (54%), but the reaction is clearly sensitive to solar neutrinos from all reactions of the p-p chain. The dominant uncertainty in the prediction derives from transitions to excited states in $^{71}$Ge, whose matrix elements must be determined by (p,n) studies. Bahcall *et al.* [25] have derived a minimum rate in a Gallium experiment of 80 SNU, based on a 'minimum' model which assumes that only pp and pep neutrinos are generated in the sun and that the sun is in energy equilibrium. This is a minimum model in that it relies only on the fundamental idea that pp fusion powers the sun, and derives fluxes based on considerations of energy balance alone. If Gallium experiments measure fewer than 80 SNU, this would strongly indicate that the neutrinos are altered in transit from sun to earth.

There are two existing Gallium experiments, in Italy and the USSR. GALLEX — in the Gran Sasso underground laboratory — consists of 30 tons of Gallium as 8.13M $GaCl_3$ solution (see Kirsten [27]), whereas SAGE (Soviet-American Gallium Experiment) plans to use eventually 60 tons (currently taking data with 30 tons) of molten metallic Gallium. Only the SAGE experiment will be described in any detail here, since it has already reported preliminary results. Much of the Germanium extraction and counting procedure is common to the two experiments.

The SAGE detector is located in a purpose-built laboratory beneath Mount Andyrchi in the Northern Caucasus, which furnishes a shielding of 4700mwe. The 30 tons Gallium currently in use are contained in PTFE-lined reactors of $2m^3$ volume which are heated so that the Gallium is kept molten (m.p. 29.8°C), and continuously stirred.

The length of a run during which $^{71}$Ge, which constitutes the signal in this experiment, is accumulated in the Gallium is typically about 4 weeks, and is dictated by the $^{71}$Ge half-life. At the beginning of this period, $\simeq 120\mu g$ natural Germanium is added to the Gallium as a carrier and as a tracer whose measurable extraction efficiency is used to determine that of $^{71}$Ge. At the end of a run, dilute HCl is added to the reactors and the Ga/HCl mixture emulsified by stirring. On allowing the emulsion to separate, Germanium is retained in the aqueous phase, and is drawn off from the reactors, the separate extracts being then combined. The dilute solution is then concentrated by vacuum distillation, and brought up to 9N concentration by addition of further HCl. An Argon purge transfers the Germanium, as $GeCl_4$ gas, into $1l$ water. Solvent extraction into $CCl_4$ followed by back-extraction into water further reduces the volume of material in which the Germanium is contained[2]. Finally, a small volume of the gas Germane, $GeH_4$ is evolved by addition of Sodium Borohydride, and this, with a measured quantity of Xenon, is transferred into a miniature quartz proportional counter, where it is retained for 2-3 months. The Germanium extraction efficiency is determined by atomic absorption spectroscopy and finally verified by measurement of the volume of synthesised Germane.

$^{71}$Ge decays by electron capture (the inverse of reaction 1.26) with a half-life of 11.4 days. The only signature of electron capture by $^{71}$Ge is the Auger electron emission of the resulting

---

[2] $GeCl_4$ is soluble in water at pH7, but not at low pH: this allows an Argon purge to remove it from strong acid and allows its partition constant between aqueous and organic phases to be controlled by controlling the pH of the aqueous phase.

$^{71}$Ga atom. Auger electrons following K and L capture (of 10.4keV and 1.2keV energies respectively) are thus detected by the ionisation which they deposit in the counter. Pulses from the counter are passed to an ADC and are also differentiated, allowing their pulse height and rise time to be determined.

Since the expected number of detectable $^{71}$Ge decays is only four, taking account of the counting and extraction efficiencies, detector backgrounds must clearly be kept to around 1 month$^{-1}$. The dominant source of background is fast electrons traversing the counter, originating from natural radioactivity — cosmic rays are not significant. The required background suppression is achieved by fabricating the counter of ultra-pure materials and inserting it into a cavity within a NaI crystal, itself surrounded by a large passive shield. The crystal serves as an anti-coincidence shield and vetoes events associated with external activity. Further background rejection is obtained by imposing pulse height and rise time cuts on the data — an extended ionisation track corresponding to an electron crossing the counter gives a slower pulse than does the point-like energy deposit resulting from an Auger electron. The position of the window around the 10.4keV K peak in pulse-height/risetime space is determined by individually calibrating the counters using an $^{55}$Fe source of 5.9keV X-rays. The position of the energy window is determined by scaling linearly with energy and its width with $\sqrt{E}$. The position and width of the risetime window is taken to be identical for the K peak and $^{55}$Fe. Including neutron-irradiated Germanium in a counter confirmed this procedure's validity.

Backgrounds to the $^{71}$Ge signal include production by secondary protons initiating the reaction $^{71}$Ga(p,n), the protons deriving from external neutrons, cosmic ray muons and internal radioactivity. These backgrounds have been estimated at not more than 0.025 atoms per day per 30 tons Gallium, to be compared with a signal of 1.17 atoms/day (see Bahcall [16] or Abazov *et al.* [26]). Another background arises from long-lived cosmogenic $^{68}$Ge produced while the Gallium was on the surface: it decays by electron capture and is thus *completely indistinguishable* in the proportional counter from $^{71}$Ge. This background source could only be removed by repeated extractions.

The $^{71}$Ge content of a counter was determined by maximum-likelihood fitting of the data to a 11.4$d$ decay plus a constant background. Abazov *et al.* report a best fit to their data from four extractions of 0 SNU with 68% and 95% confidence limits of 72 SNU and 138 SNU respectively, not allowing for a possible difference between the extraction efficiencies of carrier Germanium and $^{71}$Ge. The experiment awaits calibration with a $^{51}$Cr neutrino source.

## 1.4 Proposed solutions to the solar neutrino problem

Two main classes of solution to the Solar Neutrino Problem have been proposed. The first comprises the Non-Standard Solar Models which alter the measured neutrino flux by some modification of the assumptions which underlie the SSM. Most of these models lower the core temperature of the sun by a small amount which, because of the great temperature sensitivity if the $^{8}$B flux predictions ($\sim T^{18}$ according to Bahcall and Ulrich [8]), is sufficient to lower that flux by the required factor. Although these models postulate modifications to the simplest-possible assumptions of the SSM, such changes are within the framework of the standard model of electroweak interactions.

By contrast the second class of proposed solutions to the SNP introduces physics beyond the standard model to account for the observed deficit of detectable neutrinos. The most popular model postulates that $\nu_e$ emitted by the sun are converted to another flavour state *in transit*, and are then undetectable in radiochemical detectors and induce a greatly reduced response in Cherenkov detectors., Hypothetical Weakly Interacting Massive Particles have also been proposed as a means of lowering the solar core temperature by introducing another energy transport mechanism. In order to be effective, however, there are strict requirements on their mass and cross-sections for scattering and annihilation. They are not discussed further here. Bahcall [16] gives an overview of proposed solutions to the SNP.

### 1.4.1 Non-standard solar models

Many modifications to the SSM have been proposed since it became apparent that the $^{37}$Cl experiment yielded values which were significantly lower than predicted. Since the experiment is primarily sensitive to $^{8}$B neutrinos, most of these models aim at reducing this flux, the commonest method being to lower the central temperature of the sun whilst maintaining the luminosity. This approach works because the $^{8}$B flux is strongly temperature dependent via the Coulomb barrier controlling the reaction

$$^{7}\mathrm{Be} + p \longrightarrow {}^{8}\mathrm{B} + \gamma \tag{1.27}$$

which is followed promptly by:

$$\begin{aligned} {}^{8}\mathrm{B} &\longrightarrow {}^{8}\mathrm{Be}^{*} + e^{+} + \nu_e \\ {}^{8}\mathrm{Be} &\longrightarrow 2\alpha \end{aligned}$$

Bahcall & Ulrich [8] estimate that:

$$\phi(^{8}\mathrm{B}) \propto T_c^{18}$$

($T_c$ the central temperature) on the basis of 1000 SSM's constructed by allowing five of the most uncertain input parameters to take random values normally distributed according to their estimated uncertainties. Although this result can be taken as meaning that the prediction of the $^{8}$B flux is very sensitive to central temperature, and is thus correspondingly unreliable, it also follows that a measurement of the flux $\phi(^{8}\mathrm{B})$ determines this temperature to better than 1%, and thus constitutes a uniquely accurate probe of conditions in the solar core.

Non-Standard Solar Models (NSSM's) have been recently reviewed by, for example, Bahcall [16] and Newman [37]. Some of the main possibilities are outlined below.

**Rapid core rotation.** Were the solar core to be rotating very much more rapidly than the surface (which has a 27 day period), an extra term would be introduced into the equation of hydrostatic equilibrium:

$$2\rho(r)\Omega^2(r)\frac{r}{3}$$

The result of this would be to decrease the load on thermal pressure and thus lower the core temperature $T_c$ for the same total pressure. Bahcall shows that for a 1% effect, the core angular velocity would have to be 1000 times greater than that at the surface. The consistency of this requirement with the current limit on solar oblateness ($\leq 2 \times 10^{-5}$) has not been investigated. However, from helioseismological measurements, no evidence has to date been found which indicates that omega is a function of $r$ down to about $0.3R_\odot$ [34, 35, 36]. Indeed, the constancy of $\Omega$ is surprising, requiring a transport mechanism for angular momentum in the convectively stable core, since a mechanism is known by which the solar wind can brake the sun's rotation.

**Strong core magnetic field.** The function of a strong magnetic field confined to the solar core is much the same as that of core rotation. An extra term for the magnetic pressure is added to the hydrostatic equilibrium equation which allows a decrease in core temperature for the same pressure. Such fields have been investigated theoretically and are found to have decay times much less than the age of the sun, therefore requiring some unspecified mechanism to maintain them.

**Accretion.** A key assumption upon which solar interior opacity calculations are based is that the (unobservable) interior heavy-element composition is identical with that at the (observable) surface, taken to be the primordial composition. This assumption clearly breaks down if some accretion of the interstellar medium has occurred onto the solar surface. At present there is not thought to be enough material available for accretion unless the sun has, at some time in its history, passed through a dense cloud. If heavy elements have been accreted onto the surface, this would imply an over-estimate of the interior opacity with a consequent lowering of the central temperature. Newman concludes that the probability of sufficient accretion having occurred is in the region of 5%.

**Initial homogeneity.** A further key assumption required for setting up the initial conditions for the SSM is that the sun was initially homogeneous. This clearly requires the existence of a well-mixed pre-main-sequence phase in stellar evolution, presumably of relatively short duration. The subject of stellar collapse from a diffuse cloud has been treated in detail by Winkler and Newman [41, 42, 43], who critically review previous treatments of the problem, emphasising computational difficulties and the dependence of the results on the chosen initial conditions. They present a full hydrodynamic treatment for the simplified case of the collapse of a non-rotating, spherically symmetric, slightly Jeans-unstable cloud. (The Jeans condition for stability is that the gravitational and thermal energy of the cloud be equal).

In their model, Winkler and Newman show that convection is not important until a late stage in the collapse, but cut off their treatment slightly before the star reaches a zero-age main-sequence state, when nuclear burning and convection are expected to complicate matters. The time-scale for the collapse is a few times $10^5$ years. It is clear that angular momentum must be considered in a real case, and that spherical symmetry is almost certainly broken — the shape of the solar system strongly suggests a disk structure and accretion disks are known to be associated with T-tauri stars. These modifications, however, would introduce many more parameters into the model.

In summary, it seems that no reliable model of the pre-main sequence phase exists, and it is far from clear whether or not a star must necessarily pass through a convectively mixed state.

**Mixing in the core.** SSM's show that, with time, core temperature increases as hydrogen is depleted there (and thus, in the absence of any compensating effect, the p-p rate decreases). A suggested mechanism for lowering of the core temperature is thus that the core is mixed with material from the outer layers, which is richer in hydrogen. Bahcall, Bahcall and Ulrich [40] have shown that mixing must have been extensive in order to obtain agreement with the $^{37}$Cl experiment. There are a number of objections to the mixing hypothesis:

1. Mixing of hydrogen-rich gas into the core would undoubtedly lengthen the lifetime of stars if it were universal. This is undesirable since the ages of stars in the oldest globular clusters are apparently already as great as that of the universe. The fraction of mixed material thus cannot be large without a contradiction, which seems to rule out the extensive mixing scenario required by Bahcall, Bahcall and Ulrich.
2. Mixing a star requires an energy input to counter the gradient of mean molecular weight built up by hydrogen burning to helium: to transport hydrogen into the core requires that heavier helium be displaced from the bottom of the gravitational potential well. Spruit [39] concludes that the supply of rotational energy to achieve this throughout the core does not now exist in the sun and never has existed. He also notes that a thin region at the base of the convective zone may be thus mixed, and that this can account for the lithium depletion seen in the sun and other stars. Dilke and Gough [38] have demonstrated that the $^3$He gradient built up by nuclear burning could induce an instability of the core to low-order g-modes, with the possibility of mixing of the core at these times; the mixing process would itself then smooth out the gradient and the instability condition would not then be fulfilled until the gradients had built up once more. The consequence of this would be large, periodic variations in solar luminosity with associated excursions of the $^8$B neutrino flux. Although Dilke and Gough suggested this mechanism as a cause of terrestrial ice ages, there is no hard evidence for such luminosity excursions. Even a small damping, moreover, would stabilise the core to this perturbation.

**Non-Maxwellian statistics.** Newman points out that it is not demonstrated that the two-body Maxwell-Boltzmann velocity distribution is correct in the presence of long-range Coulomb forces. Since the nuclear reaction rates depend entirely upon particles in the extreme tail of the distribution (see discussion in Section 1.1), a small distortion could conceivably alter the rates significantly. Conversely, that plasma effects do distort the M-B tail has also not been shown.

### 1.4.2 Neutrino oscillations

The possibility that the weak interaction neutrino eigenstates might not be identical with the mass eigenstates was first raised by Pontecorvo [44] in a study of lepton number non-conservation possibilities. He postulated processes such as $\nu_e \rightleftharpoons \mu_\mu$ and $\nu \rightleftharpoons \bar{\nu}$ which would result in a decrease in observable solar neutrinos at the earth's surface. Gribov and Pontecorvo [45] pointed out that these transitions led to neutrino oscillations *in transit* between their points of production and detection, in analogy to the neutral Kaon system, *ie.* that the probability that a particle created as $\nu_e$ will be observed as $\nu_e$ varies sinusoidally with source-detector distance, in the case that the mass eigenstates are not degenerate.

#### Vacuum oscillations

We can in general express the flavour eigenstates as a linear superposition of the mass eigenstates. In the two-neutrino case usually discussed the expression takes the form of a rotation matrix containing one parameter $\theta$:

$$\begin{pmatrix} \nu_e \\ \nu_x \end{pmatrix} = \begin{pmatrix} \cos\theta & \sin\theta \\ -\sin\theta & \cos\theta \end{pmatrix} \begin{pmatrix} \nu_1 \\ \nu_2 \end{pmatrix} \tag{1.28}$$

where the second neutrino 'flavour' above, $\nu_x$, may be identified with $\nu_\mu$, $\nu_\tau$ or a linear combination of the two. In the mass representation the Schrödinger equation takes the form

$$i\frac{\partial}{\partial t}\begin{pmatrix} \nu_1 \\ \nu_2 \end{pmatrix} = \begin{pmatrix} E_1 & 0 \\ 0 & E_2 \end{pmatrix} \begin{pmatrix} \nu_1 \\ \nu_2 \end{pmatrix} \tag{1.29}$$

where $E_1$ and $E_2$ are the energies of the two mass states of masses $m_1$ and $m_2$, having equal momentum. (Units such that $\hbar = c = 1$ are used throughout). Under the change of representation given by Equation (1.28), it is easily shown that the Hamiltonian matrix is transformed so that the time evolution of the flavour states is given by

$$i\frac{\partial}{\partial t}\begin{pmatrix} \nu_e \\ \nu_x \end{pmatrix} = \frac{\Delta m^2}{4E} \begin{pmatrix} -\cos 2\theta & \sin 2\theta \\ \sin 2\theta & \cos 2\theta \end{pmatrix} \begin{pmatrix} \nu_e \\ \nu_x \end{pmatrix} \tag{1.30}$$

where $E \equiv (E_1 + E_2)/2$ and $\Delta m^2 \equiv m_2^2 - m_1^2$.

This gives rise to 'vacuum oscillations' in the case $\Delta m^2 \neq 0$, $\theta \neq 0$, and the probability of observing as $\nu_e$ a neutrino created as $\nu_e$ at $t = 0$ is, by elimination from Equation (1.30),

$$|\langle \nu_e | \nu_e \rangle_t|^2 = \sin^2 2\theta \cos^2\left(\frac{\Delta m^2}{4E} t\right) \tag{1.31}$$

and it can be seen that the amplitude of the oscillations depends on the vacuum mixing angle $\theta$. Vacuum oscillations cannot therefore cause a large reduction in flux unless the mixing angle is large.

The argument of the oscillatory term may be re-expressed in terms of a vacuum oscillation length

$$L_V \equiv \frac{4\pi E}{\Delta m^2}$$

and the oscillatory behaviour of the electron neutrino flux may thus be written

$$\cos^2\left(\frac{\pi R}{L_V}\right) \tag{1.32}$$

where $R$ is the distance travelled by the neutrino in time $t$. $L_V$ is thus the distance over which the two mass states evolve a phase difference of $\pi$ due to their different time dependance.

Bahcall & Frautschi [46] evaluated the possibilities for vacuum oscillations as a solution to the known deficiency of solar neutrinos observed by Davis. They demonstrated that it is important to average over the energy spectrum of the emitted neutrinos (the $^8$B spectrum) in order to obtain the effect of vacuum oscillations on the observed flux, and concluded that an effect large enough to explain the $^{37}$Cl result was only obtained for a finely-tuned value of $\Delta m^2$, and that for most values of $\Delta m^2$ the maximum possible effect is a factor of 2 reduction in the flux, which occurs for maximum mixing ($\sin^2 2\theta = 1$). In comparison with the Cabibbo angle observed in the quark sector, $\sin^2\theta_C = 0.05$, the amount of mixing required for vacuum oscillations substantially to reduce the solar neutrino flux is large, and even then the probable (*ie.* non-fine-tuned) flux reduction is insufficient to explain the known deficiency.

### Matter oscillations — the MSW effect

Wolfenstein [47] first pointed out, among other mechanisms, that standard weak interactions may modify neutrinos' oscillation properties in the presence of matter. This occurs because electron neutrinos possess a charged-current interaction with electrons, via $W^+$ exchange, which muon and tau neutrinos do not. All types possess the neutral current $\nu - e$ scattering interaction, but since this is flavour-independent to high accuracy it has no effect on $\nu_e \rightleftharpoons \nu_x$ oscillations.

Addition of the Wolfenstein term $\sqrt{2}G_F n_e|\nu_e\rangle\langle\nu_e|$ to the mass matrix and omission of the diagonal neutral current terms yields, in the flavour representation,

$$i\frac{\partial}{\partial t}\begin{pmatrix}\nu_e\\ \nu_x\end{pmatrix} = \frac{\Delta m^2}{4E}\begin{pmatrix}-\cos 2\theta + \frac{4E}{\Delta m^2}\sqrt{2}G_F n_e & \sin 2\theta\\ \sin 2\theta & \cos 2\theta\end{pmatrix}\begin{pmatrix}\nu_e\\ \nu_x\end{pmatrix} \tag{1.33}$$

and it may be shown that the new mass matrix may be re-expressed in the form

$$\frac{\Delta_M}{2}\begin{pmatrix}-\cos 2\theta_M & \sin 2\theta_M\\ \sin 2\theta_M & \cos 2\theta_M\end{pmatrix}$$

where

$$\tan 2\theta_M = \frac{\tan 2\theta}{1 - \frac{4G n_e E}{\sqrt{2}\Delta m^2}\sec 2\theta} \tag{1.34}$$

$$= \frac{\tan 2\theta}{1 - \frac{L_V}{L_e}\sec 2\theta} \tag{1.35}$$

$$L_e \equiv \frac{\sqrt{2}\pi}{Gn_e} \tag{1.36}$$

$$\Delta_M^2 \equiv \left(\frac{\Delta m^2}{2E}\right)^2 \left\{\left(\cos 2\theta - \frac{2E}{\Delta m^2}\sqrt{2}Gn_e\right)^2 + \sin^2 2\theta\right\} \tag{1.37}$$

Neutrinos oscillate in this case with an oscillation length $L_M$ (corresponding to $L_V$ in Equation (1.32)) given by

$$L_M^2 = L_V^2 \left\{1 - 2\frac{L_V}{L_e}\cos 2\theta + \left(\frac{L_V}{L_e}\right)^2\right\}^{-1} \tag{1.38}$$

It can thus be seen that the presence of matter gives rise to an effective mixing angle $\theta_m$ and further that mixing is resonant (*ie.* $\theta_m = \pi/4$) for a critical electron density given by

$$n_{e,res} = \frac{\sqrt{2}\Delta m^2 \cos 2\theta}{4GE} \tag{1.39}$$

at which density $L_M = L_V/\sin 2\theta$.

This resonance only exists for $\Delta m^2 > 0 \Rightarrow m_2 > m_1$. If $\theta$ is small, this amounts to the condition that $\nu_e$ be lighter than the neutrino ($\nu_\mu$, $\nu_\tau$) with which it is mixed. That this resonance exists $\forall \sin^2 2\theta$ raises the possibility that matter oscillations — the Mikheyev Smirnov Wolfenstein or MSW effect — may occur within the sun for a wide range of parameters ($\sin^2 2\theta$, $\Delta m^2$), thus avoiding the necessity for fine tuning these parameters.

Although the above discussion has been applicable mainly to the two-neutrino case (*ie.* in the approximation that the third neutrino flavour is weakly mixed with the first two), the ideas apply equally in the more complex three-neutrino case, which has been studied by Kuo and Pantaleone [106]. The mixing matrix in that case contains 4 parameters — three angles and a phase — and is analogous with the KM matrix in the quark sector. They demonstrate that only 2 parameters, both mixing angles, affect the oscillation and that the masses enter as $m_2^2 - m_1^2$ and $m_3^2 - m_1^2$ *ie.* in $\Delta m^2$ combinations as before. Although the oscillation behaviour is in general more complex, separate resonances are predicted in the limiting cases of small mixing angles or large $\Delta m^2$.

### MSW effects on predicted neutrino fluxes

Rosen and Gelb [48] numerically integrated Equation (1.33) taking into account the SSM predictions concerning regions of the sun in which neutrinos are produced and the variable density (and hence variable $n_e$) within the sun. They note that there are two limiting cases for MSW oscillations in the sun, which depend on the parameters $\sin^2 2\theta$, $\Delta m^2$ and the density gradient of the solar material. These limits give rise to distinct parts of a contour of constant flux on a $\sin^2 2\theta - \Delta m^2$ plot.

It is a well known result of time-dependent perturbation theory (see Davydov [50] for example) that a sufficiently slowly-varying perturbation causes no transitions between states of a discrete spectrum. As a neutrino travels through the sun it encounters a density gradient $dn_e/dr$ which affects the local mass eigenvalues: a sufficiently slowly-varying density does not cause transitions between the mass eigenstates. This limit is said to be adiabatic and occurs when the scale height of the solar density distribution, defined by

$$h_0^{-1} \equiv -\frac{1}{n_e}\frac{dn_e}{dr} = \frac{d\ln n_e}{dr}$$

is long compared to $L_M$. The converse case corresponds to the sudden approximation in perturbation theory, according to which a perturbation is complete in a time short compared to a characteristic frequency of the system — in this case there is a large probability of transitions between mass eigenstates.

Bahcall [16] presents an informative, illustrative MS diagram (a contour of constant flux reduction in a $\sin^2 2\theta - \Delta m^2$ plane) for the $^{37}$Cl result, $\simeq$ 2 SNU. This is reproduced in Figure 1.3. The horizontal and vertical lines are solutions in the adiabatic approximation — *ie.* that the probability of transitions between mass eigenstates is negligible. The former is the resonance condition: for $\Delta m^2 \sim 10^{-4} eV^2$ neutrinos of energy $E \gtrsim 7$MeV pass through resonance (that is, the central solar density is sufficiently high to allow this to occur). Its upper boundary (in $\sin^2 2\theta$) is fixed by the increasing $\nu_e$ component of $\nu_2$ into which the $\nu_1$ eigenstate is converted, and its lower boundary by the limits of validity of the adiabatic approximation. The vertical line is the large-$\sin^2 2\theta$, small-$\Delta m^2$ solution in which all energies which contribute to the capture rate are converted — *ie.* all relevant neutrinos are produced above their resonant density — and $\nu_e$ survival is entirely due to the $\nu_e$ component of $\nu_2$, thus $\Pr(\nu_e) = \sin^2 2\theta$. The diagonal line is the non-adiabatic contribution and is given by (see Rosen and Gelb [48])

$$\log_{10}(\sin^2 2\theta) + \log_{10}(\Delta m^2) \simeq -7.5 \tag{1.40}$$

and represents the restoration of $\nu_e$ due to transitions *after* complete conversion.

Rosen and Gelb show that the spectra in the adiabatic and non-adiabatic cases are very different. In the case of the horizontal line of Figure 1.3, the higher-energy neutrinos are suppressed and it follows that the $^{71}$Ga experiment would be expected to yield a result equal to its SSM prediction. In the non-adiabatic case, all energies are suppressed, but especially low and intermediate energies, implying a very low rate for the Gallium experiment. The vertical line solution in Figure 1.3 gives an energy-independent suppression. The fact that the spectra are different in these three cases constitutes an important experimental diagnostic.

### The experimental determination of MSW parameters

The MSW effect is capable of changing both the magnitude of the $\nu_e$ flux at the earth and also its energy spectrum. Radiochemical detectors($^{37}$Cl and $^{71}$Ga) are sensitive only to the integrated flux (weighted by their energy-dependent neutrino absorbtion cross-sections) above their respective thresholds, and so yield little spectral information. Electron scattering experiments (Kamiokande-II) provide spectral information, but with limited statistics and only for the high-energy end of the neutrino spectrum.

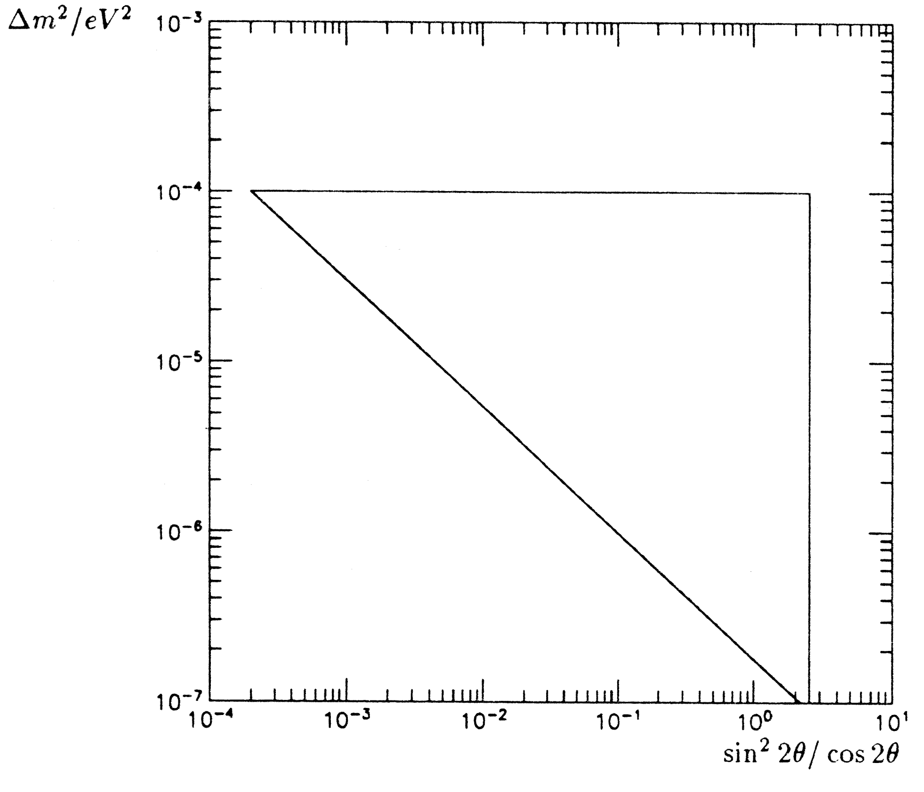

Figure 1.3: Illustrative equal rate contour for the $^{37}$Cl experiment

Bahcall, Rosen and Gelb [49] have surveyed the effects of a wide range of MSW parameters on observable electron recoil spectra above a 5MeV threshold. They calculate that although oscillations can reduce the total electron scattering cross-section by as much as a factor of 5 due to the lower scattering cross-section of the muon neutrino relative to the electron neutrino, the spectral shapes resulting from plausible MSW parameters will not deviate by more than 20% from each other, and that the difference is maximum at the lowest energies. It follows that achieving low detection thresholds and good energy resolution is essential if electron scattering is to be used as a diagnostic for MSW solutions to the Solar Neutrino Problem. No analysis of Kamiokande data has been performed which attempts to deduce MSW parameters from the observed energy spectrum: $\nu - e$ scattering smears the energy response of the detector since a range of incident neutrino energies can give rise to a scattered electron of given energy, and furthermore the statistical accuracy of the available Kamiokande data appears too poor.

The fact that the energy-dependent neutrino absorbtion cross-sections $\sigma_{abs}(E)$ of radiochemical detectors are different, and in particular that their detection thresholds are different, implies that their results, when combined, may form an MSW diagnostic. In particular, the $^{71}$Ga capture rate is dominated by pp and $^{7}$Be neutrinos ($E < 0.42$MeV and lines at 0.384MeV and 0.862MeV respectively) and that of the $^{37}$Cl experiment by $^{8}$B neutrinos ($\overline{E} = 6.71 MeV$). Taken together, the Chlorine and Gallium results will thus distinguish between MSW solutions which suppress high- and low-energy neutrinos differently.

An MSW plot showing regions of the $\sin^2 2\theta - \Delta m^2$ plane consistent with the Homestake and Kamiokande results is given by Totsuka [32] and reproduced in Figure 1.4. It shows that, if the ratio of the fluxes detected by each experiment is taken at face value, then the adiabatic solution is nearly excluded. When sufficient statistics are available from Gallium neutrino detectors, they will afford a further diagnostic for MSW parameters.

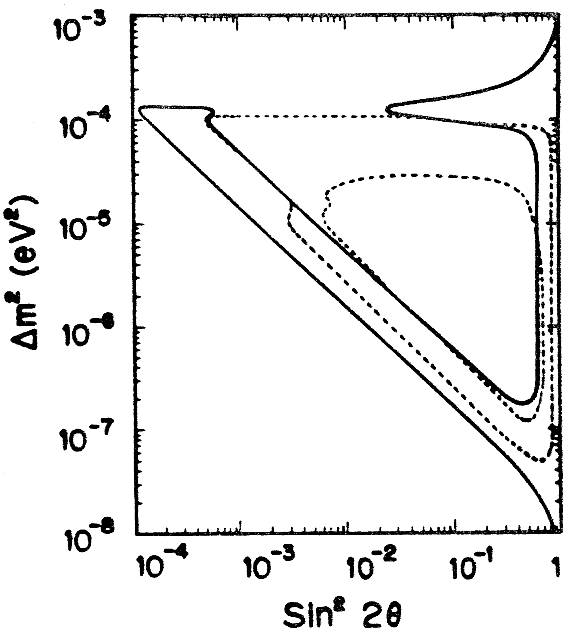

Figure 1.4: Regions of MSW parameter space allowed by Homestake and Kamiokande-II data.

# Chapter 2

# The Sudbury Neutrino Observatory

## 2.1 An outline description of the detector

The Sudbury Neutrino Observatory is under construction at the 2070$m$ (6800ft) level of the Creighton nickel mine, operated by INCO Limited, near Sudbury, Ontario. It is a water Čerenkov detector whose detecting element is 1000 tons of heavy water, $D_2O$, monitored by approximately 10,000 photomultipliers. The use of 1$kt$ heavy water as a detecting element was proposed by Chen in 1984 [1, 2] but heavy water had been considered as early as 1966 by Kelly and Uberall [54]. The detector is intended to be sensitive not only to electron neutrinos but also to muon and tau neutrinos, and in this way will distinguish unambiguously between those solutions of the SNP which lower the neutrino flux and those which involve neutrino oscillations. The neutral current detection of $\nu_x$ is unique to this experiment.

Figure 2.1 shows in cross-section the present design for the detector [55, 56]. The main features of the design are summarised below.

1. The cavity is roughly barrel-shaped with a maximum diameter of 22$m$ and height of approximately 30$m$. It is lined with a stainless steel containment vessel. Thermal insulation is included behind the liner since the rock temperature at the 6800ft level is 41°C and the water will be cooled to limit noise in the photomultipliers. A gas-tight steel deck structure supports the heavy water containment sphere and retains an inert gas blanket over the detector. Only filtered air will be allowed into the detector cavity, which will in effect be a clean area so as to minimise contamination with radioisotopes.

2. The central detecting element, 1$kt$ of 99.92% pure $D_2O$ (remainder $H_2O$), is contained in a sphere of radius 6$m$. Acrylic (*ie.* polymethyl methacrylate *or* 'perspex') has been chosen for the construction of the sphere because of the optical properties of this material and the low levels of radioactive contamination which may be achieved in it. Since the Cherenkov spectrum varies as $1/\lambda^2$, ultra-violet transparency of the acrylic sphere is essential, and largely dictated the choice of material. The vessel is to be

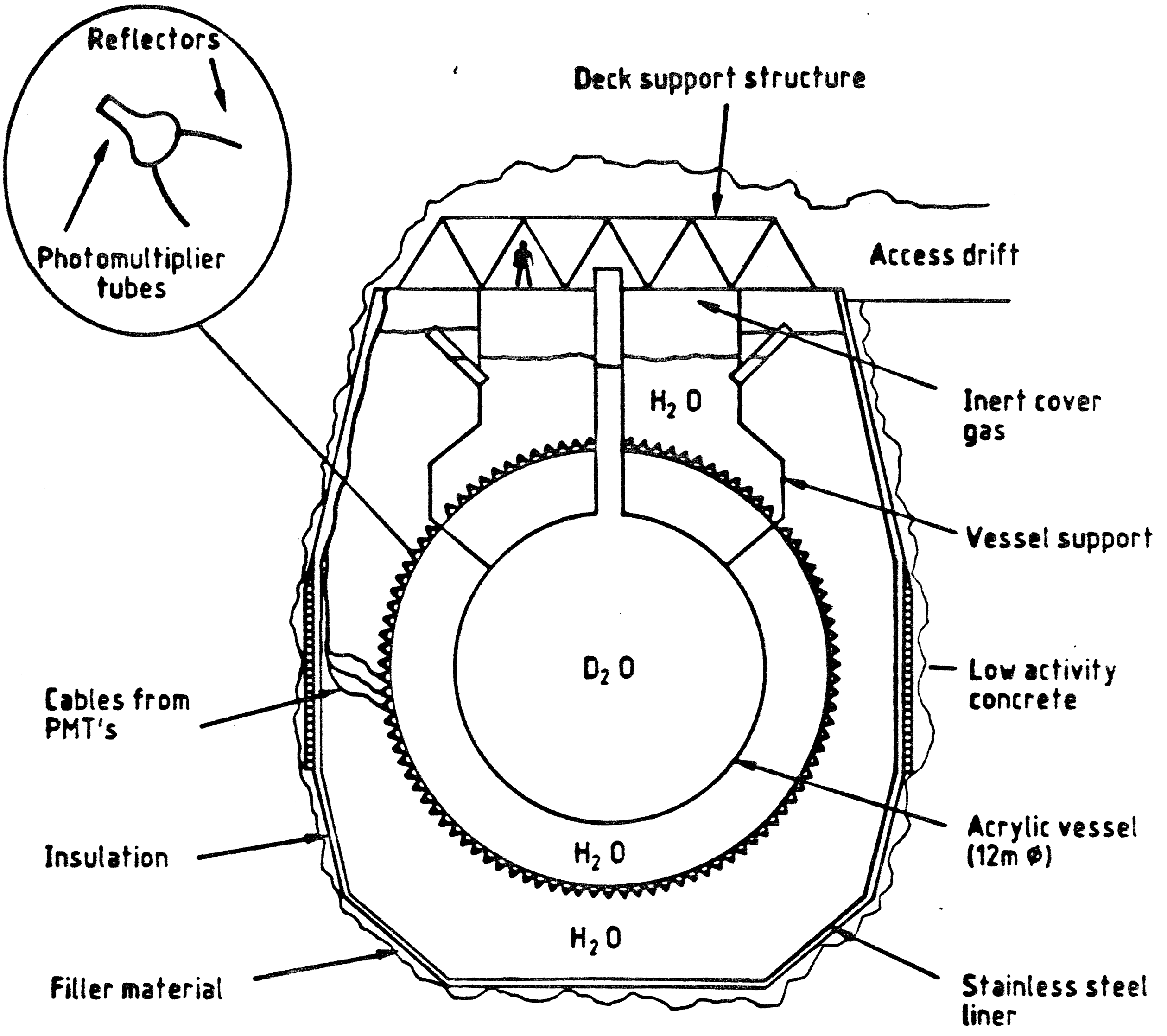

Figure 2.1: A schematic of the Sudbury Neutrino Observatory.

suspended from the steel deck by Kevlar ropes, and its thickness in its various parts has been chosen to enable the sphere to resist buckling.

3. Outside the acrylic sphere there will be at least $5m$ thickness of light water, approximately $7kt$.

4. At a radial distance of $2.5m$ from the acrylic vessel, photomultiplier tubes (PMT's) are mounted on a support structure of stainless steel. The PMT's will be 10" diameter hemispherical-envelope tubes manufactured by Hamamatsu Photonics, having bialkali KCsSb photocathodes and be sufficient in number to achieve 30% projected photocathode coverage of the sphere. The effective coverage of the tubes will be enhanced by a factor of around 2 by the fitting of 'concentrators' - curved reflecting surfaces designed to accept light from within the heavy water and reject it from the light water, with a consequent improvement in signal-to-background and vetoing of cross-talk between tubes. Behind the PMT sphere is an opaque screen which prevents light entering the PMT sphere from without, and which offers a high impedance to radial water flow across the PMT sphere.

5. Each PMT will be instrumented by a preamplifier and discriminator. The discriminator outputs will be used to generate a system trigger which could be anywhere in the range from 20 to 200 channels firing in a $150ns$ interval, depending on the detector backgrounds. The analogue preamp pulse will also be used to time the PMT hit, and will be digitised to determine the charge deposition. Each PMT will thus produce timing and pulse height information, to be used in event reconstruction. More detail on data acquisition may be found in [56].

6. The heavy and light water in the detector will both be continuously cycled through a purification apparatus to keep down the levels of contaminants. Since water purification and monitoring are the major subject of this work, the SNO water system will be described in more detail in Section 2.4.

## 2.2 Neutrino detection in SNO

The heavy water in SNO will serve both as the neutrino absorber and as the detector for the reaction products. In all cases, the end product of a neutrino interaction is the production of Čerenkov photons which will be detectable by the PMT array. The method of production of fast electrons is, however, different for each reaction mechanism.

### 2.2.1 Neutrino interactions in heavy water

There are three principal reactions possible for solar neutrinos in heavy water: they are —

**Neutrino-electron scattering**

$$\nu_x + e^- \longrightarrow \nu_x + e^- \tag{2.1}$$

The electron scattering (ES) reaction is in principle sensitive to all three flavours of neutrino, but in practice at solar neutrino energies, the cross-section to electron neutrinos is between six and seven times greater than to muon or tau neutrinos (since the $\nu_e$ reaction can proceed via a CC or NC diagram whilst the $\nu_\mu$ and $\nu_\tau$ only participate in NC reactions with $e^-$). In practice, therefore, this reaction is sensitive to $\nu_e$. The reaction gives a poor determination of the incoming neutrino energy spectrum because a monoenergetic beam is capable of giving rise to a range of differing electron recoil energies. Although the $\nu - e$ scattering cross-section is an order of magnitude smaller than that of the absorbtion process (Equation (2.2) below), the recoil electron is kinematically constrained to travel in a forward cone with respect to the incoming neutrino direction, and this forward peaking can be used to separate the $\nu - e$ scattering signal from the absorbtion reaction. The reaction thus affords evidence that the flux derives from the sun — this has been seen in the Kamiokande II detector. The estimated rate of detectable ES events in SNO is $1.0 \times 10^3 kt^{-1} yr^{-1}$ for a 5MeV threshold, full SSM flux and no oscillations [16].

### Absorbtion, or inverse beta decay

$$\nu_e + d \longrightarrow p + p + e^- \quad Q = -1.44 \text{ MeV} \tag{2.2}$$

This charged current (CC) reaction, which has no equivalent for a neutrino flux incident on a light water detector, is sensitive only to electron neutrinos, but gives rise to an electron which carries essentially the full energy of the incoming neutrino less the threshold energy (given by Kelly and Uberall [54]) and thus supplies spectral information for the $\nu_e$ flux. The angular distribution of the product electron is given by $[1 - 1/3\cos(\theta_e)]$, implying a two-to-one backward-to-forward asymmetry with respect to the direction of the sun.

The cross-section of the absorbtion reaction has been accurately calculated by Nozawa *et al.* [29] and is tabulated in Bahcall & Ulrich's Table IX. The average cross-section as a function of minimum accepted electron recoil energy is obtained by Bahcall & Ulrich (Table VIII) for $^8$B and hep neutrinos, using the cross-sections of Nozawa *et al.* This quantity is required for a measurement of total flux above threshold, disregarding any spectral information.

The high cross-section for this interaction relative to $\nu - e$ scattering constitutes a major advantage of the SNO detector over conventional (light) water Čerenkov detectors. Under the same assumptions as above, the anticipated rate is $1.2 \times 10^4 kt^{-1} yr^{-1}$.

### Neutral current disintegration

$$\nu_x + d \longrightarrow \nu_x + p + n \quad Q = -2.226 \pm 0.003 \text{ MeV} \tag{2.3}$$

The Q-value for this neutral current (NC) reaction has been determined by Mobley and Laubenstein [59]. This reaction is unique to SNO and is flavour-independent, providing a measurement of the total neutrino flux above threshold, independent of oscillations.

Therefore, although this reaction affords no spectral information and no directional information (both are lost in the processes of neutron thermalisation and capture) it enables SNO to distinguish between oscillations and a faulty SSM as solutions of the SNP. It is the principal reason for doing the experiment.

A state-of-art calculation of the cross-section for the neutral current reaction is presented by Bahcall *et al.* [28]. The calculation includes the effects of forbidden corrections and meson exchange currents. They average the cross-section over the $^8$B and hep neutrino spectra to obtain:

$$\langle\sigma(^8\mathrm{B})\rangle = 0.41(1 \pm 0.1)10^{-42}\,cm^2 \tag{2.4}$$

$$\langle\sigma(hep)\rangle = 1.15(1 \pm 0.1)10^{-42}\,cm^2 \tag{2.5}$$

The error estimate derives from consideration of a number of different approximations and plausible sets of nuclear parameters, and is not therefore a statistical error. They also obtain the result $r \equiv \sigma(NC)/\sigma(CC)$ as a function of neutrino energy to an error of 0.5%, *ie.* that quantity is much more nearly model independent and its measurement constitutes a test for flavour oscillations. For the SNO detector, they derive a NC event rate of:

$$4.5(1 \pm 0.38)10^3 kt^{-1} yr^{-1}$$

where the error is dominated by the uncertainty in the predicted $^8$B neutrino flux in SSM's. The prediction takes no account of the detection efficiency in SNO for the reaction.

### 2.2.2 Detection of fast electrons

The first two neutrino interactions above give rise to a fast electron as their detectable product. The detection of fast electrons in SNO relies on the production of Čerenkov radiation, with the heavy water therefore functioning both as the neutrino target and as the detecting (*ie.* radiating) medium. Production of Čerenkov photons proceeds according to the expression

$$\frac{dN}{dx\,d\omega} = \frac{\alpha}{c}\left(1 - \frac{1}{\beta^2 n^2}\right) \tag{2.6}$$

The photons are propagated normal to the surface of the well-known 'Cherenkov cone' whose half-angle is given by $\cos(\theta) = 1/(\beta n)$ ($\simeq 41°$ in heavy water for highly relativistic electrons) and whose axis is the instantaneous direction of travel of the radiating electron. The threshold kinetic energy below which Čerenkov light is not produced by electrons in heavy water is 0.262MeV, the refractive index of heavy water being 1.333.

The resulting pattern of radiated photons is greatly complicated by multiple Coulomb scattering of the electron, which limits the angular resolution of the detector to about 25° according to Monte Carlo studies [55]. The spectral distribution can be seen from Equation (2.6) to be flat in frequency, which implies the well-known $1/\lambda^2$ wavelength dependence: this fact gives rise to stringent requirements on the UV transmission properties of heavy and light water, acrylic and PMT glass so as to maximise the available signal. In addition, PMT's are required which have good sensitivity at short wavelengths — bialkali photocathodes have the required properties in this respect. The photons radiated by a fast electron propagate to the PMT array where a fraction is detected.

The total number of radiated photons is approximately proportional to the electron's path length, and thus to its energy. About 350 photons per $cm$ are radiated in the spectral range 300 to $650nm$ to which the PMT's are sensitive. Hence the total number of photomultipliers hit serves as an energy measurement for the electron, assuming that multiple hits on a single tube may be neglected. Approximate energy calibration can be done by Monte Carlo, using measurements of the phototubes' overall efficiency and a description of the stopping of low-energy electrons in water. An experimental energy calibration will clearly be necessary in addition.

The electron energy can thus be obtained from the number of hit PMT's. The PMT's to be used in the detector, however, have a TTS[1] of approximately 2.5 nanoseconds, which allows accurate timing of the arrival of a photon. An event reconstruction algorithm will thus allow the origin of the photons to be localised to about $0.5m$. This done, the electron's initial direction may be estimated as the line connecting the vertex to the centroid of the hit pattern on the spherical array of tubes. The energy, direction and position of the electron may thus be determined: no further information is available.

### 2.2.3 Detection of free neutrons

The production of a free neutron is the only signature of the important neutral current reaction. The detection method must clearly involve capture of the neutron onto some nucleus with consequent production of detectable gamma rays.The default option at the time of writing is the addition of NaCl to the heavy water, but other chlorine compounds and the inclusion of neutron detectors in the heavy water volume are under consideration.

#### Distributed neutron detection

**Pure heavy water** Deuterium has a capture cross-section for thermal neutrons of 0.5mb (hence its use as a moderator in power reactors) and in the absence of any additive in the $D_2O$, Monte Carlo studies [55, 56] indicate that only 1/4 of neutrons generated within the heavy water will be captured on deuterium, 1/4 will be captured on the 0.15% light water contamination in the heavy water (with the production of a sub-threshold 2.223MeV gamma-ray) and the remainder will leak into the light water to be captured onto protons. A monoenergetic 6.25MeV gamma-ray is generated by capture on deuterium, which is detectable because of the Čerenkov radiation of Compton scattered electrons.

---

[1] A photon incident on a photocathode gives rise to a photoelectron, which in turn gives rise to a delayed pulse at the anode, having propagated an avalanche down a series of dynodes. The mean time between the photon's arrival and the production of the pulse is known as the Transit Time, and the FWHM of this quantity as the Transit Time Spread (TTS). It is this latter quantity which determines how accurately the arrival time of a photon can be known.

**Sodium Chloride** The addition of 0.25% (2500$kg$) NaCl into the heavy water would introduce $^{35}$Cl, which has a capture cross-section of 43 barns, and would modify the neutron transport properties of the heavy water so as to contain 83% of the neutrons generated there. This reaction has a Q-value of 8.6MeV and gives rise to a gamma-ray above 6MeV with a probability of 60% [57] which may be detected via a Compton scattering process.

The NC response (an 8.6MeV energy deposition, with losses arising from the Čerenkov threshold) lies well within the energy range of the CC and ES reactions; the smearing of the capture gamma-ray's energy by the processes of Compton scattering and Čerenkov radiation implies that the NC signal cannot be distinguished from the CC signal, except inasmuch as the NC signal is isotropic (when averaged over many events), and the CC signal which has a 2:1 backward: forward asymmetry with respect to the solar direction. However, it is intended to operate the detector for a year without the additive, followed by a year's operation with the additive, thus allowing an estimation of the NC signal by subtraction of the two event rates.

Other chlorine-rich compounds are under consideration as distributed neutron detectors. Chloral Hydrate is a possible candidate.

### Discrete neutron detectors

The principal objection to use of distributed neutron detection in SNO is that the NC signal would only be distinguishable from the CC signal by subtraction of low-statistics measurements. Apart from the uncertainties involved in such a subtraction, it does not allow the possibility of searching separately for short-term variations in the CC or NC event rate. Such variations could be seasonal or associated with sunspot numbers.

A clear, real-time separation of the CC and NC signals is clearly desirable. This could be achieved by using localised, discrete neutron detectors containing small amounts of a nuclide having a large capture cross-section for thermal neutrons. A suitable choice is currently thought to be $^3$He which undergoes the reaction

$$^3\mathrm{He}(n,p)^3\mathrm{H} \quad Q = 0.77 \text{ MeV} \tag{2.7}$$

with a cross-section $\sigma_c = 5327b$. The inclusion of $^3$He-filled proportional counters within the heavy water is under investigation. It is proposed to arrange strings of 1$m$ long by 2.54$cm$ o.d. cylindrical counters, filled with $^3$He at 3 atm. pressure, on a 1$m$ grid. The array is designed to achieve a capture efficiency of 25% for neutrons produced in the $D_2O$: that such a low efficiency can produce an equally accurate determination of the NC signal is due to the fact that no subtraction of the CC signal is required [61]. The strings of counters would be buoyant and would thus have to be restrained from the lower surface of the acrylic sphere.

A serious problem inherent in this proposal concerns the levels of radioactive contaminants likely to be present in the materials of the counters, since any source of ionisation may give rise to an event in such a counter. It is intended for the array of counters to contribute a background event rate not exceeding 0.1 events per day, *cf.* the calculation of Bahcall *et al.* [28] which predicts $4.5 \times 10^3$ NC events per kiloton-year for the full SSM flux ($\simeq 12d^{-1}$).

## 2.3 Detector backgrounds

The assessment of backgrounds in SNO, or any other solar neutrino experiment, is of critical importance as it is manifestly impossible to switch off the signal. In the preceding section the signals expected from neutrino events were discussed, and a process contributing to background is therefore one which gives rise to either a fast electron or a free neutron in (or near) the heavy water, or mimics the signals due to such events.

Backgrounds in the SNO detector derive from two distinct causes. The more important by far is the decay of radioisotopes in the detector and in the surrounding rock, which will be dealt with in detail in this section. A secondary cause is the incidence of cosmic-ray particles on the detector, but this latter is relatively unimportant in the SNO detector because of its depth below ground.

### 2.3.1 Cosmogenic backgrounds

The experience gained from Kamiokande II has shown what sort of events can be produced by cosmic-ray muons incident on a water Cherenkov detector: the background derives in this case from the production of high-energy ($\leq$ 15MeV endpoint) beta-emitters from spallation of $^{16}$O, such as $^{8}$B, $^{12}$B and $^{12}$N, which produce Cherenkov-radiating electrons in the central volume. However, the muon intensity at the SNO detector is a factor of $\simeq$ 200 lower than at the Kamiokande detector, implying that only about 1.5 muons per day will give rise to a spallation event above threshold [55]. This very low rate renders them easy to veto from the coincidence of a muon signal followed by a beta-decay event (*ie.* Cherenkov radiation which successfully reconstructs into the central volume) within the relatively long half-lives ($1/100s < t_{1/2} < 1s$) of the above nuclides.

Background events also arise from cosmic-ray-derived neutrinos, created in the upper atmosphere. The fluxes of atmospheric $\nu_e$ and $\nu_\mu$ have been calculated by Gaisser and Stanev [62] for neutrino energies down to 10MeV and the resulting background in the Homestake detector shown to be about 3 orders of magnitude lower than the observed event rate. Atmospheric neutrinos are not therefore a significant background.

### 2.3.2 Radiogenic backgrounds

The energies characteristic of radioactive decay coincide, inevitably, with those characteristic of solar neutrinos and it is essentially this fact which allows radioactivity in or near the detector to mimic events due to neutrinos. It will be shown that radioactive decay is capable of giving rise to fast electrons or free neutrons in the central volume of the detector, or to PMT hit patterns which reconstruct as genuine events. The major sources of radioactivity in the detector are the inevitable trace quantities of isotopes in the natural decay chains headed by $^{232}$Th and $^{238}$U (and to a lesser extent $^{235}$U), together with $^{40}$K and a contribution from fission of $^{238}$U. These trace contaminants are present at some level in all materials.

The process by which electrons above threshold (expected to be around 5MeV) may be produced is the Compton scattering of high energy gamma-rays. No gamma decays of sufficient energy to produce electrons above threshold exist in the natural decay chains and thus the sources of such gammas are neutron capture (neutrons derive from $(\alpha, n)$ reactions) and fission. Low-energy gammas are copiously produced by the natural decay chains and are capable of scattering electrons in the light or heavy water and generating a Cherenkov background which may be above threshold if a coincidence between two decays occurs within the resolving time. The finite energy resolution of the detector may also result in a sub-threshold prompt beta-gamma coincidence being recorded as an event above threshold.

A serious background to the NC measurement arises from the photodisintegration of the deuteron by gammas of energy greater than 2.223MeV, which occur in both the Thorium and Uranium chains. Since the full SSM predicts 12 neutrons per day due to neutrino events, it is intended that the photodisintegration rate be kept below 1 neutron per day, which imposes the most stringent limits on the water purity.

### Radioactivity from the rock

The sources of high-energy gammas (*ie.* greater than $\simeq$ 3MeV, the highest energy occurring in the natural decay chains) from the rock surrounding the detector are spontaneous fission of $^{238}$U, neutron capture and $(\alpha, p\gamma)$ reactions on the whole range of elements which make up the rock and the stainless steel liner: the neutrons derive from $(\alpha, n)$ reactions and the alphas from the natural decay chains. The rock also produces neutron fluxes due to the $(\alpha, n)$ reactions and fission: these neutrons may capture on detector materials with the production of gamma-rays.

Measurements have been carried out in the mine to determine the neutron and gamma ray fluxes due to activity in the various rock types [55, Annex 10]. These data have in turn been used to determine the shielding requirements for the detector and to estimate the residual gamma and neutron fluxes into the detector [55, Annex 9]. The rocks in the Creighton mine divide into two types: above the steeply sloping ore body, in the 'hanging wall', the rock is a uniform Norite, whereas below it the 'footwall' rocks are varied, being mainly Gabbro with inclusions of various types of granite and diorite. The measurements indicate the the Norite is lower in $^{232}$Th (3.3ppm), $^{238}$U (1.2ppm) and $^{40}$K (0.012% of natural potassium) by a factor of about 2, the footwall rocks being very variable. The Norite also gave a neutron flux of 3000 $n\,m^{-2}d^{-}1$, a factor of 5 lower than from the footwall rocks. These measurements, and the fractured structure of the footwall rock, lead to the natural choice of the Norite as the host rock for the detector.

Neutrons entering the detector are rapidly captured in the outer light water layer after travelling only $\simeq$ 20*cm* [55, Annex 1]: they generate a harmless 2.223MeV gamma-ray. High-energy gammas are more of a problem since they have a much longer range in water. However, Monte Carlo calculations [56, 55, Annex 9] indicate that the measured gamma-ray flux from the rock will give rise to backgrounds in the $D_2O$ at least one order of magnitude below the expected CC signal above a 5MeV threshold. They give rise to a negligible NC background. It is also intended to attenuate the neutron flux from the rock by addition of Boron to the filler[2] between the (inevitably uneven) cavity wall and the stainless steel containment tank; this will reduce the flux of high-energy gammas due to neutron capture on the stainless steel and on the low-activity concrete which lines the waist of the cavity.

### Radioisotopes in the detector

**Gammas from heavy water** 'High purity of the heavy water is dictated by the fact that in both the $^{232}$Th and $^{238}$U decay chains gammas are produced which have energies above 2.223MeV, the binding energy of the deuteron. If these gammas are produced in the heavy water, then it is clear that some will photodisintegrate a deuteron before falling below this threshold (by Compton scattering). The photodisintegration of the deuteron, with the production of a free neutron, exactly mimics the *only* signature of a NC event, *irrespective of the method used to detect the neutrons.* This process thus forms an indistinguishable background to the NC disintegration process and must be reduced to a level small compared to the expected NC signal, and monitored in order to verify that such levels have indeed been achieved.

By considering the branching ratios to gammas of energies above threshold, it may be shown [55] that $1nd^{-1}$ is produced by a $^{232}$Th concentration in the heavy water of $3.7 \times 10^{-15} g/g$ or by $4.5 \times 10^{-14} g/g$ $^{238}$U (assuming secular equilibrium in the chains). These concentrations correspond to $1.3ddt$ in the Thorium chain or $48.4ddt$ in the Uranium chain ($1ddt$ is 1 disintegration per day per ton and is the natural unit for these activities).

**Gammas from light water** The light water may also contain traces of Thorium and Uranium, is in close proximity to the heavy water (the attenuation coefficient for 2.6MeV gammas in water has been determined as $4.96m^{-1}$ [55, Annex 9]) and may thus contribute to the disintegration of the deuteron. It has been calculated [55] that $0.13 \times 10^{-12} g/g$ $^{232}$Th or $1 \times 10^{-12} g/g$ $^{238}$U in the light water will produce $1nd^{-}1$ in the heavy water. The limits thus imposed on the light water purity are clearly much less stringent than in the case of the heavy water. These levels of contamination, however, give rise to significant backgrounds to the CC process and it is intended to maintain the light water purity at the same levels as that of the heavy water.

**Gammas from PMT's** The glass of the PMT's will be the largest contributor of Uranium and Thorium in the detector, and is situated close to the heavy water. For this reason, glass of extremely low Uranium and Thorium concentrations (20ppb) has been identified by the collaboration and will be used to fabricate the PMT envelopes. The contribution to backgrounds from beta-gamma events in the PMT's is not thought to be significant above a threshold of 4MeV [56].

---

[2] 20% of natural Boron is $^{10}$B which has a cross-section of $3837b$ to thermal neutron capture *via* the reaction $^{10}\mathrm{B}(n,\alpha)^{7}\mathrm{Li}$

**Gammas from the stainless steel structure** Neutrons produced by $(\alpha, n)$ reactions in the PMT's may capture on the PMT support structure (although they will have been attenuated by passing through light water). Because of the high capture cross-section of iron ($\simeq 2.6$b) relative to Aluminium (0.231b) [51], Aluminium would be the preferred material for construction of the PMT support were it not for the electrolytic corrosion which would result from the presence of the stainless steel liner. The low-activity PMT glass allows stainless steel to be used for the PMT support without unacceptable capture backgrounds.

**Radioactivity in the acrylic** After the heavy water itself, the most serious source of background events is trace Uranium and Thorium in the acrylic vessel. Gammas and neutrons produced there are not shielded from the heavy water and so the radio-purity of the acrylic is a critical item. Mass spectroscopy, neutron activation and alpha counting methods have all been used [56] to determine the levels of contamination in acrylic and sensitivity at the $pg/g$ level has been achieved. It has also been reported that the Uranium and Thorium concentrations of the acrylic are non-uniform. Concentrations of $1.9 \times 10^{-12} g/g$ $^{232}$Th and $3.6 \times 10^{-12} g/g$ $^{238}$U in the acrylic have been shown not to contribute too large a background [56].

### 2.3.3 The influence of radiogenic backgrounds on detector design and operation

The concentric design of the SNO detector is strongly influenced by the need to minimise radiogenic backgrounds. The requirement to shield the heavy water from gamma-rays from the rock sets the minimum size of the cavity, so that a $5m$ water shield can be included. Although water is clearly not the best material for attenuation of gamma rays, a light water shield was chosen for SNO as it has the advantage that it is possible to purify it to levels probably not attainable with any other material. It is also necessary as a support for the $D_2O$, since the buoyancy resulting from its similar density enables a much lighter, thinner container to be used than would otherwise be possible, with consequent improvements in optical transmission and total included activity. Water is also cheap and, being a liquid, easily installed. Low-activity concrete has been included in the design around the waist of the cavity where the boundary of the $D_2O$ volume is closest to the cavity walls, and is exposed to the highest gamma-ray flux.

The positioning of the PMT sphere is also dictated by the radioactivity in the glass envelopes. A distance of $2.5m$ from the front face of the tubes to the acrylic sphere has been chosen to provide sufficient attenuation of gammas originating from this source. The use of very-low-activity glass, as opposed to a conventional glass, reduces the PMT backgrounds from a dominant effect to an effect comparable to those due to the heavy water, light water and acrylic [56].

The choice of acrylic as the material from which to construct the heavy water containment sphere was dictated by the requirements for structural strength, UV transparency and radio-purity. Since the heavy water may not be shielded from activity in the acrylic, this activity must be controlled by choosing sufficiently clean material, and the levels of activity must be independently measured so that these backgrounds can be estimated.

Given that the detector is constructed of the cleanest available materials, most of the remaining backgrounds are subject to vetoing by event reconstruction [56]. Figure 2.2 shows the reconstructed radii of Monte-Carlo-simulated beta-gamma events in the PMT glass and Figure 2.3 shows the same quantity for events originating in the heavy water, light water and acrylic.

The accuracy of event reconstruction, that is the extent of the distribution in space of the reconstructed positions of events occurring at a point, is critical to rejection of backgrounds. The distance scale which characterises this distribution is expected to vary with the TTS of the tubes and the square root of the number of hit tubes. The advantage of achieving high reconstruction accuracy is clearly that background events due to activity outside the $D_2O$ will not generally be reconstructed within it. If too many external events are being falsely reconstructed into the $D_2O$, a fiducial cut may be imposed on the data requiring the reconstructed vertex to be within a sphere smaller than the acrylic vessel. In this case, a better reconstruction accuracy implies a smaller loss of fiducial volume. This may be particularly important if the acrylic is dirty or other external backgrounds (PMT's, rock) are higher than anticipated.

A further criterion of acceptability of an event is its energy. It is known that the energies of radiogenic background events are not much higher than 3MeV, whereas the detector threshold will be around 5MeV. A background arises, therefore, from low-energy events reconstructing to higher energies due to the tail of the energy resolution of the detector. The energy resolution is determined by the number of detected photons from the event, the fractional uncertainty in the mean value of this quantity being estimated by $1/\sqrt{N}$, thus maximising N for a given electron energy maximises the energy resolution of the device. This consideration demonstrates that energy resolution is important for background rejection as well as obviously desirable for measuring the spectral distribution of the radiating electrons.

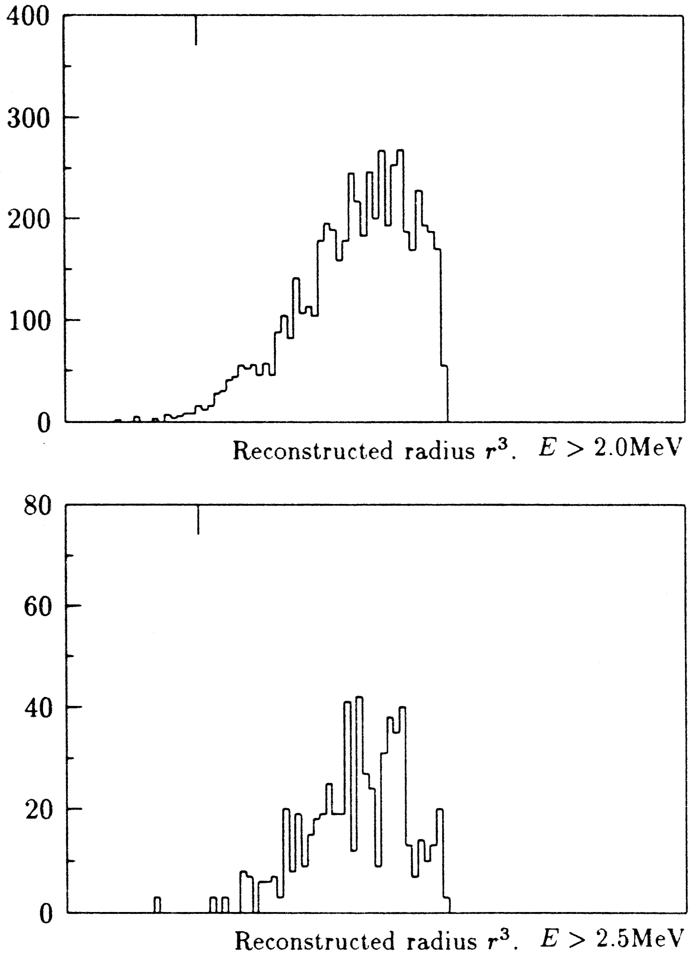

Figure 2.2: Reconstructed radii of simulated events above 2.0MeV and 2.5MeV due to activity in the PMT glass. The position of the acrylic sphere ($r = 6m$) is marked by the vertical line at the top of each frame.

Good vetoing of backgrounds thus requires both accurate vertex reconstruction and good energy resolution. These are achieved by maximising the amount of information carried in the PMT hits which result from an event, which is in turn achieved by maximising their number and the accuracy with which they are located in space and time. Maximising the number of hits due to a given event is clearly achieved by maximising the probability that a radiated photon is detected by a PMT: this requires long optical attenuation lengths in heavy and light water and as great an effective photocathode area as possible. The first of these objectives is automatically achieved by purification of the water [55] and the second by choosing large-area photomultipliers and fitting them with concentrators which increase their effective area at the expense of their angular acceptance. The timing accuracy of a PMT firing is limited by the TTS of the tube: the vertex reconstruction accuracy is expected to be linear in this parameter. The improvement in vertex reconstruction which has been obtained since tubes of TTS $< 3ns$ became available is a factor of about 2 [56]. The location in space of a hit is made poorer by choosing large tubes, but this is inevitable from budgetary constraints (an array of tens of thousands of small, fast tubes would be prohibitively expensive).

A secondary advantage of installing reflectors on the tubes is that, as mentioned in Section 2.1, they narrow the angular response of a tube. The principal free parameter in the design of a concentrator for a given tube is a cutoff angle: photons incident on the (cylindrically symmetric) PMT/Concentrator combination at polar angles (measured from the axis of symmetry) greater than this cutoff angle have a greatly reduced probability of hitting the photocathode. The result is that, for an appropriate choice of design, the tube may be made much less sensitive to the light water than to the heavy water, with consequent rejection of gamma backgrounds from the PMT's, light water and other external sources. This occurs because an event originating there generates many fewer hits than an event of equal energy in the central volume: thus it either does not trigger the detector (because too few tubes fire) or appears below threshold. A final advantage of reflectors, which could equally be achieved with blinkers, is that the PMT's are shielded from cross-talk *ie.* activity in one tube which generates Cherenkov or other light there does not trigger adjacent tubes, with a consequent reduction in the number of spurious coincidences between tubes.

The above discussion demonstrates that events (*ie.* radiating electrons, however produced) occurring beyond the heavy water may be vetoed by accurate event reconstruction. Furthermore, events occurring close to the edges of the $D_2O$ due to activity in the acrylic or $H_2O$ may be rejected by a fiducial cut: the elimination, if possible, of the necessity for such a cut is the object of efforts to obtain clean light water and acrylic. The same considerations do *not* apply to radiogenic background events in the heavy water.

Radiogenic backgrounds originating in the heavy water may clearly not be reduced by shielding. Furthermore, since they are approximately homogeneously distributed throughout the heavy water, and neutrino events are necessarily homogeneously distributed, the signal-to-noise ratio is not changed by imposing a fiducial cut. The contribution to CC background due to high-energy beta-gamma events in the heavy water could in principle be reduced by accurate energy resolution, but this is in fact fixed by the type and number of PMT's to be installed.

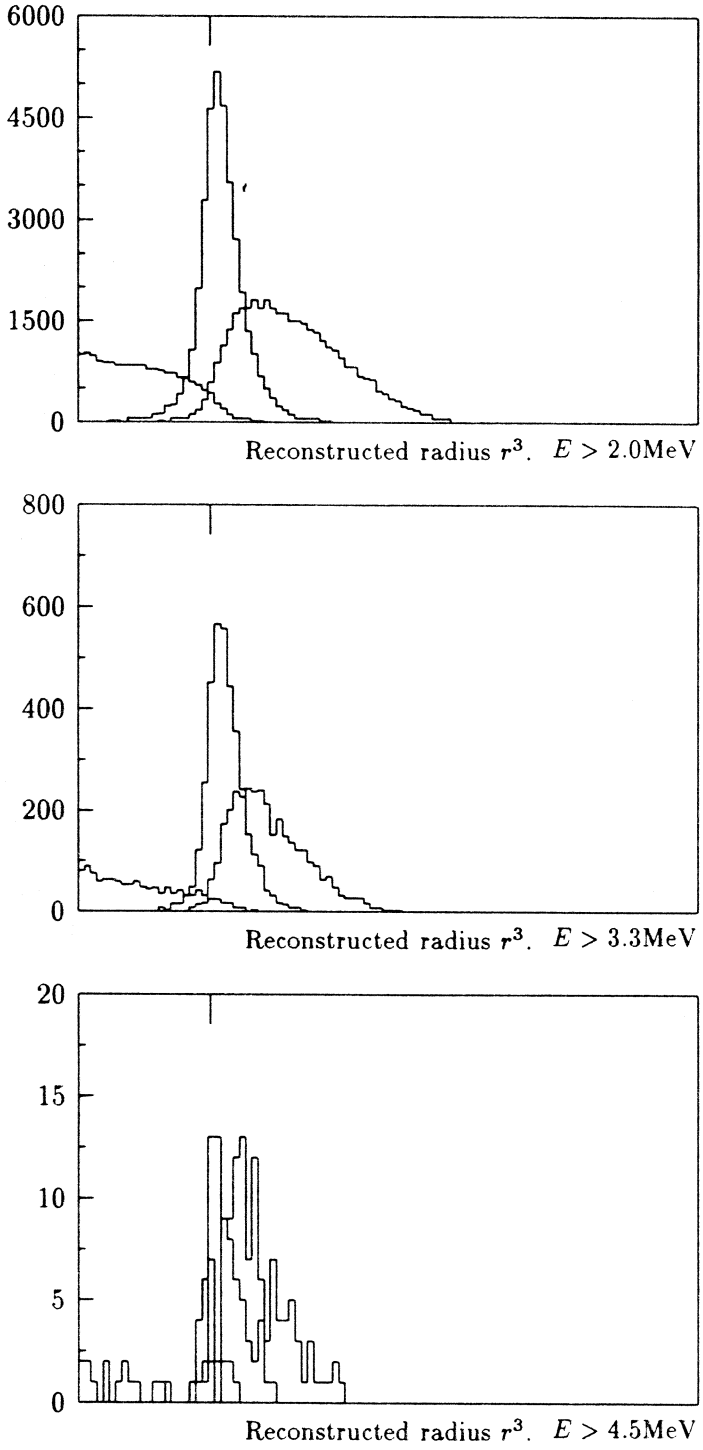

Figure 2.3: Reconstructed radii of simulated events above 2.0Mev, 3.3MeV and 4.5MeV due to activity in the heavy water, acrylic and light water. The position of the acrylic sphere ($r = 6m$) is marked by the vertical line at the top of each frame.

The NC background due to photodisintegration of the deuteron by high-energy gammas from the decay of members of the $^{232}$Th and $^{238}$U chains in the heavy water may not be vetoed at all: the production of free neutrons, homogeneously distributed at their point of origin, is the only signature of a NC event and affords no means of distinguishing genuine from background events.

## 2.4 Backgrounds due to activity in heavy and light water

In Section 2.3.2 it was stated that the target purity levels for the heavy and light water in the SNO detector are $1.3ddt$ in the $^{232}$Th chain and $48.4ddt$ in the $^{238}$U chain. In this section the purification of water to these levels is briefly discussed and the subsequent monitoring of the activities is fully discussed.

### 2.4.1 The SNO water handling system

Both the heavy and light water in SNO will continuously be cycled from the cavity through a purification apparatus and back into the cavity in order to maintain their ionic purity and optical (UV) transparency. The purification apparatus is described in [56] but its details and performance are beyond the scope of this discussion. The only parameter of immediate relevance is the throughput of the polisher stage, to be used for cycling the water, which is 150 litres per minute.

The necessity for continuous cycling arises from the solvent properties of water: a sample of ultra-pure water, if left to stand in a container, begins immediately to degrade in purity because of its well-known property of being an aggressive solvent, *ie.* it will leach material from all surfaces with which it comes into contact. Since all materials contain radioisotopes at some level, this constitutes a mechanism whereby purified SNO water may become contaminated. Materials in the cavity expected to leach activity in this way include the PMT glass, liner, PMT support structure and concentrators. An additional factor forcing continuous cycling is biological activity: microorganisms, notably Caulobacters, show the ability to survive and multiply under a wide range of conditions, including pure-water systems [66]. If contamination of the SNO water with dissolved ions were allowed to increase, conditions might become more favourable for the growth of a wider variety of non-photosynthetic organisms, some species being intolerant of high salt concentrations. Biological growth in SNO is most undesirable because of the increased scattering and absorbtion of light which would result, with obvious consequences for event reconstruction.

The water purification cycles for the light and heavy water will necessarily be separate since contamination of heavy with light water would be costly to reverse. The heavy water cycle is the simpler since the conditions to which this water is exposed are simple, *ie.* it contacts no detector component except the acrylic sphere and the plastic pipework to and from the purifier. It is expected that little activity will be leached from these plastic surfaces (since they will be selected to be low in contaminants and are very insoluble) and thus the purity of the heavy water should not prove a problem unless the purifier is not capable of eliminating to the required levels the elements in the Thorium and Uranium chains. (No manufacturer publishes data concerning the removal of actinides from water to $10^{-15} g/g$ levels). The situation with respect to the light water is very much more complex. The light water comes into contact with glass and stainless steel (and other materials), both of which are expected to leach or dissolve to some extent in water (the dissolution of glass has recently been demonstrated by Trent [65]) and both of which contain levels of Thorium and Uranium orders of magnitude higher than those in acrylic ($\simeq$ 40ppb for PMT glass compared with $\sim$ 1ppt for acrylic). The light water will thus continually be loaded with isotopes from these chains.

It should be noted that leaching of radioisotopes into the light water is only a background problem if the material is transported by the flow *towards* the heavy water: the total amount of activity in the detector is not changed by the leaching process; only its distribution is changed and this only *increases* backgrounds if the material moves towards the $D_2O$, otherwise it has little effect. A strategy for minimising the effect of leaching into the light water will thus be implemented irrespective of the contamination levels achieved by the purifier. Freshly purified light water will be injected into the cavity near the outer surface of the acrylic vessel and the outlets for the flow arranged such that the streamlines are as nearly radial as possible. This ensures that the light water closest to the acrylic sphere, to which the detector is clearly most sensitive as a source of background, has been freshly purified and is thus as clean as possible. The intended radial flow should ensure that any material leached from any surface, such as the PMT glass, is carried away from the heavy water and is thus made less dangerous, *ie.* it then makes a smaller contribution to background.

A radial light water flow pattern is clearly an idealisation: in practice it will be complicated considerably by convection and by the presence of the PMT sphere, its support structure and cabling. The heat flux into the detector from the rock has been estimated as $10kW$ with an additional $2kW$ contribution from the PMT bases [56]. A computer simulation of the water flow pattern in the detector resulting from these heat loads has been performed, with the result that large-scale convective movements outside the PMT sphere seem unavoidable, but that inward water movements within it may be avoided if it offers sufficiently high impedance to water flow [64].

### 2.4.2 Detailed consideration of backgrounds in SNO due to activity in the light water

This discussion focuses on those decays in the Thorium and Uranium chains capable of giving rise to backgrounds in the detector - either to the CC or NC signal. The decays which give rise to backgrounds are the same for each signal and are the (few) high-Q beta decays in the chains. In the CC case, these decays give rise to a background because of the finite energy resolution of the detector: the reduction of these activities acts to reduce the energy threshold above which the CC reaction will be detectable above background, with a consequent increase in signal rate. In the NC case, the background process is photodisintegration of the deuteron by gamma rays exceeding 2.223MeV in energy. The effect of reducing these activities is proportionately to reduce the background to this signal.

Since, as mentioned previously, it is impossible to determine the background rate in a solar neutrino detector by performing a 'source off' measurement, its determination by independent experiments is crucial to the success of the SNO experiment. A full calculation of the background rates induced by radioactive decay requires a knowledge of the distribution throughout the detector of all relevant radioisotopes. Such a calculation would use this information, together with the gamma-ray attenuation lengths and neutron transport properties of the detector materials, to determine by MC methods the production of fast electrons and free neutrons in or near the heavy water. Such calculations have, in fact, already been performed [55, 56] with assumed concentrations of $^{238}$U, $^{232}$Th *etc.* in the various detector components, and constitute the calculation of detector backgrounds. However, an important failing of these calculations is that, for lack of data to the contrary, they generally assume secular equilibrium (SE) in the chains[3], and it will be shown below that this assumption is likely to be wrong for most materials considered. Furthermore, a homogeneous distribution of activity in the $H_2O$ is assumed, which will also be seen to be improbable.

Some contributions to the required distribution (of activities of all relevant isotopes throughout the detector) are, indeed, well determined: the activities in the rock, shielding material, PMT's, acrylic and other static detector components are all, at least in principle, known or measurable in separate experiments. Some such experiments have been carried out. The concentrations of these activities in the water, however, will not be known before the detector is built and must thus be measured *in situ*. This section, and the remainder of this work, is largely concerned with the contribution to detector background arising from radioactivity in the light water: many of the same considerations apply to the heavy water. Henceforth, the activities in the fixed detector components will be ignored because backgrounds due to those activities are treated (measured and rejected) by quite separate methods than those appropriate to the dissolved activities. Furthermore, not all radioisotopes are of equal concern: the criterion to be used for discrimination between decays capable of generating a serious background and all others is the deuteron photodisintegration threshold, 2.223MeV, since this is the background process which imposes the most stringent purity requirement on the heavy water. A gamma above this threshold is known hereafter as a 'troublesome' gamma-ray.

The high-Q decays in the $^{232}$Th and $^{238}$U chain are shown in Figures 2.4 and 2.5. In the $^{238}$U chain, the beta decay of $^{214}$Bi has $Q = 3.27$MeV and is the dominant source of high-energy gammas. A 2.45MeV gamma arises from this decay with a branching ratio (BR) of 1.57%, and a 2.29MeV gamma with a 0.33% BR. The total BR to all other troublesome gammas is approximately 0.16%. In the $^{232}$Th chain, a 2.614MeV gamma arises with essentially 100% BR from the beta decay of $^{208}$Tl, itself a 36% branch of the chain, which populates states in $^{208}$Pb above the $3^-$ first excited state. Almost all the resulting gamma-ray cascades pass through this state, with the emission of the 2614keV gamma-ray. (The difference

---

[3] Secular equilibrium occurs in a radioactive decay chain when the rates of decay of all members except the head member and lowest member are balanced by their rate of production due to decay of an immediate parent. A simple relation between the concentrations of isotopes in the chain and their half-lives follows.

between the tolerable levels of Thorium and Uranium in the heavy water (see Section 2.3.2) arises largely from the very different BR's to troublesome gammas). Since $^{214}$Bi and $^{208}$Tl are the isotopes which generate the dangerous gammas, it is the distribution of *these* isotopes in the water which should, ideally, be determined. In fact, it is the distribution of the points at which these nuclides *decay* which is required, but the concentration and decay distributions are identical to within a scaling factor.

### Departures from secular equilibrium

The following discussion will suggest that the assumptions implicit in the MC calculations referred to above, that the activities in the water are uniformly distributed and that SE holds, are implausible. This will be seen lead to a requirement for the sampling of the water in the detector cavity.

There are two sources of radioactive contaminants in the SNO water: the first is activity leached from the detector components with which the water comes into contact and the second is activity in the outflow of the polisher (which must necessarily be very low if the experiment is to be feasible). The rate of leaching of a species from a surface will clearly be proportional to its concentration in the bulk material, but may also depend on its solubility or on its mobility within the material. Few measurements have yet been made of the leaching rates of the various species from the relevant materials (except in the case of glass [65]) but it is clear that if SE does not hold in the parent material, then it is very unlikely to hold amongst the leached species. Because of their very different chemical properties, SE is equally unlikely in the feed or the purified water.

The concentrations of radioisotopes in the fixed parts of the detector (PMT's, support structure, concentrators *etc.*) depend on the concentrations in the raw materials of which they are made and on the chemical enrichment or depletion which occurs during manufacture. Assuming SE to hold for the raw materials, it is likely to be disturbed during manufacture since the elements in the chains have very different chemical properties. It follows that the leached species are unlikely to be in secular equilibrium throughout the chains.

Certain parts of the chains will, however, be in equilibrium: those species whose half-lives are short compared to 1 year (a reasonable estimate for the time between manufacture of the detector components and their installation) will clearly be in equilibrium with their immediate parents. Thus the Thorium chain will be in equilibrium from $^{228}$Th downwards, but $^{232}$Th, $^{228}$Ra and $^{228}$Th will probably be in disequilibrium in at least some detector components. In the Uranium chain, the section from $^{226}$Ra to $^{210}$Tl and $^{214}$Po will be in SE, but disequilibrium will obtain above and below this section. Since troublesome gamma-rays (TG's) do not arise from the lower part of the chain, and the upper part is decoupled from the TG rate by the 1600 $y$ half-life of $^{226}$Ra, only this central section of the chain need be considered. In the event that leaching rates depend solely on concentrations within the bulk material, a measurement of the dissolved activity of any one species in a section of chain in SE suffices to determine the activities of all other species in that section (assuming that the dominant source of activity in the water is indeed leaching from detector materials).

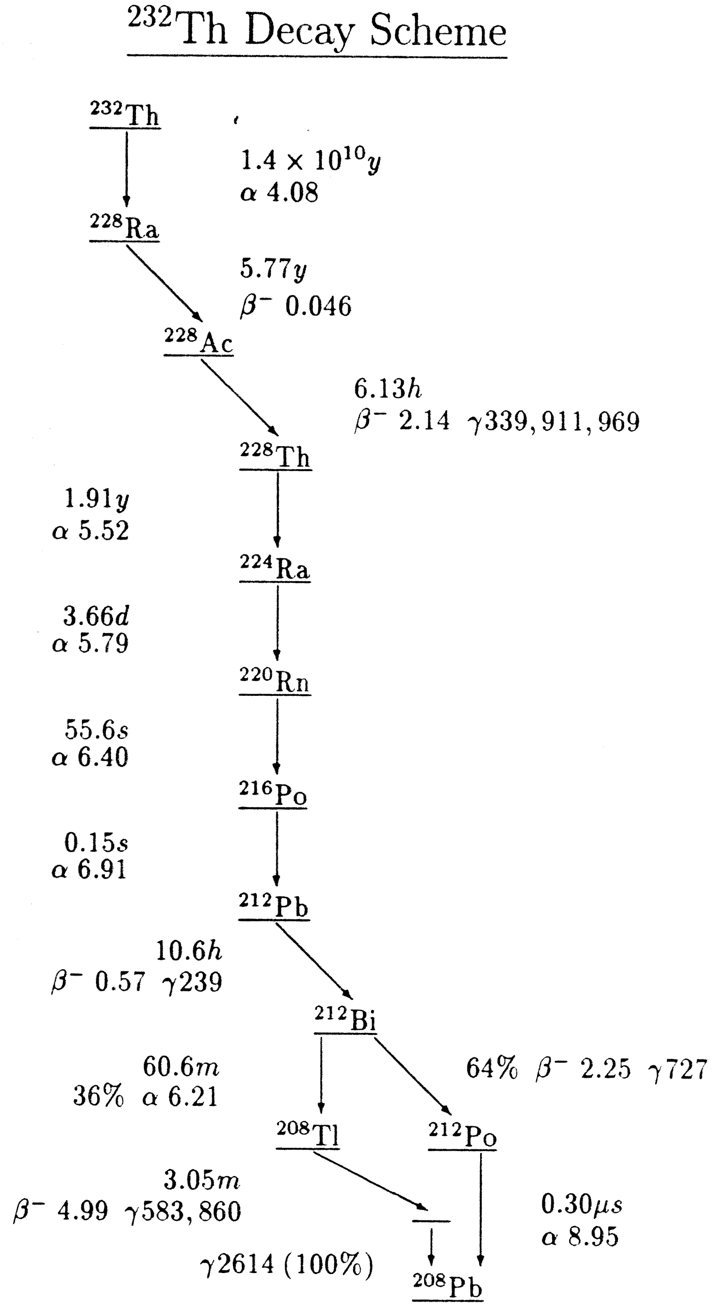

Figure 2.4: Simplified schematic of the $^{232}$Th decay chain. Half-lives of all decays are given, together with Q-values in MeV of $\alpha$ and $\beta^-$ decays and energies in keV of important $\gamma$ radiations.

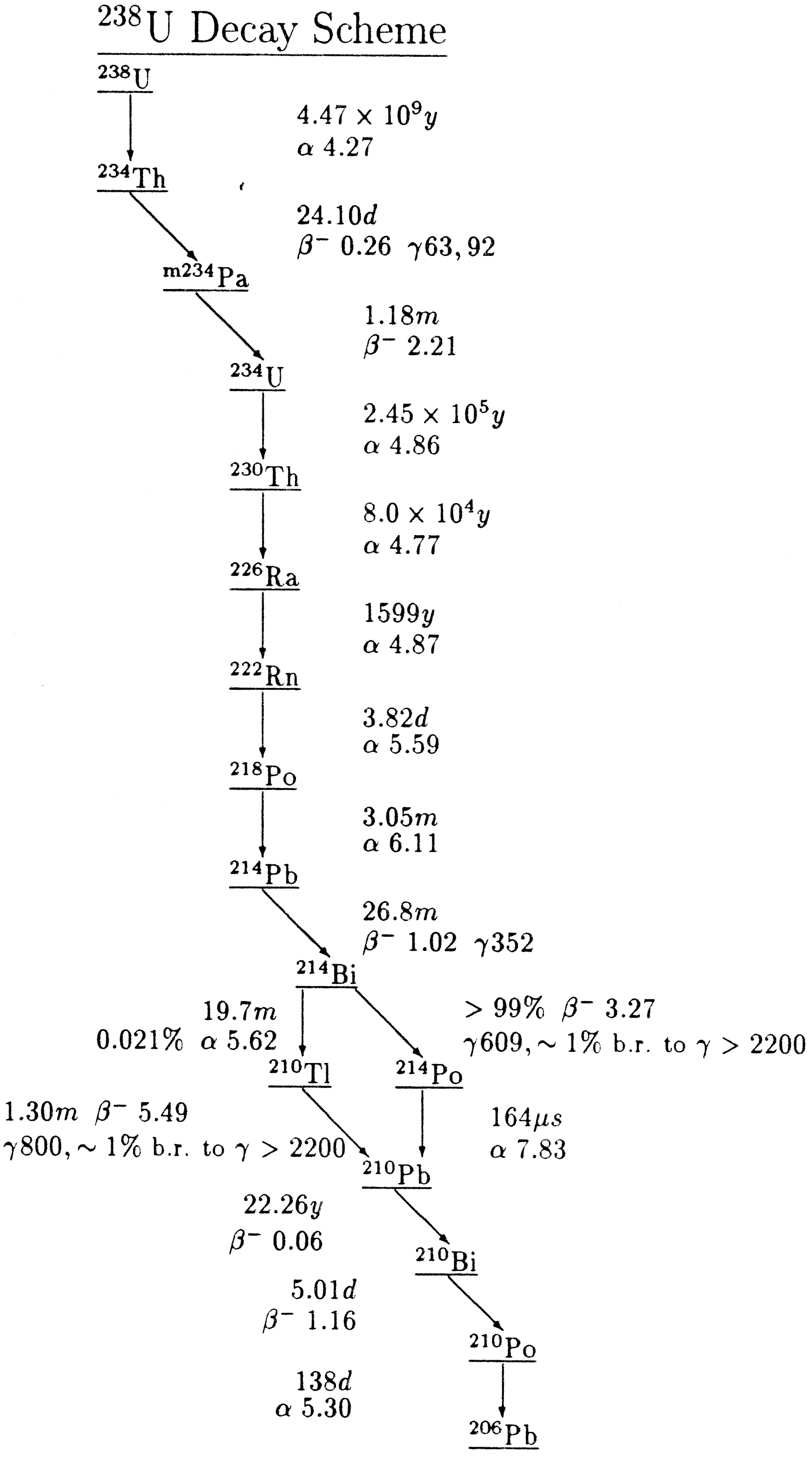

Figure 2.5: Simplified schematic of the $^{238}$U decay chain. Half-lives of alldecays are given, together with Q-values in MeV of $\alpha$ and $\beta^-$ decays and energies in keV of important $\gamma$ radiations.

The second respect in which the MC assumptions concerning activity in the water are likely to be wrong concerns the uniformity of its distribution. Convective cells in the water flow pattern, if present, could result in water being trapped in eddies: the levels of contamination in these regions would presumably build up with progressive leaching. The light water may thus develop non-uniform radioisotope concentrations and it is clear that contaminants could be moved towards the heavy water sphere from the PMT sphere or the steel liner.

## 2.5 The assay of SNO water

It has been established that the concentration of dissolved activity in the SNO cavity will probably be non-uniform and in secular disequilibrium. The backgrounds in the detector due to activity in the water, however, depend on the distribution of $^{208}$Tl and $^{214}$Bi decays in the detector: knowledge of the concentrations at which the species in the Uranium and Thorium chains which are released into the cavity by the purifier has been shown to be insufficient to determine this distribution, even if the water flow pattern in the cavity is known. It follows that during the operation of the detector, water sampled from a number of locations in the cavity must be assayed. In the main part of this section, the case of the $^{232}$Th chain will be considered, and the similarity of the $^{238}$U chain finally noted.

### 2.5.1 Assay of the Thorium chain

The $\sim 10^{-15} g/g$ limiting concentrations deduced in Section 2.3 refer to the head members of the chains on the assumption of secular equilibrium. The isotopes whose decay gives rise to troublesome gamma-rays (TG's), however, have very much shorter half-lives and so must be present in the water at concentrations many orders of magnitude lower still. In view of the different half-lives present, the disintegration per day per ton (*ddt*) is a more useful measure than the concentration, since it is constant for all species in a chain in secular equilibrium.

The radioassay of water at the level of 1*ddt* is not thought to be possible by direct counting of samples. Direct chemical or mass spectroscopic methods are likewise not thought to be sensitive at the required levels, even for the head members of the chains. It is therefore proposed first to pre-concentrate the activity in a large sample of water into a smaller volume and then to radioassay the concentrate. The methods of pre-concentration and of subsequent counting are for the present left unspecified: the considerations in this section apply irrespective of the techniques used. Since the quantities of heavy and light water in the detector must be kept constant to avoid excessive stress on the acrylic vessel, freshly purified water must be returned to the cavity at the same rate as it is drawn off, which limits the rate of sampling to $150 l\, min^{-1}$ with the present apparatus. Since the pre-concentration stage might not be capable of efficiently extracting from so large a flow rate, this is an upper limit.

Having established which decays in the Thorium chain give rise to troublesome gamma-rays, and that regular assays of the water are necessary in order to deduce the level of detector background, it is necessary to establish which of the isotopes in the Thorium chain

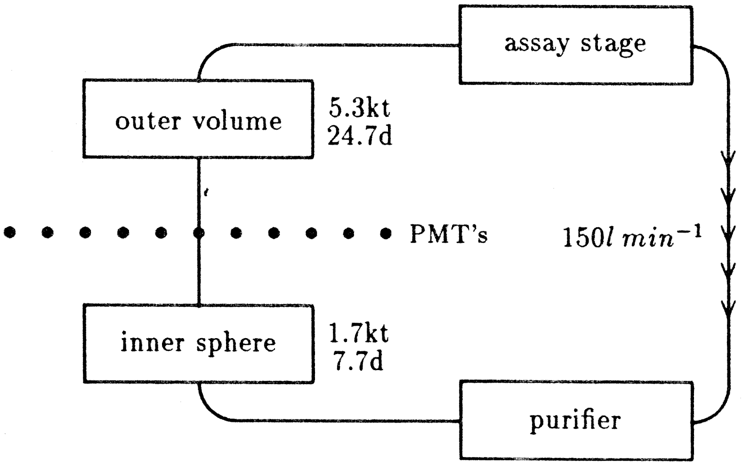

Figure 2.6: Schematic of the simplest possible water circulation pattern.

are important for assay purposes.

**Important Note**

The aim of the assay is to gain information about the rate and distribution of troublesome gamma-ray generation within the PMT sphere.

Restrictions may therefore be imposed on the isotope/s chosen for assay:

1. Only species which influence the TG rate need be assayed,
2. The sample must contain a sufficient number of atoms of the species in question in the sample to afford good counting statistics, and
3. The half-life of the species must be sufficient to allow time for the collection, preparation and counting of the sample.

An illustration is afforded by considering the simplest possible light water flow cycle — $H_2O$ is injected at the acrylic sphere and withdrawn at the outer edge of the cavity; it then passes to an assay stage and thence to the polisher before re-entering the cavity. This scheme is presented in Figure 2.6. On the simplest assumptions concerning the water flow pattern, the light water residence time in the cavity is 32.4 days, 7.7 days in the inner sphere and 24.7 in the outer. It follows from Figure 2.4 that essentially all contaminant atoms below $^{228}$Th, present anywhere within the PMT sphere, have decayed to $^{208}$Pb before reaching the outlet. All information about the concentrations of these species in the critical region of the detector has thus been destroyed by decay before assay is possible. Since the TG production within the PMT sphere depends on the concentrations of species lower than $^{228}$Th, the relevant information has not been obtained by this assay procedure[4].

It is also reasonable to assume that the water will have become contaminated with $^{228}$Th while passing through the PMT sphere and in the vicinity of the steel liner: this is indistinguishable from $^{228}$Th originally present within the PMT sphere. This example demonstrates that important information is lost by allowing too great a residence time in the cavity, and that the water in the inner sphere needs to be sampled directly. Both these considerations suggest that outflows should be provided at the PMT sphere to take water from within it.

Modifying this scenario to allow for $150l\, min^{-1}$to be taken from the inner sphere directly to the assay stage implies a residence time of just 7.7 days (2.1 $^{224}$Ra half-lives) and thus allows information on both $^{228}$Th and $^{224}$Ra concentrations within the PMT sphere to be obtained, without contamination from the PMT's themselves, and their associated support structure. This scenario gives the approximate lower limit on the realistic residence time of water in the detector before sampling, given the $150l\, min^{-1}$ capacity of the polisher. This limit is of order several days and thus species below $^{224}$Ra in the Thorium chain cannot independently be assayed as their half-lives ensure that they are in secular equilibrium with $^{224}$Ra.

We may also note from the above scenarios that species above $^{228}$Th need not be assayed as, on the time scale of several days, they are completely decoupled from TG's by the $1.9\, y$ half-life of this isotope.

The effect of secular equilibrium on the choice of isotope for assay may be illustrated by considering a limiting case, where water is allowed to flow from the cavity through the pre-concentration apparatus until the rate accumulation of activity in the concentrate is balanced by the rate of decay. It is easily seen that the limiting activity of the concentrate is $FA_w/\lambda$ where $F$ is the mass flow rate of water ($150l\, min^{-1} \equiv 9\, ton\, h^{-1}$), $A_w$ is the dissolved activity per unit mass ($1ddt \equiv 1/24\, h^{-1}\, ton^{-1}$) and $\lambda$ the decay constant of a given species. For $^{228}$Th, $^{224}$Ra and $^{212}$Pb the limiting activities are $9080h^{-1}$, $48h^{-1}$ and $6h^{-1}$ respectively. Any of these activities might in principle be measurable[5].

However, the time taken for these limiting activities to be accumulated is governed by $\lambda \sim 1/t_{1/2}$, so that such an assay of $^{228}$Th would take a much longer time than the residence time of water in the detector. It would be more reasonable to aim to collect a sample whose activity was, say, $100d^{-1} \equiv 4.2h^{-1}$, so as to afford reasonable statistics in a reasonable counting time, if the overall efficiency of extraction and counting were not too low. Such a sample would take 11–12 hours to accumulate[6] in the cases of $^{228}$Th and $^{224}$Ra, and 20 hours for $^{212}$Pb. Such a sample would contain only 60 $^{212}$Pb atoms, but 500 $^{224}$Ra atoms or $10^5$ $^{228}$Th atoms. Thus, unless the assay and counting procedures approach 100% efficiency, $^{212}$Pb is likely to afford poor counting statistics.

These considerations show the interaction of the parameters which describe the assay:

---

[4] Generation of TG's without the PMT sphere is clearly of much less significance than within it, and determination of that rate is not therefore the primary aim of the assay procedure.

[5] It has been assumed that the pre-concentration stage allows no permeation of the activity.

[6] It would, of course, take longer if the pre-concentration stage could not operate efficiently at $150l\, min^{-1}$.

- the rate at which the assay procedure is capable of processing water,
- the throughput of the polisher,
- the half lives of the elements in the $^{232}$Th chain,
- the residence time of water in the cavity before assay.

The level of activity (1*ddt*) which it is necessary to assay dictates how large a water sample must be processed to obtain reasonable counting statistics. The rate at which extraction from the sample is possible in turn dictates how long is required for collection, which imposes a minimum half-life which may be assayed. Furthermore, for a section of the chain in secular equilibrium, a species of long half-life has a proportionately greater abundance and so provides better counting statistics than a species of short half-life. These considerations all suggest the choice of a long-lived species for the assay: ideally a species would be assayed which had a long half-life and rapidly came into equilibrium with all its daughters down to the source of TG's.

In practice, the $^{228}$Th decay chain does not provide such a species on the time-scale of a typical residence time before assay, *ie.* not less than several days. An intermediate case instead applies, in which the total TG generation by the sample whilst in the cavity depends on its initial concentrations of both $^{228}$Th and $^{224}$Ra. Unless the species in the chain below $^{224}$Ra are leached into the water at rates such that their concentrations are grossly in disequilibrium, assay of these isotopes furnishes all the information still available after a residence time of several days. $^{228}$Th and $^{224}$Ra are thus established as being the key isotopes for assay of the Thorium chain.

### SNO problem — Constraints on a suitable assay procedure

The requirements placed upon a procedure suitable for the assay of water to the stated levels of activity are discussed below. They are for sufficient sensitivity, low background, speed of assay and real-time response. The important case of $^{224}$Ra assay is first considered and the modifications to those requirements for the case of $^{228}$Th assay then briefly considered.

**High sensitivity** The most significant requirement on the assay procedure is that of high sensitivity. At the level of 1*ddt*, we are attempting to assay about 5 $^{224}$Ra atoms per ton of water. It has been shown above that these concentrations lead naturally to pre-concentration followed by radioassay. Furthermore, with only a small total number of decays to be counted, reasonable extraction and counting efficiencies are essential.

Any decrease in the extraction efficiency simply results in a lengthening of the time required for accumulation of a sample of specified activity.

**Low background** The small signal to be detected requires that the background (which here refers to the background associated with the entire assay procedure, and not, for example, just to the detector background) be correspondingly small. This background can arise in essentially two ways. The first is contamination of the sample with trace $^{224}$Ra from the environment or from the apparatus. The possibility of contamination imposes severe restrictions on the materials with which the water may be allowed to come into contact after it leaves the SNO cavity. All metals, and glass, are ruled out because it is known that they contain concentrations of Radium and Thorium high compared to those in the water and are thus likely to introduce contamination by leaching or by bulk dissolution. Furthermore, the water cannot be exposed to air, since airborne dust will be a source of contamination. The only safe materials are plastics such as PTFE, polypropylene *etc.* Thus all the pipes and pumps with which the water will come into contact must be constructed of, or lined with, these materials. The material within which the Radium is to be concentrated must also be initially low in Radium content.

Radium contamination is particularly likely if reagents are added to the water before counting, and thus the smallness of the signal eliminates the commonest method for extraction and assay of Radium, used for $^{226}$Ra assay, which is co-precipitation with Barium in the form of its insoluble sulphate salt, followed by alpha-counting. This procedure exploits the similarity between the chemical properties of Radium and Barium: thus in the process of precipitation, bulk Barium acts as a carrier for Radium atoms isolated from each other. This process is infeasible for SNO because of the low Radium concentrations involved and because of the high Radium content of Barium salts, an inevitable consequence of the similar chemistry of the two elements. In the case of $^{224}$Ra, initial levels of this isotope in Barium salts will quickly decay and so are unimportant, but $^{228}$Ra will also be present and will support $^{224}$Ra for many years.

The second probable source of background to the assay procedure is detector background, from whatever source. A method of detection of the extracted Radium is thus required which has a background count rate not exceeding a few per day.

**Speed of assay** Assay procedures for $^{224}$Ra are constrained by its half-life, of approximately 3.6 days. Since it is necessary to pre-concentrate the activity in some way, the assay procedure must consist, in quite general terms, of four steps.

1. Removal from the cavity of the water volume for assay,
2. Extraction of its Radium content into some smaller mass of material,
3. Preparation of this material for counting, and
4. Counting the prepared sample.

As discussed above, the half-life of $^{224}$Ra does not result in a substantial increase in the time required to accumulate the sample. However, after extraction from the assay volume is complete, there will in general be some preparation required before the sample can be counted: this could be as simple as removing a cartridge from the water stream and placing it in a low-background gamma-ray detector (if that were a sufficiently sensitive technique). Any preparation which is necessary is subject to the requirement that it take a time not long compared to the $^{224}$Ra half-life.

**Real-time monitoring** The monitoring of activity in the detector in 'real time' is necessary if short-term variations in contamination are to be searched for. 'Real time' is here taken to mean that the frequency of sampling is as large as possible, thereby obtaining the maximum information concerning contamination in the cavity. An approximate upper limit to this frequency may be deduced if the SNO water is to be continuously sampled.

It is intended to have one apparatus counting sources generated by drawing water samples from the cavity, one source at a time. If this system is to run continuously, and if there is not to be a long delay between the extraction from a sample and counting of the resultant activity, then it follows that a given source may only be counted while the succeeding one is activated. The choice of time-scale for this procedure is limited by the half-lives in the Thorium chain, and since $^{212}$Pb is not a suitable species for assay, the natural choice is a time-scale of several days, to correspond with the $^{224}$Ra half-life.

Ideally, a sample would be counted for many half-lives, to maximise the number of counts obtained, but the counting time has been identified with the time required for activation of a sample, and it has been established that this should be comparable to a half-life. These conflicting requirements suggest that, if the water is to be continually sampled, then a compromise between them must be reached.

The above points have referred to $^{224}$Ra as it is the lowest isotope in the Thorium chain which affords any information about the activity levels in water 'deep' in the detector, by which is meant water far from the outflow to the assay stage and polisher. $^{228}$Th assay differs principally in that the statistical accuracy attainable is in principle is much higher than in the case of $^{224}$Ra. However, it is clear that the sample cannot be counted for a period of order one year, but more likely for a period of order one week. Thus, although the statistical accuracy is available, the requirement to obtain results in a reasonable time much diminishes this advantage of using a longer-lived species for assay.

**Simplifications which result if species leached are in secular equilibrium** In the special case that $^{228}$Th is leached into the water in (or near) SE with $^{224}$Ra, the assay procedure is very much less constrained. In this case assay of $^{228}$Th is equivalent to assay of $^{224}$Ra and very much slower assay procedures are possible, with the *caveat* mentioned in the preceding section that frequent monitoring is sacrificed. The requirements of high sensitivity and low background are, of course, unaffected.

It has been stated that SE of the relevant part of the Thorium chain ($^{228}$Th–$^{208}$Pb) holds in all static detector components. For leached species in this part of the chain to be in SE therefore requires only the additional assumption that their propensities to leach are equal.

Although no measurements are known of this process, processes which disrupt SE in the leachate may be envisaged:

1. Thorium is known to be very insoluble at neutral pH, whereas Radium is known to be much more readily soluble. Copious evidence of the phenomenon of 'plate-out' was obtained in the course of the work presented in Chapter 5, and was most evident in the secular disequilibrium of near-neutral $^{228}$Th solutions. This strongly suggests that Radium will be more readily leached than Thorium.

2. The copious emanation of $^{222}$Rn by steel has been reported [91], which may be an example of the possibility mentioned above (page 45), that the mobility of a species within bulk material could affect its leaching rate. This process will presumably only be significant in the Uranium chain as $^{220}$Rn lives too short a time to diffuse large distances within a lattice structure.

### 2.5.2 Assay of the Uranium chain

The case of the $^{238}$U chain is similar to the $^{232}$Th chain in that TG generation is governed by a species ($^{226}$Ra) with a lifetime long on a time-scale of days, followed by a daughter ($^{222}$Rn) with a half-life of about 4 days, all intermediate half-lives between $^{222}$Rn and $^{214}$Bi being short. There is thus an analogy between $^{228}$Th and $^{226}$Ra and between $^{224}$Ra and $^{222}$Rn with respect to the requirements to assay these species. However the very different chemical properties of these pairs of species mean that the details of the assay procedures must of necessity be very different, with the important exception that any chemical procedure which extracts $^{224}$Ra from water will extract $^{226}$Ra.

By similar arguments to those above, to obtain all available information concerning TG generation by $^{214}$Bi in a water sample, both $^{226}$Ra and $^{222}$Rn assay procedures are necessary. The typical time scale available for these assays is governed by the same considerations as applied to the $^{228}$Th/$^{224}$Ra case, with the result that sample collection and counting must operate on a time scale of several days.

# Chapter 3

# Sorption and assay of dissolved radioisotopes

## 3.1 Ions in solution

### 3.1.1 Solvation

The presence of a charged ion in solution affects the surrounding solvent molecules by virtue of its electric field. It can be seen that such ions must polarize nearby molecules, resulting in an attractive force between solvent molecules and the ion. Furthermore, in the case of polar solvents, molecules will clearly tend to align themselves in the ionic field. Burgess [84, 85] presents a model which describes the environment of a dissolved ion resulting from the effect of the ion itself on molecules of the solvent. The model may be applied to ions in any solvent, but the only case discussed here, and by far the most widely studied, is the case where the solvent is water. It is also applicable equally to anions and cations, but the discussion here focuses on metallic cations since this is relevant to actinide solution chemistry. The model neglects the effects of anions or other cations on an individual metal ion, and so is only an accurate description for dilute solutions, typically 0.01M concentration or less.

The model envisages the solvent around the ion as partitioned into three distinct zones. The innermost zone, a shell only one molecule thick, consists of molecules interacting directly with the ion and is known as the primary solvation shell. Often there are 6 molecules in this shell [85]. Because of the polar nature of the water molecule, and its non-linear shape, water molecules in the primary solvation shell of a metallic cation are aligned such that the oxygen atoms are closer to the ion and the hydrogen atoms more distant. The hydrogen atoms' net positive charge is increased by the polarising effect of the cation and this encourages hydrogen bonding between the molecules of the primary solvation shell and more distant molecules, with the result that a weakly bound secondary solvation shell is generally formed. Beyond this, a disordered zone is postulated to exist, marking the gradual transition from the ordered secondary solvation shell to the differently-ordered bulk solvent.

The extent of the secondary solvation shell is thought to depend on the charge density of the ion, *ie.* it will be large for small, highly-charged ions and small or negligible for large, monopositive ions. Various techniques have been used to investigate the solvation shells, including UV-visible and Raman spectroscopy, proton NMR and studies of thermodynamic and transport properties of solutions. Of these techniques the most important is probably NMR, which in favourable cases has been able to determine the coordination number — *ie.* the number of water molecules in the primary solvation shell — of a solvated ion by measurement of the NMR peak area: this is only possible if water molecules remain in the same environment for a time long compared to the inverse of the resonance frequency. Other methods generally measure the total number of molecules which are associated with the cation, in the primary plus secondary shells. NMR has been used by Fratiello *et al.* [83] to determine the solvation number of Thorium as 9, while other methods give values in the range 8–10.

Water molecules may exchange between solvation shells and bulk solvent, and the mean residence time for a molecule in the primary solvation shell is given by Burgess for a wide variety of ions: it varies from $\sim 1ns$ to $\sim 1d$, with the more highly charged ions generally giving longer times. Unfortunately, no data for Thorium is available.

### 3.1.2 Hydrolysis

A water molecule in the primary solvation shell of a highly-charged ion may be sufficiently polarised that it releases an $H^+$ ion, and the cation thus acts as an acid. The remaining hydroxide ion is then firmly bound to the cation, which is said to be hydrolysed. A sequence of successive hydrolysis reactions is possible, with the formation of successive hydroxoaqua-cations.

$$\begin{aligned} M(H_2O)_m^{n+} &\rightleftharpoons M(OH)(H_2O)_{m-1}^{(n-1)+} + H^+ \\ M(OH)(H_2O)_{m-1}^{(n-1)+} &\rightleftharpoons M(OH)_2(H_2O)_{m-2}^{(n-2)+} + H^+ \\ &\vdots \\ M(OH)_{n-1}(H_2O)_{m-n+1} &\rightleftharpoons M(OH)_n(H_2O)_{m-n} + H^+ \end{aligned}$$

which are characterised by equilibrium constants $K_1 \cdots K_n$ which determine the relative abundances of the species at a given pH.

$$K_l = \frac{[H^+][M(HO)_l(H_2O)_{m-l}]}{[M(OH)_{l-1}(H_2O)_{m-l+1}]}$$

Traube [86] states that the determining factor in cation hydrolysis is the 'ion potential' $Z/r$ where $Z$ is the ionic charge and $r$ the ionic radius: a higher ion potential corresponds to a greater tendency towards hydrolysis. This quantity is clearly related to the electric field in the neighbourhood of the ion. Hydrolysis of Thorium is well known and details are given in the next section. Among the alkali metals and alkaline earth elements, which include Radium, hydrolysis is only significant for the small, highly-charged $Be^{2+}$ ion. All others form simple solvated species. (Little data concerning Radium *per se* is available, but its chemistry is generally assumed to be similar to that of Barium).

Another consequence of hydrolysis is the formation, in several instances, of polynuclear species, in which two or more metal ions are linked by oxo- or hydroxo- bridges. Well-characterised cases which form a variety of polynuclear species whose stability is pH-dependent include Aluminium, Bismuth, Lead and Nickel. Thorium is also known to behave in this way.

### 3.1.3 Complexation and selectivity

All metal aquacations participate in complexation reactions of the form $M + L \rightleftharpoons ML$ with suitable ligands $L$. To form such complexes, these ligands must displace some or all of the bound water molecules by a substitution reaction.

A two-stage mechanism may be used to describe complex formation (see Burgess [85]). Initially, there is a pre-association between solvated ion and ligand, forming a loosely bound, transient species. The second step is the actual substitution, when the ligand replaces a water molecule. The substitution is normally dissociative and rate-limiting for the transition metal ions, *ie.* a solvating water molecule is first lost by the metal ion, and the nearby ligand promptly replaces it. In such cases, the rate constant therefore depends little on the nature of the incoming ligand and is slowest for small, highly-charged cations which slowly exchange solvent molecules. Substitution can also be associative in character, *ie.* the ligand bonds to the cation before a solvent molecule is lost: in this case the rate constant depends strongly on the nature of the ligand, and the transition state is rather more strongly bound than in the dissociative case.

The case of bidentate or polydentate ligands, those which have two or more coordinating sites, is more complex in that a ring-closure step is necessary after substitution at one active site. The first substitution proceeds as above, but the overall formation rate then depends on the rate of solvent exchange relative to the speed with which ring closure is possible. If solvent exchange is slow, then the loss of a second solvent molecule will promptly be followed by ring closure (for a bidentate ligand) and the formation rate constant will be little different from that for the analogous monodentate ligand. If solvent exchange is rapid, or if the ligand is bulky, then ring closure can become improbable compared with solvent return, and can be the rate-limiting step. In this case, rate constants are very dependent on the nature of the ligand.

More complex ligands, either macrocyclic or encapsulating, have correspondingly lower rate constants for complex formation, but form complexes of greatly enhanced stability and offer the possibility of selectivity based on cation size. Thus a tetradentate ligand forms a more stable complex than the bis-bidentate analogue, which is in turn more stable than the tetra-monodentate species. A complete ring structure around the central cation, as opposed to a linear polydentate ligand, also confers additional stability. Five- and six-membered rings are generally the most stable, because of the difficulty of ring closure and the associated entropy decrease for larger rings.

Well-known macrocycles and and encapsulating ligands, the crown ethers and cryptands, exhibit selectivity variations between similar cations for a given ligand. Those cations smaller than the fixed size of the cavity are unable to interact with all the coordinating groups and so form complexes of lower stability than slightly larger cations. If the cation is too large, the ligand will be above its ground state due to being 'stretched', and a smaller cation would result in a lower overall energy. Forward rate constants for formation of complexes with these ligands depend, in general, on the degree of flexibility of the ring — rigid rings giving rise to much lower rate constants than flexible rings or open-chain polydentate ligands.

### 3.1.4 The solution chemistry of Thorium

A substantial body of data exists concerning the chemistry of Thorium, and has been collated by Katzin and Sonnenberger [81]. Among known Thorium compounds are hydrides, nitrides, carbides, antimonides, arsenides and others including halides. The commonest form of Thorium is $ThO_2$, which is a refractory oxide. $Th(OH)_4$ forms as a gelatinous precipitate on adding excess alkali to a Thorium solution, and its solubility product is $\sim 10^{-40}$. Known Thorium salts include the perchlorate, several carbonates and the nitrate $Th(NO_3)_4$ which is extremely soluble, more so than any other Thorium compound. Many organometallic Thorium compounds are also known: Cardin *et al.* [80] list 39.

Traube lists ion potentials for a number of tetrapositive ions: they are found to be ordered as

$$Zr^{4+} > Pu^{4+} > Ce^{4+} > Np^{4+} > U >^{4+} Th^{4+}$$

in agreement with the statement of Katzin and Sonnenberger that Thorium is the least hydrolysed tetrapositive ion. However, it is well known to be hydrolysed on standing in solutions at near-neutral pH. Under sufficiently acid conditions, $pH < 0.5$, Thorium exists solely as a solvated $Th^{4+}$ ion. That form dominates below pH3, when hydrolysis occurs with the formation of $Th(OH)_n^{(4-n)+}$. On standing, these species polymerise. The pK values for the first two hydrolysis reactions have been measured for Thorium by Ushenko and Skorik [105] and are $pK_1 = 3.15$, $pK_2 = 6.6$. ($pK \equiv -\log_{10} K$).

Hietanen and Sillén [76] demonstrate that solutions of Thorium 'age' — that the mean number of bound OH groups per Thorium atom, Z, increases with time, and that the pH correspondingly decreases as hydroxide ions are removed from solution. They also demonstrate that $Z$ depends on pH and concentration — at 0.1mM it increases dramatically at pH4 and at 0.1M, at around pH3. At all concentrations it rises monotonically with pH.

Milić [77] demonstrates that, at relatively high (3M) concentrations of alkali and alkaline earth metal nitrates present as background ions, there is a small dependence of the equilibrium constant for Thorium hydrolysis on the nature of the other ions present. He also calculates the mean number of Thorium atoms and hydroxide ions in complexes, and shows that this depends on the presence and nature of other ions in solution. The species he considers are of the form $Th_q(OH)_p^{+(4q-p)}$, *ie.* general hydrolysed Thorium polymers.

Thorium is known to polymerise on standing in solution at near-neutral pH. Cotton and Wilkinson [73] state that in perchlorate solutions (where there is little or no interaction between anion and cation[1]) hydrolysis of Thorium becomes extensive at $pH > 3$ and that the

---

[1] The stability of the perchlorate ion $ClO_4^-$ ensures that it exhibits little tendency to participate in com-

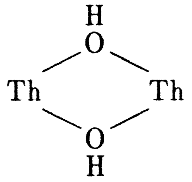

Figure 3.1: Structure of the Thorium dimer $Th_2(OH)_2^{6+}$

main ions present are $Th(OH)^{3+}$, $Th(OH)_2^{2+}$, $Th_2(OH)_2^{6+}$ and $Th_4(OH)_8^{8+}$. On increasing the pH of a solution from $\simeq 2$, the first species formed is generally $Th(OH)_2^{2+}$, followed by polymerisation. The interpretation of the dimeric species is given in Figure 3.1 and all species have additional solvating water molecules.

Katzin and Sonnenberger are in reasonable agreement, giving the principal forms as $Th(OH)^{3+}$, $Th_2(OH)_2^{6+}$, $Th_4(OH)_{12}^{4+}$ and $Th_6(OH)_{15}^{9+}$. Ahrland [82] notes that equilibrium is not rapidly established among Thorium hydrolysis products while Z is less than about 2. When Z rises to about 3, aggregates of more than 100 Thorium atoms can form.

The presence of anions capable of complexing Thorium greatly increases the number of possible chemical forms of dissolved Thorium. Allard [75] lists as known complexants $HCO_3^-$, $CO_3^{2-}$, $H_2PO_4^-$, $HPO_4^{2-}$, $PO_4^{3-}$, $F^-$, $Cl^-$, $SO_4^{2-}$ and $R\text{-}COO^-$. Katzin and Sonnenberger augment this list with the addition of iodate, bromate and chlorate. In natural waters the principal complexant is generally the carbonate ion, whose presence can considerably enhance Thorium solubility in alkaline solution.

Allard also points out that solutions of hydrolysed Thorium species are always unstable to slow precipitation. Furthermore, the positive charge on Th-OH complexes tends to induce sorption onto oxide or silicate surfaces, such as the walls of a glass container. This process of sorption of a species from solution onto the walls of a container is known as 'plate-out'.

Choppin and Rydberg [78] present data on Thorium sorption onto glass and polyethylene for Thorium solutions in the $10^{-6}$–$10^{-4}$M concentration range. They find, in particular, that the equilibrium sorption of Thorium from $2 \times 10^{-8}$M perchlorate solution onto glass passes through a maximum of 80% at pH $\simeq 4$ but that in the case of polyethylene, the increase for pH $\geq 4$ is monotonic and reaches 100% by pH7. Since the capacity of a surface for Thorium sorption is small but finite, it is easily seen that the fractional effect will be greater for very dilute solutions, as are commonly encountered with radioactive species, particularly those of high specific activity [74]. In the case of $^{228}$Th, a $10 Bq\ l^{-1}$ solution has a concentration of only $\sim 10^{-15}$M — very much lower than the concentrations at which data on Thorium chemistry is obtained ($^{232}$Th is used). Although equilibrium plate-out from such a solution might be expected to be 100%, the formation of polynuclear complexes would be correspondingly slower, increasing the useful lifetime of the solution.

---

plexation. The nitrate ion is likewise not known to complex Thorium.

Sorption onto solid surfaces, although generally undesirable, is the basis of the usual method of extraction from solution of trace radioisotopes. Flocculent precipitates such as Calcium and Iron phosphates or hydroxides are used for decontaminating large volumes of low-level radioactive waste [74].

The two phenomena of slow precipitation and plate-out of near-neutral Thorium solutions clearly imply that the concentration of such solutions is likely to decrease with time, with the consequence that such solutions, when stored between creation and use, do not have an easily predictable concentration. This fact will be seen to have very important consequences for the work described in Chapter 5, where Thorium solutions of pH $\simeq 7$ were used. Plate-out also leads to secular disequilibrium in samples taken from a $^{228}$Th solution. Dissolved $^{224}$Ra is supported both by dissolved and plated-out $^{228}$Th, since it is readily soluble. A sample taken from such a solution might therefore be expected to have an initial Radium concentration greater than can be supported by its dissolved Thorium content. This was observed to be the case in all near-neutral $^{228}$Th solutions used in the experiments described in Chapter 5.

## 3.2 Solid phase sorbents

Conditions in a solution near a solid-liquid interface are substantially different from those which exist in the bulk solution. In this section, the effect of a solid surface on a solution is briefly discussed. Sorbents of potential use in SNO are then discussed.

The solid-liquid interface has been modelled extensively by analytical and computational methods and a number of experimental methods have been used to investigate its thermodynamic and other properties [92, 93, 94, 95]. In general, a solid-liquid interface carries a surface charge density due either to the preferential sorption of a charged species from solution or the preferential dissolution of a charged species from the solid. As a result, a charge *separation* will also exist at the interface, arising from oriented dipoles bound at the surface: these may be polarised solvent molecules or oriented polar molecules. A 'point of zero charge' will also exist being that pH at which the surface charge density is zero.

The fields resulting from the surface charges influence the distribution of charged species in the solution through Maxwell-Boltzmann statistics. The electrostatic potential near the interface is determined both by the interface itself and by the resulting distribution of dissolved charged species. Poisson's equation may be solved for this situation with the result that the potential is given by $\phi = \phi_0 \exp(-\kappa x)$ where $x$ is distance from the surface and

$$\kappa^2 = \frac{e^2}{\epsilon kT} \sum_i n_i Z_i^2$$

so that $1/\kappa \equiv R_D$, the Debye-Hückel radius. The net charge density in solution is given by

$$\rho = -2n_0 Ze \sinh\left(\frac{Ze\phi}{kT}\right)$$

due to a deficiency of ions of one sign and an excess of the other in the vicinity of the surface. The energy difference between the sorbed and dissolved states of an ion is often expressed as a sum of two terms — a chemical interaction with the atoms of the solid and an electrostatic term arising from the above potential.

### 3.2.1 Inorganic sorbents for radioactive elements

A large amount of investigative work has been performed into selective sorbents for radioactive elements because of the need to reduce the activity of medium-level waste streams generated by the nuclear industry, notably by fuel re-processing plants, to acceptable levels before discharge. Among the requirements for a successful decontamination process are a large reduction in the volume of the waste and as low a cost as possible. $Fe(OH)_3/Al(OH)_3$ flocculation methods have been used at BNFL Sellafield for many years and reduce waste volumes by a factor of 5–10. Although effective, storage facilities for large volumes of precipitate are expensive. Concentration by evaporation has also been used, but the facilities are again expensive and the corrosive nature of the waste leads to a need for frequent maintenance, by remote-handling methods. Sorption onto a small amount of material, such as an ion exchanger, is an attractive method for dealing with medium-level waste since it affords a large volume reduction, requires little expensive plant, and allows inactive species to pass unaffected if a selective sorbent is used.

Hooper *et al.* [88] discuss at length the use of inorganic ion exchangers for this application and review the performance of a number of sorbents with respect to a wide range of elements occurring in waste streams. They give no information concerning Thorium or Radium sorption, however, as these are not elements of interest to the nuclear industry. Although the commonest sorbents for extraction of ions from solution are commercial ion-exchange resins, inorganic materials have a number of advantages for nuclear applications.

1. Intense radiation has little or no effect on the chemical structure of inorganic exchangers. The small observed effects are attributed to heating.

2. Nitric acid, often the carrier for waste streams, has little effect on many inorganic exchangers, in contrast to organic exchangers.

3. Inorganic exchangers can exhibit high selectivity for certain ions.

4. They can have a very high capacity, although at the expense of mechanical strength.

5. They are more compatible than organic exchangers with the materials likely to be used for final immobilisation of the waste.

Hooper *et al.* list a number of requirements which must be satisfied by a successful inorganic exchanger for use with medium-level waste streams. Many of these also apply to their use in SNO. Among them are:

1. Uncompromised performance in the presence of other dissolved species. This is of relevance to SNO in the event that a neutron absorber (*eg.* sodium chloride) is present in the stream to be assayed.

2. A high surface area to provide rapid exchange.
3. Stability under process conditions: for SNO application this means a low solubility in water at pH7. (Resistance to high radiation fluxes and low pH's is not required for SNO. Nor is regenerability, as it is not proposed to re-use contaminated absorber samples).
4. Sufficient mechanical strength to form a packed bed.
5. Availability in particle sizes which allow sufficient flow rates without unacceptable pressure drops *ie.* particle size must not be too small. (If this requirement conflicts with the requirement for high surface area, tangential filtration could be used and the packed bed arrangement abandoned).

The requirement to operate in the presence of other dissolved species is a crucial one in selecting a suitable exchanger for SNO. Leaching from detector components, and slow dissolution of the materials from which they are fabricated, will ensure that a variety of ions is present in the outlet stream from SNO at concentrations much higher than those of the relevant radioisotopes. If these species compete effectively with Thorium and Radium for sorption, *ie.* if the sorbent is not selective, the sorption of active species could be significantly slowed.

In the event that a neutron absorber is present in the heavy water, its concentration will be very much higher than that of the active species (0.25% in the case of sodium chloride). In this case, it seems likely that if the neutron absorber is adsorbed to any extent on the sites responsible for the sorption of active species, then saturation of the absorber could occur, with the result that sorption of active species would cease entirely. Thus it is essential that any absorber used to assay the heavy water cycle permit free passage of the chosen neutron absorber. Pre-treatment of the stream to remove competing species is not an option: any such treatment would carry an unacceptable risk of affecting the concentrations of active species, either by addition through further dissolution or, more likely, by their partial extraction by a sorption or other process.

Selectivity is thus an important consideration and in general, commercial ion exchangers are not selective, although inorganic exchangers generally are (see Hooper *et al.* for examples).

An important class of exchangers investigated by Hooper *et al.* was hydrated transition metal oxides — represented by hydrous titanium oxide, manganese dioxide and polyantimonic acid. These oxides are well known to act as ion exchangers, although the mechanism of absorbtion onto transition metal oxide surfaces is often uncertain and depends on the composition and crystal structures of these often non-stoichiometric compounds. Stumm and Morgan [87] give a simple model (Figure 3.2) according to which metal ions at a metal oxide–water interface have a reduced coordination and thus bind to the oxygen atom of a water molecule. This then hydrolyses with the result that hydrated metal oxide surfaces typically have 4–10 bound hydroxide groups per square nanometre. These groups are then capable of participating in $H^+$ exchange.

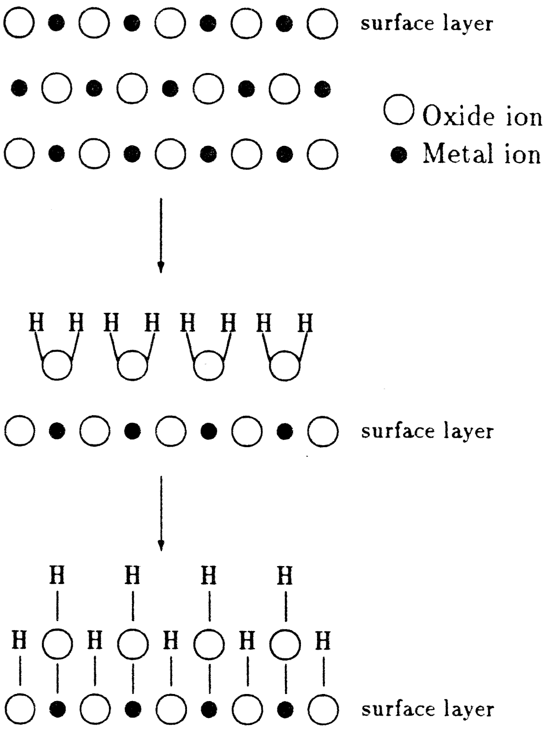

Figure 3.2: Simple model of the metal oxide – water interface showing anhydrous, hydrated and hydrolysed states.

A more realistic model of a hydrated metal oxide would give it a disorderly, non-stoichiometric structure of no well-defined crystalline type: metal atoms and hydroxide groups would exist in a range of different chemical environments. More than one type of active site might therefore be available. The degree of hydration, however, is a key parameter in determining the chemical and physical properties of hydrated metal oxides. High mechanical strength is a desirable feature if the absorber is to be used in a packed-bed arrangement, since granular material of large particle size is required if the bed is not to offer a very high impedance to water flow. Mechanical strength is afforded by a relatively 'dry' structure in which the lattice is reasonably regular.

Freshly-precipitated material is in general unsuitable for use in a packed bed since it has no mechanical strength and the particles are too fine. However, fine particles have the advantage of maximising both adsorption capacity and the adsorption kinetics. The former is of little interest for SNO application but the latter has been shown in Chapter 2 to be very significant, since it determines the size of sample which can be assayed. The conditions of precipitation can be used to control the degree of hydration.

Granularity and mechanical strength are priorities for SNO application since fine particles released from a packed absorber bed would carry with them a fraction of the adsorbed activity, leaving behind an activity less than the true quantity extracted from the assay stream. Although the mass of fines removed from a granular material is only a small fraction of its total mass, because of their large surface-area-to-mass ratio, they carry an amount of activity disproportionate to their mass. Fines production by an absorber could, if the problem were serious, therefore result in an incorrect background assessment for the SNO detector — there being no independent check — and thus an incorrect inference of the neutrino-induced event rate.

### 3.2.2 The Radium sorption properties of Manganese Dioxide

Manganese Dioxide has for a long time been known to act as a selective sorbent for Radium. The earliest references appear to be due to Ebler and Bender [99, 100] who report the separation of Radium from Barium by adsorption onto Manganese Dioxide, as part of a method of preparation from Uranium ores.

More recently, experimental work by Yamagata and Iwashima [98] demonstrated that powdered $MnO_2$ acted as an effective sorbent for a wide range of dissolved elements (Thorium and Radium were not investigated) when shaken with batches of sea-water. In consequence, $MnO_2$ came to be used for trace element analysis in oceanographic work, where currents and mixing rates may be studied using natural and anthropogenic isotopes of differing half-lives and chemical properties. In particular, Moore and Reid [96] developed a method of immobilising $MnO_2$ onto acrylic fibres, which enabled its use in an *in situ* sampler arrangement similar to a packed bed, for deep-ocean Radium assay [97]. Moore reported Radium removal efficiencies in excess of 90%, while Moore and Cook [101] report extraction of over 99% of Radium from contaminated drinking water.

The oceanographic work demonstrates the key fact that Manganese Dioxide is capable of efficiently extracting Radium from a flow of water *in the presence of* $\simeq 2\%$ *dissolved Sodium Chloride* and is thus a *prima facie* candidate as a Radium absorber for both heavy and light water in SNO.

Hooper *et al.* [88] discuss at length the known properties of $MnO_2$. About 12 naturally-occurring or synthetic crystalline forms of $MnO_2$ are known — all are amphoteric ion exchangers whose point of zero charge depends on the crystalline form. Many workers have investigated the adsorption of metal ions by $MnO_2$ over a wide range of nitric acid concentrations. The elements investigated include, but are not limited to, those of relevance to the nuclear industry, primarily Strontium, Caesium, Ruthenium, Zirconium, Uranium and Plutonium. $MnO_2$ will, under suitable conditions, absorb a very wide range of metals from alkali metals to tri- or tetravalent species. There is, however, virtually no information obtained at near-neutral pH. Little information on absorbtion kinetics exists, although several worker have reported a two-stage process consisting of a fast adsorption followed by a slower exchange step. Large variations have been found in exchange capacity, which is strongly dependent on crystalline form. Several adsorption mechanisms have been proposed, and it is clear that more than one type of adsorption site exists.

Beaven *et al.* [90] in an extensive investigation into the sorption properties of several absorbers under a range of pH conditions, with respect to several species of relevance to the nuclear industry, include $MnO_2$ in their investigation. They do not evaluate it with respect to Thorium or Radium sorption. Their method is gently to agitate a flask containing absorber and solution, taking aliquots of solution at regular intervals. By following the time evolution of the activity in the aqueous phase they gain both kinetic information and an estimate of the equilibrium position. They found that $MnO_2$ had a high affinity for almost all the elements studied under neutral or alkaline conditions. At pH2, $MnO_2$ effectively removed some species although approach to equilibrium was generally slower. Its performance in 4M nitric acid was generally better than at pH2. In all cases, of course, the extent and rapidity of sorption depends critically on the (pH-dependent) chemical form of the adsorbed species.

### 3.2.3 Manganese Dioxide on acrylic beads

The manganese-impregnated fibres developed by Moore are subject to the disadvantage that they can collapse to form a dense, impermeable mat if exposed to high flow rates. They also release into the filtrate quantities of fine $MnO_2$ particles and the packing of fibre into an extraction column is obviously not easily reproducible. Gershey and Green [79] therefore use a similar method to that developed by Moore [97] to load beads of Amberlite XAD-7 macroreticular acrylic ester with $MnO_2$. They found this material to be rapidly loaded with $MnO_2$ on immersion in a potassium permanganate solution (of unspecified concentration) at room temperature. They report that the treated resin is 5% by weight $MnO_2$.

The principal advantage of using beads over fibres is that they form a packed bed with a more regular structure, which is thus more reproducible and not prone to collapse under a pressure drop across the bed. These $MnO_2$-loaded acrylic beads are manufactured commercially by Seakem Oceanography of Dartmouth, Nova Scotia and were used for all the investigations reported here[2]. Two batches of $MnO_2$ were obtained from Seakem, with batch identifiers 86HX005-11 and 8810-02 respectively, the latter batch being several litres of material contained in a number of vessels. In the present work the material is frequently referred to, loosely, as '$MnO_2$' or 'resin'.

### The physical properties of Seakem resin

**Packing density** A number of investigations were conducted into the physical properties of the Seakem $MnO_2$-loaded beads. Gershey and Green describe the beads as of mesh size 20-50, which corresponds to a bead diameter in the approximate range $0.3mm$ to $0.5mm$. A packing density may be defined for a packed bed of $MnO_2$ by taking the ratio of the mass of $MnO_2$ used, measured when the sample is removed from its storage container, to the measured volume of the bed after wetting. The results of many such measurements yielded $0.33 \pm 0.01 g\ cm^{-3}$ for the 86HX005-11 batch and the same value for all containers of the 8810-02 batch except one: in this case the value was $0.28 \pm 0.01\ g\,cm^{-3}$. Gershey and Green report a value of $0.34\ g\,cm^{-3}$.

The packing density of a dry packed bed of this material was measured to be $0.83 g\,cm^{-3}$. On wetting, a bed of the material was easily seen to expand in volume by about a factor of 3 in about $30s$ as it absorbed water. This amount of expansion is common in polymers used as ion exchanger substrates [104].

**Surface appearance** A sample of $MnO_2$-loaded acrylic was prepared[3] for observation under an optical microscope. The mounted sample was sectioned to reveal a number of beads in cross-section. This study showed the $MnO_2$ layer to be variable in thickness between beads: cases were observed in which the $MnO_2$ was clearly visible as a distinct, black, outer layer layer of approximately $100\mu$ thickness, with a sharp boundary between this and a white inner core of acrylic resin. Other beads showed an apparently uniform $MnO_2$ distribution throughout the volume. It appears that the macroreticular [104] (*ie.* porous, literally 'netlike') structure of the beads enables permanganate ions to permeate to the centre of a bead rather than deposit $MnO_2$ as a coating on the surface, as supposed by Gershey and Green[4]. However, it is also clear that the manufacturing process does not closely control the extent of $MnO_2$ deposition. Samples of the acrylic fibres prepared by Moore were also studied by optical microscopy: the $10–15\mu$ thick kidney-shaped fibres appeared uniformly black.

The surfaces of $MnO_2$-loaded beads were also studied under a range of magnifications using scanning electron microscopy[5]. The surfaces were observed to be very smooth on a scale of $100\mu$. They showed no structure at all between $100\mu$ and $\simeq 1\mu$, at which scale the surface was slightly uneven. The visible particles of $MnO_2$ appeared roughly spherical and

---

[2] A supplier of $MnO_2$ grains without any substrate was also identified: Recherche Applique du Nord, Hautmont, France.

[3] by A.B.Knox

[4] The average pore size of XAD-7 resin is 250Å.

[5] by D. Gold

varied in size from about 0.3$\mu$ down to $< 0.1\mu$, the limiting resolution of the device used. $MnO_2$ particles smaller than this could also have been present on the surface.

**Elemental composition** Two samples of $MnO_2$-loaded beads were prepared[6] for study using the Oxford Scanning Proton Microprobe (SPM) [108, 109]. They were mounted in epoxy, sectioned and the SPM used to determine the elemental abundances in the exposed surfaces. A number of beads were studied, one of which showed the two-layered structure described above. Some of the conclusions which may be drawn from study of the whole set of results are listed below.

- The dark, outer layer is rich in Manganese, as expected, but no richer in Oxygen than the acrylic core.
- The areas of Manganese deposition are also rich in Potassium (no doubt deriving from the $KMnO_4$ used to prepare the beads) and are also associated with substantial amounts of Calcium and traces of Sodium. The presence of the latter two elements may be due to impurities in the permanganate.
- The whole bead is associated with an excess of Nitrogen over the level in the surrounding epoxy mount. The Nitrogen signal has no discontinuity at the acrylic/$MnO_2$ interface, again suggesting that the $MnO_2$ is deposited within the acrylic structure and not as a layer on the surface.
- The beads appear to be associated with an excess of Sulphur, apparently non-uniformly distributed within their volume.
- Of the two samples studied with the SPM, one had been soaked in a $^{234}$Th solution for 26 days and then allowed to dry. The bead studied showed clear rings of Uranium and Thorium, about 35$\mu$ thick, whose outer edge corresponded with the outer edge of the bead. The concentration of Uranium present appeared well in excess of the concentration of Thorium, in accordance with the expectation that most of the $^{234}$Th ought to have decayed to $^{234}$U. It is clear that the bead adsorbed Thorium, and possibly Uranium, from solution and that during 26 days' immersion, these species were able to diffuse within the bead.
- The same bead showed uniform concentrations of Copper and Iron associated with the $MnO_2$, but it is not clear whether these elements were also associated with other beads.

**Alkalinity** The $MnO_2$ beads were repeatedly found to turn alkaline any unbuffered solution with which they came into contact. This is attributed to the exchange of $K^+$ remaining in the resin after manufacture for $H^+$, a hypothesis supported by the SPM result that large concentrations of Potassium were indeed present. Although this effect was never systematically investigated, it is known from experiments not reported in this work that passing

---

[6] by A.B. Knox, J. Roberts and M. Marsh

10 tons water at pH $\simeq 7$ through $\simeq 1l$ resin at $\simeq 2l\,min^{-1}$ moves the pH upwards by about 0.3pH, corresponding to the exchange of $\sim 10^{-3}mol.$ $H^+$.

**Water content** Two samples from the 86HX005-11 batch were first weighed and then baked under vacuum at 70°C over-night. The same procedure was carried out at the same time with two samples from the 8810-02 batch. The former two samples each lost 13.1% of their mass during baking, and the latter two each lost 1.5% mass. These observations are attributed to loss of absorbed water, presumably remaining in the resins due to incomplete drying following $MnO_2$ deposition during manufacture. The 8810-02 samples measured clearly contained very much less water, and the difference could account for the different packing densities reported above. The manufacturing process does not therefore appear to guarantee reproducibility of water content between different samples within a batch.

**The release of fines** As noted in the previous section, fines release could be a serious problem for SNO application if it resulted in a significant fraction of the adsorbed activity being washed out of a packed bed. A secondary problem to be expected would be an increase in the impedance of the bed. Bigliocca *et al.* [103], in a survey of adsorption onto $MnO_2$ of a wide range of species (not including Thorium or Radium), found that after several hours contact with water, fine $MnO_2$ particles were formed. Phillips *et al.* [89] also report finding that $MnO_2$ broke down in solutions of low ionic strength (they were using granular $MnO_2$). This phenomenon was not investigated systematically in the present work, although some observations were made.

In the course of the small-scale experiments reported in this work, using a few $g$ $MnO_2$ and $\sim 100cm^3$ water, there was no visible fines production, nor any evidence that substantial activity was lost from the system due to adsorption onto fine particles not accounted for. Loss of more than about 5% of adsorbed activity can be completely excluded on the basis of these measurements. However, if $MnO_2$ is used in SNO, it will be used in beds of several hundred grams and hundreds of tons of water will flow through each batch: small-scale experiments will not necessarily be a guide to an absorber's behaviour under these conditions.

In the 10,000$l$ apparatus mentioned above, this volume of water was passed through $\simeq 300g$ $MnO_2$ samples at around $2l\,min^{-1}$. The bed was supported on a $20\mu$ filter above a $8\mu$ membrane filter. Considerable blockage of the filter stack was frequently observed, and the coarse filter was invariably found to be deep brown in colour. The fine filter was generally found to be a pale brown colour. Semi-quantitative measurements of the impedance increase were performed on a few occasions. About 2/3 of the impedance of a blocked filter stack was found to be due to the coarse filter, and the extent of the blockage was found to increase with the amount of water passed through the bed. A pre-washing treatment, in which a sample of $MnO_2$ was repeatedly slurried with batches of water in an attempt to remove fines before the $MnO_2$ was used, did not lessen the extent of blockage. A gentler method involving fluidising the $MnO_2$ sample in an upward-flowing water column, also appeared to have no effect.

Although it is clear from these observations that the resins do release fines when large volumes of water are passed through large-volume beds, further investigation would be required before all the blocking could be attributed to $MnO_2$. It was known that micro-organisms survived in the system (samples of water were successfully cultured and slimes were found on filters studied by optical microscopy) and it possible that some or all the blockage could have been due to growth of these organisms on the filters.

## 3.3 Thorium monitoring in SNO by $^{220}$Rn counting

It is clear from the discussion of Section 2.5 that pre-concentration of the activity in SNO water will be necessary before any counting can be attempted, although the methods of pre-concentration and subsequent assay were there left unspecified. $^{228}$Th and $^{224}$Ra were identified as important isotopes for determination of the photo-disintegration rate of deuterons in the heavy water. In Section 3.2 Manganese Dioxide was identified as an effective solid phase sorbent for Radium: its properties with respect to Thorium sorption do not appear to have been investigated. In this section, an assay method for $^{228}$Th/$^{224}$Ra immobilised onto $MnO_2$ resins is discussed.

### 3.3.1 $^{220}$Rn counting in a gas proportional chamber

For SNO application, a method of counting $^{228}$Th/$^{224}$Ra activities on an absorber sample is required. A sensitivity to activities of around 100 counts per day is required, without the use of long integration times, which are limited by the half-life of $^{224}$Ra. If the extraction procedure proves inefficient, the actual activity of the absorber samples could be much lower. Ideally, of course, a counting method with low background and high efficiency is required.

The proposed method for measuring the loading of $^{228}$Th and $^{224}$Ra on an absorber sample makes use of the fact that the daughter nuclide of $^{224}$Ra decay is $^{220}$Rn (see Figure 2.4). As a noble gas, Radon might not be expected to bind strongly to the surface where it was created, but to be liberated from the adsorption site. Thus if an absorber sample used for extraction of $^{228}$Th or $^{224}$Ra from SNO water is removed from stream and dried, it might be expected to act as a source of $^{220}$Rn.

Since Thoron ($^{220}$Rn) is the immediate daughter of $^{224}$Ra, its de-emanation rate from a sample is proportional to the amount of this isotope present. However, $^{224}$Ra comes into equilibrium with its parent $^{228}$Th with a time constant dictated by its half-life of $3.7d$ and several half-lives after the activation of a sample, therefore, the de-emanation rate is governed by the sample's $^{228}$Th content. Thus measurements of Thoron de-emanation from a sample could enable both its $^{228}$Th and $^{224}$Ra contents to be inferred.

The measurement of very low activities of $^{220}$Rn is not a common requirement. Because of its short half-life ($55.6s$) compared to $^{222}$Rn (a $^{238}$U descendant — $t_{1/2} = 3.82d$), its environmental concentration is so low as to be unimportant. Established methods of determining Radon concentrations in air are generally applicable to $^{222}$Rn: they make use of its high freezing point relative to other atmospheric gases, with the exception of water vapour,

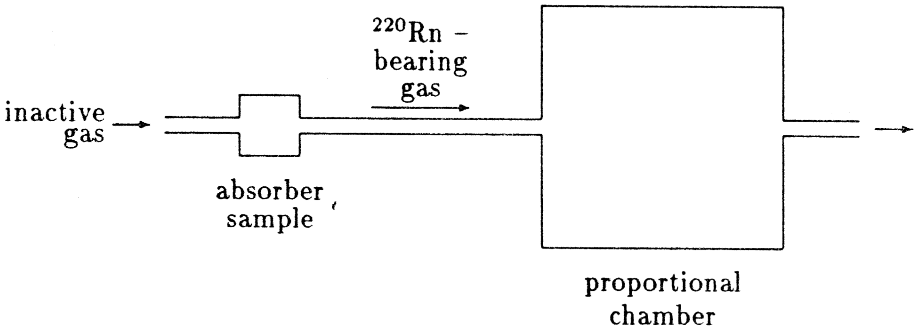

Figure 3.3: Sample-to-chamber gas flow diagram.

and relatively long half-life to accumulate Radon samples from a gas stream in a Lucas cell. A dry-ice-cooled activated charcoal filter may also be used to accumulate Radon for later transfer to a Lucas cell. An alternative approach makes use of plastic dosemeters whose surface is damaged by alpha particles: etching with alkali makes the alpha damage visible under a microscope, and the track density serves as an indicator of environmental Radon concentration.

The short half-life of $^{220}$Rn does not allow the accumulation of samples of the gas. Instead, the method which has been implemented for counting Thoron de-emanation from an absorber sample is to entrain the atoms in a gas stream as they are produced. The gas stream is allowed to pass through the dried $MnO_2$ sample and into the sensitive volume of a gas proportional chamber, as in Figure 3.3, where their alpha decay may be observed. The apparatus and experimental procedure are described in detail in Chapter 4.

The Thoron half-life also requires that the gas flow rate be sufficiently high so as to ensure that the residence time in the sample volume of the liberated atoms be small compared with 1 minute. Otherwise, a significant fraction of the signal would be lost by decay within the absorber bed. However, the opposite requirement applies when Thoron atoms reach the chamber: in this case, for high counting efficiency, it is required that the gas flow rate be as low as possible so that as many as possible of the atoms decay before being swept out of the chamber.

These two contradictory requirements on the counter gas flow rate may only be resolved if the sensitive volume of the proportional chamber is large compared with the volume of the absorber bed. Since it is clear that for good extraction from water of any ion by any absorber, large absorber volumes are preferable, it follows that the chamber volume should be as large as reasonably possible: large absorber volumes may then be accommodated while still yielding residence times in the chamber which are long compared to the Thoron half-life. Thus the first requirement on a proportional chamber suitable for $^{220}$Rn counting is that it be of as large a volume as reasonably possible.

The above argument may also be reversed. It is clear that there is a maximum absorber volume which a given counter is capable of efficiently counting. The kinetics of the adsorption process in turn limit the water flow rate through the sample at which sorption is possible with reasonable efficiency. Since the time for which an absorber may profitably be placed in the stream is limited by the $^{224}$Ra half-life (as discussed in Section 2.4), the total volume which may be sampled is also limited. It again clear, therefore, that the volume of the proportional chamber should be as large as reasonably possible.

The choice of Thoron de-emanation followed by alpha counting in a gas proportional counter offers potential benefits as a method of low-level assay of $^{228}$Th/$^{224}$Ra.

1. Most importantly, the immediate daughter of $^{220}$Rn is $^{216}$Po whose half-life is short (0.15$s$) and which also decays by alpha emission of significantly higher energy (6.9MeV *vs.* 6.4MeV). The signature of a $^{220}$Rn decay within the chamber is therefore two events of appropriate energies occurring within about 0.5$s$ of each other, the lower energy event preceding the higher. A coincidence experiment, with consequent anticipated background suppression, is therefore possible.

2. A fully contained alpha decay of 6–7MeV energy would give rise to a relatively large signal in the chamber, and should thus be distinguishable from less strongly ionising particles.

3. In principle, a high detection efficiency for contained alpha events ought to be achievable.

The amount of information obtained from the chamber concerning a given alpha decay depends of course on the design of the chamber. A single-wire device would yield only the total energy deposited and the time of the event, whereas a multi-wire chamber could allow track reconstruction with much greater consequent background rejection. A method of $^{228}$Th/$^{224}$Ra assay based on, for example, gamma-ray spectrometry, would be unlikely to achieve comparable detection efficiency or backgrounds.

### 3.3.2 $^{220}$Rn de-emanation from a Manganese Dioxide surface

In order for the method of $^{220}$Rn de-emanation to be successful, it is clearly necessary for nascent $^{220}$Rn atoms to be released from the $MnO_2$ surface. Although there are reasons for supposing that the atom will indeed be released, the process clearly needed to be demonstrated. That de-emanation occurs is demonstrated in Section 4.1.2 and in Section 5.1 the effect is investigated quantitatively.

A simple model of the process illustrates some important points. Initially, we may suppose that a $^{224}$Ra atom is adsorbed at or near the surface of a $MnO_2$ grain. If the affinity of $MnO_2$ for Radium is large, as existing data suggest, then the strongly bound atom would not be expected to migrate far into the grain so it may crudely be considered to be bound at a plane absorber surface. Its alpha decay results in the recoil of the daughter Radon atom with about 100keV energy — easily enough to free it from any chemical bonds. Furthermore, we may suppose that the alpha particle is directed either into or out of the absorber surface and that, if outwards-directed, then the Radon atom recoils inwards and is then unlikely to escape from the surface. On the basis of this simple model an escape probability of around 50% is expected. If significant diffusion of the Radium atom within the bead occurs before decay, however, the Radon escape probability would clearly be decreased below the maximum which occurs when its parent is at the absorber surface.

Bound $^{224}$Ra atoms resulting from decay of adsorbed $^{228}$Th, however, may not be at the surface of the bead. A Thorium atom at the surface may emit an alpha particle directed outwards so that the 97keV recoil tends to implant the daughter Radium atom below the surface. It can be seen that the probability of $^{220}$Rn escape could then be much lower than in the case of a $^{224}$Ra atom deposited directly onto the absorbing surface. Thus if an absorber were activated with a solution containing both $^{228}$Th and $^{224}$Ra, then the constant of proportionality relating the Radon de-emanation rate to the $^{224}$Ra activity could change with time as Radium adsorbed from solution decays, and Radium resulting from Thorium decay *in situ* grows in.

## 3.4 Programme of work

In the light of the discussions thus far in Chapters 2 and 3, the main features of the programme of work may be outlined. The aim of this investigation was to determine whether sorption of $^{228}$Th and $^{224}$Ra onto Manganese Dioxide beads followed by $^{220}$Rn-counting in a gas proportional chamber was a suitable assay technique for these elements in SNO water. This programme is summarised below.

1. **Demonstrate the principle of $^{220}$Rn counting.**
    - Develop a suitable gas proportional chamber for $^{220}$Rn counting, with associated data acquisition electronics and software, and show that it can detect $^{220}$Rn decays and $^{220}$Rn/$^{216}$Po coincidences.
    - Identify a set of operating conditions and experimental procedures which enable measurements of $^{220}$Rn de-emanation rates reproducibly to be performed.
    - Determine the counting efficiency of the device and the background levels which may be achieved.
    - Determine the efficiency of $^{220}$Rn de-emanation from a $MnO_2$ surface.
2. **Quantify the sorption properties of Manganese Dioxide.**
    - Determine the kinetics of the sorption reaction of Radium in a packed $MnO_2$ bed, and extend the information to Thorium.
    - Determine the equilibria of both sorption reactions.

The experiments performed, and results obtained, in the course of this programme are given in Chapters 4 and 5.

# Chapter 4

# Experimental apparatus: Performance and Analysis

## 4.1 First generation Cylindrical Proportional Chamber

### 4.1.1 Description of the apparatus

As discussed in Chapter 3, in order to assay the $^{224}$Ra content of a $MnO_2$ sample, it was necessary to develop a method for counting low $^{220}$Rn activities. The Cylindrical Proportional Chambers were developed for this purpose.

In this section, only a brief description is given of the First Generation Cylindrical Proportional Chamber, which was in the event a developmental apparatus. It was replaced by a second generation counter, fully described in Section 4.2. The operation, data acquisition and data analysis are described in the later section, and much is common between the two versions of the chamber. The second generation counter was used to take all the $^{220}$Rn-de-emanation data reported outside this section.

#### Design and construction

The short half-life of $^{220}$Rn ($55.6s$) renders impossible any time-consuming methods involving accumulation of a sample of concentrated activity, such as have been used for $^{222}$Rn ($t_{1/2} = 3.8d$). The principle adopted for $^{220}$Rn counting was to entrain Radon atoms into a gas stream which passes through the $MnO_2$ sample and into the sensitive volume of a gas proportional chamber. Again, the short half-life requires that the gas flow rate be sufficiently high so as to ensure that the residence time of the Radon atoms in the sample volume be small compared with 1 minute. Otherwise a significant fraction of the signal would be lost by decay within the absorber bed. However, the opposite requirement applies when the Radon atoms reach the chamber: in this case, for high counting efficiency, it is required that the gas flow rate be as low as possible so that as many as possible of the atoms decay within the chamber.

These two contradictory requirements on the counter gas flow rate may only be resolved if the sensitive volume of the proportional chamber is large compared with the volume of the absorber bed. Since it is clear that, for good extraction from water of any ion by any absorber, large absorber volumes are preferable, it follows that the chamber volume should be as large as reasonably possible so as to allow large absorber volumes while still yielding a residence time in the chamber long compared to that in the sample. Thus the first requirement on a proportional chamber suitable for $^{220}$Rn counting is that it be of as large a volume as reasonably possible.

A further requirement derives from the range of $^{220}$Rn alphas ($E = 6.29$MeV) in the gas. This will be of the order of $5cm$ at atmospheric pressure and will vary inversely with pressure. Since the pulse height recorded at the anode wires of a proportional chamber depends on the amount of ionisation produced by a charged particle, if the track is truncated as a result of the particle hitting the wall of the chamber, or passing outside the sensitive volume, then the recorded pulse height due to that particle will be reduced. In the case of a large-volume $^{220}$Rn counter, the origins of the tracks will have a distribution in space which depends on the gas flow pattern through the chamber and on the flow rate. The tracks will be randomly oriented. Thus if the gas flow pattern carries $^{220}$Rn atoms 'within range' of the chamber walls, the alpha tracks will be truncated to lengths whose distribution depends on the distances of decaying atoms from the walls. This random distribution will be modulated by the shape of the ionisation/range curve for the track and the resulting distribution will smear the resolution of the device, introducing a low-energy tail into the peak shape. Since the ionization density peaks towards the end of the track [102], there will be a tendency for any too-close approach to the walls to decrease the efficiency of detection by moving the event out of the peak.

Thus a suitable counter must have a sensitive volume as large as possible and must in addition have its smallest dimension large compared to the alpha track length: a long narrow cylinder might satisfy the first criterion but not the second.

### Description of the apparatus

The first stage CPC was designed as the simplest device to meet the above criteria. It was a single-wire proportional chamber whose sensitive region was a right cylinder of $213mm$ diameter by $300mm$ height, of volume $10.4l$. The sensitive volume was defined by three steel annuli of equal ($213mm$) inside diameter and $2.5mm$ thickness arranged on a common vertical axis. The upper and lower annuli were $50mm$ in height and the central one $200mm$: the three annuli were separated from each other by gaps of about $2mm$. The end plates of the cylindrical sensitive volume were of $3mm$ thick perspex. The upper plate admitted the $^{220}$Rn-bearing gas through a $5mm$ hole placed $25mm$ from the axis. The gas flowed downwards through the volume and an $11mm$ hole in the lower perspex end-plate acted as an exit port. The central anode wire of the detector was mounted from copper disks at the end-plates. Various diameters of wire were tested in order to optimise the energy resolution of the device.

The whole assembly was contained in a steel cylindrical pressure vessel of $250mm$ internal diameter by $367mm$ height. This was designed to withstand up to 3 atm. over-pressure to enable use of a range of working pressures. The top flange carried the gas inlet and electrical feedthroughs for HT and signal wires.

Since the chamber was a single-wire device, the only information it provided about an event within it was the total charge deposition and time of occurrence. The coincidence detection method discused in Section 3.3 could optionally be used to suppress background. In the event, the resolution of the device was often too poor to allow the events to be reliably gated on pulse height as well as time.

As a calibration source, the first stage CPC incorporated a $^{241}$Am source mounted on the outer surface of the middle annulus. $^{241}$Am decays by alpha emission, giving rise to several alpha lines around 5.50MeV. It was collimated using a brass tube of length $10mm$ and $2mm$ bore. This protruded into the sensitive volume through an aperture in the annulus, half way along its length, and pointed along a diameter of the cylinder. This source gave rise to a clear peak in the pulse height spectrum having 2% resolution (FWHM). The usefulness of this source lay mainly in the fact that it furnished a stability monitor for the gas gain of the chamber. For very long runs it was possible to stabilise the gain against variations in pressure or $O_2$ concentration by monitoring in software the position of the $^{241}$Am peak and varying the voltage applied to the anode wire in such a way as to counteract the drift. This was achieved by controlling through CAMAC an analogue voltage applied to the HT supply.

The two major flaws inherent in this design concerned the gas flow pattern and the field uniformity. Ideally, the Radon-bearing gas should flow down the chamber without ever coming near to the walls and the flow pattern should be laminar. The second requirement was certainly fulfilled under typical operating conditions, but the first was clearly not. In early experiments with the device, the annular gaps between the steel rings defining the sensitive volume acted as alternative exit ports for the gas, of total area greater than the nominal exit port in the lower end plate — thus ensuring that the streamlines diverged, carrying Radon towards the chamber walls, and that the atoms' residence time in the chamber was much shorter than expected. These gaps were later blocked. However, with only one entry and exit port to the sensitive volume, the flow streamlines could not have been parallel but must have diverged, with the consequences that

(a.) Radon was again carried towards the chamber walls,

(b.) The atoms' residence time was difficult to calculate and path-dependent.

A second flaw related to the electric field distribution within the cylinder. In the case of an infinite cylinder surrounding a central HT wire, the solution to Laplace's equation is simple and results in a field which has no longitudinal component and whose strength varies inversely with radius. In the realistic case of a finite cylinder, 'end effects' will of course be present and the distance over which they are significant is, in the absence of any potential-defining surfaces between the wire and the outer radius, of the order of the cylinder radius. Considering the dimensions of the sensitive volume as given above, it is clear that 'end effects' influenced the field distribution throughout the volume. Furthermore, it might be expected that static charges on the perspex end-plates might also influence the field distribution in an unpredictable way.

Successful operation of a proportional chamber requires good field uniformity because tracks may occur throughout its volume and may be randomly oriented. If not all field lines are radial, *ie.* if some terminate on static charges on the end plates, then the charge collection efficiency of the chamber will depend on the position of the track, with consequent loss of resolution and efficiency. It is largely to this effect that the poor efficiency and modest resolution of the first stage CPC are attributed.

### 4.1.2 Performance of the chamber and results obtained

#### Operating conditions

One of the principal aims of the work done with the first stage Cylindrical Proportional Chamber (henceforth 'CPC1') was the identification of a set of operating conditions which permitted the identification of $^{220}$Rn events. With a simple device like the CPC1, there are relatively few freely variable experimental parameters. Among the most important of those which pertain directly to the operating conditions of the chamber (as opposed to sample preparation, gas handling, data analysis *etc*) are the choice of counter gas, the anode wire diameter, the pressure at which the chamber is operated and the voltage at which the anode is held relative to an anode at earth potential. Many variations of these parameters were attempted with varying results. A set of operating conditions was eventually found which allowed the peaks due to the $^{220}$Rn and $^{216}$Po alpha decays to be readily resolved. This set of conditions is listed here:

**Gas:** 90% Argon/10% methane

**Anode wire:** 250$\mu$ copper-coated beryllium

**Pressure:** *c.* 1 psi. above atmospheric

**Anode voltage:** +2.5kV

Standard values of the third and fourth of these parameters were not defined while the CPC1 was in use — different values of each parameter were used at different times — so these values are approximate. The range of pressure variation was about 1 psi and voltages in the range 2.2-2.5kV were used.

Other wire diameters were tried, both thicker (up to 1*mm*) and thinner (down to 70$\mu$). Resolution comparable to that obtained under the above conditions was obtained using a 125$\mu$ wire and an operating voltage of +2.1kV. Operation of the chamber at a higher pressure, 14 psi, was also attempted, with a 100$\mu$ wire to compensate for the decrease in available gas gain. The intention was to increase the efficiency of $^{220}$Rn identification by shortening the track length and thus decreasing the number of tracks impacting the walls. In practice the observed rate from a constant source was almost identical to its value under standard conditions, and the $^{220}$Rn/$^{216}$Po resolution was markedly worse.

Under the set of operating conditions given above, pulse height spectra were obtained which exhibited the following features — an example is given in Figure 4.1.

1. Two resolved peaks (centred on channels 255 and 272 in the figure) were observed, corresponding to the decays of $^{220}$Rn ($Q$ = 6.40MeV) and $^{216}$Po ($Q$ = 6.91MeV). The energy resolution (FWHM) was approximately 3%.

2. A smaller, higher-energy peak corresponding to $^{212}$Po decay ($Q$ = 8.78MeV) was observed (around channel 350). The presence of this peak implies that a peak corresponding to $^{212}$Bi ($Q$ = 6.06MeV) decay, 56% as intense, must be present. However it is not resolved from the tail of the much more intense $^{220}$Rn peak. The $^{212}$Bi peak was seen only in data taken without a $^{220}$Rn source in the gas stream. These observations demonstrate that $^{212}$Pb was deposited in the chamber following $^{220}$Rn decay.

3. The sharp cut-off in the data at channel 220 is a software cut on the data, set well above the $^{241}$Am peak centred on channel 200. Events below channel 221 were not recorded.

4. The $^{220}$Rn peak was approximately 20% more intense than the $^{216}$Po peak, although the Thorium chain (Figure 2.4) suggests that the activities be equal. This may be accounted for by the hypothesis that the daughter $^{216}$Po atom is partially stripped by collisions with argon atoms or methane molecules as it recoils in the counter volume, and thus acquires a positive charge. The extent to which it then drifts in the electric field depends on the details of how quickly it neutralises. However it is clear that it may drift towards the cylindrical cathode and thus that the efficiency for detection of its decay a few tenths of a second later may be reduced by the increased chance of alphas impacting on the cathode. In the limiting case that the time required for neutralisation of the ion is long compared to the drift time to the cathode, around 50% of $^{216}$Po alphas would be expected to be directed into the cathode and thus not be observed.

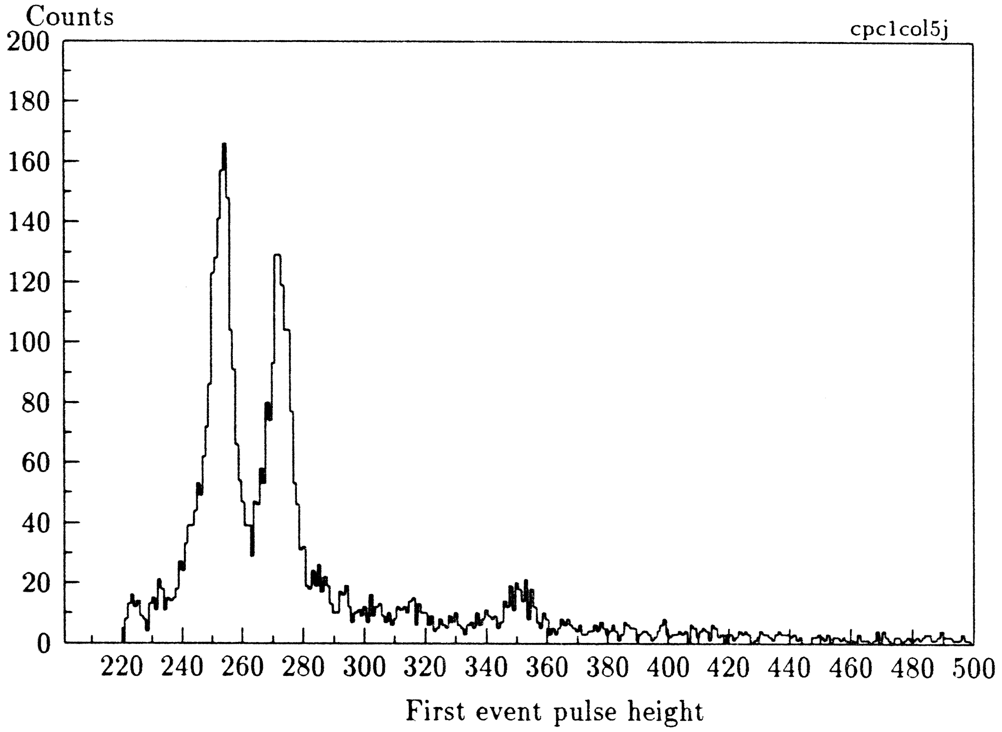

Figure 4.1: Typical high-statistics pulse height spectrum obtained with the CPC1.

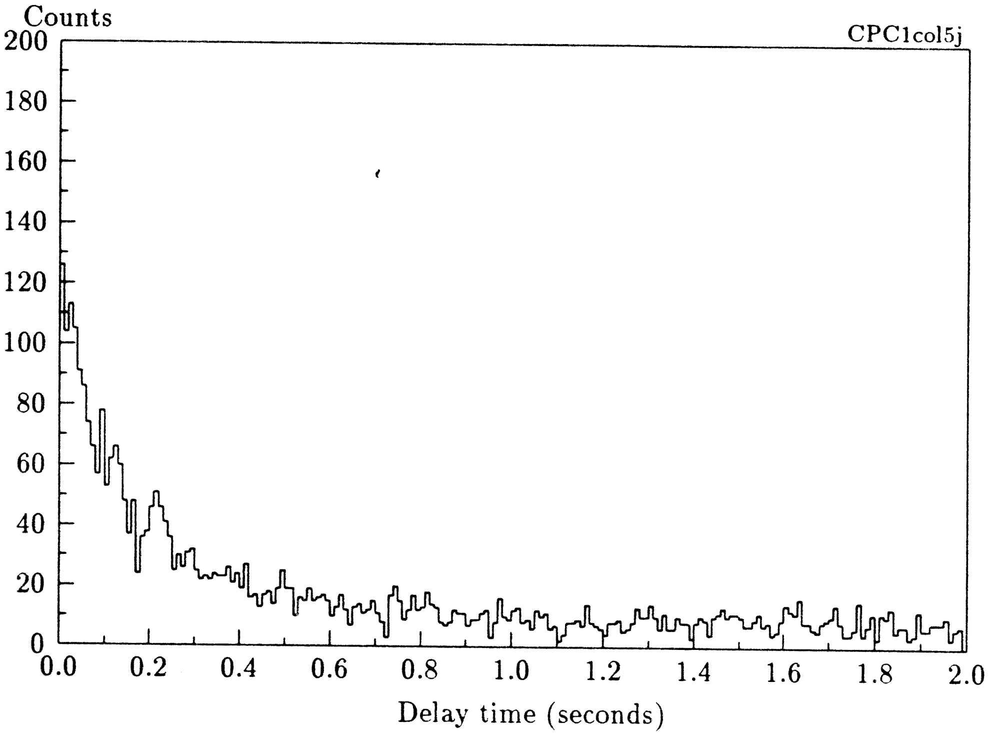

Figure 4.2: Delay time spectrum of CPC1 data set.

### Time-gating procedure

In Section 3.3 it was anticipated that $^{220}$Rn atoms decaying in the chamber would give rise to coincidences between two alpha events. One of the most important conclusions from the CPC1 work was the demonstration of the feasibility of a time-gating procedure for identification of such coincidences against a background of noise events and the low-energy tail of the detector's response to $^{212}$Po decays. A clear selectivity for $^{220}$Rn/$^{216}$Po coincidences was demonstrated by sifting the event stream for close time coincidences between the first and second of pairs of successive events, generating 'first event' and 'second event' spectra. The $^{216}$Po peak was greatly suppressed among the first events and the $^{220}$Rn peak among the second events, in accordance with the expectation that a $^{220}$Rn decay precede every $^{216}$Po decay.

The effectiveness of the gating procedure is illustrated by Figures 4.2-4.4. Figure 4.2 shows the spectrum of delay times between events whose pulse heights exceeded channel 220 (*ie.* they were not $^{241}$Am events). The figure shows a pronounced peak at small times, consistent with a 0.15$s$ half-life and attributable to $^{220}$Rn/$^{216}$Po coincidences. Figures 4.3 and 4.4 show gated spectra which result from very crude cuts on pulse height and time between events: the pulse height is required to be between channels 220 and 300 for both the first and second alpha events, and the time between events is required to be less than $0.6s$. The pulse height cuts require only that both events be of higher energy than $^{241}$Am and not higher than the upper limit of the $^{216}$Po peak; the time cut is equal to approximately 4 $^{216}$Po half-lives. It can be seen that these cuts are very generous. The figures demonstrate that even with wide gates, strong suppression of events of the 'wrong' type occurs in each spectrum, *ie.* $^{216}$Po events are suppressed in the 'early event' spectrum and $^{220}$Rn events are suppressed in the 'event' spectrum.

It should be noted that the above is only one of a number of possible gating procedures. Another possibility is to impose a 4-half-life cut on the time between events alone, and no pulse height cut. That procedure, although crude, is simple to use and effectively suppresses the background due to noise events uncorrelated in time. A more stringent procedure applies tight cuts around each peak ($^{220}$Rn and $^{216}$Po) separately, in addition to a time cut which may be more or less severe. This procedure affords the greatest background suppression possible with the CPC1.

Tighter cuts of course give better suppression of spurious events but lower efficiency for genuine events.

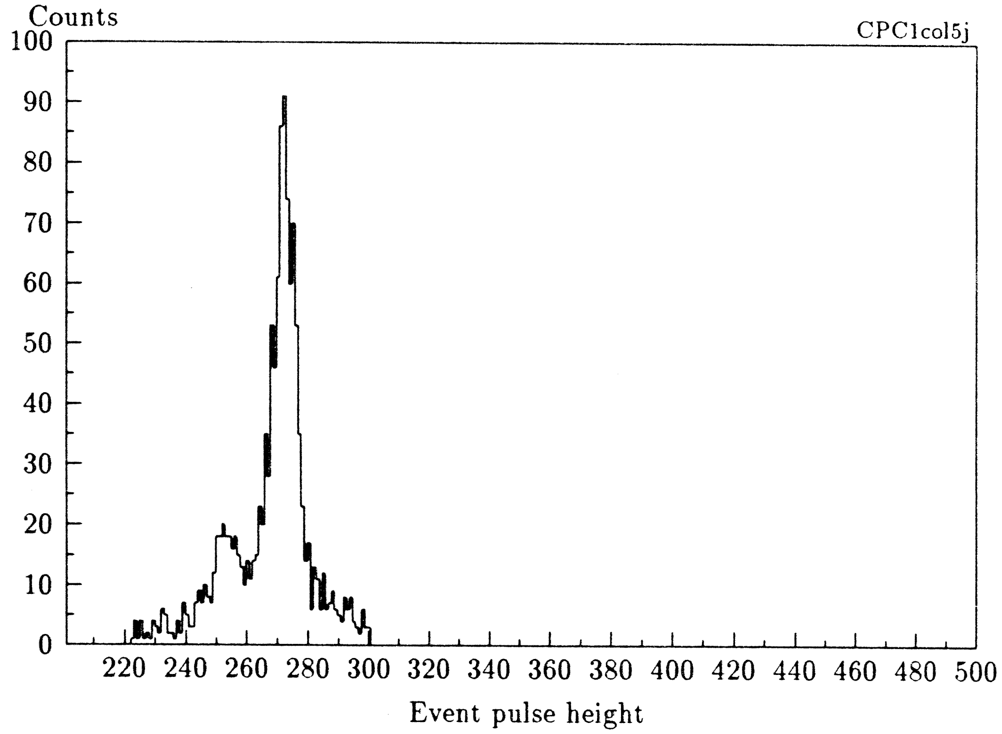

Figure 4.3: Second event pulse height spectrum ($^{216}$Po decays) after loose gating procedure.

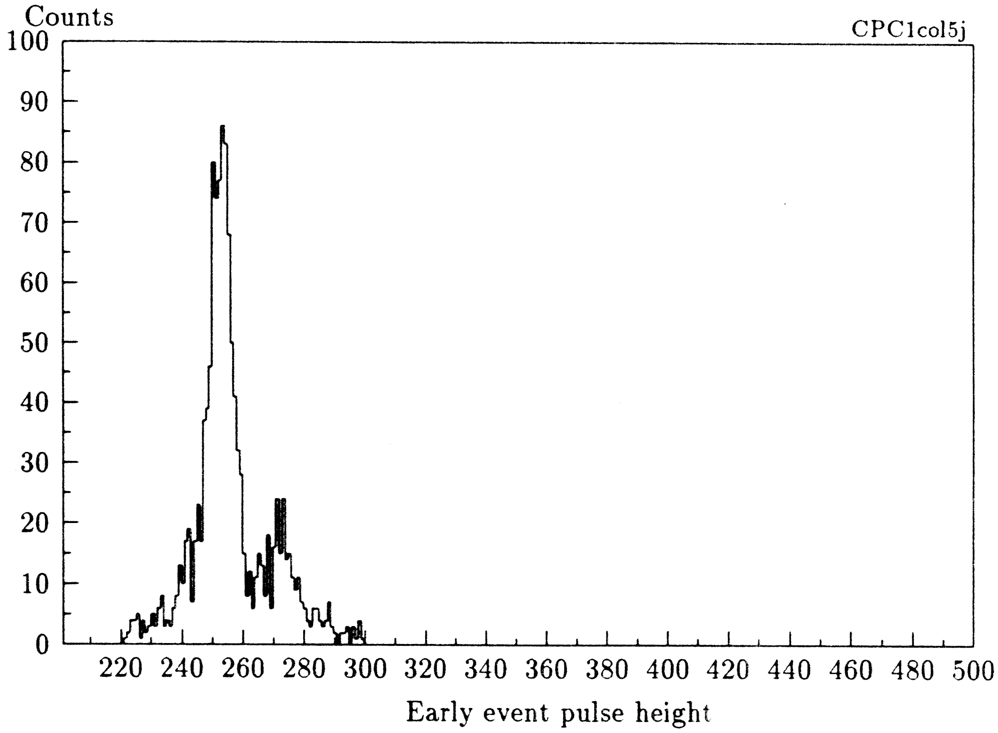

Figure 4.4: Pulse height spectrum of early events ($^{220}$Rn decays) after loose gating procedure.

## Background

The assessment of backgrounds is of particular importance for the evaluation of the technique of $^{220}$Rn/$^{216}$Po coincidence counting for the assay of low activities of $^{224}$Ra. In discussing backgrounds or efficiencies of a CPC for $^{220}$Rn counting, a distinction must be made between the two available methods of analysing data. The first is a coincidence mode in which it is required for the identification of a $^{220}$Rn decay that two events occur within a time window of approximately $0.5s$ and each has a pulse height which satisfies windows which may be more or less stringent. The second is the 'singles' mode in which no cut is made on the time information and the only requirement for the identification of a $^{220}$Rn decay is that it survive a pulse height cut. The differences between these two analyses are discussed a the end of this section, however it is clear that they give rise to very different efficiencies and backgrounds. The results from the CPC1 may be summarised thus:

1. With no liner in place, background rates of $5 \times 10^{-3}s^{-1}$ in singles were obtained. In the coincidence mode, a rate of $0.2 \times 10^{-3}s^{-1}$ was obtained at a flow rate of $0.37l\,min^{-1}$Ar/Me and $0.8 \times 10^{-3}s^{-1}$ at $0.55l\,min^{-1}$Ar/Me. With runs 4 hours long, $1\sigma$ statistical errors of 10% were obtained for the singles count rates, but the numbers of coincident events were sufficiently low that the above coincidence rates should not be regarded as significantly different.

2. The sensitive volume was later lined with a sheet of Kapton, coated on the inside with electro-deposited Copper. This was expected to have low $^{220}$Rn emanation and to act as a barrier inside the steel annuli, around which Radon from that source could not diffuse before decaying.

   With the Kapton liner in place and zero gas flow, (*ie.* with a static volume of Ar/Me in the chamber) a singles count rate of $(0.4 \pm 0.1) \times 10^{-3}s^{-1}$ was reproducibly obtainable with only fresh, uncontaminated materials lining the sensitive volume. This is a factor of 10 down on the rate without a liner. Four coincident events were observed in a total of 47.3hrs accumulation, indicating a coincidence rate of order $0.02 \times 10^{-3}s^{-1}$. These numbers indicate the level of background due to noise events and to $^{220}$Rn de-emanated from the walls of the sensitive detector volume. These background levels were recovered after exposure to an active $MnO_2$ source and from this fact a limit may be placed on the extent to which $^{228}$Th is carried into the chamber from such a source. It is found that $4 \times 10^{-4}$ $^{228}$Th atoms at most are deposited in the chamber per $^{220}$Rn atom decaying there.

3. The chamber background was not changed when Ar/Me was passed into the chamber through uncontaminated external pipework at flow rates of up to $1.2l\,min^{-1}$. It may be concluded from this data that the Ar/Me used for the counter gas (supplied by BOC Special Gases) contains not more than 0.2 $^{220}$Rn atoms per litre when it reaches the detector (the time taken for the gas to travel from the cylinder head to the detector was normally of order 1/20th of the $^{220}$Rn half-life when no samples were placed in

the stream). In order to investigate further the $^{220}$Rn concentration of the gas stream, a transit delay volume was inserted into the gas stream between the cylinder and detector. This was a cylinder $2500mm$ long by $95mm\,\phi$, lined with copper-clad Kapton and having a volume of $18l$. This was introduced so as to allow any $^{220}$Rn present in the gas stream to decay before reaching the detector. Its introduction yielded no noticeable decrease in the detector background. The conclusion from this investigation was that counts from $^{220}$Rn in the counter gas (which could have originated from diffusion or recoil of Radon atoms from the cylinder walls) were not significant in comparison with the total background count.

4. Using the operating conditions given on page 76, the backgrounds with zero gas flow were $2 - 3 \times 10^{-3}s^{-1}$ in singles and $0.1 \times 10^{-3}s^{-1}$ in coincidence. These levels were reproducibly obtainable over two months of operation. The increases in these levels can be attributed to an improvement in efficiency accompanying the great improvement in resolution. On this assumption, they suggest an efficiency improvement of about a factor 5. Again, given clean external tubing, this background level was not increased by a gas flow of $1.2l\,min^{-1}$.

### The counting of wet sources

The CPC1 was used to carry out a large number of trials to evaluate the feasibility of counting $^{220}$Rn extracted directly from solution. One reason for attempting this was that $^{220}$Rn extraction from a solution already filtered through an $MnO_2$ column would give a direct measure of the $^{224}$Ra permeation when compared with a similar measurement made on the source before $MnO_2$ filtration. This is particularly useful if accurate measurement of a small permeation is required, for which purpose counting the $MnO_2$ column will not suffice. Furthermore, the method allows $^{224}$Ra assay independent of the chemical environment of the Radium atoms: $MnO_2$ may not extract Radium in some (hypothetical) complexed form and residual Radium in this form may be assayed by this technique if recoil is assumed to free $^{220}$Rn from any parent complex.

The method adopted for extracting $^{220}$Rn from a solution of $^{224}$Ra was to bubble the counter gas stream through the solution. Since it is easily shown that the efficiency of this process varies inversely as the radius of the bubbles, for a given volume flow rate of gas, it was advantageous to use bubbles as small as possible. It was also important to ensure that the whole volume of the solution came into close proximity to the bubble stream. These requirements were met by placing the test solution in a glass gas-washing vessel of $400ml$ capacity and $60mm$ diameter. The solution was retained above a coarse glass frit and gas was passed from below through the frit, which split the flow into many streams of bubbles, and then bubbled up through the solution. At the flow rates used ($1l\,min^{-1}$), the solutions were violently agitated and clearly well mixed.

There are considerations which suggest that the efficiency of $^{220}$Rn extraction from a solution by this method might be high. In general terms, there must exist an equilibrium partition for Radon between the gas phase and solution in water, characterised by a partition constant. This will determine the equilibrium partial pressure of Radon in the gaseous phase for a given concentration in the aqueous phase. However, in the case of a clean gas stream entering the solution, the initial partial pressure of Radon is essentially zero and thus the reaction $\mathrm{Rn}_{(aq)} \rightleftharpoons \mathrm{Rn}_{(g)}$ is initially displaced in favour of the gaseous phase. The Radon extraction efficiency by this method could therefore, in principle, be close to 100% if the Radon concentration in the gas stream is not allowed to build up to the extent that the above reaction is significantly reversed, *ie.* if the flow rate of gas is sufficiently high. There are other factors which also favour high flow rates. A higher flow rate results in a decrease in the time available for a dissolved $^{220}$Rn atom to decay before encountering a bubble surface and should also result in turbulent conditions inside the bubbling vessel, thus avoiding a situation where only a fraction of the solution is 'sampled' by the gas stream, where that fraction is limited by the distance which a $^{220}$Rn atom can diffuse through water within its 1 minute half-life.

A serious problem with this method is of course the requirement to dry the gas before allowing it to enter the CPC. Water vapour is well known to be capable of accepting free electrons and its presence at significant partial pressures in an ionisation chamber thus has a detrimental effect on the performance of the detector. It was frequently observed that when the gas stream was insufficiently dried the response of the device suffered and the gain drifted wildly. The drying of the gas stream was thus an important requirement. A suitable drying procedure had to satisfy the obvious requirements that it not contribute $^{220}$Rn to the gas stream (and preferably not $^{222}$Rn either) and that it not involve long residence times of the gas stream in the drier, which would result in the loss by decay of $^{220}$Rn. The natural choice of method for drying the gas stream is to pass it through a cartridge containing a solid-phase sorbent, on which there is also the requirement that it does not have an active surface which might adsorb Radon or any other component of the gas mixture (*ie.* $CH_4$).

- Commercial $P_2O_5$ drying agent was found to be unacceptable because it de-emanated $\simeq 1 \times 10^{-3} s^{-1}$ $^{220}$Rn (in coincidence with $^{216}$Po), which was of the order of 10 times the background coincidence rate. This was attributed to the presence of a filler, 25% of $CaSO_4$: because of the similarity in chemical properties between Calcium and Radium, it is not surprising that a Calcium compound should be contaminated with Radium.

- A $100ml$ column ($18mm\,\phi$ by $400mm$ length) of silica gel was found to adsorb 85% of $^{220}$Rn under typical conditions of use ($1.2l\,min^{-1}$flow rate), and was clearly acting as an indiscriminate sorbent.

- Analar $P_2O_5$ dispersed in polypropylene swarf was found to be acceptable.

- A bubbling vessel filled with $100ml$ concentrated sulphuric acid was found to be frequently effective for gas-drying, but this method was not found to be reliable. It had the additional disadvantage that fine droplets of the acid were carried along with the gas stream and slowly attacked the tubing, fittings and even the interior of the chamber.

A major disadvantage inherent in the bubbling of wet sources was the tendency for small droplets of water to be entrained, suspended, in the gas stream and thus carried out of the source bubbler and further into the system. The result was that $^{228}$Th and $^{224}$Ra from $^{228}$Th solutions were found extensively to contaminate the tubing, the drying agent and the chamber. This was a far more serious problem than $^{212}$Pb contamination because of the long half-lives of the $^{224}$Ra and $^{228}$Th isotopes used as spikes. The only effective remedy was frequently to replace the contaminated components. Furthermore, the drying of the gas stream never seemed to be 100% effective and the chamber's behaviour when used with wet sources was rarely reliable. These problems associated with the technique render it a difficult assay method for the $^{224}$Ra content of water, but a certain amount of data was nonetheless taken with the CPC1 using wet sources. It is clear, however, that the technique is unsuitable for use where ultra-low backgrounds are required.

Apart from the conclusions reached about the feasibility of bubbling wet sources as an assay method for their $^{224}$Ra content, one important investigation was performed using this technique with the CPC1. The relative count rates from two separate sources of roughly known strength were established, one a $1Bq$ dry $MnO_2$ source and one a $0.1Bq$ wet source. Despite the poorly known source strengths, it was possible to conclude that the $MnO_2$ source was counting with about 2/3 the efficiency of the bubbled wet sources. This parameter, the relative efficiency of wet and dry sources, was further investigated using the CPC2 and the extraction of $^{220}$Rn from a $MnO_2$ surface was directly measured using a Ge(Li). These investigations are reported in later sections, and give results consistent with the factor of 2/3 quoted here.

### $^{212}$Pb accumulation

A side-effect of continued operation of the CPC on a daily basis was found to be the build-up of activity in the chamber due to residual $^{212}$Pb, the product of $^{216}$Po decay. Clearly, when $^{216}$Po decayed to produce $^{212}$Pb atoms, some fraction of these were deposited on the interior surfaces of the chamber: if they remained charged for any length of time then they presumably drifted to the cathode. Since the different amplitudes of the Radon and Polonium peaks (noted above) imply that $^{216}$Po itself tends to drift towards the cathode before decay, this process will also give rise to $^{212}$Pb deposition. Thus activity was introduced into the chamber which gave rise to alpha particles of two energies, 6.1MeV and 8.8MeV, having relative intensities of 1.78:1. The presence of these alphas is inescapable in a proportional chamber in which $^{220}$Rn decays. A number of points may be noted:

1. The most important feature of these peaks is that they decay in intensity with the $^{212}$Pb half-life of $10.6\,hr$. (Measurements were made after an episode of considerable $^{212}$Pb contamination which were consistent with this half-life). Since this half-life is not unacceptably long, it was always possible to allow the detector to cool down for 2–3 days after use with particularly active sources, and thus avoid the problems associated with this incidental activity.

2. The problems arising from these activities were twofold. The first was the simple problem of background in the pulse height spectrum. The $^{212}$Po decay is the highest

naturally-occurring alpha decay and was well clear in pulse height from all others seen in the chamber. However, all peaks observed in the CPC were associated with long low-energy tails and thus even the $^{212}$Po alpha contributed some background under the $^{220}$Rn peak. However, it was rarely serious. More commonly, a significant level of spurious $^{220}$Rn events were generated by the $^{212}$Bi decay, which gave rise to a peak not resolved from the $^{220}$Rn peak. This occurred when the CPC had been used with fairly active sources (of order $1s^{-1}$) within two or three days before a weak source of $^{220}$Rn (of order $0.01s^{-1}$) was counted. Under these circumstances, a background correction was performed by determining the area of the distinct $^{212}$Po peak, making use of the known branching ratio to these decays to estimate the $^{212}$Bi peak area, and subtracting this from the $^{220}$Rn peak area. The details of this procedure are given in Section 4.2.3 since it was fully developed during CPC2 work, when operating conditions were well known and stable over long periods of time.

3. A secondary problem associated with the presence of non-$^{220}$Rn activity in the chamber concerned the timing information recorded with each event. Electrical noise events generated by charge leakage also contributed to this effect. In addition to pulse height, a further parameter is recorded for each event above the $^{241}$Am peak. This parameter is the time (to the nearest $1/100s$) since the last event whose pulse height exceeded that level. In this way it was possible to determine which events occurred within, say, $0.6s$ of each other and were therefore candidate $^{220}$Rn/$^{216}$Po coincidences. The difficulty caused by high-energy pulses was that if such a spurious event, not related to a $^{220}$Rn decay, occurred shortly after a $^{220}$Rn decay but before its associated $^{216}$Po decay, then the timing information connecting these events was irretrievably lost with the result that the coincidence efficiency was decreased and, worse, was a function of the levels of background activity in the chamber. Because of the uncertainty involved, the CPC2 data was not in general analysed with a coincidence requirement: simple integration of the peak area sufficed, along with a small background subtraction.

## 4.2 Second generation Cylindrical Proportional Chamber

### 4.2.1 Description of the apparatus

**Construction of the CPC2**

The second stage CPC was designed to remedy the principal faults in the CPC1 design, namely:

1. The gas flow pattern within the CPC1 was poorly defined. The gas entered and left through single off-axis ports in the end-plates of the active volume and thus, on the reasonable assumption of laminar flow, different volume elements of the flow took paths through the apparatus which were very different in character, that is, a fraction of the gas remained near the centre of the chamber at all times whereas other fractions took paths which were longer and nearer to the chamber walls. The obvious undesirable

consequences of this flow pattern were that alphas originating at different points in the gas had very different detection efficiencies due to the different probabilities of containment of the resulting tracks. Also the mean residence time for gas in the chamber was difficult to estimate reliably.

2. The fields in the chamber were very non-uniform. This has the obvious bad consequence that charge collection efficiency was very dependant upon the start position of the track and on its orientation in the chamber. Although it was demonstrated that the CPC1 was capable of reasonable resolution with the correct choice of anode wire diameter and voltage, its $^{220}$Rn detection efficiency was estimated at about 10%.

The CPC2 made use of the same cylindrical pressure vessel in which the CPC1 was contained, with an extension along its axis to a total internal length of $393mm$. The cylindrical wall was lined with copper-clad Kapton, a plastic material electrolytically coated with a layer of highly pure copper, found with CPC1 to greatly reduce $^{220}$Rn backgrounds emanating from the stainless vessel. Apart from the cylindrical walls of the chamber, the largest area of stainless steel exposed to the incoming gas streams is the lower face of the top flange: sheets of PTFE were included as a barrier to $^{220}$Rn originating from this source. Access to the pressure vessel was only by the top flange, thus imposing the design constraint that the all assembly work on the chamber had to be complete before this flange was in place. This led to the solution used in CPC1&2 of mounting all the internal parts of the counter on the top flange.

The central design feature of the CPC2 was the incorporation of manifolds at the top and bottom of the pressure vessel, whose function was better to define the gas flow pattern within the sensitive volume. The top manifold accepted two separate gas streams, one via a $^{220}$Rn source, the active gas stream, and the other not having passed via the source, the inactive stream. The active stream was directed into a cylinder of $140mm$ diameter centred on the axis of the pressure vessel. The thick annulus surrounding this inner cylinder carried the inactive gas stream, intended to help prevent the active stream from approaching too closely the chamber walls, with the resultant loss in $^{220}$Rn-alpha containment. The manifolds were of polypropylene and were bolted through onto the upper and lower flanges of the pressure vessel respectively. The two streams were physically separated within each manifold by an annular partition, O-ring sealed to the flange. The circumference of each manifold was likewise sealed to ensure that the flow was directed entirely through the ports.

The gas ports into the sensitive volume were $45mm$ lengths of $1mm$ bore copper pipe, $\simeq 1.5mm$ o.d., which projected $38mm$ beyond the manifolds' surfaces. Each of the two gas streams was admitted to, and vented from, the sensitive volume via 24 such pipes, thus equal flow rates in the two streams resulted in equal exit velocities of the gas from the pipes. It may be shown by evaluation of Reynolds' number that, for any reasonable flow rate used with the chamber, flow through the pipes is laminar, and thus that flow through the volume of the chamber may also be expected to be laminar. The effects of the copper pipes, therefore, are to shield the active gas stream from the chamber walls and to allow easier estimation of the residence time within the chamber of the gas. The pipes were arranged in concentric rings

| Ring # | Diameter/$mm$ | No. Pipes |
|---|---|---|
| 1 | 40 | 6 |
| 2 | 80 | 6 |
| 3 | 115 | 12 |
| 4 | 156 | 12 |
| 5 | 204 | 12 |

Table 4.1: Diameters of rings and numbers of pipes in each ring of copper pipes on each manifold.

around the anode wire. The diameters of these rings and the number of pipes in each ring are given in Table 4.1 and were chosen to encourage the flow pattern into the parabolic form which is necessary if there is to be no radial flow. A cross-section of the CPC2's construction is shown in Figure 4.5.

The second requirement on the CPC2 was the solution of the problem of poorly defined fields in the CPC1. This clearly required potential-defining surfaces at the ends of the chamber to set up the required logarithmic potential distribution. Since the equipotentials are circular, and the copper pipes were arranged in rings, they were themselves used as potential-defining structures. They were thus connected together by a resistor chain which defined the potential distribution appropriate to a $125\mu$ anode wire, found from CPC1 results to be an acceptable choice of wire diameter. The resistor chains were located on the outer faces of the manifolds, away from the chamber's sensitive volume.

The anode wire was supported at its top end from the top manifold and at its lower end from an 'anode support plate'. This latter was a polypropylene plate held at a distance of $330mm$ from the face of the top manifold by three aluminium rods connecting the two: thus the support plate depended only on the top manifold, which was itself bolted only to the upper flange of the pressure vessel. The support plate overlapped the lower set of copper pipes and thus was pierced by holes which allowed them to project through into the sensitive volume. Since the gas flow did not therefore extend as far as this plate, it did not interfere in the flow pattern set up by the pipes. Guard rings were provided for the anode wire at each of its ends.

The electrical supplies necessary for the anode wire, guard rings and two sets of copper pipes were fed through the upper flange. The voltages applied to the two sets of pipes were separately controllable. These voltages were applied to the inner rings, and the voltages of the remaining rings controlled by identical resistor chains.

**The $^{241}$Am reference source** A weakness of the CPC1 design was that the $^{241}$Am reference source mounted within the chamber was fixed in position and orientation. It was fixed rigidly to the outer surface of the stainless steel cylinder which defined the sensitive volume and was collimated so that the alphas moved along a diameter in the plane which

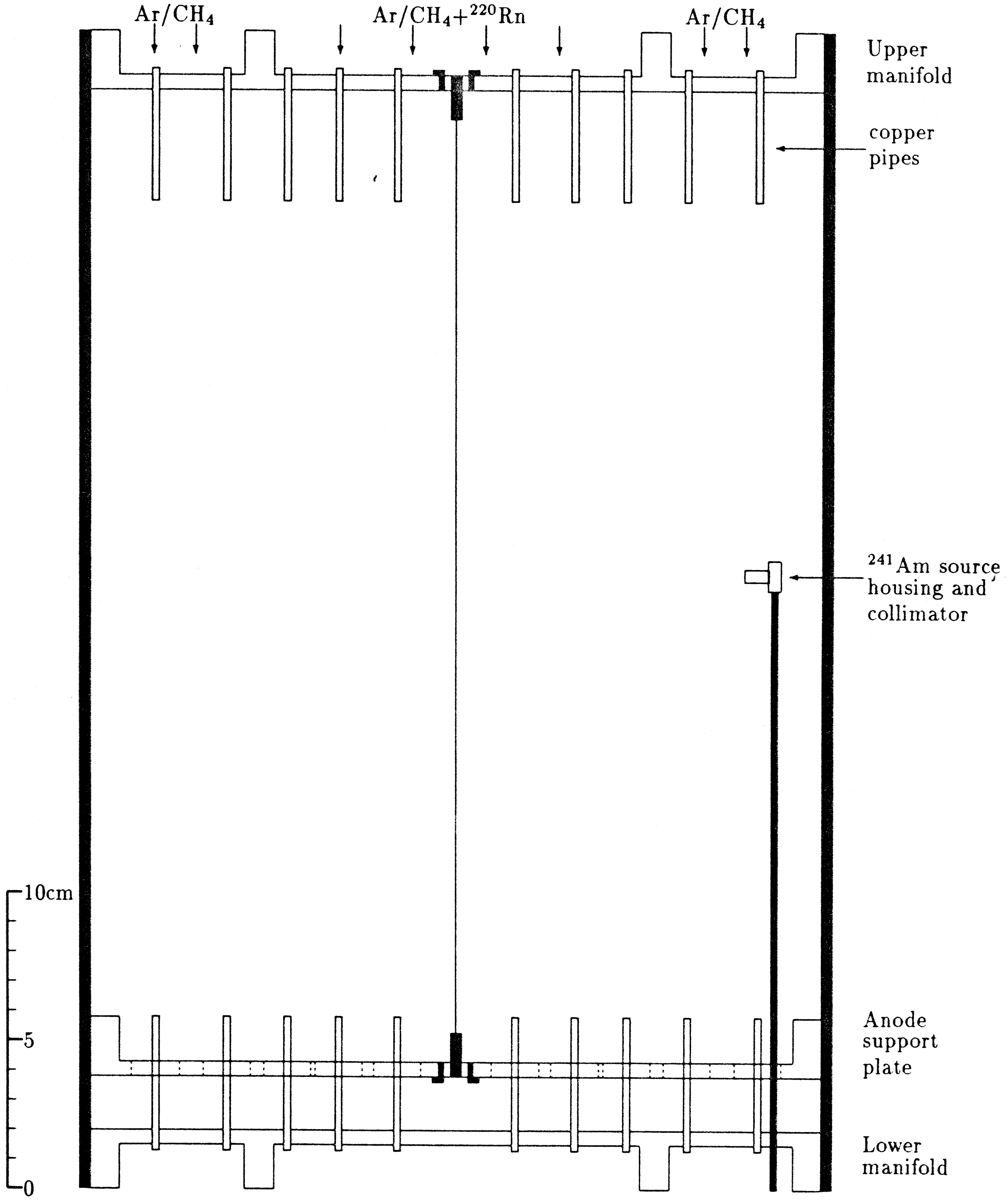

Figure 4.5: Section through CPC2 chamber. Details of internal wiring and supports have been omitted.

bisected the chamber. The beam of alpha particles which it generated thus only sampled the conditions in a small, fixed volume of the chamber in the region where the fields were most uniform. A line was thus observed in the pulse height spectrum which was insensitive to the variation in the response of the chamber over its volume. The amplitude of the $^{241}$Am pulses afforded information only on the gas gain of the chamber near its centre, and was thus sensitive only to the pressure of the gas and to its quality (*ie.* the level of $O_2$ or water vapour present). The Americium source was thus useful as a monitor of these global properties of the chamber. This was particularly useful when bubbling wet sources, when it was common to observe gas contamination and consequent variation of gain during a measurement.

The CPC2 design included the facility for limited movement of the $^{241}$Am source. It was mounted in a brass casing incorporating the same collimator as previously used, *ie.* $10mm$ long by $2mm$ bore, which directed the beam into a horizontal plane. This was in turn mounted on the end of a silver steel shaft which projected, parallel to the chamber axis, through the lower polypropylene manifold and the lower flange of the pressure vessel via a double-O-ring seal. The feedthrough was on a radius of $110mm$ from the axis of the chamber and allowed movement of the source along a vertical axis and also rotation about that axis.

The first, longitudinal, degree of freedom of movement of the source allowed the surveying of the chamber response as a function of $z$, the displacement of the source parallel to the chamber axis. This afforded information about the field uniformity along the length of the chamber, which could not be assessed in the CPC1 design. It thus allowed the selection of suitable voltages for application to the copper pipes.

The second, rotational, degree of freedom allowed the beam to be directed along the diameter of the chamber or at any angle to it. This movement afforded information on the variation in the charge collection efficiency with distance from the wire. This was a source of concern since the fields near the edge of a cylindrical volume are necessarily weak, which could give rise to electron drift times longer than the integrating time of the amplifier, with a consequent loss of detection efficiency for events whose tracks included a segment in the outer region of the chamber. Comparison of the chamber's response to $^{241}$Am alphas directed along a diameter with the response to those at a large angle to a diameter therefore compared the collection efficiency near the edge of the chamber with that nearer to the centre and should have revealed any non-uniformity. This comparison was only useful, however, if the range of the alphas was comparable to the chamber radius: this was clearly the case in the CPC when operated at a pressure close to 1 atm. As a subsidiary benefit, rotation of the alpha source allowed it to be 'switched off' by directing it outwards along a diameter, towards the chamber wall. In this orientation, no ionization could drift to the anode wire. The results of trials which investigated the chamber's response as the position and orientation of the source were varied are presented in Section 4.2.3.

### External fittings and gas handling

The principal function of the gas-handling pipework external to the CPC was to allow counter gas to be passed from the cylinder through the $^{220}$Rn source to the CPC and then to exhaust.

Among the additional requirements placed on a successful arrangement were that

1. It allowed for the monitoring of flow rates both into the inner CPC cylinder via the source and into the outer CPC cylinder and the control of these flow rates,
2. It allowed the selection of one of a number of possible sources for counting at any one time,
3. It allowed for the evacuation of both the CPC and the ($MnO_2$) sources,
4. It allowed the establishment of stable, reproducible operating conditions in the chamber, and
5. It did not contribute appreciable $^{220}$Rn to the gas stream.

A schematic of the gas handling pipework which was implemented is shown in Figure 4.6. The features of the system included:

1. Flowmeters (Platon model GTV) on the gas lines to the sample (and thence to the inner cylinder of the chamber) and to the outer cylinder allowed the reproducible setting of gas flow rates by means of stainless steel needle valves (a) and (b) mounted at the base of the tube. Reproducibility of flow rate settings to better than 3% was easily achievable and the manufacturers quoted 3% absolute calibration errors. Reproducibility of gas flow rates was essential to ensure that the fraction of $^{220}$Rn decaying in the dead volumes between the sample and the CPC sensitive volume were the same for each run. This dead volume was about $50cm^3$ due to the tubing alone: there was an additional contribution from the volume of the glass columns used to contain $MnO_2$ samples.
2. The shutoff valves upstream and downstream of both sample positions allow one sample to be isolated from the stream while the other is on stream. This allows samples to be changed while the CPC is running without disturbing in any way the conditions in the chamber. This was valuable because it enabled an efficient use of time: as many as eight or ten samples could all be counted on the day after their creation, with a consequent increase in accuracy of the $^{224}$Ra assay.

   The preparation of $MnO_2$ sources for counting consisted of maintaining them under rough vacuum for a period of time, since in storage they inevitably absorbed both water and oxygen from the air. The external tubing allowed them to be evacuated independently of the chamber and of each other. Flushing the samples with a flow of Ar/Me was also attempted as a method of removing these molecules from the samples but was found to be very ineffective: good results could not be obtained even after several hours of flushing, whereas the samples were ready for exposure to the chamber after only one hour of pumping followed by a short ($10min$) Ar/Me flush. Furthermore, snap connectors in the lines to and from the sample positions allowed the insertion of differing types of sample into the stream. In particular, it was possible to insert either glass columns holding $MnO_2$ sources or a series of glass vessels for bubbling wet sources.

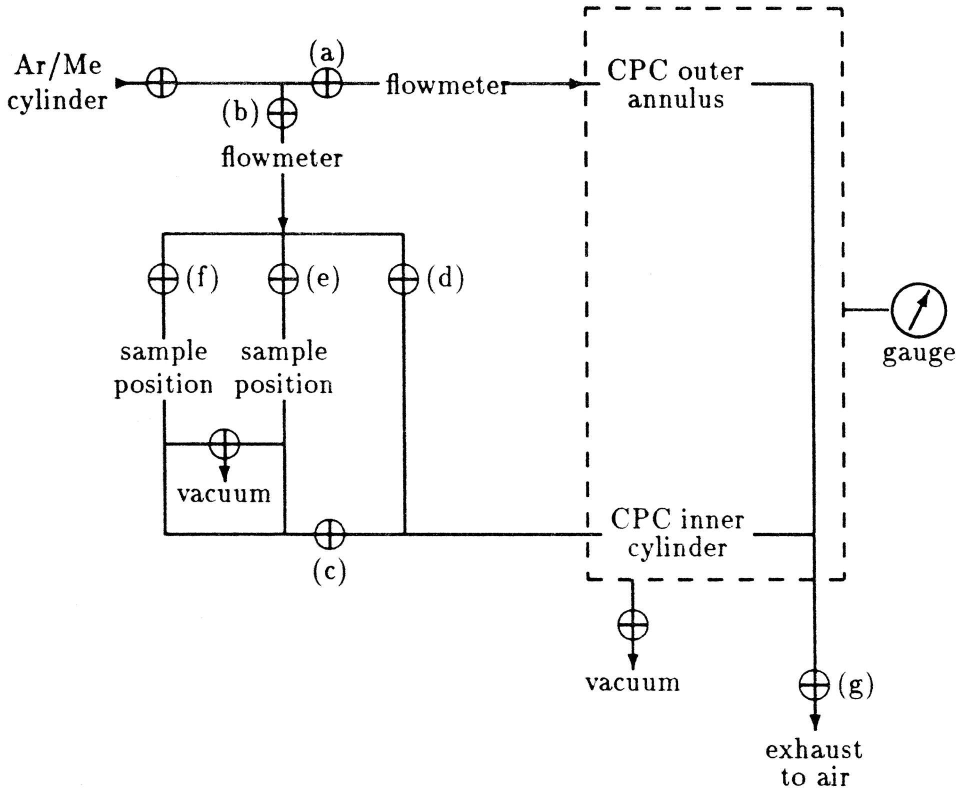

Figure 4.6: Schematic of the CPC's external gas handling pipework.

3. The connection of a vacuum pump allowed the chamber to be evacuated independently of the samples. Evacuation of the chamber was necessary before each series of measurements to remove oxygen and water vapour which had diffused into it since its last use. The consequences of excessive oxygen or water in the chamber were a lowered gain and, worse, drift of gain during use, as these molecules were gradually flushed out. Drift of gain of more than about 2% in the course of a run (low activity sources regularly required between one and two hours of counting time) had a significant effect on the $^{220}$Rn/$^{216}$Po separation in the pulse height spectrum (by increasing the overlap of the peaks) and thus affected the chamber's efficiency. The alternative method of removing oxygen and water from the chamber by flushing with Ar/Me was found to work only very poorly: the time required for the chamber to be cleared of oxygen was very long (several hours) and the procedure used a large volume of gas. The chamber was never capable of maintaining high vacuum, and nor was this found to be necessary — only a roughing pump was ever used to evacuate the chamber and pipework as this served to remove sufficient $O_2$ to allow a relatively short flushing time to stabilise the system. Typically, the chamber was pumped overnight and then flushed with Ar/Me for up to an hour before use: this gave stable conditions in the chamber throughout a day's use.

4. The principal feature of the CPC external pipework and fittings was that its construction was very largely of non-metallic materials, mainly reinforced PVC and nylon. This was essential in order to minimise contamination of the gas stream by $^{220}$Rn from the walls of the tubing. The source of $^{220}$Rn would contain $^{228}$Ra and $^{228}$Th and release $^{220}$Rn by diffusion to the surface within its $1min$ half-life, or by recoil. Materials which contain substantial traces of Radium and Thorium, and are thus undesirable materials for use in contact with the gas stream before it reaches the CPC, include metals, in particular stainless steel and brass, which are both commonly used for gas handling, and glass, the commonest material for the construction of flowmeters. Plastics, however, are known to be relatively free of radioactive contaminants and are thus suitable materials for this application.

   All the tubing was PVC and nylon. Most of the shutoff valves were of polypropylene, nylon and PTFE construction. All the T-pieces and elbow-pieces were moulded in nylon. The major exceptions to the general rule of using all- plastic construction for the gas-handling system were the brass sample outlet valve (c) and the sample bypass valve (d). The flowmeter tubes were of borosilicate glass construction in stainless steel mountings, which also contacted the gas. Needle valves (a), (b), (e) and (f) were of stainless steel. The shutoff valve mounted just after the cylinder was also of brass. Brass fittings fixed the two lengths of tubing which supplied the inner and outer volumes of the CPC to the top flange of the stainless steel pressure vessel. It may be assumed, therefore, that the gas stream was susceptible to a certain amount of $^{220}$Rn contamination from some components of the system, which was clearly not ideal.

The fact that the external tubing was constructed of plastic materials eliminated any possibility of pumping it to high vacuum, both because slow leaks at the joints between lengths of tubing could never entirely be eliminated, and because most plastics are permeable to air. Within these limitations, however, the materials used to fabricate the gas handling system were found to be entirely adequate with the exception of probable contamination at a low level with $^{220}$Rn.

5. The detailed procedures followed in order reproducibly to establish the operating conditions within the CPC are the subject of Section 4.2.2. The principal variable governed by the setting up of gas flow rates through the sample and into the outer CPC volume was the pressure within the chamber, which has a considerable influence on gas gain. (Small pressure variations also have a small effect on the range of alpha particles in the gas and hence on the fraction hitting the walls or otherwise having part of their track in an insensitive volume of the detector. Such variations thus in principle change the efficiency of the chamber, but this is not thought to be a large effect). Consequently, it was important that the pressure in the chamber should not drift in the course of a run by an amount sufficient to cause a significant shift in the peak position. This requirement was satisfied by setting the gas flows to standard values using the needle valves mounted upstream of the flowmeters. The needle valve (g) mounted below the output flowmeter was kept at the same setting throughout the period of operation of the chamber and thus constituted a constant impedance between the chamber outlet and a long tube which lead out to exhaust. All other taps and valves in the system were used in only two positions, either fully open or fully closed, thereby ensuring that they did not constitute additional variables. By setting the regulator at the cylinder head to a standard 5 psi (approximately), conditions of constant pressure in the chamber could be maintained during the runs. Reproducibility between runs was not exact with the simple controls available, and fine gain adjustments were performed at the main amplifier stage.

**Arrangements for containing and counting different types of $^{220}$Rn sources** As mentioned above, the CPC gas handling system is flexible as regards the nature of the $^{220}$Rn source to be counted. Snap connectors were installed at the inlets and outlets to the sample positions which allowed any source of $^{220}$Rn to be inserted. The two types of source used were:

- Dry $MnO_2$ sources, and
- Wet sources, *ie.* solutions of $^{228}$Th/$^{224}$Ra in dilute nitric acid.

Of these two possible types of source, the most important by far was the first. Results using this type of source were found to be reliable and reproducible whereas the counting of wet sources was subject to many experimental difficulties.

**Containment of dry $MnO_2$ sources** To assay $^{228}Th/^{224}Ra$ contained in a dry $MnO_2$ sample by $^{220}Rn$ de-emanation from the $MnO_2$ surfaces, it is necessary to pass Ar/Me through the sample in such a way that $^{220}Rn$ extraction from the sample is as efficient as possible, does not vary between measurements on the same sample and does not vary between samples. It is, of course, also necessary to contain the $MnO_2$ so that no fraction is lost during a measurement or between measurements. A further desirable feature is that the dead volume associated with the sample container and the tubing connecting it to the CPC be as small as possible so that $^{220}Rn$ is transferred to the CPC with minimum loss due to decay.

The method used for the containment of $MnO_2$ sources in order to satisfy the above requirements was to place them in a glass column, mounted vertically, and pass Ar/Me through them at $1.03l\,min^{-1}$. The gas was passed upwards through the sample: this ensured that the whole sample was agitated and thus that

(a.) it did not 'pack down' into a dense mass of high impedance, and

(b.) there was no opportunity for the formation of a stable channel within the sample through which the majority of the gas flow passed — this would result in part of the sample not being exposed to a moving gas stream and hence in a lowered overall $^{220}Rn$ extraction efficiency.

A further advantage of this method of containment was that the sample could be placed in the column prior to activation with $^{228}Th/^{224}Ra$ solution, the solution then passed through the column and the sample finally dried in the column before exposure to the chamber in the same column. The advantages of this procedure over some alternative involving activation and counting of the sample in separate containers were firstly that the possibility of contamination of the sample in the process of handling was minimised and secondly that there could be no loss of sample between activation and measurement. A disadvantage of using glass columns is that a certain level of $^{220}Rn$ contamination may result from $^{228}Th$ in the glass; this was not thought to be a serious problem at the levels of activity assayed by the CPC.

The $MnO_2$ samples counted with the CPC fell into two classes based on their mass: the lighter ones had a mass of order $0.3 - 0.5g$ and the heavier $9 - 11g$. It was therefore necessary to use two different sizes of container to hold them. The larger of the two was a glass chromatography column of internal dimensions $215mm$ length by $18.37mm$ internal diameter. Tapered ground glass joints at either end allowed its easy insertion and removal from the gas stream and, when greased, formed a gas-tight seal. Near the bottom of the column, a sintered glass frit retained the resin but easily passed both Ar/Me and water, respectively during the counting and the activation of the sample. The lighter samples were contained in smaller glass columns: these were $190mm$ long by $5.85mm$ internal diameter. Each of these glass tubes had a restriction $30mm$ from one end, of approximately $3mm$ bore, which served to retain a plug of acrylic wool whose function was similar to that of the frit in the larger columns, *ie.* to retain the resin in the column during the activation and counting procedures. A second acrylic wool plug, which had no analogue in the chromatography columns, was inserted into these columns above the resin: its function was to prevent the Ar/Me flow up through the column lifting the grains out of it, which tended to happen in the case of the small columns because, for the same volume flow rate, the flow velocity was 9 times higher.

The reason for arranging the gas flow to be upwards through a vertically-mounted column has been stated above: to agitate the sample during counting so that no one region of it is exposed to a greater gas flow than any other. The necessity for using a narrow-bore column in which to count the smaller samples is related to this. When samples whose masses were in the region of $0.5g$ were counted in $18.37mm$ bore fritted chromatography columns, the layer of absorber on the surface of the frit had a thickness of only approximately $2mm$ (the thickness of 4–5 layers of beads) when uniformly distributed. However, it was observed that the Ar/Me flow tended to re-distribute this thin layer of absorber in such a way that it covered only a restricted area of the frit. This observation implies that the frit is non-uniform *ie.* that some areas of it offer less impedance to gas flow than do others. Furthermore, it was clear that the gas flow, more rapid through some areas of frit than others, displaced the resin out of its path and into areas where the flow velocity was low. Consequently, non-uniform frits act to ensure that small $MnO_2$ samples are counted inefficiently, being displaced to regions of low gas flow. This problem does not apply to large samples in large columns, since these samples formed a bed several *cm* thick in the $18.37mm$ bore and it was observed that the whole column was agitated by the flow. One would also expect the thick resin bed to mitigate the effects of a non-uniform frit by acting to distribute the flow uniformly across its cross-section, acting itself rather similarly to a frit. The problem also does not exist in the case of a small sample in a small column, because in this case the whole sample is severely agitated by the flow rate actually used, so much so that a plug of acrylic wool was needed to prevent the beads being blown out of the column.

The dry $MnO_2$ samples generally were created in pairs consisting of one large and one small sample. For this reason, the pipework which could be inserted into either of the two sample positions in Figure 4.6 included adaptors which allowed for the connection in parallel of two columns, one large and one small, with three-way taps for switching between them as indicated in Figure 4.7. The adaptors to the large (chromatography) column were of glass, and adapted the tapered ground glass ends of the columns to 1/4" reinforced PVC tubing. The adaptors used for the small columns were polypropylene fittings which compressed an O-ring onto the outer surface of the glass. In both cases, the gas seal at the adaptors was found to be entirely adequate.

The $0.1\mu$ filter placed downstream of the columns was a PTFE membrane of diameter $45mm$ in a nylon housing, the filter being found to have negligible impedance to gas flow. It was included as a precaution against small grains of $MnO_2$ being loosened from the surfaces of the beads by abrasion due to their agitation in the gas stream. These small grains could presumably be carried along with the gas stream and into the CPC where, since they would be active, they could constitute a long-lived source of $^{220}Rn$ background if deposited. In practice, no evidence that $MnO_2$ powder was loosed from the beads was found. Had this

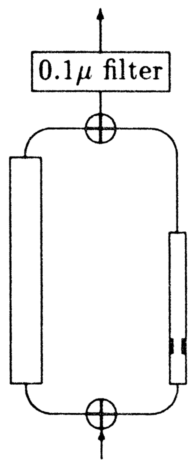

Figure 4.7: Arrangement of two columns containing $MnO_2$ at a sample position in the gas handling pipework.

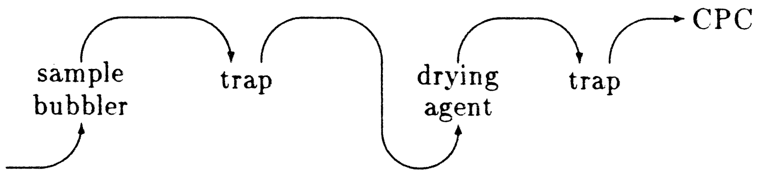

Figure 4.8: A schematic showing the sequence of glass vessels used for bubbling gas through active solutions into the CPC.

been the case, the filters might have been expected to show black deposits and the background in the chamber should have increased steadily with exposure to $^{228}$Th-bearing $MnO_2$.

Evidence that activity was not lost from the beads in the course of CPC measurements also arose incidentally during the work described in Section 5.1, in which $MnO_2$ samples were exposed to gas flows for periods much longer than in CPC work. By counting a source in equilibrium before and after $180ks$ continuously in a flow of $800cm^3min^{-1}$ $Ar/CH_4$, activity loss was not more than 1.5%. At that rate of loss, the activity loss from a sample in the course of several CPC measurements would never have been significant.

**Containment of wet sources** The principle of assay of wet sources by bubbling has been mentioned in Section 4.1.2. Some results were there presented and some of the problems associated with the technique mentioned. Here the apparatus used to contain the sources will be described in more detail, although the technique was very rarely used with the CPC2. The sequence of vessels used is indicated in Figure 4.8.

The main bubbling vessel was a glass gas washing vessel of $560ml$ volume. The gas stream entered through a sintered glass frit at the bottom of the vessel, passed up through the solution under test, and out through a tapered ground glass joint at the top of the vessel. Following the bubbler were three further glass vessels, a bubbler vessel of $280ml$ volume containing a drying agent (often $\simeq 100ml$ concentrated sulphuric acid), with a trap either side to prevent bulk acid being blown into the chamber or sucked into the source. The entire assembly was inserted into the gas handling arrangement of Figure 4.6 at either of the sample positions, making use of the flexibility afforded by a modular design.

This arrangement was subject to several experimental difficulties. The first was the difficulty of removing oxygen from the source solution and the acid. In the case of counting dry $MnO_2$ sources, the removal of $O_2$ from them was not a problem and was accomplished by maintaining them under rough vacuum as described above. In the case of wet sources, this was clearly not appropriate and there was no alternative to oxygen removal by extensive flushing with Ar/Me. This process was very time-consuming and not very effective. In addition to removal of $O_2$ from the source and acid, the same flush removed it from the trapping vessels also. Evacuation of any part of the system was ineffective as it was always necessary to open the system in order to add the source. Other difficulties associated with the bubbling of wet sources have been outlined elsewhere and relate to the problems of drying the gas and the inevitable contamination of the whole apparatus by fine drops of the source being entrained in the gas stream.

A further problem intrinsic to any bubbling apparatus concerns the dead volumes associated with the bubbler vessel, drying vessel and traps. In the apparatus described above they total $1.1l$, thus at a flow rate of $1.03l\,min^{-1}$they introduce a dead time of $1.1min$ and thus a 56% $^{220}$Rn loss by decay. The glass apparatus used for the bubbling of wet sources with the CPC must be assumed to be a source of $^{220}$Rn, since glasses are known to contain $^{232}$Th at the level of typically 0.1–1ppm. Measurements demonstrated that the background counting rate clearly attributable to the glassware was of the order of $0.02s^{-1}$.

The most serious problem associated with the bubbling of wet sources concerns the rates of noise pulses in the chamber and its stability during long runs. It was clear that noise rates were much higher when acid was used for drying than otherwise, and this must be attributed to droplets of $H_2SO_4$ entering the chamber. Furthermore, in many cases, it was found that the source could be bubbled and the dried gas admitted to the chamber for only a limited time before the performance of the chamber deteriorated: in these cases the rate of noise pulses rapidly increased. This seems to imply that conc. $H_2SO_4$ failed adequately to dry the gas stream after that time. It was found that $\simeq 30min$ was the longest run feasible using this drying agent. These difficulties with the counting of wet sources resulted in very little useful data being taken with this method.

### Data acquisition electronics

The detection of $^{220}$Rn by the CPC relies on the collection of ionization produced by the alpha decay of this isotope. Furthermore, the short half-life of the daughter $^{216}$Po ($0.15s$) allows also for the detection of delayed coincidences between the two decays (in the limit that the mean interval between $^{220}$Rn decays is long compared to $0.15s$. The chamber was

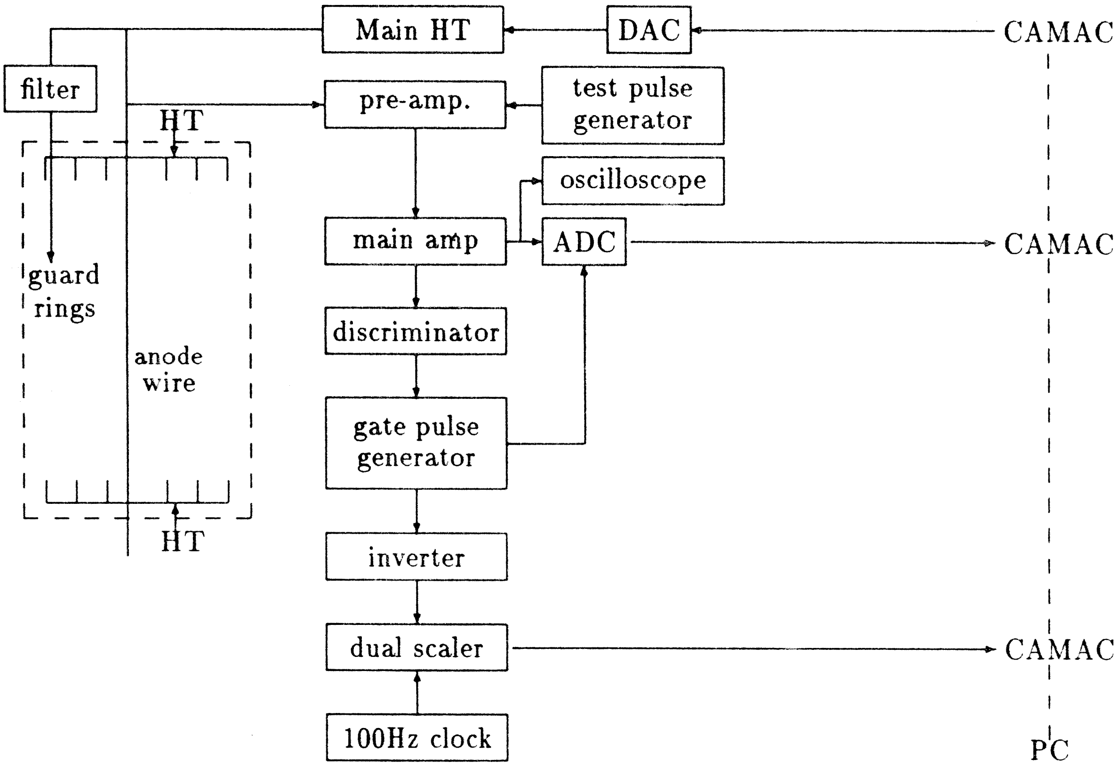

Figure 4.9: Schematic of the CPC data acquisition electronics.

not always operated under these conditions). Thus the signature of a contained $^{220}$Rn/$^{216}$Po event in the chamber consists of two pulses of well-defined amplitude in coincidence within about 0.5$s$. If the detector is to be used to detect coincidences, therefore, the elapsed time between events must be measured and stored, in addition to pulse height information.

The CPC was always intended as a low-rate counter of large-amplitude (several MeV alpha particle) events. This fact obviated the need for fast or low-noise electronics, allowing instead the use of relatively simple components. Similarly, there was no severe requirement for speed of the data acquisition software. The data acquisition electronics and software which was implemented, and is described below, was successful in acquiring data up to the maximum rate ever counted in the chamber, about 20 $^{220}$Rn decays per second (with associated $^{216}$Po decays).

The electronics and software was thus required to measure and store, for each event observed in the CPC, its amplitude and the time interval since the previous event. The computer used for acquisition, storage, preliminary analysis and display of the data was a Tandon model TM7002 PC which was interfaced to the data aquisition electronics via CAMAC. The schematic of the data acquisition electronics is given in Figure 4.9.

Most aspects of the figure are self-explanatory, only a few requiring comment. It can be seen that all pulses received by the amplifier are passed to the ADC, however the function of the discriminator is to ensure that the low-amplitude noise pulses are ignored: pulses exceeding the discriminator level of about 0.7V trigger a gate pulse generator which opens the ADC gate for a time ($4.4\mu s$) sufficient to allow the ADC to digitize the maximum of the pulse. The shaping constant of the amplifier is chosen to be $8\mu s$ to allow for the charge collection in the relatively weak fields in some parts of the chamber to be complete. The gate pulse is also passed to a toggling scaler (Sension model 1009A) which continually receives pulses at a rate of 100Hz from a precision crystal-controlled clock. The 1009A is a dual-scaler device which counts clock pulses into one of two scalers: the arrival of a trigger pulse causes the destination of the clock pulses to be switched, *ie.* it causes accumulation into one scaler to cease and the other scaler to begin counting pulses. The inactive scaler is then read into CAMAC and cleared ready for the next event. The scaler thus records in 1/100's of a second the time between two events which exceed the discriminator threshold. In fact this was set very low and further discrimination performed in software.

The main HT supply used to apply volts to the central anode wire of the CPC was an ORTEC model 456 ±0–3kV supply, which had the facility that its output could be controlled by means of a small (0-12V) analogue voltage generated externally: this allowed the control of the anode voltage from software via a DAC. The reason for including this feature was that it enabled the gas gain of the system to be stabilized against small, slow variations in pressure or gas composition (*eg.* moisture or oxygen content) during long runs (up to 24 hours). This was done by monitoring in software the centroid of the peak resulting from the $^{241}$Am reference source which was mounted in the detector: drift of this peak due to those effects could be counteracted by making small changes in the anode voltage. In practice, this feature was not much used with CPC2, where it had the disadvantage that change of the anode voltage was undesirable because the voltages applied to the upper and lower sets of copper pipes were fixed — it could thus adversely affect the resolution by distorting the logarithmic potential distribution. The feature was much more used with CPC1 where, in the absence of field-shaping surfaces, the distortion of the field distribution was not increased by altering the anode potential. The data reported here were taken without the use of this method of gain stabilisation: it was found in general that conditions in the chamber could be sufficiently well-regulated for it to be unnecessary.

### 4.2.2 Experimental procedures

This section describes in detail the procedure followed for counting $MnO_2$ sources with the CPC2. The requirements on a successful procedure are:

**Reproducibility** (a.) It is of the highest importance that the conditions of use of the CPC be repeatable from measurement to measurement on a single sample. $MnO_2$ samples were activated with $^{228}$Th solutions, with its $^{224}$Ra daughter, because it was then possible in one experiment to assess the behaviour of $MnO_2$ with respect to both Thorium and Radium. This was done by observing the time evolution of the $^{220}$Rn activity of the sample.

Samples activated with a $^{228}$Th/$^{224}$Ra solution carry *a priori* unknown activities of both of these isotopes. As noted in Section 3.3, $^{220}$Rn counting may be used to determine the initial sample loadings of both $^{228}$Th and $^{224}$Ra, by observing its time evolution. This requires that the overall $^{220}$Rn detection efficiency of the system must be identical from measurement to measurement on the same sample. Thus there is a requirement on the long-term repeatability of CPC operating conditions.

The determination of initial $^{228}$Th and $^{224}$Ra sample loadings from several CPC measurements of its $^{220}$Rn activity is the subject of Sections 4.4.1 and 4.4.2.

(b.) It is also of importance that the overall efficiency of $^{220}$Rn detection by the system not vary from sample to sample. If the $^{228}$Th/$^{224}$Ra contents of samples differently prepared are to be compared so as to determine the optimum conditions of use of $MnO_2$ absorbers, it is clear that it must be possible to treat different samples in such a way as to ensure equal counting efficiencies, or at least well-known relative counting efficiencies.

**Stability** The principal factors determining the overall gain of the system are the voltage applied to the anode wire and the pressure and composition of the chamber gas. Factors determining the efficiency of $^{220}$Rn detection include the residence time of gas in the detector, the electric field configuration (determined by the three separately controllable voltages) and the gas flow pattern.

It is required that the conditions in the chamber, in the sample and in the pipework external to the chamber not vary in the course of a run, in particular that it is possible to perform long runs under stable conditions which are the same as those in effect during short runs. Failure to meet this requirement introduces the possibility that the counting efficiencies of active and relatively inactive sources could be different, due to the very different counting times required for assay of such sources, thus destroying comparability between samples. In general, it also would result in the counting efficiency varying between measurements on a single sample as the activity of the the sample changed with time. This is thus a requirement on the short-term *stability* of operating conditions as opposed to the above requirements on their long-term *reproducibility.*

### Standard operating procedure

It should be emphasized that it is not assumed here that the operating conditions used with the CPC2 are optimum. The primary aim of the experimental procedure used to assay $MnO_2$ samples — specified below — is to achieve **reproducibility** with *reasonable* efficiency rather than the highest possible $^{220}$Rn detection efficiency. Consequently —

1. The pressure at the cylinder head was set at about 5 psi in excess of atmospheric, and this setting was not altered during the lifetime of an Ar/Me cylinder, which was typically of order 2 months and included many measurements. The reproducibility between independent settings of this pressure was certainly better than 10%.

2. Before a day's operation, the entire system of chamber, pipework and samples, as far as the cylinder shutoff valve, was evacuated overnight to counter excessive outgassing of oxygen or water following surface adsorption of these molecules by metal and plastic parts of the apparatus. This was found to be essential in order to prevent slow drift in gain during the counting of samples: the gain was in these cases seen to gradually increase over a period of hours as the concentrations of these molecules in the chamber decreased.

3. Before use, the chamber was flushed with a flow of about $200 cm^3 min^{-1}$ Ar/Me for not less than 30 minutes to flush residual oxygen and water vapour.

4. Before counting, each sample was prepared by keeping under rough vacuum for not less than 1 hour. Those four samples counted first on any day were pumped overnight. Since the samples were, between measurements, stored in air, this procedure was essential for partial outgassing of the above molecules. After pumping, Ar/Me was carefully admitted to each sample through a needle valve. Care was required at this stage to prevent excessive flows resulting in an uprush of the sample. Having admitted the gas into the column containing the sample, the sample was in every case flushed with $100 cm^3 min^{-1}$ Ar/Me for about 30 minutes, the outflow being vented directly to air, not through the chamber. This procedure of pumping and flushing was found to be necessary ensure that the sample did not cause any drift in gain during counting due to injection of oxygen and water into the chamber.

5. After the sample and chamber had been flushed as above, the Ar/Me flow rates through the sample and into the outer cylinder of the CPC were set to standard values using the needle valves associated with the two flowmeters upstream of the chamber. Because of the fact that all other impedances in the gas stream were fixed, unchanging between measurements, these needle valves effectively control the conditions in the whole system. These conditions are, explicitly:

   **Dead time** There was inevitably a certain dead volume between the $MnO_2$ samples and the active volume of the CPC2, due to lengths of tubing and to the volumes of the glass columns used to contain the samples. The extent of $^{220}$Rn loss by natural decay in this volume is governed by the flow rate of active gas from the sample to the chamber, which determines its residence time in the dead volumes.

   **$^{220}$Rn extraction** Of the $^{220}$Rn atoms produced within the sample, some fraction will be de-emanated into the gas stream as it passes through the sample. There is no *a priori* reason for supposing that this fraction is 100%, or that it is independent of flow rate. The other possible influence, the gas composition, was never varied. Measurements which determine the $^{220}$Rn extraction efficiency from a $MnO_2$ sample are presented in Section 5.1. They imply that the flow rates used resulted in good $^{220}$Rn extraction which was reproducible and depended only weakly on the sample size. For the present, it need only be noted that the same flow rate of gas through the sample was used for every sample, independent of its size. This rate was $1.03 l\, min^{-1}$ Ar/Me, and was reproducible certainly to better than 5%. In the case of a $10g$ (dry weight) $MnO_2$ sample, this flow rate equivalent to approximately 85 bed volumes per minute, and approximately 2100 in the case of a $0.4g$ sample (these being typical 'standard' sample sizes).

**Flow pattern and residence time** Although no calculation of the flow pattern in the chamber was performed, it is sufficient for the purposes of ensuring repeatability that the flow pattern be the same for all measurements. This could not be directly verified by observations made on the chamber, but it is assumed that for similar flow rates, the resulting pattern of gas flow within the chamber will be sufficiently similar not to introduce any gross variation in $^{220}$Rn detection efficiency due to differences in the probability of containment of the alpha tracks.

For maximum detection efficiency, it is of course necessary to maximize the $^{220}$Rn residence time within the chamber: ideally this should be many times the 1 minute half-life. To ensure repeatability, it is again not necessary to assume that the chamber is operating under optimum conditions, only that the conditions are similar for all measurements. This will be the case if the total flow rate through the chamber and the flow pattern within it are identical. Both conditions are necessary to ensure that the mean residence time is repeatable: the first is known to be the case from observations of the input and output flowmeters, the second is assumed.

**Pressure** No active pressure control was included in the apparatus, and so the pressure in the chamber was determined by the pressure at the cylinder head, by the impedances in the gas stream and its flow rates. All impedances were fixed and readily reproducible (all valves and taps were fully open or fully closed) while the chamber was in operation, with the exception of the flow-controlling needle valves, which thus constituted the sole variable impedance to gas flow. From Figure 4.10 it can be seen that the variable impedance is in series with a set of constant impedances. The pressure in the chamber can hence be seen to be equal to atmospheric pressure plus the pressure drop across those impedances between the chamber volume and the outlet to the air. If the flow rate is set to a repeatable value, it follows that the chamber pressure must necessarily be in excess of atmospheric by a constant amount. This excess was about 2 psi.

6. After a source was first exposed to the chamber, that is after gas which had passed through the sample first entered the chamber, a period of equilibration was necessary during which fine adjustments were made to the gas flow rates into both regions of the chamber until they achieved their standard values. The equilibration period also served to allow $^{220}$Rn concentrations throughout the system to achieve their equilibrium values. Such a period was clearly necessary to allow time for $^{220}$Rn from the sample to reach the detector, but this delay was short — under 5 seconds. After this time has elapsed, however, it is easily seen that the $^{220}$Rn activity in the chamber will begin

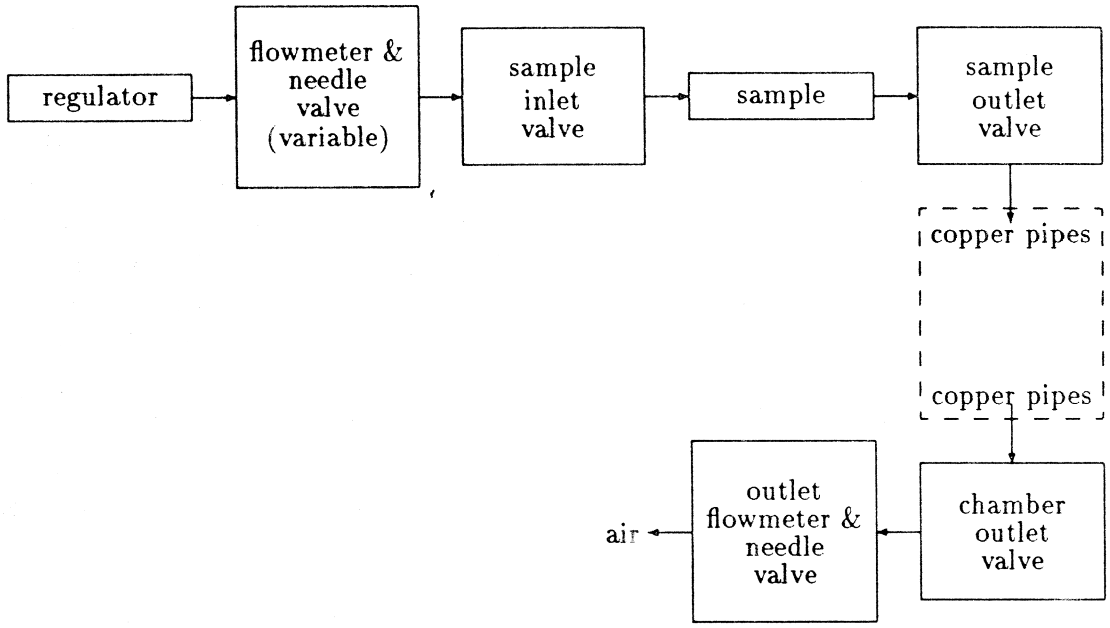

Figure 4.10: Schematic of the CPC gas flow showing the impedances between inlet and exhaust.

to rise towards its equilibrium value with a time constant equal to the $^{220}$Rn lifetime, and independent of gas flow rate. In a chamber of infinite volume, the observed $^{220}$Rn decay rate would tend towards a value equal to the rate of injection of atoms.

The response of real chamber to a $^{220}$Rn decay might reasonably be expected to depend on position in the chamber (see Section 4.2.3) and so the response to a stream of $^{220}$Rn atoms would not be expected to stabilize until the gas has reached the farthest parts of the chamber: since the volume of the central cylinder was approximately 4.3$l$, the active gas stream reached the exit ports (the lower set of copper pipes) after about 5 minutes. Since 5 half-lives of $^{220}$Rn are sufficient to allow essentially an equilibrium concentration of $^{220}$Rn to accumulate, the equilibration time was fixed at 5 minutes and for this length of time after the samples were first exposed to the chamber, no data was recorded.

7. The equilibration period also allowed adjustments to be made to the gain of the system. In the absence of any active pressure control, precisely reproducible pressures within the chamber were not obtainable: small differences between runs in the gas flow rates yielded small pressure differences in the chamber, and hence measurably different gas gains. These were compensated for by manual fine adjustment of the amplifier gain: the criterion was that the $^{241}$Am peak should be centred on channel 200 in the pulse height spectrum. For all runs, the Americium source was placed midway along its range of travel, directed along a diameter. It was found to be easy to make the small adjustments necessary to set the peak centroid to within ±2 channels. The

advantage of ensuring that Americium appeared always at the same channel was that this procedure effectively calibrated the energy scale and ensured that the $^{220}$Rn and $^{216}$Po peaks appeared at approximately the same position in the spectrum of every run. The data analysis was thus simplified and the confidence in its equal treatment of all runs increased.

8. By the commencement of data-taking, conditions in the chamber were in general sufficiently stable so that run lengths in excess of 2 hours were easily possible. A longer period of flushing through the source and chamber removed more oxygen from the system, further reduced the tendency to drift and made 12 hour runs feasible. The stability of the system was monitored by the $^{241}$Am reference source. The resulting line normally had a FWHM of 5 channels, corresponding to a 2.5% resolution. Since the source was fixed in position for the duration of a run, the pulse height due to $^{241}$Am alphas was not sensitive to variations in conditions over the chamber volume. The pulse height therefore served as a valid diagnostic for such properties as the overall system gain. By observing the $^{241}$Am FWHM, runs during which the gain drifted appreciably, by an amount of order 2% or more, were readily detected. Such drifts were normally due to leaky pipework admitting oxygen or to an insufficiently dry $MnO_2$ sample injecting water vapour into the stream. Runs during which excessive drift occurred were rejected, since the changed peak shape due to $^{220}$Rn would have resulted in a change in the detection efficiency resulting from the application of pulse height cuts, even after the analysis procedure given in Section 4.4.1.

9. After occasions where the chamber was used to count an active source (several *Bq*), it was not possible to count low-activity sources until the $^{212}$Pb activity (half-life of $10.6hr$) had died away. Thus it was occasionally necessary to allow the chamber to 'cool' while standing idle for a few days. As a corollary to this, where possible it was standard practice in the course of a day's measurements to count the less-active sources before the more active ones.

### 4.2.3 Performance of the CPC2

#### Background

Many blank runs were conducted during the operational life of the CPC2 to determine the singles $^{220}$Rn background rate, without any coincidence requirement between $^{220}$Rn/$^{216}$Po decays. The procedure was to duplicate the conditions prevailing in the chamber when a sample was under test, *ie.* the standard conditions of flow rate were used, resulting in the usual pressure in the chamber. The flow to the inner part of the detector could either pass through the sample bypass line, or via a sample position with a small fitting replacing an active sample. Runs were also performed with static gas in the chamber, *ie.* no gas flow. With gas flowing through the sample lines, the background rate was $\simeq 10 \times 10^{-3}s^{-1}$. With gas flow through the sample bypass line, or with static gas, a rate of around $1 \times 10^{-3}s^{-1}$

was observed[1].

The known sources of background events are:

**Managanese dioxide from samples** Admitting gas into evacuated $MnO_2$ samples occasionally caused an uprush of beads, which could lodge in the pipe-work. If these were allowed to accumulate, they of course constituted a genuine source of $^{220}$Rn, which could not be distinguished from $^{220}$Rn originating from later samples. This problem was solved by the inclusion of plugs of acrylic wool in the gas stream at the top of the columns, which freely passed gas but retained beads of $\simeq 0.3mm\ \phi$.

A potential further mechanism by which $MnO_2$ could accumulate in the plastic pipe-work was the formation of fine particles due to abrasion between beads and their suspension in the gas stream. The $0.2\mu$ PTFE filters were installed to detect this, but never appeared to accumulate any deposit.

The measurements reported above strongly suggest that contamination of the sample lines was a dominant background. While changing the external pipe-work definitely lowered backgrounds, there was clearly a residual $10^{-2}s^{-1}$ rate whose source was not traced. It is assumed to be due to some fitting, such as a brass shutoff valve, which was not replaced.

**Wet sources** As mentioned in Section 4.1.2, the bubbling of wet sources inevitably spread contamination throughout the system with the result that both pipework and chamber became loaded with $^{228}$Th and $^{224}$Ra. No solution to the problem of source droplets leaving the bubbling vessel was found, so that although some useful data was taken with the CPC2 using this technique, it was eventually abandoned.

**$^{212}$Pb deposits** The most serious of all sources of background were the alpha decays in the chamber resulting from $^{212}$Pb deposited therein by previous measurements. When weak sources were counted with the CPC, it could occur that the residual $^{212}$Bi rate was comparable with the $^{220}$Rn rate from the sample. Although the resolution of the device was sufficient clearly to distinguish the centroids of the peaks due to $^{212}$Bi decay (Q=6.21MeV) and $^{220}$Rn decay (Q=6.40MeV), the width of the $^{220}$Rn peak was such that its tail substantially overlapped the $^{212}$Bi peak. As a result, it was necessary to apply a correction to the apparent number of $^{220}$Rn events: this procedure is detailed in the Section 4.4.1. Nevertheless, the accuracy of $^{220}$Rn assessment the presence of a significant activity of $^{212}$Pb was necessarily limited and the only method of entirely circumventing this background was to allow the chamber to cool for several $^{212}$Pb half-lives. In practice the chamber was often allowed to cool for two days.

**Electrical noise** Spurious pulses were often observed which were attributed to leakage of charge across insulating surfaces within the detector. The dominant contribution originated at the upper polypropylene manifold. The fact that the surface was not ideal, *ie.* was to some extent scratched, encouraged the leakage of charge along the scratches

---

[1] The values quoted for background rates were obtained with the analysis recipe given in Section 4.4.1.

from the guard rings to the inner ring of copper pipes. Once started, the problem tended to become worse with time, and was always present to some extent. Thus it was periodically necessary to clean all surfaces within the chamber, and polish some using mild abrasive.

Most pulses due to electrical leakage were of large amplitude and overflowed the ADC. These pulses, 'saturation pulses', appeared in channel 572 of the pulse height spectrum, well clear of the energy region of interest, so that they did not themselves contribute a background. However, the 'saturation peak' had a tail extending down in energy to the region where genuine alpha events were observed (around channels 250-300) which therefore could contribute to background. The analysis of Section 4.4.1 makes a correction for this effect.

A further effect of the presence of leakage was to interfere with the $^{220}$Rn/$^{216}$Po coincidences. For the purpose of recording the elapsed time between events, the software disregarded events below about 6MeV, thus eliminating $^{241}$Am. However, a high-energy pulse due to leakage could occur between a $^{220}$Rn decay and its following $^{216}$Po decay, with the result that the two would not be recorded in coincidence. In this way the rate of saturation pulses affected the efficiency of $^{220}$Rn/$^{216}$Po coincidence detection. The fact that the saturation rate varied considerably with time thus prevented reproducible coincidence measurements and led to the use of the singles $^{220}$Rn rate as the measure of the source's activity[2].

**Contribution due to a clean column** The glass columns used to contain $MnO_2$ samples were in all cases cleaned before use by successively:

1. soaking for several days in detergent, followed by
2. a number of water rinses ,
3. rinses with distilled fuming nitric acid and finally
4. further water rinses.

This severe treatment was intended to avoid $^{220}$Rn background originating from Thorium and Radium on the walls of the column, and to avoid cross-contamination between runs. Measurements were performed which indicated that such columns contributed no measurable $^{220}$Rn to the stream.

### Variation of chamber response with position

This section describes an experiment which mapped the response of the chamber over its volume, as far as was possible using the reference source arrangement described in Section 4.2.1. The results principally concern the variation of the chamber's response along its axis.

---

[2] After the data sets reported herein were taken, further software cuts on pulse height were imposed, much reducing this problem.

We may consider a response function $R(r,z)$ of the detector, defined by the channel into which a pulse is binned which arises from ionisation at the point $(r,z)$ in the cylindrical polar coordinate frame of the CPC. The significance of the response function lies in the fact that an alpha track can be regarded as a sum of small elements which are sensitive only to the response function of the chamber at a point[3]. Thus a given decay samples the response of the chamber along the track length. If the chamber's overall response (its resolution and efficiency) is to be understood, it is ideally necessary to determine the response function over the entire volume of the detector. For example, a $^{220}$Rn decay near the top of the chamber could give rise to a track directed either upwards or downwards: if upwards then the track would probably enter the region of the copper pipes, where the charge collection might be expected to be poor, but if downwards then the track's entire length would be within the central volume of the chamber where charge collection might be expected to be good. The peak shape resulting from $^{220}$Rn decays would then be given by an integral, over the chamber volume, of $R$ weighted by the probability of an alpha track overlapping the point $(r,z)$.

The experimental variables which determine the response function are of course the voltages applied to the anode wire and copper pipes. These voltages were selected empirically as those which gave the chamber adequate resolution, where the criterion is always the separation of the $^{220}$Rn and $^{216}$Po peaks. The standard voltage applied to the anode was +2.12kV and those to the inner rings of copper pipes 575V (upper set) and 410V (lower set).

From the above definition, it is clear that it is impossible to measure the response function over the volume of the chamber point by point. The approach used to gain some information about this function was to scan the $^{241}$Am reference source through its available travel in $z$, and to vary the angle to the diameter at which it was directed. Experiments were performed which surveyed the chamber by varying $z$ of the source and noting the centroid channel of the resulting peak. The procedure was carried out both with the beam directed along a diameter and at $\simeq 45°$ to a diameter. The channel number in which the centroid of the $^{241}$Am peak appeared is plotted in Figure 4.11 along the vertical axes *vs.* $z$ displacement along the horizontal axis. The error bars represent the FWHM of the peak, and reflect the fact that the beam was not tightly collimated. The plotted results are those obtained when the beam was directed along a diameter — essentially identical results were obtained when the beam was at 45° to the diameter. The normalisation was fixed by adjusting the amplifier gain such that the $^{241}$Am peak appears at channel 200 when the source is in in its usual position for normal chamber operation: that is at $z = 14cm$ and directed along a diameter. The standard operating conditions of gas flow *etc.* were of course used for measurements of the response function.

The data show a marked variation in $R$ with $z$, and an asymmetry between the two ends of the detector, from which it is clear that the chosen pipe voltages were incorrect. However, it is noteworthy that the response shows no dependence on the direction in which the beam was directed. This implies that the charge collection efficiency appears to be the same near the periphery of the chamber as towards the centre. As an approximation, therefore, it may

---

[3] There is an implicit assumption here, certainly not always true, that the presence of neighbouring charges does not affect the response to a given element of charge.

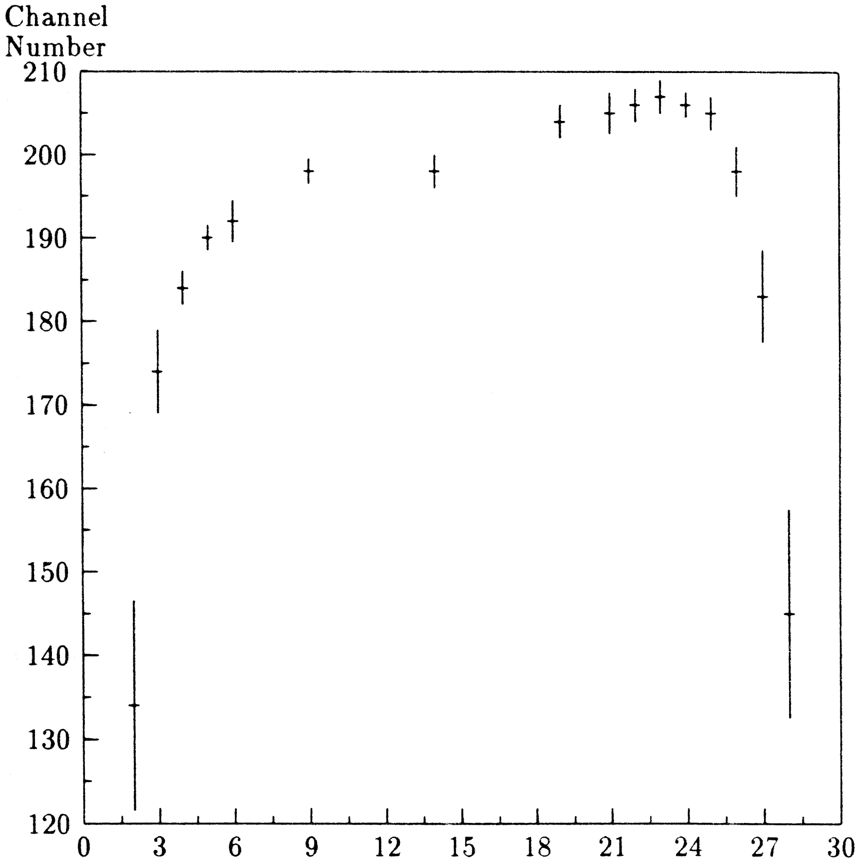

Figure 4.11: Variation in chamber response to the $^{241}$Am reference source with displacement along axis. Error bars indicate FWHM of peak.

be assumed independent of $r$. Problems might have arisen in this respect because the fields are necessarily very weak near the edge of the chamber, which leads to long drift times for ionisation created near the walls. The two effects which follow from this are:

(a.) Significant recombination during the drift from the outer region of the chamber to the avalanche region, and

(b.) Drift times sufficiently long as to exceed the integrating time of the preamp.

That this does not seem to have occurred indicates that the anode voltage, and hence the drift velocities, were sufficient.

### Typical spectra

A number of spectra are presented here which illustrate the behaviour of the CPC2 in a number of respects. Figure 4.12 shows a typical CPC pulse height spectrum resulting from exposure to a $^{220}$Rn source. Figure 4.13 shows peaks due to $^{212}$Bi and $^{212}$Po decay, in the absence of any $^{220}$Rn decays. Figure 4.14 shows a case where $^{212}$Bi constitutes a significant shoulder on the $^{220}$Rn peak and Figure 4.15 shows an extreme case where the $^{212}$Bi rate exceeds the $^{220}$Rn rate. Figure 4.16 illustrates the long tails associated with the $^{220}$Rn and $^{216}$Po peaks.

Two characteristic features of the peaks shown in Figure 4.12 may be noted:

1. The peak shape is skew and shows that the chamber exhibits a sharply-defined maximum response to the decay of each species. This limiting response corresponds to an event fully contained in that central region of the chamber which has a roughly constant charge collection efficiency (see Figure 4.11). The long low-energy tail (Figure 4.16) could in principle be due to a number of processes which may reduce the response below its maximum. The principal cause of this tail is thought to be the non-uniform charge collection of the chamber.

   The effect of the longitudinal variation of the field in the chamber is illustrated by Figures 4.17 and 4.18. The former shows a scan of the $^{241}$Am source in $z$, and the latter figure shows a $^{220}$Rn spectrum recorded before the scan. On dis-assembling the CPC, a large dust particle was found wrapped around the wire at $z = 10cm$.

2. Although a $^{220}$Rn decay is followed in all cases by the alpha decay of $^{216}$Po, the latter peak in Figure 4.12 clearly has a much lower amplitude than the former. As noted in Section 4.1.2, this is attributed to drift of the daughter Polonium ion towards the cathode. The large (approximately 30-40%) discrepancy in the areas of the two peaks suggests that this effect is a large one and that many Polonium ions arrive at the cathode before decay.

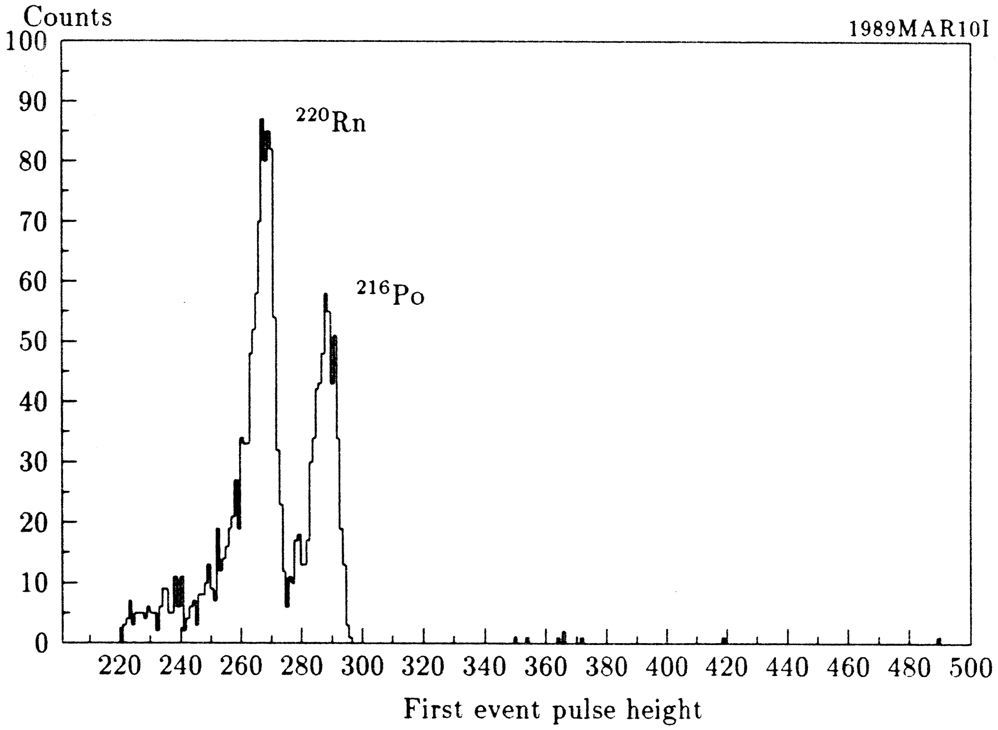

Figure 4.12: Typical energy spectrum due to $^{220}$Rn decay in the Cylindrical Proportional Chamber.

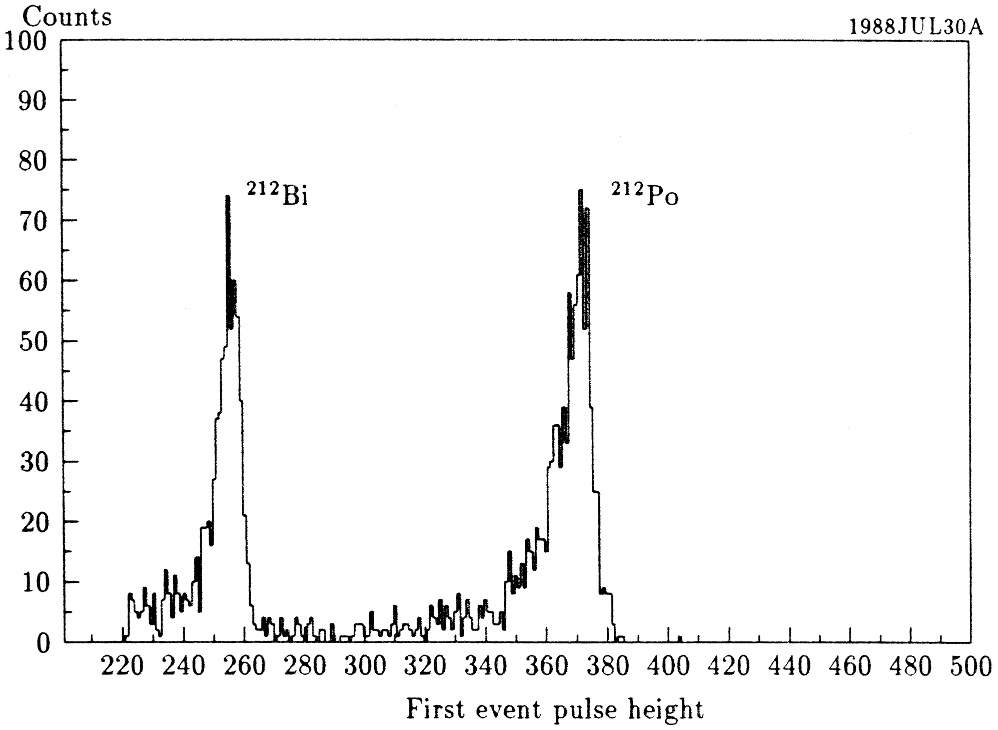

Figure 4.13: CPC output spectrum showing $^{212}$Bi and $^{212}$Po peaks, resulting from residual $^{212}$Pb in the chamber.

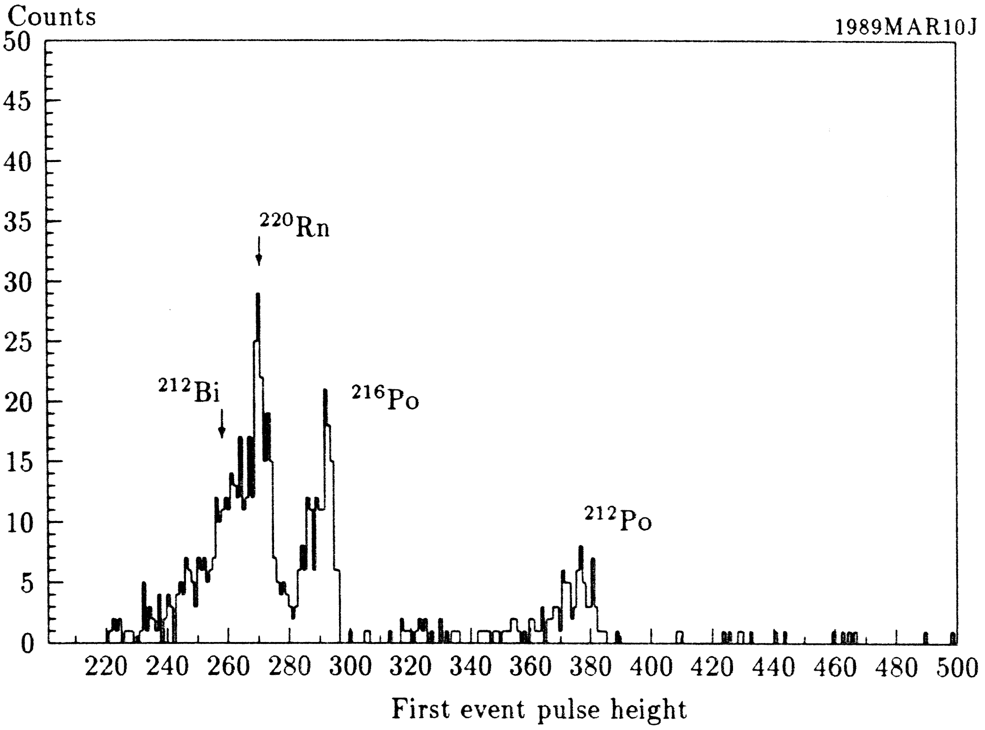

Figure 4.14: CPC output spectrum showing substantial $^{212}$Bi contamination in the $^{220}$Rn peak, and a peak due to $^{212}$Po.

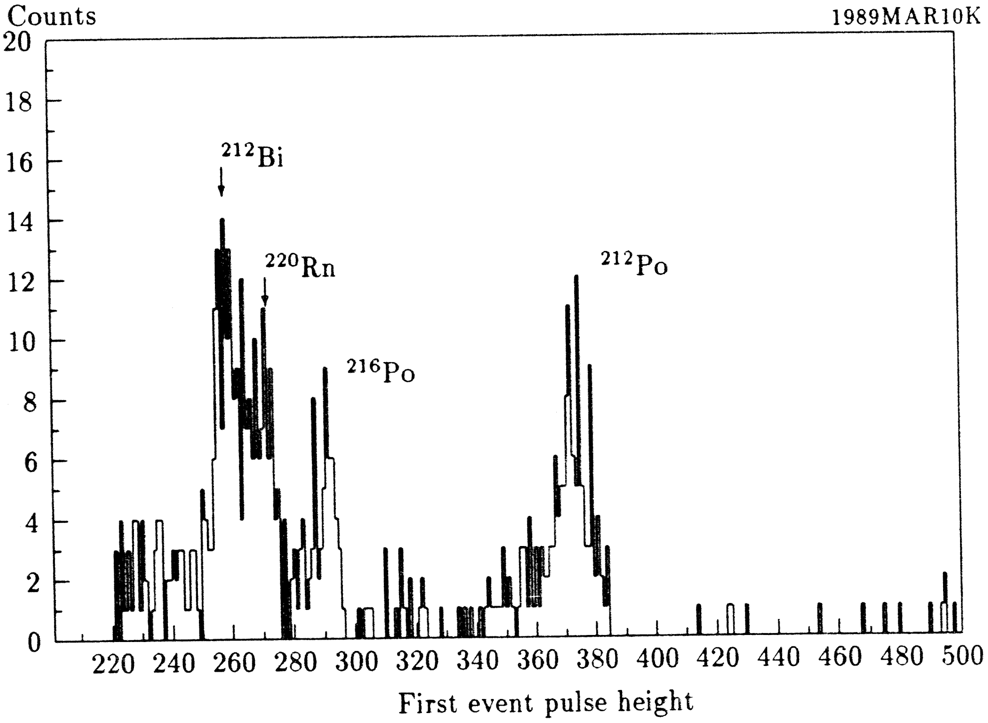

Figure 4.15: CPC output spectrum showing $^{212}$Bi contamination present at a level exceeding the rate of $^{220}$Rn decay.

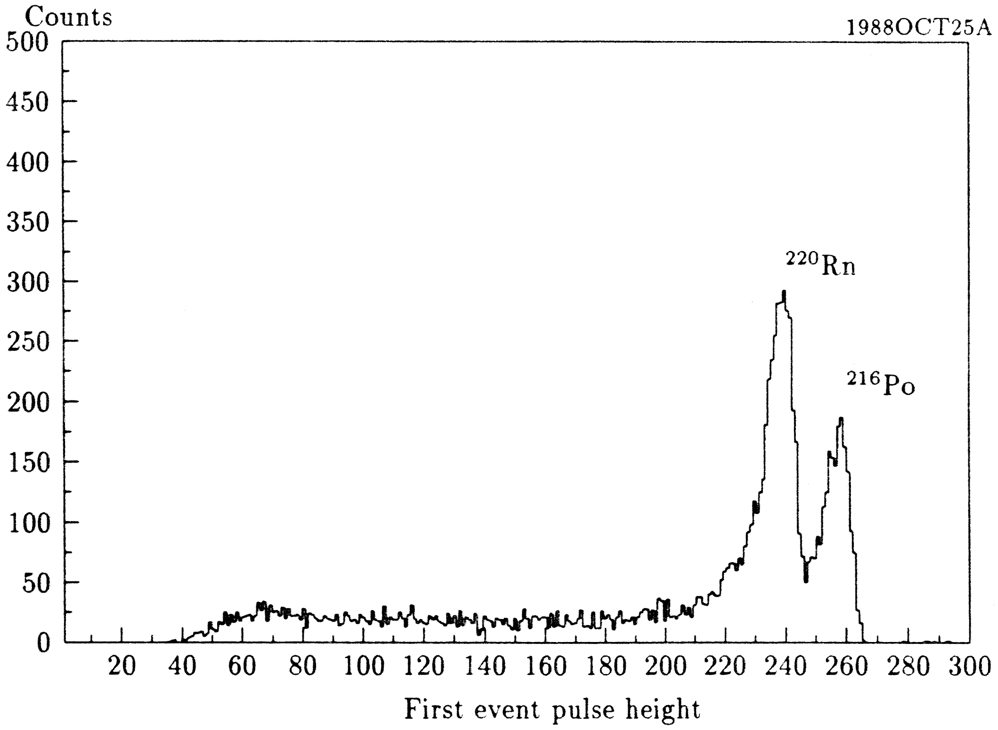

Figure 4.16: CPC output spectrum under non-standard operating conditions, showing the long, flat tail associated with the $^{220}$Rn and $^{216}$Po peaks.

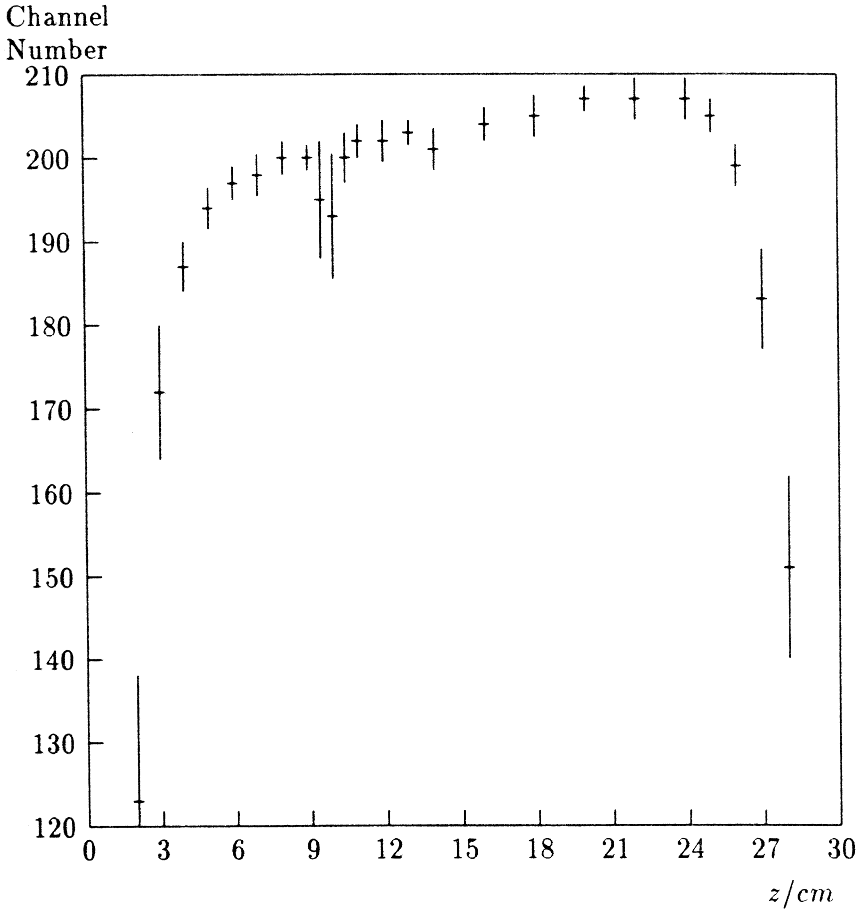

Figure 4.17: Variation in chamber response to the $^{241}$Am reference source with displacement along axis. Error bars indicate FWHM of peak. A dust particle was found on the wire at $z = 10cm$.

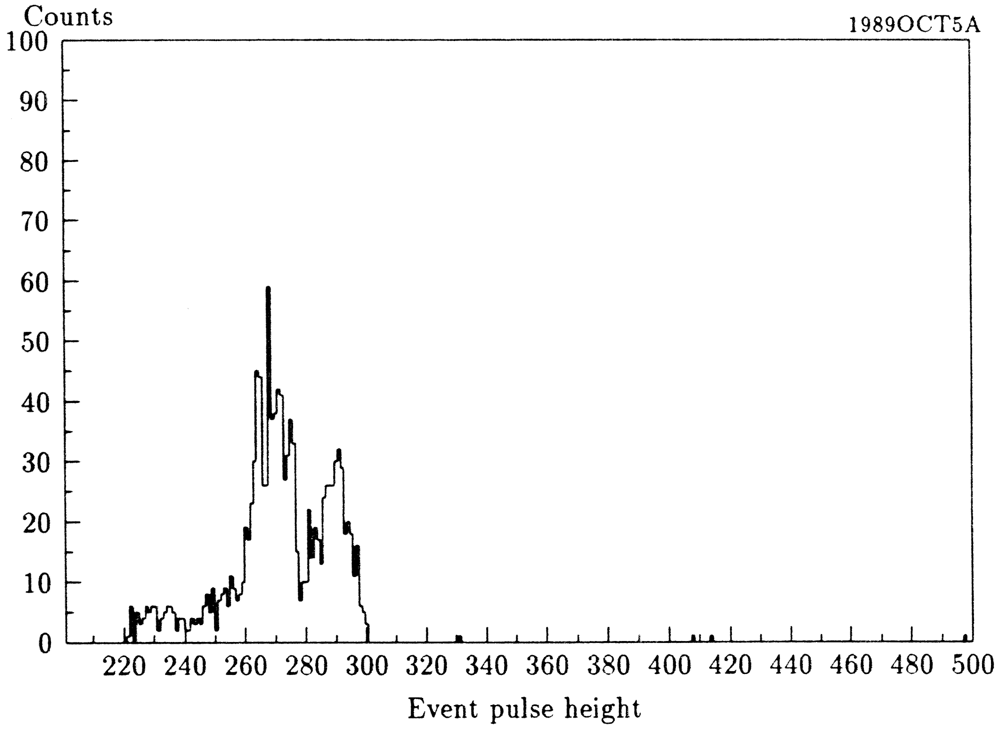

Figure 4.18: Response of the chamber when the field distribution was distorted as shown in Figure 4.17.

**Energy linearity**

In Section 4.4.1 ratios are obtained which specify the positions (channel numbers) of the $^{212}$Bi, $^{212}$Po and $^{216}$Po peaks relative to the $^{220}$Rn peak. The ratios obtained and the corresponding ratios of Q-values for the decays are given in Table 4.2. It can be seen that the ratios calculated from observed CPC pulse height spectra ($X_r$) are in approximate agreement with the ratios of the known Q-values to approximately 1%. Thus the energy linearity of the device is established over the energy range of interest.

## 4.3 Lead-shielded Ge(Li) gamma-ray detector

As an auxiliary apparatus to the CPC, a Lithium-drifted Germanium gamma-ray detector (EG&G Model GMX-25200) was used. Its principal purpose was to assay $^{228}$Th and $^{224}$Ra in forms inaccessible to CPC counting, usually in solution. It was also used for assay of other species which could not be counted with the CPC.

A Lead 'cave' was built which afforded at least 100$mm$ thickness of Lead, covering 99.7% of the solid angle around the crystal, the opening being a port for the cold finger. The sample space had dimensions W.100$mm$ x L.144$mm$ x H.260$mm$ , the dimensions chosen to contain a 1$l$ capacity vessel. The horizontal equator of the crystal casing was arranged to be 101$mm$ above the floor of the cave, to correspond roughly with the height of the centre of 1$l$ vessels of the types used to contain active solutions.

The crystal was operated at -2kV and signals from the pre-amplifier were passed through a pulse-shaping amplifier to a CATO 4k multi-channel analyser, which stored the resulting pulse height spectrum. The CATO allowed the definition of Regions of Interest (ROI's) in the spectrum — ranges of channels which were chosen to bracket gamma-ray peaks of interest. The number of counts in a peak, and hence a measure of the activity of a sample, was determined by summing the number of counts within the ROI and performing a linear background subtraction: a Compton background level was deduced from the averaged contents of channels either side of the ROI. The CATO returned this number and its 1$\sigma$ error at completion of a run. For measuring 240keV and 352keV activities, 9 channels either side of the peak were used to determine the background level. In the case of the 92keV peak due to $^{234}$Th other peaks were nearby and a more restricted, asymmetric range was used to determine background.

| $Q_\alpha$ | $X_r$ | species | $Q_\alpha/Q_{Rn}$ |
|---|---|---|---|
| 6.21 | 0.9565 | $^{212}$Bi | 0.9703 |
| 8.95 | 1.3865 | $^{212}$Po | 1.3984 |
| 6.40 | 1.0000 | $^{220}$Rn | 1.0000 |
| 6.91 | 1.0770 | $^{216}$Po | 1.0797 |

Table 4.2: Energy linearity of the CPC.

| $E_{cal}$ | Source | Typical ROI | $E_{pk}$ |
|---|---|---|---|
| 238.63 | $^{228}$Th | 275 - 289 | 238.4 |
| 351.92 | $^{226}$Ra | 417 - 430 | 352.2 |
| 609.31 | $^{226}$Ra | 739 - 753 | 609.3 |
| 1173.21 | $^{60}$Co | 1440 - 1462 | 1173.1 |
| 1332.47 | $^{60}$Co | 1639 - 1662 | 1332.4 |

Table 4.3: Actual line energies $E_{cal}$, sources, typical ROI's and fitted energies $E_{pk}$ of gamma-rays used for calibration of the Ge(Li) apparatus.

### 4.3.1 Energy calibration and efficiency

An energy calibration of the apparatus was achieved by fitting a quadratic form to the centroids of 5 well-identified peaks, using a function supplied by the CATO. The peaks used, and their actual and fitted energies, appear in Table 4.3, together with a long-lived parent of the radiation. A calibration good to ±0.2keV throughout the range was achieved, which was adequate for identification of additional peaks.

To obtain an absolute efficiency calibration of the crystal with a specific sample geometry, it was exposed to a standard $^{228}$Th source, known to be in equilibrium. The source geometry corresponded exactly to one of the 'standard geometries' detailed in Section 4.3.3 below (#1).

The source was $11.04 \pm 0.13$kBq $^{228}$Th in $1l$ 0.5M nitric acid. The choice of 0.5M for the acid strength was made so as to avoid as far as possible the slow plate-out of Thorium onto the container walls, since this would alter the concentration of the solution during long-term storage. A much stronger acid solution was undesirable because of the risk of slow degradation of the polyethylene container, with consequent contamination of the solution.

The $^{228}$Th was supplied by Amersham International in $5cm^3$ 0.5M nitric acid contained in a glass ampoule, but had previously been diluted, care having been taken to minimise Thorium plate-out onto the transfer syringe by rinsing thoroughly with acid[4]. The $1l$ source was counted many times for periods between $500s$ and $1500s$, and was several times repositioned during this procedure, to reflect any errors due to the necessarily finite precision with which the position of a source could be fixed. The data obtained were found to be perfectly consistent with a constant activity, given the statistical errors on the measured activities, implying that the source was repositioned with sufficient accuracy that the resulting errors were negligible.

Since the source was relatively active, the dead time of the CATO was significant, around 5–10%. This was corrected for by sending a train of pulses into the crystal's pre-amp, of sufficient amplitude as to appear in the spectrum well above natural gamma-rays. The rate

---

[4] The empty ampoule was counted and shown to contain $< 0.1\%$ of total Thorium, a much smaller fraction than the supplier's quoted uncertainty in the absolute activity. It is assumed that Thorium loss onto the syringe was very much less than this, since the solution had been stored in the ampoule for 22 months, but contacted the syringe for less than a minute.

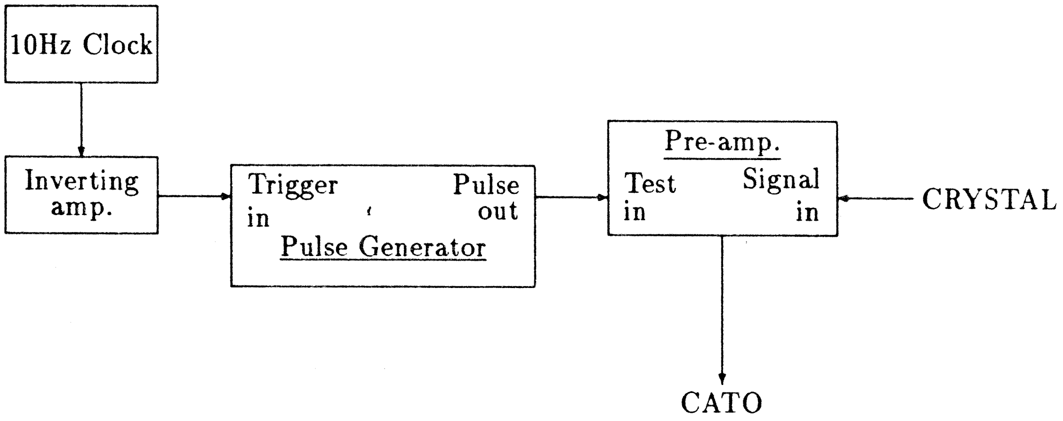

Figure 4.19: Schematic of electronics used for dead time correction during the efficiency calibration of the Ge(Li) detector.

of these pulses was controlled by a precision oscillator (HYTEC Model 95), which was used to trigger a pulse generator. The number of such pulses appearing in the spectrum thus directly measured the live time of the particular run. A schematic of the electronics is given in Figure 4.19.

The result of the efficiency calibration experiments is a rate of counting 240keV gammas from a source of known strength in a known geometry, which yields a factor K by which an observed 240keV activity must be multiplied to determine the $^{228}$Th activity in any source of the same geometry.

$$K = 182.9 \pm 3.0$$

Since the branching ratio for production of 240keV gammas is 43%, the inferred overall efficiency for detection of 240keV gammas in this counting geometry is $\simeq$ 1.3%.

### 4.3.2 Background levels.

A number of runs were performed with no active source in the cave, to determine the background level in the ROI's corresponding to the gamma-rays of most interest, *ie.* 239keV and 352keV. In the case of the $\simeq$ 240keV line, the data resulting from these runs were consistent with a constant background rate of $0.00315 \pm 0.00013s^{-1}$. However, the 352keV data were inconsistent with a constant background level, and showed clear evidence for significant $^{226}$Ra content in one of the source mountings. This period apart, the data imply a constant background rate of $0.00059 \pm 0.00012s^{-1}$. The appropriate higher background level was subtracted whenever the more active source mounting was used. A high-statistics background spectrum is shown in Figure 4.20, which also labels many of the most significant peaks by their energy in keV. The sources of these peaks are listed in Table 4.4.

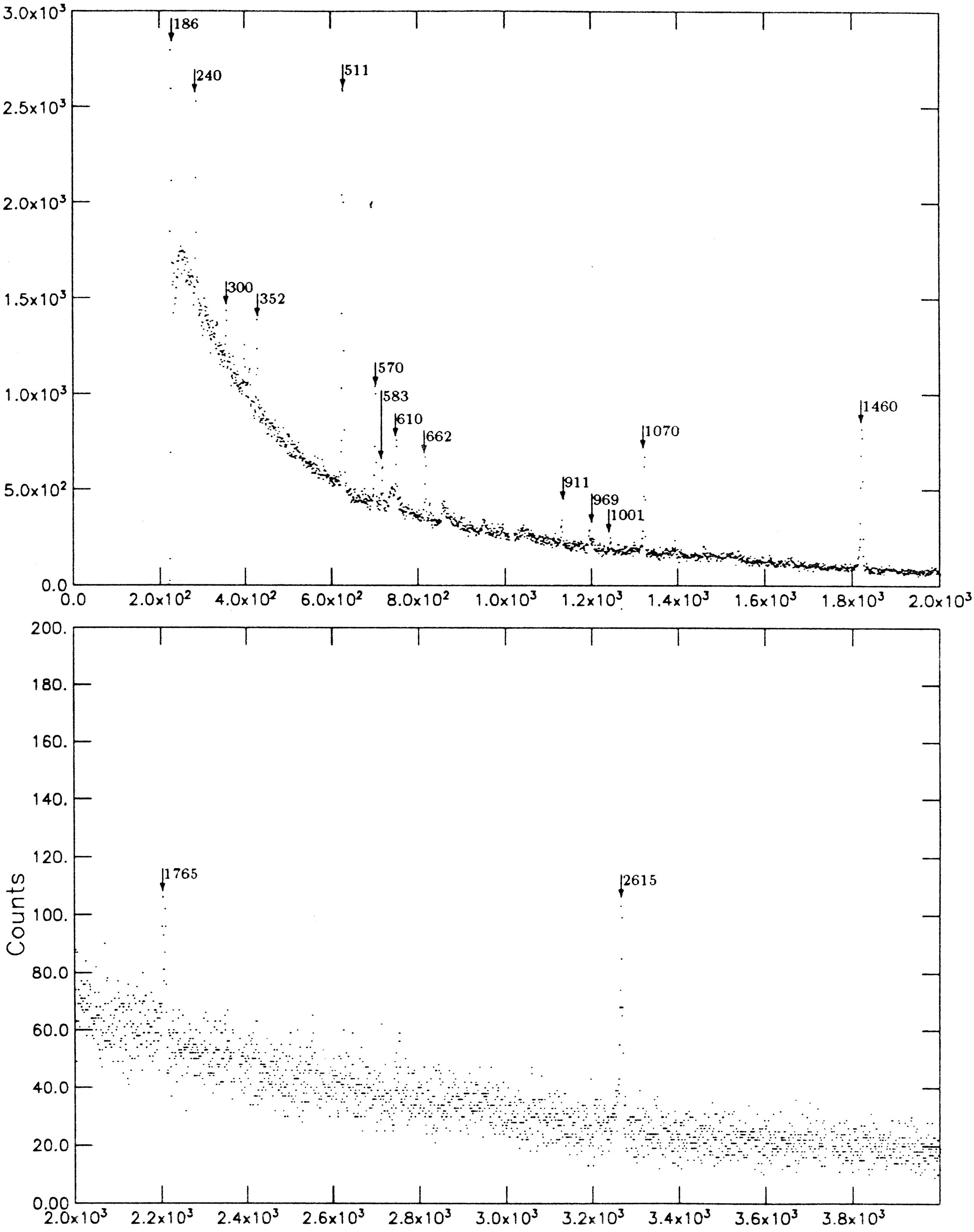

Figure 4.20: Ge(Li) detector background spectrum with peaks labelled by energy in keV

| Energy (keV) | Parent isotope |
|---|---|
| 186 | $^{235}$U |
| 240 | $^{232}$Th |
| 300 | $^{232}$Th |
| 352 | $^{238}$U |
| 511 | $e^+$ |
| 570 | $^{207}$Bi |
| 610 | $^{235}$U |
| 662 | $^{137}$Cs |
| 911 | $^{232}$Th |
| 969 | $^{232}$Th |
| 1001 | $^{238}$U |
| 1063 | $^{207}$Bi |
| 1460 | $^{40}$K |
| 1765 | $^{238}$U |
| 2615 | $^{232}$Th |

Table 4.4: Assignments of various lines in Ge(Li) background spectrum.

**Appearance of non-natural peaks**

The peaks in the background spectrum may be all attributed to natural sources (*ie.* $^{238}$U, $^{235}$U, $^{232}$Th chains and $^{40}$K) with the notable exceptions of peaks at 570keV and 1063keV. These were attributed to the decay of the 38-year half-life non-natural isotope $^{207}$Bi to a state $^{207m}$Pb which is not populated by cascades in the $^{235}$U chain, of which $^{207}$Pb is the lowest member. The history of the Lead surrounding the Germanium crystal is not known, but one reaction known to produce $^{207}$Bi is $^{208}$Pb(d,3n) [51], and other obvious candidate reactions are $^{208}$Pb(p,2n), $^{207}$Pb(p,n) and $^{206}$Pb(p,$\gamma$). Since decay of $^{207m}$Pb gives rise to both gammas in a cascade (Figure 4.21), it seems certain that some of the Lead blocks in the shield must have been irradiated by protons or deuterons, and were thus an unfortunate choice of shielding material.

A peak due to $^{137}$Cs is also visible in background. A $^{137}$Cs source was at one stage used for energy calibration, and it is assumed to have leaked slightly.

### 4.3.3 The source geometries used with the Ge(Li) gamma-ray detector, and the determination of their relative counting efficiencies.

Solutions of a number of different volumes had at various times to be assayed for $^{228}$Th and $^{224}$Ra using the Ge(Li) detector, and it was frequently necessary to compare the activities of samples of different sizes. To this end, samples were only counted in a small number of different 'standard' geometries, and a series of measurements carried out to cross-calibrate the counting efficiencies of these different arrangements.

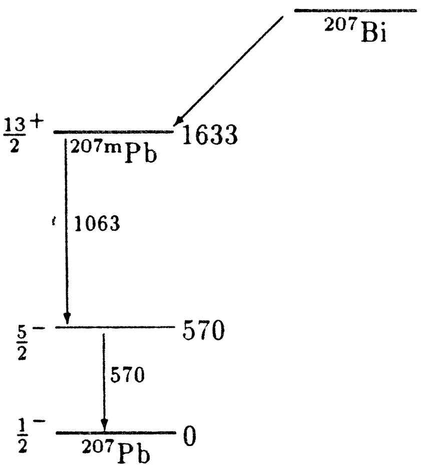

Figure 4.21: Simplified level scheme showing production of a 1063keV-570keV gamma-ray cascade following the decay of $^{207}$Bi

All the standard geometries refer to solutions held in polyethylene vessels of either circular or square cross-section: the dimensions of these vessels are given in Table 4.5. For counting, all styles of vessel (except #7 below) were placed flush against the face of the Ge(Li), and centred in the cave with respect to lateral movement. Some of the vessels were placed on blocks of heights chosen to align the crystal axis with the centre of the source, maximising the counting efficiency to be expected from the arrangement. The reference surfaces for positioning the sources were thus the Ge(Li) face, the side walls of the cave and the floor of the cave.

In order to cross-calibrate between the different geometries, a single $^{228}$Th source was prepared in 3M nitric acid. Accurately known weights were decanted from this solution into each of 7 containers, the volumes being made up to the stated capacity (in Table 4.5) with 3M nitric acid. Each of these cross-calibration sources was then placed in the Ge(Li) apparatus and the counting rate of 240keV gammas measured. Since the masses of solution in each container were known, these measurements yielded relative counting efficiencies for the various sample geometries. The count rates of 240keV gamma-rays, per gram of $^{228}$Th solution in the container, are given for each cross-calibration source in Table 4.6. These results, combined with those of Section 4.3.1, enable conversion from a 240keV count rate to a $^{228}$Th activity, for sources in any of the standard geometries.

## 4.4 Data analysis

### 4.4.1 CPC data analysis procedure

The aim of the data analysis procedure is to derive from a pulse height spectrum such as that shown in Figure 4.12 a statistic which is proportional to the number of $^{220}$Rn atoms decaying in the chamber during a run. In the simplest case, this would be the integral of the

|  | Capacity *ml* | Diameter *mm* | Side *mm* | Wall Thickness *mm* | Wall density $g.cm^{-2}$ | Elevation *mm* |
|---|---|---|---|---|---|---|
| 1 | 1000 | 90.9 |  | 1.15 | 104 | 0 |
| 2 | 1000 | 99.0 |  | 0.93 | 84 | 0 |
| 3 | 1000 |  | 80 | 0.93 | 92 | 0 |
| 4 | 100 | 60.8 |  | 1.05 | 96 | 82 |
| 5 | 200 | 60.8 |  | 1.05 | 96 | 67 |
| 6 | 500 |  | 70 | 0.8 | 73 | 48 |
| 7 | 6 | 16.6 |  | 1.4 | 110 | 72 |

Table 4.5: Definition of the standard counting geometries. The elevation given is the height above the floor of the cave to which the container is raised. Diameter/Side are outer dimensions.

| Style | Specific activity |
|---|---|
| 1 | 0.01993±0.00016 |
| 2 | 0.01846±0.00017 |
| 3 | 0.02249±0.00018 |
| 4 | 0.05438±0.00043 |
| 5 | 0.04557±0.00038 |
| 6 | 0.03332±0.00034 |
| 7 | 0.1358±0.0011 |

Table 4.6: The count rate of 240keV gamma-rays, per unit mass of $^{228}$Th solution in the sample, for each standard geometry.

spectrum between fixed limits chosen to contain the $^{220}$Rn peak. The major difficulty arose from the fact that the gas gain of the chamber varied from run to run (see Section 4.2.2), with the result that the centroid of the $^{220}$Rn peak was not always in the same position and that a fixed window was inappropriate. It was therefore necessary to determine the position in the spectrum of the $^{220}$Rn peak and then to impose a window between limits defined *relative* to this position.

The procedure adopted was to fit to the spectrum a sum of two skew, kurtosoid gaussians of the form:

$$y(x) = \sum_{i=1}^{2} A_i \exp\left[-\frac{1}{2}\left(\frac{x - X_i}{\sigma_i + \eta_i(x - X_i)}\right)^{\beta_i}\right] \tag{4.1}$$

where the parameters to be determined for each of the two peaks are the amplitude $A$, peak position $X$, 'width' $\sigma$, skewness $\eta$ and power $\beta$. If all these parameters were freely variable for each peak, this would result in a fit with 10 free parameters.

The method of maximum likelihood (see Eadie[67] or Baker and Cousins [68], for example) was used to determine the optimum parameters for each spectrum, generated by the exposure of a $^{220}$Rn source to the chamber. The likelihood function was formed from a product of Poisson distributions:

$$L = \prod_{i=236}^{310} \exp(-y_i)\frac{y_i^{n_i}}{n_i!} \tag{4.2}$$

where $y_i$ is the predicted number of events in channel $i$ ($y(x_i)$ from Equation (4.1)) and $n_i$ the measured number. This leads to the negative log-likelihood function

$$-\ln L = -\sum_{i=236}^{310} (-y_i + n_i \ln y_i) \tag{4.3}$$

as the function to be minimised. A simple least-squares fit to the theoretical curve (with implied Gaussian statistics) would have been wholly inappropriate to the present case, since the number of counts in any channel was frequently less than 10.

The MINUIT code from the CERN program library was used to locate the minimum in likelihood space and to perform the error analysis. Before the entire CPC data set could be analysed systematically, a number of modifications to the simple procedure using Equations (4.1) and (4.3) were necessary.

**Equate peak shapes** In practice, the parameters $\sigma$, $\eta$ and $\beta$ were constrained to be identical for each peak. This is reasonable if the peak shape is a consequence of the charge collection properties of the chamber, and the results of Section 4.2.3 suggest that this depends mainly on the longitudinal coordinate. Since a $^{216}$Po atom is expected to drift primarily in a radial direction after its creation, its subsequent decay should be at approximately equal $z$ to that of its $^{220}$Rn parent. It follows that the two peak shapes are expected to be broadly the same. (Acceptable fits do, indeed, result from this procedure).

Setting $\sigma_1 = \sigma_2$, $\eta_1 = \eta_2$, $\beta_1 = \beta_2$ reduced the number of free parameters from 10 to 7. The determination of the remaining parameters was carried out by fitting the spectrum in the range of channel numbers from 236 to 310, sufficient to cover all possible variations in chamber gain while comfortably containing both peaks.

**Re-parametrise** The parameters $A_2$ and $X_2$ were re-expressed as

$$\left.\begin{aligned} A_2 &= A_1/A_r \\ X_2 &= X_r X_1 \end{aligned}\right\} \qquad (4.4)$$

so that the fitted parameters were $A_1$, $A_r$, $X_1$, $X_r$, $\beta$, $\sigma$ and $\eta$. With this description, it can be seen from Equation (4.1) that $\sigma, \eta$ and $\beta$ describe the shape of both peaks, $A_r$ and $X_r$ describe their *relative* height and location, and $A_1$ and $X_1$ specify the overall scale and offset of the spectrum. Incidentally, this re-parametrisation demonstrates that the fitted function satisfies the condition given by Baker and Cousins which is sufficient for preservation of the area, *ie.* that the fitted function be expressible in a form where one of the parameters is an overall scale factor.

**Pre-condition** During trials of the fitting procedure, it was found that in sparse data sets, the numbers of events available were sufficiently small that the position of the minimum located by a seven-parameter fit was sensitive to the initial parameter values. It was found necessary to 'precondition' the fit by fixing at reasonable values the parameters $A_r$, $X_r$, $\beta$, $\sigma$ and $\eta$ which together describe the overall shape of the spectrum. The fitting procedure was then two-staged, consisting of a two-parameter fit of $A_1$ and $X_1$ using the simplex method [69], followed by re-fitting with all parameters free, using a more sophisticated algorithm due to Fletcher [70]. The first stage was found adequately to precondition the fit so that the second converged reliably to the minimum. The necessity for this pre-conditioning stage by variation of just two parameters was the reason for the re-parametrisation given in Equation (4.4).

**Fix energy scale** A trial of this procedure was conducted on a large data set. One of the results was that the fitted values of $X_r$ were found to be tightly clustered about 1.077 with standard deviation $\simeq 10^{-3}$. The sharpness of this distribution suggested that this parameter could be regarded as a constant: adopting this practice was equivalent to letting the $^{220}$Rn peak establish the energy scale and using this to deduce the position of the $^{216}$Po peak. $X_r$ was thus fixed at 1.077 and no longer regarded as a free parameter.

**Fix skewness** In the same set of trials, it was found that the three parameters $\sigma$, $\eta$ and $\beta$ were very highly correlated amongst themselves; correlation coefficients greater than 0.99 were common. It was clear that the available data were not fixing these parameters, *ie.* that at least one of them was redundant. The skewness $\eta$, as the least variable of the three, was therefore fixed at a typical value, and no longer regarded as a free parameter.

**Correct for residual $^{212}$Pb** The presence of residual $^{212}$Pb in the chamber gave rise to a peak close to $^{220}$Rn (see Section 4.2.3 and Figures 4.14 and 4.15). The consequences of this were:

(a.) A window chosen to bracket the $^{220}$Rn peak unavoidably included part of the $^{212}$Bi peak.

(b.) The $^{212}$Bi peak also constituted a shoulder on the $^{220}$Rn peak. Since the $^{220}$Rn peak and $^{216}$Po peak are constrained in the fitting procedure to have equal widths $\sigma$, this distortion of the $^{220}$Rn peak shape leads to an incorrect fit — the fitted value of $X_1$ is biased low.

These two effects were both compensated for by making use of the $^{212}$Po peak which necessarily accompanies the $^{212}$Bi peak. From the amplitude of the $^{212}$Po peak in a given data set, an estimate of the amplitude of the unresolved $^{212}$Bi peak was obtained. An estimate of the $^{212}$Po peak amplitude was obtained thus:

1. The spectral region between channels 340 and 400 was modelled by a skew Gaussian:
$$A_{Po} \exp\left[-\frac{1}{2}\left(\frac{x - X_{Po}}{\sigma_{Po} + \eta_{Po}(x - X_{Po})}\right)^{\beta_{Po}}\right] \tag{4.5}$$
in which the low statistics generally available precluded allowing $\sigma_{Po}$, $\eta_{Po}$ or $\beta_{Po}$ to vary. They took values obtained by fitting a high-statistics $^{212}$Po peak.
2. The variable $X_{Po}$ was not fitted as a free parameter, the statistics being sufficiently low that random clusters of events could seriously distort the fit. Instead, the $^{220}$Rn peak position, $X_1$, was taken as providing the energy scale and the $^{212}$Po peak position was fixed relative to $X_1$ by an expression of the form
$$X_{Po} = const \times X_1 \tag{4.6}$$
This constant was determined empirically from several data sets which exhibited substantial $^{212}$Po peaks, so that $X_{Po}$ could be accurately determined for each, and also high $^{220}$Rn activities, so that the presence of $^{212}$Bi events did not appreciably distort the $^{220}$Rn fit. The value of this constant was determined to better than 1%.
3. The low level of $^{212}$Po in most runs was such that the noise rate in the $^{212}$Po window was frequently comparable to the rate of genuine events, with the result that an independent estimate of the former was required. This noise rate, or 'high-energy background', was estimated by averaging over 100 channels chosen to be above the $^{212}$Po peak: channels 401–500 were used.
4. For each data set the region of the spectrum between channels 340 and 400 was thus fitted to a function of the form:
$$A_{Po} \exp\left[-\frac{1}{2}\left(\frac{x - X_{Po}}{\sigma_{Po} + \eta_{Po}(x - X_{Po})}\right)^{\beta_{Po}}\right] + B_{HE} \tag{4.7}$$
in which $A_{Po}$ was the only free parameter, the high-energy background being determined from step 3. Taking account of $^{212}$Bi activity thus required that

an extra parameter be introduced into the fit. However, this parameter was largely determined by the data in channels 340–400 and was, as such, very weakly correlated with the remaining parameters: its inclusion was found not to affect the precision of their determination.

Having obtained an estimate of $A_{Po}$, the amplitude and position of the $^{212}$Bi peak were required. They were determined relative to those of $^{212}$Po from several data sets in which significant $^{212}$Pb-derived activities were present, but no significant $^{220}$Rn (such as Figure 4.13). From this analysis, the relative amplitude of the two peaks, $A_{BP}$, was determined to 10% and the ratio of the peak locations to better than 1%. Since in the fitting procedure $X_{Po}$ was determined from $X_1$, $X_{Bi}$ thus also stood in a known relation to $X_1$. We therefore have

$$\left.\begin{aligned} A_{Bi} &= A_{BP}A_{Po} \\ X_{Bi} &= X_{BR}X_1 \end{aligned}\right\} \tag{4.8}$$

where $A_{Po}$ and $X_1$ are determined from the data and $A_{BP}$ and $X_{BR}$ are determined from independent data sets.

Having fitted the $^{212}$Po peak amplitude, a set of estimated parameters $A_{Bi}$, $X_{Bi}$, $\sigma_{Bi}$, $\eta_{Bi}$ and $\beta_{Bi}$ was obtained for the $^{212}$Bi peak, where the shape parameters again were obtained from a high-statistics data set. A term

$$A_{Bi}\exp\left[-\frac{1}{2}\left(\frac{x - X_{Bi}}{\sigma_{Bi} + \eta_{Bi}(x - X_{Bi})}\right)^{\beta_{Bi}}\right] \tag{4.9}$$

was therefore added to the fitting function (4.1) in the likelihood maximisation procedure. Thus the distortion of the fit by the $^{212}$Bi activity was duly accounted for.

**Correct for $^{212}$Po tail** The tail of the $^{212}$Po peak extended under the $^{220}$Rn peak and so gave rise to a final correction. A relation of the form

$$A_{tail} = A_{TR}A_{Po} \tag{4.10}$$

between the $^{212}$Po peak amplitude and the amplitude of its tail was used. The constant of proportionality was determined to about 13% accuracy from a high-statistics data set. The sum of this constant background and the background deduced by averaging above the $^{212}$Po peak (under step 3 above) was included as a constant term added to Equation (4.1).

With all the above modifications in place, the function fitted to channels 236–310, around the $^{220}$Rn peak, was

$$\begin{aligned} y(x) &= \sum_{i=1}^{2} A_i \exp\left[-\frac{1}{2}\left(\frac{x - X_i}{\sigma + \eta(x - X_i)}\right)^{\beta}\right] \\ &+ A_{Bi}\exp\left[-\frac{1}{2}\left(\frac{x - X_{Bi}}{\sigma_{Bi} + \eta_{Bi}(x - X_{Bi})}\right)^{\beta_{Bi}}\right] \\ &+ B_{HE} \\ &+ A_{TR}A_{Po} \end{aligned} \tag{4.11}$$

in which the free parameters were $A_1$, $X_1$, $A_r$, $\sigma$, $\beta$ and $A_{Po}$. The function fitted to channels 340–400, around the $^{212}$Po peak, is given in Equation (4.7). A typical example of the results of the fitting procedure is given in Figure 4.22.

The error assigned to each parameter was the appropriate diagonal element of the covariance matrix. This assignment contains the implicit assumption that the likelihood function is closely parabolic in the neighbourhood of the minimum — an assumption checked in detail for the critical parameter $X_1$ and found to be valid.

The window used for integrating the $^{220}$Rn peak was chosen to extend 7 channels above $X_1$ and 18 channels below. The number of counts due to $^{220}$Rn decay in the chamber was assigned to the integral over this window, corrected for backgrounds evaluated as above:

$$\begin{aligned} N_{cts} &= \sum_{i=X_1-18}^{X_1+7} n_i \\ &- A_{Po}A_{BP}\int_{x=X_1-18}^{X_1+7} \exp\left[-\frac{1}{2}\left(\frac{x-X_{Bi}}{\sigma_{Bi}+\eta_{Bi}(x-X_{Bi})}\right)^{\beta_{Bi}}\right] dx \\ &- 25(B_{HE}+A_{TR}A_{Po}) \end{aligned} \tag{4.12}$$

It is clear from Figure 4.16 that only a fraction of $^{220}$Rn decays in the chamber appear in the peak, and furthermore that the $^{220}$Rn peak includes part of the $^{216}$Po tail. If the chamber was operated reproducibly, these effects were the same for each run and may be absorbed into the overall efficiency.

In addition to good data sets, the fitting procedure was also applied to data sets for which the chamber was known to be operating incorrectly (*eg.* due to gain drift or incorrect voltages applied to the copper pipes). In every case, the observed fit was poor or contained unphysical values of the parameters. Although it was possible within MINUIT to impose boundaries on allowable values of a parameter, this was not done so that poor fits would be readily apparent. Data sets which yielded poor fits were excluded from the results presented herein by applying cuts on the fitted parameters.

### Window sensitivity tests

Since the tail of the $^{220}$Rn peak has no sharp lower limit, the position of the lower bound in the likelihood product (Equation (4.2)) is arbitrary. The data acquisition software imposed a cut in the data at channel 221 to avoid contamination of the data resulting from the tail of the $^{241}$Am peak, which usually counted at a higher rate ($1.55s^{-1}$) than $^{220}$Rn in the chamber. This sets a lower bound on the extent of the fitting window, and does not allow fitting of very much of the $^{220}$Rn/$^{216}$Po tail. Furthermore, it was observed while performing trial fits that the $\Xi^2$ per degree of freedom improved[5] when data below channel 230 were excluded, *ie.* that the skew gaussian is not a good fit to an extended, essentially flat, tail.

In view of the arbitrary nature of the choice of lower window bound, the sensitivity of the crucial fitted parameter, $X_1$, to this variable was investigated. A substantial data set

---

[5] $\Xi^2$ is defined by Baker and Cousins, who refer to it as $\chi^2_{\lambda,p}$, and is a goodness-of-fit measure appropriate to Poisson statistics.

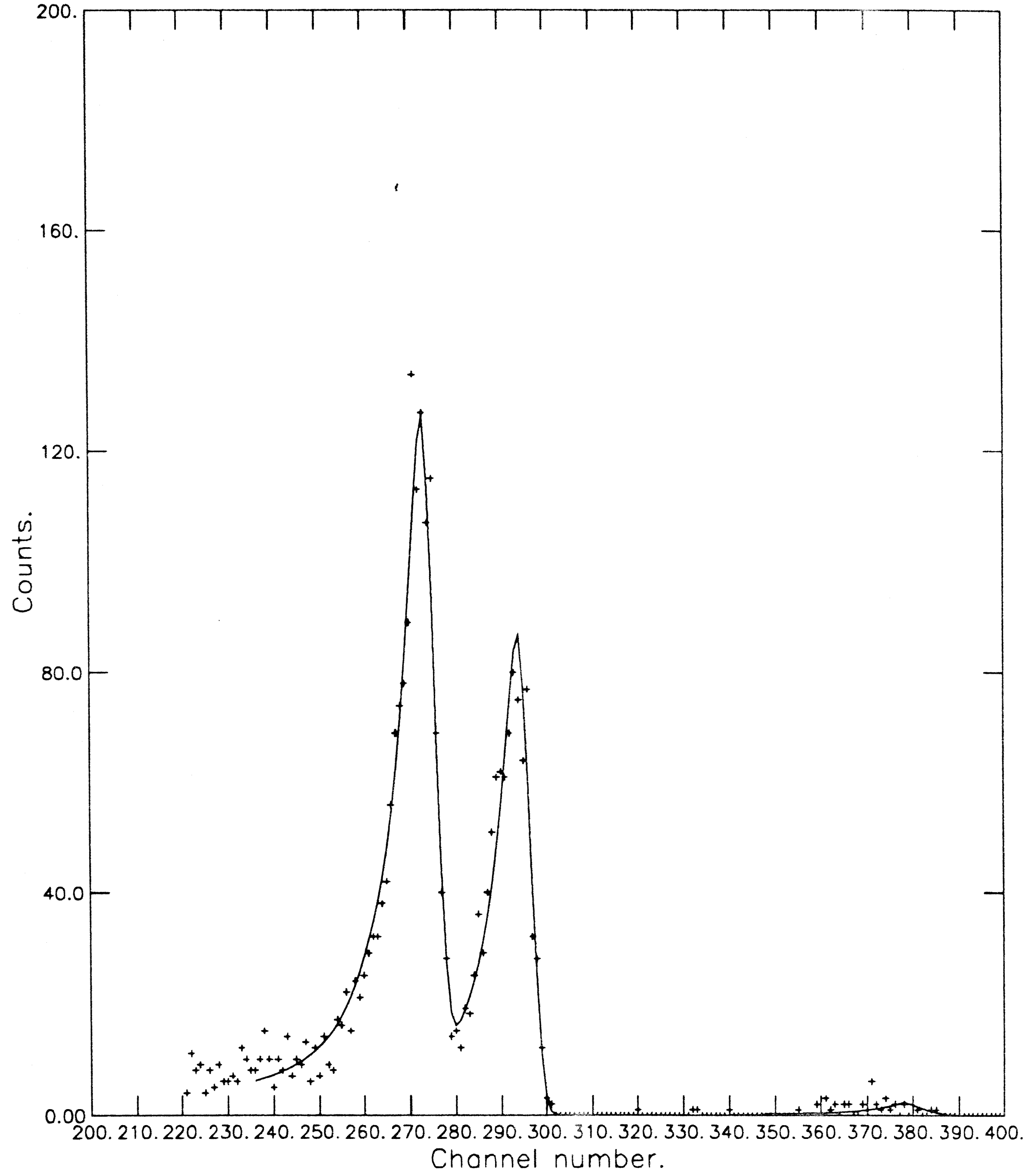

Figure 4.22: Typical CPC output spectrum and fitted curve, showing small $^{212}$Pb contamination.

(167 separate CPC runs) was analysed three times, with the lower bound set at channels 231, 236 and 241 in turn (236 being the standard value adopted for the analyses presented herein). The choice of a five-channel separation in these limits was arbitrary, but was chosen to be larger than the range over which $X_1$ was observed to vary. The test thus mimics the effect of poorly-reproducible chamber gain moving the peaks with respect to a fixed window.

A 'standard' value $X_{236}$ was defined as the value of $X_1$ when the lower window bound was 236: $\hat{\sigma}$ was defined as the standard deviation of this quantity. $X_{231}$ and $X_{241}$ were defined similarly. The histograms in Figure 4.23 plot the quantities $(X_{231} - X_{236})/\hat{\sigma}$ and $(X_{241} - X_{236})/\hat{\sigma}$ as abscissae and number of data sets as ordinate. It may be seen that the movement is generally less than $0.2\hat{\sigma}$.

It was also verified, for a trial data set, that the variation in $N_{cts}$ which resulted from substituting $X_1 \pm \hat{\sigma}$ for $X_1$ in Equation (4.12) was smaller than the $\sqrt{N_{cts}}$ statistical error, generally by a factor of 20 or more. This therefore strictly limits to not more than a 1% effect the importance of window sensitivity of $X_1$ with respect to determining $N_{cts}$.

### Error Analysis

The quantity $N_{cts}$, as defined in Equation (4.12), is a well-defined function of the numbers of events $n_i$ in the bins of a pulse height spectrum, and as such is not subject to any error. In this section and hereafter, $N_{cts}$, when divided by the duration of the run, is regarded as an estimator for the rate of detected $^{220}$Rn events. As an estimator, it is subject to an error.

Regarding $N_{cts}$ as an estimator of a true value $\widehat{N_{cts}}$, the major source of error is that resulting from the Poisson statistics of the sum in Equation (4.12). In all the data sets considered herein, the approximation is made that this error is Gaussian-distributed with standard deviation $\sqrt{N_{cts}}$, an approximation which is justified by the fact that $N_{cts}$ is rarely less than 100. This is in marked contrast to the individual $n_i$, where the assumption would not have been appropriate.

The other sources of error in $N_{cts}$ are those which result from the errors in the estimates of $X_1$, $A_{Po}$ and $B_{HE}$ and uncertainties in the constants $X_{BR}$, $A_{BP}$ and $A_{TR}$. From the general expression for propagation of errors [53] the overall uncertainty in $N_{cts}$ is given by

$$\begin{aligned}
\sigma^2_{N_{cts}} &= \sigma^2_{X_0} \left(\frac{\partial N_{cts}}{\partial X_1}\right)^2 + \sigma^2_{A_{Po}} \left(\frac{\partial N_{cts}}{\partial A_{Po}}\right)^2 + 2\mathrm{Cov}(X_1, A_{Po}) \left(\frac{\partial N_{cts}}{\partial X_1}\right) \left(\frac{\partial N_{cts}}{\partial A_{Po}}\right) \\
&+ \sigma^2_{A_{BP}} \left(\frac{\partial N_{cts}}{\partial A_{BP}}\right)^2 + \sigma^2_{X_{BR}} \left(\frac{\partial N_{cts}}{\partial X_{BR}}\right)^2 \\
&+ \sigma^2_{B_{HE}} \left(\frac{\partial N_{cts}}{\partial B_{HE}}\right)^2 + \sigma^2_{A_{TR}} \left(\frac{\partial N_{cts}}{\partial A_{TR}}\right)^2 \qquad (4.13)
\end{aligned}$$

in which there is clearly no correlation between the constants $X_{BR}$, $A_{BP}$ and $A_{TR}$ and the parameters $X_1$, $A_{Po}$ and $B_{HE}$. $B_{HE}$ is likewise uncorrelated with $X_1$ and $A_{Po}$, being derived from a different part of the spectrum. The quantities $\sigma_{A_{BP}}$, $\sigma_{X_{BR}}$ and $\sigma_{A_{TR}}$ are known from their separate determinations, $\sigma_{B_{HE}}$ is evaluated in the Gaussian approximation, and the quantities $\sigma_{X_1}$ and $\sigma_{A_{Po}}$ are calculated within MINUIT, along with the small covariance between these two parameters.

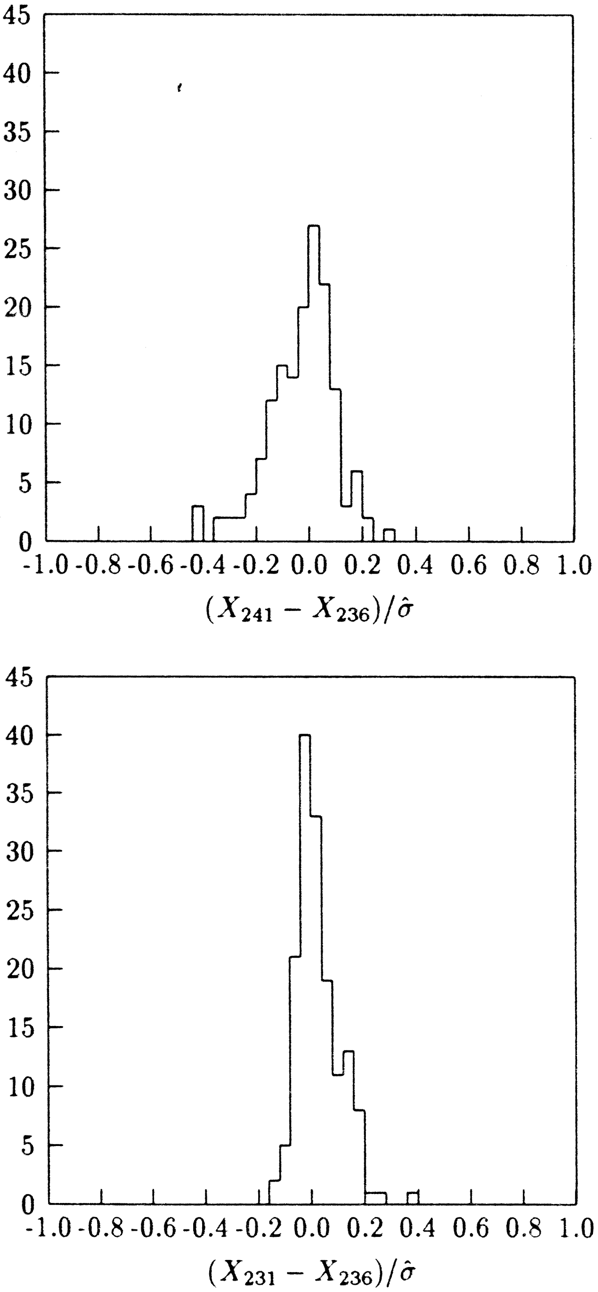

Figure 4.23: Window sensitivity of the fitted value of $X_1$.

Of the derivatives in Equation (4.13), four are trivial:

$$\left(\frac{\partial N_{cts}}{\partial A_{BP}}\right), \left(\frac{\partial N_{cts}}{\partial A_{Po}}\right), \left(\frac{\partial N_{cts}}{\partial A_{TR}}\right) \text{ and } \left(\frac{\partial N_{cts}}{\partial A_{B_{HE}}}\right)$$

and the remaining two given by:

$$\left(\frac{\partial N_{cts}}{\partial X_{BR}}\right) = -A_{Po}A_{BP}\frac{\partial}{\partial X_{BR}}\int_{x=X_1-18}^{X_1+7} S(x - X_{Bi})\,dx \tag{4.14}$$

$$\left(\frac{\partial N_{cts}}{\partial X_1}\right) = \frac{\partial}{\partial X_1}\left(\sum_{i=X_1-18}^{X_1+7} n_i\right) - A_{Po}A_{BP}\frac{\partial}{\partial X_1}\int_{x=X_1-18}^{X_1+7} S(x - X_{Bi})\,dx \tag{4.15}$$

in which $S(x - X_{Bi})$ is the skew gaussian function of Equation (4.1). To evaluate the derivatives of $\int S\,dx$ appearing in Equations (4.14) and (4.15), the integral may be transformed thus:

$$\begin{aligned}\int_{x=X_1-18}^{X_1+7} S(x - X_{Bi}) &= \int_{x'=X_1-X_{Bi}-18}^{X_1-X_{Bi}+7} S(x')\,dx' \\ &= \int_{x'=X_1(1-X_{BR})-18}^{X_1(1-X_{BR})+7} S(x')\,dx' \end{aligned} \tag{4.16}$$

in which form its dependences on $X_1$ and $X_{BR}$ are explicit. Thus

$$\begin{aligned}&\frac{\partial}{\partial X_1}\int_{x=X_1-18}^{X_1+7} S(x - X_{Bi})\,dx = \\ &\quad [S(X_1(1 - X_{BR}) + 7) - S(X_1(1 - X_{BR}) - 18)](1 - X_{BR})\end{aligned} \tag{4.17}$$

$$\begin{aligned}&\frac{\partial}{\partial X_{BR}}\int_{x=X_1-18}^{X_1+7} S(x - X_{Bi})\,dx = \\ &\quad [S(X_1(1 - X_{BR}) + 7) - S(X_1(1 - X_{BR}) - 18)](-X_1)\end{aligned} \tag{4.18}$$

The remaining differential in Equation (4.15), which gives the contribution to $\sigma_{N_{cts}}$ due to the uncertainty in the location of the window, was estimated by interpolation in the unsmoothed data.

### 4.4.2 Determination of the isotopic loadings of active sources

The object of measuring the activity of a sample, whether these measurements were made with the Cylindrical Proportional Chamber or with a Ge(Li), was always to determine the sample's initial loading of the isotopes of interest. In the former case, the relevant isotopes were $^{228}$Th and $^{224}$Ra and in the latter included $^{228}$Th, $^{224}$Ra, $^{234}$Th and $^{226}$Ra. In all cases, the method by which these quantities were determined was to observe the time evolution of the sample's activity and use this information, and the known decay properties of the isotopes (taken from [51]), to fit the data to a sum of decaying exponentials with time constants characteristic of the isotopes involved.

The method may be illustrated by the important case of the decay series

$$^{228}\mathrm{Th} \rightarrow {}^{224}\mathrm{Ra} \rightarrow {}^{220}\mathrm{Rn} \tag{4.19}$$

as monitored by the CPC. The CPC measures the rate of $^{220}$Rn production by the sample which, as noted in Section 3.3, can be used to gain information on its $^{228}$Th and $^{224}$Ra loadings, by making measurements over a suitable period. In principle two measurements, the first made immediately after the creation of the sample and the second after several $^{224}$Ra half-lives, would suffice to determine the sample's initial loading of both $^{228}$Th and $^{224}$Ra.

In practice, it was necessary to perform many activity measurements on any given sample. The first, trivial, reason for this was that the precision of the measurements was necessarily finite, and the second that it was rarely possible to measure the activity of a sample *immediately* after its creation (for example, $MnO_2$ samples had to be dried before exposure to the CPC). This second consideration implied that it was necessary to extrapolate back to the zero of time (the time of the sample's creation) from a series of measurements in order to determine the initial activity. Since the information concerning the sample's $^{224}$Ra loading was only available shortly after a sample's creation, most CPC samples were counted on the day following their creation and again on the following day, to make the extrapolation as reliable as possible.

The activity of a $^{228}$Th/$^{224}$Ra sample, as a function of time, was represented by an expression of the form

$$A(t) = a_1 \exp(-\lambda_{^{228}Th} t) + a_2 \exp(-\lambda_{^{224}Ra} t) \tag{4.20}$$

and it is trivial to show that

$$\left.\begin{array}{rcl} A_{Th} & = & \frac{\lambda_{Ra}-\lambda_{Th}}{\lambda_{Ra}} a_1 \\ A_{Ra} & = & a_2 + a_1 \end{array}\right\} \tag{4.21}$$

(In Equation (4.21) the subscripts *Ra* and *Th* refer throughout to $^{224}$Ra and $^{228}$Th). Hence if a series of activity measurements are fitted to a function of the form (4.20), the fitted parameters determine the *initial* loadings of the two isotopes $A_{Th}$ and $A_{Ra}$.

Another common case, the decay scheme

$$^{226}\mathrm{Ra} \rightarrow {}^{222}\mathrm{Rn} \rightarrow \cdots \rightarrow {}^{214}\mathrm{Pb} \rightarrow {}^{214}\mathrm{Bi}$$

was monitored by gamma-rays from the decays of $^{214}$Pb and $^{214}$Bi. Since the half-lives of these isotopes and that of $^{218}$Po are all short compared to that of $^{222}$Rn, and short compared to the duration of any exposure of a $^{226}$Ra-loaded sample to a Ge(Li) detector, the rate of production of these gammas can be regarded as an indicator directly of the activity of $^{222}$Rn. The situation is thus exactly analogous to that of the decay scheme (4.19), expressions analogous to (4.20) and (4.21) hold, and an identical fitting procedure was used.

A more complex case was the gamma-ray monitoring of the decay series

$$^{228}\mathrm{Th} \overset{1.91y.}{\rightarrow} {}^{224}\mathrm{Ra} \overset{3.66d.}{\rightarrow} \cdots \rightarrow {}^{212}\mathrm{Pb} \overset{10.6h.}{\rightarrow} \tag{4.22}$$

In this case the half-life of $^{212}$Pb, whose decay gives rise to the 240keV gamma used as a monitor, is not short compared to the time between the sample's creation and its first measurement. The effect had to be accounted for and a three-parameter fit to an expression of the form

$$A(t) = a_1 \exp(-\lambda_{^{228}Th} t) + a_2 \exp(-\lambda_{^{224}Ra} t) + a_3 \exp(-\lambda_{^{212}Pb} t) \qquad (4.23)$$

was carried out in such cases. It is again trivial to show that

$$\left.\begin{array}{lcl} A_{Th} & = & \frac{(\lambda_{Ra}-\lambda_{Th})(\lambda_{Pb}-\lambda_{Th})}{\lambda_{Ra}\lambda_{Pb}} a_1 \\ A_{Ra} & = & \frac{\lambda_{Pb}-\lambda_{Ra}}{\lambda_{Pb}} a_2 + \frac{\lambda_{Pb}-\lambda_{Th}}{\lambda_{Pb}} a_1 \\ A_{Pb} & = & a_3 + a_2 + a_1 \end{array}\right\} \qquad (4.24)$$

for the initial $^{228}$Th, $^{224}$Ra and $^{212}$Pb activities.

In contrast to the case of the CPC data sets where the individual histogram bins generally had too few counts for a Gaussian approximation to Poisson statistics to be valid, the integrated number of counts due to an activity measurement was sufficiently large (typically several hundred) that the approximation was reasonable. Thus for fitting a series of timed activity measurements on a sample to a sum of exponentials, the least squares fitting procedure (see Press *et al.* [52] or Bevington [53] for example) was always used.

From the Equations (4.20) and (4.23) above, it is clear that the fitting problem is linear in the $M$ parameters and may be expressed in the form

$$A(t) = \sum_{k=1}^{M} a_k X_k(t) \qquad (4.25)$$

where the functions $X_k$ are in this case decaying exponentials. This linear problem admits of an exact solution, obtained by inversion of the design matrix

$$\alpha_{kj} = \sum_{i=1}^{N} \frac{X_j(t_i) X_k(t_i)}{\sigma_i^2}$$

where the sum is over $N \geq M$ observations. The standard errors of the estimated parameters are given by the diagonal elements of the inverted matrix. The initial activities of the isotopes were determined from the fitted parameters using Equation (4.21) and Equation (4.24) taking due account of the correlations between the fitted parameters. The fitting procedure was performed by two independent codes as a precaution against coding errors. Identical results were obtained.

### The treatment of background subtraction

Equations which describe the time evolution of a sample's activity as a sum of exponentially decaying terms contain the implicit assumption that the activity decays eventually to zero. It follows that such expressions do not in fact describe a sequence of measured activities of a sample, since the limit as $t \to \infty$ of such a sequence is equal to the detector background and is thus non-zero. To apply equations such as (4.20) to a sequence of measured activities thus requires that detector background be subtracted from each activity measurement before fitting.

The alternative procedure — that is, directly fitting the measured activities to the expression and then subtracting background from the inferred initial isotope loadings — can be seen to be incorrect since the algorithm will find the curve which best fits the data points but which is forced to tend asymptotically to zero, and this will distort the fit if a correct extrapolation from the data is non-zero. The difference between the isotopic loadings of the sample inferred from correct and incorrect procedures is small if the measured activities are large compared to background and measurements are only made during a period short compared to the longest relevant half-life. (This was often, but not always, the case). In the converse case, however, where low-activity samples are monitored over a period sufficient for their activity to change by a substantial factor, the two procedures can yield *very* different answers.

The uncertainty in the detector background is combined quadratically with the uncertainty in the fitted isotope loadings after fitting. The alternative — combining it individually with the uncertainty of each data point before fitting — is clearly incorrect.

## 4.5 Ge(Li)/CPC efficiency cross-calibration

Measurements are reported in this section which establish the counting efficiency of the CPC2 relative to the Ge(Li). Since the absolute efficiency of the latter was determined, as described in Section 4.3.1, by exposure to an absolutely calibrated source, the absolute efficiency of the CPC is thus determined.

The basic method used was to count the same $MnO_2$ samples in both systems. The Ge(Li), however, was used to count samples of a number of different sizes: the only one which was suitable for this experiment was the smallest, Style #7, since active $MnO_2$ samples never exceeded a few $cm^3$ volume. A cross-calibration was thus established between the CPC and this Ge(Li) geometry. The other geometries were related to this one by the measurements described in Section 4.3.3.

A set of $MnO_2$ samples was selected for use as cross-calibration sources between Ge(Li) and CPC. The criteria for the selection were:

1. that the samples be relatively active so as to afford good counting statistics,
2. that they be big enough to fill a $6ml$ capacity 'Style #7' container (described in Section 4.3.3), and
3. that their CPC count rates had previously been well determined.

A large number of old CPC sources was available from which the selection could be made, and a suitable set was found. (They were in fact B columns from the flow rate trials reported in Section 5.2). Each of four $MnO_2$ samples was divided into three, of accurately known weights. Two of each three samples were sufficiently large to fill a Style #7 container and were therefore acceptable. The sample set selected thus consisted of eight samples in total.

Each sample was counted in the Ge(Li) apparatus and yielded a count rate of 240keV gamma-rays. For comparison with the CPC rates, the Ge(Li) rates were corrected for two factors:

1. the fraction of the original CPC sample making up each Ge(Li) sample, and
2. the elapsed time between the samples' exposures to Ge(Li) and CPC.

After these corrections, the Ge(Li) and CPC rates should have been proportional, obeying a relation of the form

$$A_{CPC} = R \times A_{Ge(Li)} \tag{4.26}$$

the constant of proportionality, $R$, being the relative efficiency of the two systems. This was only found to be the case when the CPC activities were corrected for background, which was known much less accurately than the 240keV background in the Ge(Li) apparatus.

A straight-line least-squares fit was thus performed on CPC count rate *vs.* corrected Ge(Li) count rate. As noted in Section 4.4.2, subtraction of a background rate from the fitted parameters of a decaying exponential is invalid: background subtraction must be performed before fitting. The CPC count rates to be compared with the Ge(Li) count rates were thus non-linear in the assumed CPC background rate, $B$, and the straight-line fit was not trivial. The general minimiser MINUIT was used to select values of $R$ and $B$, pass $B$ to the exponential fitter and receive back values of $A_{CPC}$ for each sample. It then evaluated $\chi^2$ for the straight-line fit and varied $R, B$ to achieve a minimum. The values obtained were:

$$\begin{aligned} R &= 7.20 \pm 0.12 \\ B &= (-5.1 \pm 2.6) \times 10^{-3} \end{aligned}$$

This result, together with those of Sections 4.3.1 and 4.3.3, enable calculation of a measure of overall effectiveness of the CPC: the result is that the device counts $^{220}$Rn events at a rate of

$$(26.83 \pm 0.70) \times 10^{-2} \, \frac{s^{-1}}{Bq}$$

where the unit is $^{220}$Rn events per second per Becquerel. This ratio is an overall $^{220}$Rn counting efficiency. To deduce an efficiency for the CPC *per se*, other effects which have to be included are the $^{220}$Rn extraction efficiency from the source (Section 5.1), the dead volumes between source and chamber and the different gamma-ray attenuations of water and $MnO_2$–loaded acrylic beads (since it was assumed that a $MnO_2$ sample counted equally efficiently in the Ge(Li) apparatus as a solution of the same shape and size). Taking these effects into account, the efficiency of the CPC for counting $^{220}$Rn atoms reaching its inlet port is around 45%.

The factor $R$ given above is crucial in allowing the free intercomparison of sources of different types (solutions counted in the Ge(Li) apparatus and $MnO_2$ samples with the CPC), and this was essential for the analysis of the flow rate trials presented in Section 5.2.

# Chapter 5

# Investigations into Manganese Dioxide as a sorbent for SNO

## 5.1 The de-emanation of $^{220}$Rn from small $MnO_2$ samples

The proposed method of counting the absorber samples which have been used for extraction of $^{228}$Th and $^{224}$Ra from water in the SNO detector is the de-emanation of $^{220}$Rn from the dried samples into a large-volume proportional chamber. A counter gas is to be passed through the sample and into the chamber: while passing through the sample, $^{220}$Rn is entrained by the stream and carried into the chamber where the $0.15s$ coincidence between $^{220}$Rn and $^{216}$Po alpha decays should be easily observable. Only $^{224}$Ra and $^{228}$Th may be assayed by this method.

The design of the apparatus is dictated by the relatively short half-life of $^{220}$Rn — $55s$. For good counting efficiency it is necessary to remove the gas from the $MnO_2$ sample container in well under a minute, to transfer it to the chamber also in well under a minute, and to hold the gas in the chamber for a time long compared to one minute. These requirements are reconciled by using a chamber of large volume. The intended counter is of $50l$ volume, so that the gas flow rate cannot be much higher than $20l\,min^{-1}$. The proposed absorber volume is $10l$ so the gas flow rate should ideally be considerably larger than $10l\,min^{-1}$. Neglecting dead volumes associated with pipework connecting sample to detector, it is clear that the best compromise is a flow rate of a few bed volumes per minute. This argument will be made quantitative later in this section.

The possibility exists that that there might be a tendency for Radon atoms to adhere to $MnO_2$ surfaces. The basis for this supposition is that Radon is the most polarisable of the noble gases and electric fields near the $MnO_2$ surface might be sufficient for it to be bound, however weakly. Thus, after release of a Radon atom from a surface, repeated re-adsorption onto another surface, followed by release at some later time, would increase the effective residence time of a Radon atom within the sample and decrease the fraction extracted.

The other obvious factor influencing the de-emanation efficiency is the initial probability of escape of a Radon atom from the absorber surface. The crudest model of this process envisages $^{220}$Rn produced by the decay of $^{224}$Ra on a plane absorber surface. The alpha decay results in a recoil energy of the Radon atom of about 100keV: we may suppose that this is directed either into or out of the surface of the absorber and that if inwards-directed then the Radon atom does not escape from the surface. On the basis of this model an escape probability of 50% is expected.

In view of the fact that the $^{220}$Rn extraction efficiency from an absorber column could not be assumed to be 100% , it was thought necessary to determine this quantity, and also to search for evidence of re-adsorption. Furthermore, the possibility of re-adsorption has profound consequences for the interpretation of data from the 'flow-rate' trials (reported in Section 5.2) which were performed to determine the speed of extraction of Thorium and Radium onto $MnO_2$ beads. Since the $MnO_2$ samples in question were counted using Radon de-emanation, and since they came in two different sizes (about 0.3g and about 10g), sufficiently strong re-adsorption would result in differing efficiencies for counting samples of the two different sizes, and invalidate conclusions based on the assumption that counting efficiency did not depend on sample size.

The samples resulting from flow rate trials were de-emanated into the CPC using a flow of about $1l\,min^{-1}$of Argon/10% $CH_4$ independent of sample size: thus is was most important to test this flow rate and the above sample sizes, although these parameters are not the values of most relevance to SNO.

### 5.1.1 Experimental

In order to determine the $^{220}$Rn extraction efficiency from a $MnO_2$ column independently of the CPC, the 240 keV gamma-ray line in the decay of $^{212}$Pb was used as a diagnostic. In an aged $^{228}$Th-loaded $MnO_2$ source, the production rate of this gamma is determined by the (essentially constant) decay rate of $^{228}$Th. However, $^{212}$Pb lies below $^{220}$Rn in the $^{232}$Th chain so that if at times $t > 0$ $^{220}$Rn is removed from the sample, by passage through it of a flow of Ar/Me gas, then the rate of 240keV gammas produced by the sample decays with the $10.6hr$ half-life characteristic of $^{212}$Pb, since this isotope is no longer supported. It is clear that if $^{220}$Rn is extracted with less than 100% efficiency, then the level to which the 240keV activity decays is characteristic of the extraction efficiency, since the activity is then supported by the decay of $^{220}$Rn *not* extracted by the flow.

An apparatus was constructed which allowed a variety of aged $MnO_2$ samples, held in glass columns, to be placed against the face of a shielded Ge(Li) detector, as in Figure 5.1. PVC tubing connections to the top and bottom of the columns allowed gas to be passed through the column from bottom to top, as in the CPC arrangement. Downstream of the column, outside the Lead cave, one of two flowmeters could be inserted into the gas stream, which together had a calibrated range extending from about $30cm^3min^{-1}$ to $1l\,min^{-1}$of Ar/Me. Although the flowmeters were precision instruments, and had been individually calibrated by the manufacturer for air at STP, they were re-calibrated before use in these experiments with Ar/Me at room temperature and pressure, to avoid the use of uncertain corrections. A water-displacement method was used.

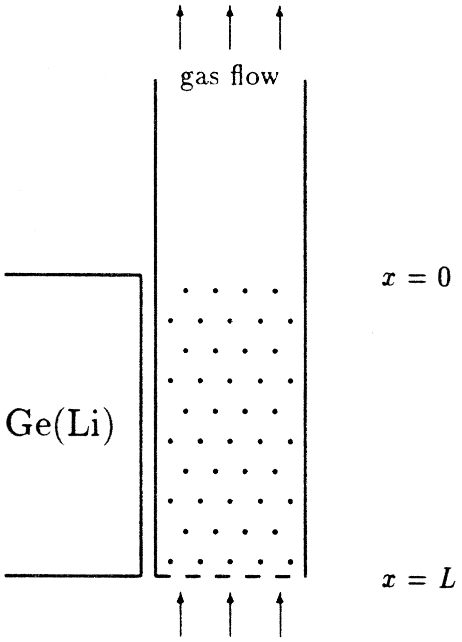

Figure 5.1: Diagram showing arrangement of $MnO_2$-loaded column during $^{220}Rn$ de-emanation efficiency measurements.

The main sequence of trials was performed by passing Ar/Me at known flow rates through $MnO_2$ beds loaded with $^{228}$Th, initially in secular equilibrium. The flow rates were controlled by varying the pressure at the regulator, and by adjustment of a PTFE needle valve upstream of the sample column. These experiments were known as 'disappearance experiments', since the Radon was *removed* from the sample column by the gas flow. Before each trial, the sample was counted several times, typically 9 or 10, for 10,000 seconds each time. This allowed the equilibrium rate of 240keV gamma counting to be determined to an accuracy of better than 1%. Ar/Me gas was then passed through the sample at a constant, known rate for about two days and the sample counted repeatedly throughout this time: the duration of the counts was again $10ks$. A series of measurements of the column's activity was thus obtained, which decayed with the $10.6hr$ half-life of $^{212}$Pb.

### 5.1.2 Results and analysis

The sources used for the $^{220}$Rn extraction experiment were $^{228}$Th sources initially in equilibrium. If, at time $t > 0$, a fraction $\eta$ of the $^{220}$Rn produced in the sample is removed, and only a fraction $(1 - \eta)$ feeds down the chain to support $^{212}$Pb, then the $^{212}$Pb activity varies with time according to the expression

$$A_2(t) = A_1 \exp(-\lambda_2 t) + (1 - \eta)A_1 \frac{\lambda_2}{\lambda_2 - \lambda_1}(\exp(-\lambda_1 t) - \exp(-\lambda_2 t)) \tag{5.1}$$

in which $A_1$ is the initial $^{228}$Th activity, $A_2$ the $^{212}$Pb activity and $\lambda_1, \lambda_2$ the decay constants of $^{228}$Th and $^{212}$Pb respectively. In the approximation that $^{228}$Th decay is insignificant during an experiment which lasts three days (*ie.* $\lambda_1 = 0$), this reduces to

$$\eta = 1 - \frac{A_2(\infty)}{A_2(0)} \tag{5.2}$$

By performing a linear least-squares fit to the activity data, the parameters $A_1$ and $(1 - \eta)A_1$ of Equation (5.1) were determined, from which the $^{220}$Rn extraction efficiency $\eta$ was easily determined, taking proper account of the covariance between the two parameters. Relatively active sources were used for these experiments, so that the number of counts recorded in the 240keV peak is typically over 2,000 in 10,000 seconds. The large number of counts performed on the samples while tracking their activity over two days resulted in accurate determinations of the extraction efficiency.

The results of the sequence of trials are collected in Table 5.1 and displayed in Figure 5.2. The Table gives percentage extraction efficiencies and Ar/Me flow rates in $cm^3 min^{-1}$ and in Bed Volumes per Minute (BVM), *ie.* the gas flow rate is reduced to a scale variable which relates to the time spent by the gas in the sample volume. The graph gives extraction efficiencies *vs.* flow rates in BVM. It can be seen from the graph that, although there is at least one outlier, the points clearly lie on a smooth curve which appears to possess an asymptote not lower than 65% extraction.

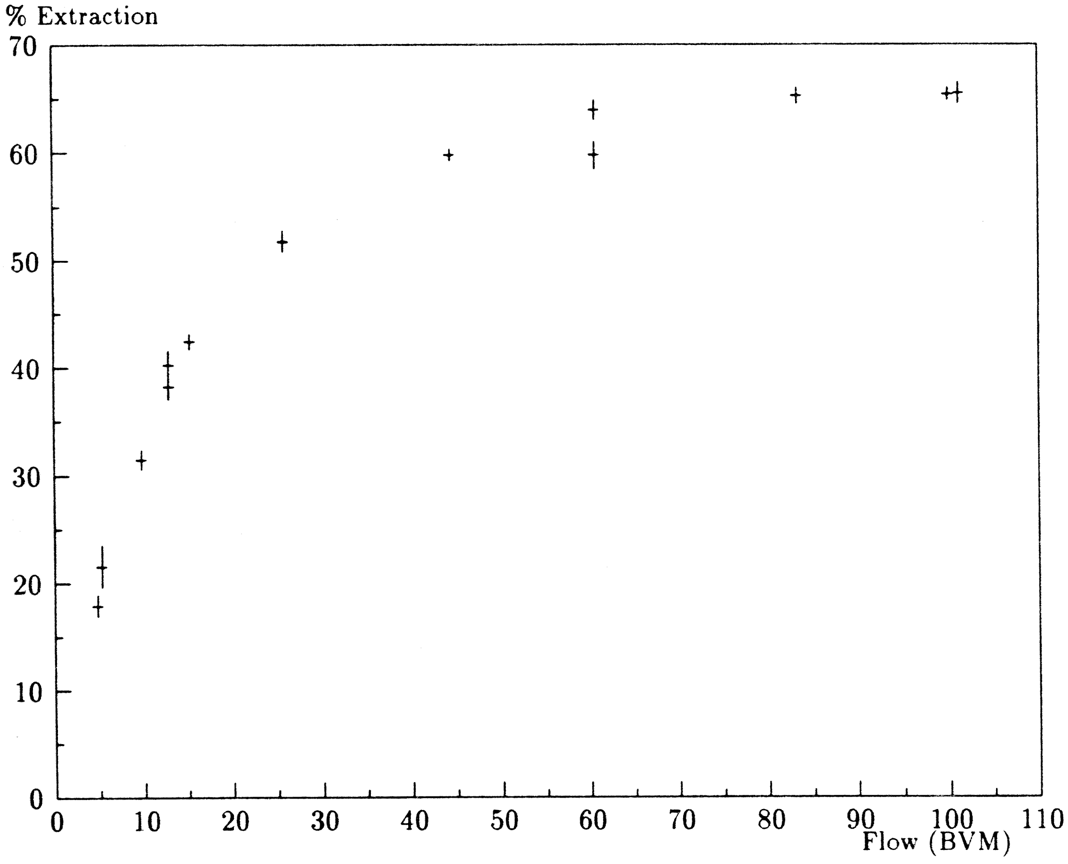

Figure 5.2: Graph of measured $^{220}$Rn extraction efficiency from $MnO_2$ samples *vs.* Ar/Me flow rate in BVM.

| Run ID | Volume | Flow rate | | $^{220}$Rn Extraction |
|---|---|---|---|---|
| | $cm^3$ | $cm^3 min^{-1}$ | BVM | Efficiency % |
| 1000-1 | 7.9 | 800 | 101.2 | $65.46 \pm 1.00$ |
| 1000-3 | 13.2 | 800 | 60.6 | $63.92 \pm 0.92$ |
| 600-1 | 13.2 | 340 | 25.8 | $51.76 \pm 0.99$ |
| 400-1 | 13.2 | 170 | 12.9 | $40.23 \pm 1.36$ |
| 400-2 | 13.2 | 170 | 12.9 | $38.21 \pm 1.17$ |
| 200-1 | 13.2 | 70 | 5.3 | $21.55 \pm 1.97$ |
| 200-2 | 13.2 | 70 | 5.3 | $21.56 \pm 1.47$ |
| 1000-4 | 13.2 | 800 | 60.6 | $59.76 \pm 1.30$ |
| 1100-1 | 13.2 | 1100 | 83.3 | $65.24 \pm 0.76$ |
| 340-1 | 13.2 | 340 | 25.8 | $51.73 \pm 0.76$ |
| 54-1 | 0.54 | 54 | 100.0 | $65.38 \pm 0.62$ |
| 24-1 | 0.54 | 24 | 44.4 | $59.81 \pm 0.59$ |
| 202-1 | 13.2 | 202 | 15.3 | $42.43 \pm 0.76$ |
| 130-1 | 13.2 | 130 | 9.8 | $31.45 \pm 0.92$ |
| 63-1 | 13.2 | 63 | 4.8 | $17.88 \pm 1.02$ |

Table 5.1: Table of $^{220}$Rn extraction efficiencies from $MnO_2$ columns *vs.* Ar/Me flow rate.

### 5.1.3 Detailed discussion

#### A simple model

In this section a simple model of $^{220}$Rn production and escape from a $MnO_2$ bed will be developed and the data of Table 5.1 will be analysed in terms of this model.

Consider the release of $^{220}$Rn atoms at a distance $x$ below the *top* of a $MnO_2$ column (as in Figure 5.1) of length $L$ and cross-sectional area $A$ (the gas flow is bottom to top). If the mean drift velocity of the gas through the column is $u$ then the fraction reaching the top of the column before decay is $\exp -x/u\tau$. The contribution from an element of length $dx$ to the total flux of Radon atoms leaving the column is thus:

$$\alpha R_0 \frac{dx}{L} \exp\left(-\frac{x}{u\tau}\right)$$

where $R_0$ is the total $^{220}$Rn production rate in the entire column and $1-\alpha$ is the fraction trapped by embedding in the surface of the $MnO_2$ due to recoil (and so never escaping). Integrating over the column length yields for the rate at which Radon atoms escape the column:

$$R_{esc} = \frac{\alpha R_0 u\tau}{L}\left[1 - \exp\left(-\frac{L}{u\tau}\right)\right] \tag{5.3}$$

We may express $u$ relative to the drift velocity in an empty column of cross-sectional area $A$

$$u \equiv \beta u_0 = \beta \frac{F}{A} \tag{5.4}$$

where $F$ is the volume flow rate of the Ar/Me gas through the column. The flow rate in BVM, however, is given by

$$B \equiv \frac{F}{AL} \tag{5.5}$$

and hence

$$\frac{R_{esc}}{R_0} = \alpha\beta B\tau \left[1 - \exp\left(-\frac{1}{\beta B\tau}\right)\right] \tag{5.6}$$

An obvious cause for $\beta \neq 1$ is the fact that the $MnO_2$ occupies most of the volume within the column so that the fractional free volume in which the gas drifts is $1 - f_p$, where $f_p$ is the packing fraction for a collection of spheres of similar but unequal diameters. This effect alone implies

$$\beta = \frac{1}{1 - f_p}$$

The importance of the parameter $\beta$ is that, if re-adsorption of $^{220}$Rn is occurring within the $MnO_2$ column, then it can be modelled by assuming that repeated adsorptions and releases occur as the atom travels up the column, with result that it spends only some fraction $\xi$ of the time free, thus multiplying its drift velocity by this factor. The parameter $\beta$ thus gives directly the degree of adsorption to which Radon atoms are subject while in a packed bed of $MnO_2$, if $f_p$ is known.

The two unknown parameters in Equation 5.6, $\alpha$ and $\beta$, were determined by non-linear least-squares fitting of the data in Table 5.1. The CERN MINUIT package was used with the following results:

$$\left.\begin{aligned} \alpha &= 0.7219 \pm 0.0050 \\ \beta &= 0.0411 \pm 0.0011 \end{aligned}\right\} \tag{5.7}$$

The $\chi^2$ of the fit indicated that it was perfectly satisfactory. The shape of the data in Figure 5.2 suggests that another possible function which may fit the data is $\alpha[1 - \exp(-\beta x)]$. This function was fitted to the same data to test its model-sensitivity and a $\chi^2$ obtained which was sufficiently large to reject the *ad hoc* function at the the 0.1% level.

### A correction

The above model gives the fraction of $^{220}$Rn atoms escaping the sample, but this is not necessarily equal to the fraction which give rise to a detectable gamma-ray in the Ge(Li) detector. The two are different if:

(a.) $^{220}$Rn daughters can escape the sample before decay, or

(b.) $^{220}$Rn daughters decay after leaving the sample, but in such a place as to be visible to the Ge(Li) detector.

Relevant daughters of $^{220}$Rn are $^{216}$Po and $^{212}$Pb. Both these species may presumably be taken to be 'sticky' *ie.* to stick to any available solid surface. If this is so, then it seems unlikely that any appreciable number of atoms of these species will escape the $MnO_2$ sample if the initial $^{220}$Rn decay occurred within it. The other effect, however, is more plausible. A

$^{216}$Po or $^{212}$Pb atom produced in the volume just above the sample may stick to the glass walls of the column and later give rise to a 240keV gamma, originating not much further from the detector than those from within the MnO$_2$. This effect is clearly of most importance at low flow rates.

The extent to which $^{212}$Pb atoms stick to the column walls is not known, but an extreme case may be considered in which every one migrates immediately, horizontally, to a wall and sticks. On this assumption, the signal in the Ge(Li) due to such atoms may be crudely estimated. We consider those $^{220}$Rn atoms which have left the absorber bed and drift up the column at a speed $u_0$, defined in Equation (5.4): let these atoms pass the plane $x = 0$, marking the upper boundary of the absorber bed, at a rate $R_{esc}$, travelling in the direction of decreasing $x$. The rate at which they are deposited onto an element of the column between $x$ and $x + dx$ is given by:

$$R_{esc} \exp\left(-\frac{|x|}{u_0\tau}\right)\frac{dx}{u_0\tau} \tag{5.8}$$

In equilibrium, after several $^{212}$Pb half-lives, the rate of decay of deposited $^{212}$Pb will be equal to the above rate of deposition. To calculate the Ge(Li) signal produced by these decays, therefore, the source is very crudely modelled by a vertical line source at the centre of the column. The detector is assumed to be at a point distant $a$ from the line source. The signal due to $^{212}$Pb decay above the absorber bed is thus:

$$S_{esc} = \frac{R_{esc}}{u_o\tau}\int \frac{\exp\left(-\frac{|x|}{u_0\tau}\right)}{x^2 + a^2} dx \tag{5.9}$$

where the integral is over an appropriate range of $x$ (see below).

To obtain from this the correction to the efficiencies tabulated in Table 5.1, we note that the quantity there tabulated is an efficiency derived from the uncorrected signal ratio:

$$\eta = 1 - \frac{S(\infty)}{S_0} \tag{5.10}$$

from Equation 5.2, where $S$ represents the rate observed in the Ge(Li) rather than the true $^{212}$Pb decay rate in the absorber sample, and $S_0$ and $S(\infty)$ are the initial and asymptotic $^{212}$Pb count rates. The required quantity, however, is not the signal ratio but the actual extraction efficiency

$$\eta' = \frac{R_{esc}}{R_0} \tag{5.11}$$

thus it is necessary to express $\eta'$ in terms of $\eta$ and the correction integral Equation (5.9).

In the spirit of taking the detector to be located at a point, we may take the initial count rate $S_0$ to be related to the (constant) $^{220}$Rn production rate in the source by:

$$S_0 = \frac{R_0}{a^2} \tag{5.12}$$

and $S(\infty)$ as the sum of two terms:

$$S(\infty) \quad = \quad \text{(Signal due to non-escaping Radon)} +$$

$$\text{(Signal due to escaping Radon)} = \frac{R_0 - R_{esc}}{a^2} + R_{esc} I \tag{5.13}$$

defining $S_{esc} = R_{esc} I$ in Equation (5.9). On substitution from Equations (5.13), (5.12) and (5.11) into (5.10) we obtain:

$$\eta' = \frac{\eta}{1 - a^2 I} \tag{5.14}$$

$a^2 I$ has been evaluated numerically for the lowest-BVM measurements, *ie.* 5BVM and 10BVM, for which the correction is clearly largest. The limits over which the integral $I$ is evaluated are taken as 2.5 and $25cm$ — the upper limit is the distance above the crystal axis at which the gas path leaves the cave and the lower limit is at the top of the column. The distance $l$ behind the Ge(Li) face at which the centre of the crystal could be considered to be located was estimated independently[1] and clearly $a = l +$ radius of column.

The estimated correction is 4% at 10BVM and 8% at 5BVM, and these might be expected to be maximum corrections, since all $^{212}$Pb has been assumed to stick immediately on production. Finally, for the 5BVM runs, and many of the higher-BVM runs, a Lead block was placed directly above the crystal to act as an absorber for gammas originating from above the absorber volume, thus further diminishing the correction. No account of has been taken of this in the above analysis, which again therefore represents an upper limit.

**Another correction**

An extraction experiment commences with a uniform distribution of $^{212}$Pb in the source volume. As the experiment progresses, the centre of this distribution must move upwards since the parent $^{220}$Rn has a steady drift velocity upwards. This effect will change the efficiency for detection of gammas from the sample at the end of the experiment with respect to its initial value. No account has been taken of this effect, which will be largest in the high-BVM cases, in contrast to the previous correction. The simple model does not warrant any such small correction.

### 5.1.4 The Appearance Experiment

The model of Radon re-adsorption clearly predicts that $^{220}$Rn entering a $MnO_2$ bed should show a tendency to stick there, rather than being freely swept through. An experiment was therefore performed in which an inactive column of $MnO_2$ is used as an absorber in a stream of $^{220}$Rn-bearing Ar/Me gas.

This situation may be analysed in terms of the simple model given in the previous section and it is easily seen that $^{212}$Pb loads the column in an exponential profile $\exp(-\frac{x}{u\tau})$, where $x$ is distance from the gas inlet to the column, and hence that the fraction escaping the column is given by

$$\frac{N_{esc}}{N_0} = \exp(-\frac{1}{\beta B_T}) \tag{5.15}$$

---

[1] A source was counted at several different distances from the Ge(Li). To the accuracy with which it was positioned, the data were a good fit to an inverse square law.

An 18.37$mm$-diameter glass column was loaded with 11.93$cm^3$ (dry volume) $MnO_2$ which had previously been treated in a similar way to the samples used in the 'flow-rate trials' reported in Section 5.2. In those trials, $^{228}$Th sources in approximately 10mM $HNO_3$ were neutralized with Sodium Hydroxide, with in some cases the addition of a buffer. For this trial, the Thorium source was replaced by an inactive 10mM $NaNO_3$ solution, but in all other respects the treatment of the column was unchanged. Thus the $MnO_2$ sample was soaked in pure water, decanted into a glass column and then 100$cm^3$ water followed by 100$cm^3$ 10mM $NaNO_3$ followed by 100$cm^3$ water were passed through it at a known flow rate. The column was then vacuum-baked overnight in order to dry it. The object of duplicating the treatment afforded the columns of the flow-rate trials was to duplicate as far as possible the surface condition of the $MnO_2$-loaded beads, inasmuch as it may be influenced by the process of wetting and then drying, with its associated expansion and contraction.

The prepared column was placed against the end-window of a shielded Ge(Li) counter, the centre of the column aligned with the crystal axis, in the same apparatus as was used for the disappearance experiments. PVC tubing was arranged so that the 0.54$cm^3$ column used in the disappearance experiments could be included upstream of this column, enabling Ar/Me gas to be passed through the smaller (source) column, entraining $^{220}$Rn in the process, and then into the 11.93$cm^3$ absorber column. The flow rate was controlled as previously, with a calibrated flowmeter and PTFE needle valve.

160$cm^3min^{-1}$ Ar/Me was passed through the two columns for 26 hours. The 240keV-gamma activity of the absorber column was continually monitored as before, by repeatedly counting for 10,000 seconds throughout the experiment's duration. The use of a small source column and a large absorber column meant that the BVM flow rates in the two were very different, being respectively 296 and 13.4, so that extraction from the source column and absorption in the absorber column could simultaneously take large values, maximising the available signal. The experiment was referred to as an 'Appearance Experiment' because, in contrast to the disappearance experiments, $^{212}$Pb activity in the column was expected to grow from zero rather than to decay.

The absorber column's 240keV-gamma activity was observed to rise during the experiment, with the expected half-life. Least-squares fitting was used to determine the asymptotic 240keV-gamma activity as $0.1155 \pm 0.0020 s^{-1}$. The curve of activity *vs.* time extrapolated back to an initial activity equal to the measured background. Substantial loading of the column with $^{212}$Pb was therefore observed.

Determination of the fractional absorption of incident $^{220}$Rn represented by the above count rate requires that a number of factors be taken into account.

1. The absorber column was placed against the Ge(Li) face, as stated above. The source column had previously been counted a number of times, also when placed against the Ge(Li) face. Since the source and absorber columns were of different diameters, the count rate expected from the absorber column given 100% absorption requires a geometrical correction. The fact that the absorber column's loading of $^{212}$Pb is non-uniform, being concentrated at the lower end of the column, nearest the gas inlet,

further complicates the counting geometry.

2. Equation (5.15) implies a 26% escape probability for $^{220}$Rn entering the absorber column, substituting $B = 13.4$ and the values of $\alpha, \beta$ deduced above. The percentage $^{220}$Rn extraction from the source is likewise well known from the disappearance experiment results, and is predicted to be 70% at 296BVM.

3. The dead volume between source and absorber columns allows time for Radon to decay before reaching the latter column: this was measured to be $28cm^3$: 11.4% of $^{220}$Rn released by the source thus decays before reaching the column.

Taking into account the dead volume between source and absorber, the 70% extraction efficiency expected from the source column, and the expected 26% escape probability from the absorber, but no correction for counting geometry, an asymptotic rate of $0.1320 \pm 0.0077s^{-1}$ is predicted, higher than that observed. The error arises mainly from the uncertainty in the source column activity.

A crude calculation was performed to estimate the geometrical correction. It was found to be more than large enough to bring the calculated and measured figures into agreement and, if taken at face value, implies that no Radon escapes the absorber column.

## 5.2 The kinetics of Thorium and Radium adsorption onto Manganese Dioxide

It is intended to use a 'packed bed' of $MnO_2$ as an absorber of trace Thorium and Radium in the water recirculation system of the SNO detector. In this section a series of measurements is reported which aim directly to determine the performance of such a packed bed with respect to adsorption of these elements.

It was shown in Section 2.5 that the flow rate at which the assay stage of the water recirculation cycle operates is a critical parameter, which determines the mass of water which can be assayed and hence the statistical accuracy of the assay procedure (the isotopes which yield information of interest are determined independently by the residence time of water in the cavity). It was clear that high flow rates, consistent with high extraction efficiency, are desirable. The measurements reported here yield information on the variation with flow rate of the extraction efficiency of Thorium and Radium by packed beds of $MnO_2$. pH was also introduced as a variable, since Moore and Reid [96] used hydrochloric acid to elute Radium from $MnO_2$-loaded fibres, demonstrating that the equilibrium constant for the sorption process may be sufficiently changed under acid conditions that the Radium desorbs. Furthermore, any critical pH dependence of the absorber's performance near pH7 would clearly render it unsuitable for use in SNO, there being no possibility of buffering the water since introduction of buffers would carry an unacceptable risk of trace contamination.

The passage of an active solution through an absorber column separates the active material into two portions: that retained on the absorber and that remaining in solution in the filtrate. The work of Moore *et al.* demonstrated that $MnO_2$ is a good sorbent for Radium under conditions of near-neutral pH, so that if a source of known strength is passed through a $MnO_2$ column under such conditions, then the effluent should be low in activity. This suggests that the most accurate measure of extraction efficiency under such conditions is the ratio of the activities of filtrate and source rather than the activity ratio of sorbent to source — the latter being near 1.0 under favourable conditions. This consideration leads to the requirement for a monitor of the Radium permeation through a $MnO_2$ bed. Since Radium extraction efficiencies $> 90\%$ have been achieved with $MnO_2$, a sufficiently large $MnO_2$ column is a possible monitor.

The procedure adopted for the determination of Thorium and Radium extraction from an active source of known pH was thus to pass a $100cm^3$ aliquot of the source through two $MnO_2$ packed beds in succession — the first containing a small mass of absorber and the second a much larger mass. The first bed thus performs the primary extraction and the second acts as a monitor of the effluent from the first bed. This procedure is subject to the objection that any activity in the source which is in some form, such as a complex, not subject to adsorption onto $MnO_2$ will permeate the first column and not be picked up by the second. Thus the procedure is only sensitive to atoms in a suitable chemical form, rather than to the total content of Thorium and Radium. This valid objection was checked, in some measurements, by retaining the permeates from the second column and using the Ge(Li) apparatus described in Section 4.3 to determine their activities. Gamma-counting is clearly insensitive to the chemical form of the active species.

The shape of the packed beds was in all cases cylindrical, the direction of flow being parallel to the axis. It was found necessary to ensure that the cylindrical packed beds had lengths much greater than their radii, since otherwise there was a tendency for the water flow to find an easy channel through the bed and displace $MnO_2$ from its path, with the result that the contact between solution and $MnO_2$ surface was poor, most of the solution simply bypassing the absorber completely. In a properly arranged cylindrical absorber bed, the water flow showed no tendency to find a preferred path and appeared to be distributed throughout the volume by capillary attraction into the interstices between neighbouring beads.

Since the trials reported in this section were intended to investigate the kinetics of the absorption process, some measure is required of the time for which the solid and liquid phases were in contact. The empirically well-known parameters were the volume rate of flow of the solution, accurately determined from the time taken for the $100cm^3$ source solution to be pumped from the reservoir, and the expanded volume of a wet resin sample, obtained from the dry mass of the resin sample used and from the known relation between dry mass and expanded volume (known from measurements on many samples). Therefore when an active solution flows through an absorber bed and is distributed uniformly through it, an empirical measure of the time for which a volume element of the solution is in contact with the absorber may be formed from the bed volume and the flow rate. Defining $\mathcal{F}$

$$\mathcal{F} = \frac{F}{V} \tag{5.16}$$

where $F$ is the rate of flow of the source solution, in $cm^3min^{-1}$, and $V$ is the volume occupied by the resin bed, in $cm^3$. $\mathcal{F}$ is thus the flow rate expressed in bed volumes per minute. The parameter used as an empirical measure of the time available for sorption of solutes onto the absorber bed was formed thus:

$$\mathcal{R} = \frac{1}{\mathcal{F}} \tag{5.17}$$

$\mathcal{R}$ is known as the Residence Time. It should be noted that it is a purely empirical number and does not correspond to the time for which a volume element is actually within the absorber bed, since the bulk of the absorber itself occupies most of the bed volume, greatly decreasing the available free volume occupied by the solution. The time for which a volume element of solution is within the absorber bed is thus determined by the packing fraction of the $MnO_2$-loaded beads when wet. This quantity was not investigated.

A further complication arises from the fact that absorption presumably occurs only at the $MnO_2$ surfaces, and the migration of dissolved ions to these surfaces from the bulk solution is governed by diffusion, and is not a process which is directly investigated by these experiments. The time for which an ion might be said to be 'near' an absorbing surface is not therefore well-defined. However, if it is established what value of $\mathcal{R}$ is required for good extraction of a given species by a given absorber, then it relates directly the flow rate of water requiring assay to the required volume of an absorber bed. $\mathcal{R}$ is thus the parameter needed for the design of the assay stage in the SNO water recirculation plant.

### 5.2.1 Procedure

For each trial, a number of pairs of glass columns containing packed beds of $MnO_2$–loaded acrylic beads were prepared. The two columns of a pair were known as the 'A' and 'B' columns. Before loading with $MnO_2$, each column had been subjected to the cleaning procedure given in Section 4.2.3 to minimise the risk of cross-contamination between trials. The A column was a 5.85$mm$ bore borosilicate glass tube of approximately 150$mm$ length with a constriction about 20$mm$ from one end. The $MnO_2$ sample was retained above a plug of acrylic wool which was itself retained by the constriction. The B column was a borosilicate glass chromatography column of 18.37$mm$ bore and approximately 220$mm$ length, having a sintered glass frit fused to the tube walls near one end. This served to retain the beads while allowing easy permeation of water. Each column was loaded with pre-soaked resin whose dry weight was accurately known: typically the A columns were loaded with $\simeq$ 0.3g and the B columns with $\simeq$ 11g. The two columns of a pair were connected in series by short lengths of PVC tubing. Four such pairs of columns were prepared for each trial with the exception of the FLOW8 trial, for which two pairs were prepared. The individual columns activated in the course of a trial were thus labelled 1A, 1B, 2A, ..., 4B – columns having the same number being paired in the obvious manner.

Each pair of columns was in turn connected to a peristaltic pump P, as shown in Figure 5.3, whose pumping speed was variable. Through each pair 100$cm^3$ water was then passed, followed without interruption of flow by 100$cm^3$ of $^{228}$Th–spiked source solution, followed likewise by 100$cm^3$ water. Between runs, only the rate of flow of source and water through the columns was varied. Of the four runs, No. 1 (activating columns 1A and 1B)

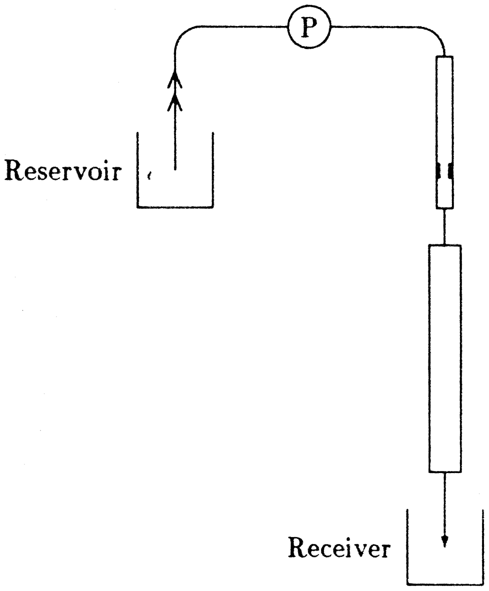

Figure 5.3: Arrangement of two $MnO_2$ columns for the FLOW trials.

was invariably the slowest, with the flow rate being increased each time so that No. 4 (4A and 4B) was the fastest. The time (accurate to the nearest second) taken for the source aliquot to be pumped from the reservoir was noted for each run, as was the time at which the run was started. After activation, all pairs of columns were vacuum baked to remove water prior to counting with the CPC.

In the cases of four of the seven trials reported here (FLOW6, 7, 8 and 9), an aliquot of the active source was taken on the day of the trial and sealed in a polyethylene vessel suitable for counting with the Ge(Li) detector described in Section 4.3. Furthermore, selected filtrates, *ie.* permeates from a pair of columns, were retained after these trials. They also were collected in vessels suitable for use with the Ge(Li), and formed a check on the overall extraction of each species due to a pair of columns. In the remaining three cases (FLOW3, 4 and 5), no aliquot was taken on the day of the trial but aliquots were taken both before and after the trial. No filtrates were retained from these trials.

### 5.2.2 Preparation of $^{228}$Th-spiked solutions

The active solutions used for the flow-rate trials reported in this section were all prepared by dilution of aliquots from a single stock $^{228}$Th solution. The stock solution consisted of $^{228}$Th in 1.6M nitric acid: this strong acidity was required to minimise the extent to which Thorium plated out onto the walls of the polyethylene container in which the solution was stored. The specific activity of the diluted solutions was typically about $100 Bq\, l^{-1}$.

The dilution was followed by adjustment of the pH of the resulting solution to the value required for the trial. In the case of unbuffered solutions, the adjustment was performed by careful addition of alkali, while continuously monitoring the solution with a calibrated pH meter capable of reading to an accuracy of ±0.01pH. The accuracy with which it was possible to set the pH of such unbuffered solutions was variable, but always better than 0.5pH. In the case of buffered solutions, an initial adjustment of pH to approximate neutrality was carried out, followed by the addition of the appropriate buffer salts. A final value typically within ±0.05pH of the nominal pH was obtained without further adjustment. The pH's measured for the various sources are given in Table 5.2.

The trials should ideally have tested the performance of $MnO_2$–loaded beads in conditions as nearly as possible identical to those expected in SNO — *ie.* water of very low ionic strength containing parts in $10^{15}$ Thorium. The Thorium present in SNO will of course be predominantly $^{232}$Th whereas the isotope used for all trials reported here was $^{228}$Th. The very different half-lives of the two isotopes ($1.4\times10^{10}y.$ *vs.* $1.91y.$) imply that although the specific activities used for the flow-rate trials were much higher ($100Bq\,l^{-1}$) than those necessary for SNO operation ($1ddt \equiv 10^{-8}Bq\ l^{-1}$), the spiked sources used for these trials nevertheless had $^{228}$Th concentrations $\sim 3\times10^{-15}g/g$, comparable to the $^{232}$Th concentrations desired for SNO. The trials therefore constituted an investigation of the performance of the $MnO_2$ resins under conditions of concentration appropriate to the SNO detector.

The criterion of very low ionic strength could not be met in the laboratory, because the $^{228}$Th stock was necessarily held in acidic solution. This alone contributed $\sim 10^{-2}$M $NO_3^-$ to the sources, and gave rise to the requirement to neutralise or buffer the sources, requiring the addition of other ions in concentrations up to ten times larger. The trials did not therefore test the sorption properties of $MnO_2$ in the absence of appreciable concentrations of all other ions, which leaves uncertainties as to the effects of other ions on the sorption process.

The compositions of the sources are given briefly below, together with their nominal pH.

FLOW3 This source made up from 10 ± 0.5cc stock $^{228}$Th solution in 685 ± 5cc total volume. The source was adjusted to pH7 using potassium hydroxide solutions and dilute nitric acid.

FLOW4 The source for this trial was made up with $13.5 \pm 0.5cm^3$ stock $^{228}$Th solution in a total volume of $1013 \pm 5cm^3$. It was buffered to pH4 using phthalate buffer.

FLOW5 The source for this trial was made up from $11.0 \pm 0.5cm^3$ stock $^{228}$Th solution in $1000 \pm 5cm^3$ total volume. The pH of the source was adjusted to pH4 with KOH and dilute $HNO_3$. No buffer salts were present.

FLOW6 The source for this trial was made up from $10 \pm 0.03cm^3$ stock $^{228}$Th solution in a total volume of $1026 \pm 5cm^3$. The solution was buffered to pH2 using KCl and HCl.

FLOW7 The source for this trial was made up from 9.606 ± 0.003g stock $^{228}$Th solution in a total mass of $1000 \pm 0.2g$ of solution. The solution was buffered to pH9.1 using 0.01M borax ($Na_2B_4O_7.10H_2O$).

FLOW8 The source used for this trial was that used for FLOW6.

FLOW9 The four runs comprising this trial were performed with two different source solutions – the principal difference being that one contained 0.25% dissolved NaCl whereas the other did not. Both sources were adjusted to between pH6.5 and 7.0 using NaOH solutions. The sources were made up from:

1. 8.439$g$ stock $^{228}$Th solution in 975.5$g$ total mass.
2. 8.427$g$ stock $^{228}$Th solution in 1011.8$g$ total mass.

Source #2 contained 2.500$g$ dissolved NaCl.

### 5.2.3 Analysis

The main analysis of the flow-rate trials proceeded in stages thus:

1. The count rate of $^{220}$Rn events was determined for each of a series of CPC measurements of each column, using the procedure described in Section 4.4.1. All aliquots of the relevant source solution were counted a number of times with a Ge(Li), whether or not such aliquots were taken at the time of the trial. In cases where one or more filtrates were retained, these, too, were sealed and counted repeatedly with the Ge(Li) detector.

2. The procedure of in section 4.4.2 was used to infer from the data initial activities of $^{228}$Th and $^{224}$Ra loaded onto each column. The same analysis was performed for data resulting from Ge(Li)-counting of all samples of the source solution and all filtrates. From the known cross-calibration between all Ge(Li) source geometries and the CPC (Section 4.5), the equivalent CPC activity of these liquid sources was obtained. In particular, the activity of the 100$cm^3$ source aliquots used to activate the columns was determined as an equivalent CPC activity: this activity would be the initial activity of a 100%–extracting column as measured with the CPC. In cases where no source aliquot was taken at the time of the trial, this activity was obtained by linear interpolation between aliquots taken before and after the trial.

   However, it was established in Section 5.1 that $^{220}$Rn de-emanation efficiency is a function of BVM flow rate, and the CPC/Ge(Li) cross-calibration sources were all $\simeq$ 9.7$g$ samples in B-type columns. The efficiency cross-calibration is therefore only valid for CPC samples of this type. The activities of A-columns are over-estimated with respect to B-columns, and with respect to the cross-calibration sources, because their $^{220}$Rn de-emanation efficiency is higher and the dead volume associated with the column is lower. For this reason, the fitted $^{228}$Th and $^{224}$Ra activities of each column are subject to two corrections: the first normalises to the $^{220}$Rn de-emanation efficiency of a 9.7$g$ column, a $\simeq$ 15% correction, and the second corrects for the difference in dead volumes between the two column types, a $\simeq$ 4% correction.

3. For each pair of columns, the extraction efficiency of the A column for each species was determined by forming the ratio of the observed and expected activities, determined

| Source identifier | $^{228}$Th activity $/s^{-1}$ | $^{224}$Ra activity $/s^{-1}$ | pH |
|---|---|---|---|
| FLOW3 | $3.330 \pm 0.200$ | $4.580 \pm 0.320$ | $7.10 \pm 0.10$ |
| FLOW4 | $5.150 \pm 0.250$ | $5.380 \pm 0.260$ | $3.95 \pm 0.05$ |
| FLOW5 | $2.087 \pm 0.088$ | $3.770 \pm 0.280$ | $4.00 \pm 0.10$ |
| FLOW6 | $3.680 \pm 0.220$ | $3.330 \pm 0.330$ | $1.96 \pm 0.02$ |
| FLOW7 | $1.714 \pm 0.042$ | $2.931 \pm 0.097$ | $9.12 \pm 0.02$ |
| FLOW8 | $3.235 \pm 0.082$ | $3.122 \pm 0.099$ | $1.96 \pm 0.02$ |
| FLOW9 (Runs1&2) | $1.550 \pm 0.036$ | $2.536 \pm 0.084$ | $6.90 \pm 0.10$ |
| FLOW9 (Runs3&4) | $0.224 \pm 0.010$ | $1.752 \pm 0.064$ | $6.60 \pm 0.10$ |

Table 5.2: Listing of source strengths and conditions of pH used for flow rate trials. Activities are expressed in equivalent CPC counts per second.

from the previous two steps. By subtraction of the observed A column activity from the source activity, the activity of each species entering the B column was determined. By comparison with the observed activity, the extraction efficiency of the B column for each species was determined.

4. Having determined the $^{228}$Th and $^{224}$Ra extraction efficiencies for each column involved in the trial, these were related to the residence time $\mathcal{R}$ of the solution in each column. The very different masses, and hence volumes, of resin in the A and B columns enabled two very different ranges of residence time to be investigated by the trials.

### 5.2.4 Results and Interpretation

Table 5.2 gives a listing of the activities of $^{228}$Th and $^{224}$Ra in $100cm^3$ of each source used for flow rate trials, together with the measured pH of each source. It can be seen that trials were conducted at nominal pH's of 2, 4, 7 and 9, with solutions which were generally in secular disequilibrium. The disequilibrium in these sources, and in many other cases not given here, is attributed largely to the plate-out of Thorium from solution onto the walls of the storage container between the times at which the solution was created and used. As expected, there is little disequilibrium at low pH. The activities of the sources are all in the same range — about $3Bq$ $^{224}$Ra in a $100cm^3$ aliquot. The activity values are derived by the method specified in Section 5.2.3 and are quoted with $1\sigma$ errors.

The individual CPC activity measurements are listed in Appendix A, as are the fitted $^{228}$Th and $^{224}$Ra activities for each column at the time of its activation (before corrections are applied). From this information, extraction efficiencies were determined according to the procedure outlined in Section 5.2.3 and are related to residence times $\mathcal{R}$ in Tables 5.3 to 5.9, where they are presented with $1\sigma$ errors. A-columns and B-columns are grouped in these tables, as most information is obtained from trends in the efficiencies.

FLOW3 (Table 5.3, pH7) The most important result of this trials derives from the A-column

Radium results: it is that Radium extraction efficiencies are high, even for residence times in the region of $1s$, and $> 90\%$ Radium extraction is achieved. (The zero residence time listed for column 4A corresponds to the fact that no $MnO_2$ was loaded into this column: it was used as a dummy to test extraction in the absence of any absorber). These results confirm the basic premise that $MnO_2$ has a high affinity for Radium at near-neutral pH.

A-column Thorium extraction efficiencies, by contrast, are low and B-column efficiencies are seen to reach only 40% even after $200s$ residence time. Columns 1B and 4B are seen to have very similar $\eta_{\mathrm{Th}}$ and identical residence times: the passage through column 1A is thus demonstrated not to affect Thorium sorption onto column 1B.

Comparison between columns 1B and 4B yields the surprising fact that passage of the solution through an A-sample appears to suppress Radium extraction in the B-column, although not Thorium extraction. This could be accounted for if $K^+$ leached from the A-column were successfully competing with Radium for its adsorption sites. Even traces of potassium would be present in concentrations many orders of magnitude greater than $^{224}$Ra.

Since Column 4A was a special case, a background run was performed after each individual CPC measurement of its activity; the column being replaced by a cleaned polyethylene tubing connector. This permitted independent background subtraction from each measurement, rather than the subtraction of a constant background as was done for all other samples generated by the series of trials. The results of this procedure are included in Table 5.3. Thorium extraction by column 4A is clearly non-zero, an observation consistent with the known tendency of Thorium to plate out onto available surfaces. The Radium extraction of the same column is small but apparently non-zero.

The acrylic wool plugs were removed from column 4A and the empty glass column counted three further times with the CPC, again with a background run performed immediately afterwards. The rate due to $^{228}$Th adsorbed onto the glass was found to be $0.0117 \pm 0.0026s^{-1}$ compared with $0.1386 \pm 0.0050s^{-1}$ with the wool plugs in place. Thus removal of the wool plugs reduced the $^{228}$Th activity in the column by an order of magnitude.

FLOW4 (Table 5.4, pH4) The A-column Radium data exhibit a similar trend to that observed at pH7, *ie.* good extraction is achieved with residence times of about $10s$. It may be seen that Radium extraction is approximately 40% even for a residence time of $1s$, so that again Radium extraction is rapid. B-column Radium extraction is again roughly constant, with a possible suppression of the Column 1B value, although the statistical significance is low.

A-column Thorium extractions are seen to be only slightly lower than the corresponding Radium extraction, in marked contrast to the pH7 case, FLOW3. There is also a possible suppression, of low significance, of Column 1B Thorium extraction, which was not observed in the FLOW3 trial.

| Sample ID | Th extraction % | Ra extraction % | $\mathcal{R}/s$ |
|---|---|---|---|
| Col.1A | 10.29 ± 0.76 | 91.73 ± 7.01 | 13.73 |
| Col.2A | 4.65 ± 0.39 | 75.51 ± 5.67 | 1.81 |
| Col.3A | 3.25 ± 0.28 | 69.87 ± 5.24 | 1.10 |
| Col.4A | 3.61 ± 0.28 | 0.64 ± 0.23 | 0.00 |
| Col.1B | 37.75 ± 2.70 | 32.66 ± 30.44 | 213.79 |
| Col.2B | 15.49 ± 1.11 | 88.03 ± 26.81 | 35.32 |
| Col.3B | 11.73 ± 0.81 | 96.26 ± 23.58 | 17.82 |
| Col.4B | 39.77 ± 2.59 | 99.44 ± 7.64 | 213.93 |

Table 5.3: FLOW3 efficiencies *vs.* residence time in seconds for an unbuffered pH7 source. All $MnO_2$ samples were batch 86HX005-11.

| Sample ID | Th extraction % | Ra extraction % | $\mathcal{R}/s$ |
|---|---|---|---|
| Col.1A | 82.80 ± 4.20 | 86.90 ± 5.50 | 10.78 |
| Col.2A | 54.19 ± 2.84 | 63.35 ± 3.91 | 3.54 |
| Col.3A | 51.07 ± 2.71 | 63.54 ± 4.02 | 2.20 |
| Col.4A | 37.62 ± 2.03 | 41.82 ± 2.80 | 0.95 |
| Col.1B | 75.94 ± 22.19 | 49.51 ± 23.10 | 218.16 |
| Col.2B | 94.43 ± 10.45 | 73.00 ± 11.73 | 70.71 |
| Col.3B | 97.46 ± 10.12 | 74.01 ± 12.10 | 36.79 |
| Col.4B | 92.99 ± 7.53 | 79.54 ± 8.23 | 18.17 |

Table 5.4: FLOW4 efficiencies *vs.* residence time in seconds for a buffered pH4 source. All $MnO_2$ samples were batch 86HX005-11.

| Sample ID | Th extraction % | Ra extraction % | $\mathcal{R}/s$ |
|---|---|---|---|
| Col.1A | 52.78 ± 2.65 | 87.51 ± 6.85 | 18.56 |
| Col.2A | 29.96 ± 1.44 | 70.35 ± 5.55 | 3.03 |
| Col.3A | 19.58 ± 1.08 | 50.73 ± 3.90 | 1.34 |
| Col.4A | 12.00 ± 0.71 | 37.50 ± 2.98 | 0.57 |
| Col.1B | 11.34 ± 1.27 | 2.08 ± 1.80 | 232.92 |
| Col.2B | 22.25 ± 1.47 | 72.19 ± 18.81 | 61.02 |
| Col.3B | 25.11 ± 1.57 | 84.80 ± 13.10 | 36.83 |
| Col.4B | 23.28 ± 1.28 | 83.15 ± 10.17 | 18.58 |

Table 5.5: FLOW5 efficiencies *vs.* residence time in seconds for an unbuffered pH4 source. All $MnO_2$ samples were batch 86HX005-11.

FLOW5 (Table 5.5, pH4) A-column Radium extraction in the FLOW5 trial exhibits the same trend as is observed in the previous two trials: it is again rapid and around 90% extraction is achieved. Suppression of Column 1B Radium extraction is on this occasion extremely marked.

A-column Thorium data in this trial exhibit a behaviour intermediate in character between the two cases of similar kinetics to Radium (FLOW4) and very much slower kinetics (FLOW3). In this case a residence time of nearly $20s$ yields a Thorium extraction $\simeq 50\%$ as compared with 90% (FLOW4) and 10% (FLOW3).

B-column Thorium extraction efficiencies are very much lower than observed in FLOW4, and all are markedly lower than might have been expected on the basis of A-column values.

Noting that the residence times for columns 1A and 4B are, by chance, identical, the passage of source through the A column has clearly suppressed Thorium extraction in the B column. This is in marked contrast to the case of FLOW3 in which a direct comparison was made between B column extractions in cases when the source had and had not previously passed through a $MnO_2$–loaded A column.

The behaviour of Thorium in this trial may be explained by the fact that passage of water through the $MnO_2$-loaded beads is known to increase its pH. On this basis, the effluent from the A columns would be expected to be pH>4, and presumably this effect would be more pronounced at longer A column residence times — there then being more time available for the exchange of $H^+$ for $K^+$ which is assumed to be occurring (see Section 3.2.3).

From the FLOW3 and FLOW4 trials it is known that thorium may be well extracted at pH4 but is not well extracted at pH7. An increase in the pH of a source initially at pH4 might therefore be expected to worsen extraction of Thorium, accounting for the suppressed B column extraction seen in FLOW5. The fact that this behaviour was not observed in the case of the FLOW4 trial is easily accounted for by the fact that the FLOW4 source was buffered, whereas the FLOW5 source was not. The same effect can account for the lowered A-column extraction efficiencies: as the solution passes through the A-column, its pH is raised and extraction by the remainder of the column is worsened.

FLOW6 (Table 5.6, pH2) In this trial, Thorium extraction efficiencies show the same trend as is observed in FLOW4 of rapid and efficient extraction. The variation with residence time is, indeed, very similar to that of FLOW4.

Although Radium extraction at pH2 by the A columns varies monotonically with residence time, as expected, the extraction is quite noticeably slower than has been observed hitherto. This accords with the expectation the Radium extraction must eventually become poor as the pH is lowered. As noted above, acid has been used to elute adsorbed Radium from $MnO_2$ beds, so it is clear that the equilibrium constant for the

| Sample ID | Th extraction % | Ra extraction % | $\mathcal{R}/s$ |
|---|---|---|---|
| Col.1A | 84.77 ± 5.26 | 58.60 ± 6.12 | 11.49 |
| Col.2A | 70.39 ± 4.36 | 30.90 ± 3.32 | 2.69 |
| Col.3A | 38.59 ± 2.38 | 15.43 ± 1.75 | 0.93 |
| Col.4A | 26.96 ± 1.68 | 10.04 ± 1.20 | 0.48 |
| Col.1B | 42.41 ± 17.18 | 116.19 ± 28.49 | 249.93 |
| Col.2B | 104.33 ± 21.54 | 102.42 ± 15.02 | 57.97 |
| Col.3B | 100.11 ± 9.91 | 111.98 ± 13.41 | 31.22 |
| Col.4B | 99.30 ± 8.27 | 101.81 ± 11.65 | 12.99 |

Table 5.6: FLOW6 efficiencies *vs.* residence time in seconds for a buffered pH2 source. All $MnO_2$ samples were batch 86HX005-11.

| Sample ID | Th extraction % | Ra extraction % | $\mathcal{R}/s$ |
|---|---|---|---|
| Col.1A | 7.32 ± 0.38 | 81.54 ± 3.01 | 6.57 |
| Col.2A | 10.19 ± 0.45 | 88.13 ± 3.34 | 2.11 |
| Col.3A | 6.59 ± 0.38 | 71.77 ± 2.79 | 1.22 |
| Col.4A | 3.61 ± 0.30 | 24.47 ± 1.07 | 0.39 |
| Col.1B | 30.17 ± 1.04 | 51.91 ± 10.62 | 178.49 |
| Col.2B | 20.58 ± 0.79 | 102.73 ± 32.23 | 50.75 |
| Col.3B | 16.08 ± 0.63 | 106.41 ± 13.92 | 32.78 |
| Col.4B | 9.90 ± 0.50 | 87.27 ± 4.34 | 16.93 |

Table 5.7: FLOW7 efficiencies *vs.* residence time in seconds for a buffered pH9 source. Samples 2A and 3A were batch 8810-02, the remainder batch 86HX005-11.

sorption process changes dramatically at low pH. Furthermore, the B-columns show quantitative extraction with no suggestion of suppression at low flow rates.

The fact that columns 1A and 4B have similar values of $\mathcal{R}$ but very different Radium extractions suggests that the passage of the solution through column 4A *enhances* Radium extraction in column 4B. This might occur if the HCl/KCl mixture used to establish the pH were not an effective buffer, particularly as the resin adds $K^+$, and that the transition in the equilibrium constant is near pH2.

FLOW7 (Table 5.7, pH9) Thorium extractions by Columns 2A&3A in this trial are clearly anomalously high, both by comparison with Columns 1A&4A and with Column 1A of FLOW3. Columns 2A&3A alone contain batch 8810-02 resin. B-column Thorium extractions appear comparable to those of FLOW3.

A-column Radium extractions are again efficient. Columns 2A and 3A may be com-

| Sample ID | Th extraction % | Ra extraction % | $\mathcal{R}/s$ |
|---|---|---|---|
| Col.1A | 72.34 ± 2.23 | 46.94 ± 2.10 | 6.31 |
| Col.2A | 51.69 ± 1.52 | 25.75 ± 1.34 | 1.54 |
| Col.1B | 72.78 ± 7.62 | 114.74 ± 8.13 | 165.54 |
| Col.2B | 90.42 ± 5.22 | 101.06 ± 5.18 | 38.92 |

Table 5.8: FLOW8 efficiencies *vs.* residence time in seconds for a buffered pH2 source. Sample 2B was batch 8810-02, the remainder batch 86HX005-11.

pared with columns in trials FLOW3 – FLOW5: there is some indication that Radium extraction by these columns is better than obtained with 86HX005-11 batch resin at pH7 and pH4 for comparable $\mathcal{R}$.

FLOW8 (Table 5.8, pH2) The Radium extractions of A- and B-columns show qualitatively similar behaviour to those of FLOW6, performed with the same pH2 source, although the columns test the extraction at different residence times in the two trials. Thorium extractions likewise show behaviour which is qualitatively similar to FLOW6.

FLOW9 (Table 5.9, pH7) This trial was performed in order directly to test the influence of dissolved sodium chloride on the sorption properties of $MnO_2$. In addition, $MnO_2$ batch 8810-02 was used throughout in order to obtain a body of data enabling comparison of the adsorption properties of this batch with the 86HX005-11 batch used for the large majority of previous samples. Runs 3&4 were conducted in the presence of salt.

It is apparent from Table 5.9 that the A-column Thorium extraction efficiencies are very much higher than those observed in previous high-pH trials (FLOW3 and FLOW7). There is some suggestion that the presence of salt suppresses Thorium extraction in the A-columns, but the effect does not appear in the B-column data.

Inspection of the Radium extractions affords some evidence for slowdown of Radium extraction in those cases (Runs 3 and 4) when NaCl was present — columns 2A and 4A have very similar residence times and very different Radium extractions; column 2B shows Radium extraction consistent with 100% whereas column 4B does not, despite a residence time usually sufficient for $\simeq$ 90% Radium extraction. It thus appears that the presence of 0.25% NaCl is suppressing Radium sorption.

### 5.2.5 Information from filtrates

The cases in which filtrates were retained were Run 4 of FLOW6 and FLOW7, Run 2 of FLOW8, and Runs 2&4 of FLOW9. All were repeatedly counted in a standard geometry with a Ge(Li) detector, from which data estimates of their initial Thorium and Radium loadings were determined. Since the activities of the sources were also determined by $\gamma$-counting

| Sample ID | Th extraction % | Ra extraction % | $\mathcal{R}/s$ |
|---|---|---|---|
| Col.1A | $54.43 \pm 1.58$ | $111.78 \pm 4.53$ | 6.42 |
| Col.2A | $33.34 \pm 1.03$ | $74.22 \pm 3.14$ | 1.19 |
| Col.3A | $41.62 \pm 3.04$ | $92.90 \pm 4.07$ | 7.76 |
| Col.4A | $22.87 \pm 2.43$ | $50.62 \pm 2.30$ | 1.21 |
| Col.1B | $27.81 \pm 1.78$ | $0.00 \pm 0.00$ | 152.17 |
| Col.2B | $45.09 \pm 1.91$ | $109.64 \pm 16.72$ | 39.11 |
| Col.3B | $54.18 \pm 6.36$ | $23.34 \pm 15.04$ | 181.52 |
| Col.4B | $49.21 \pm 4.67$ | $56.95 \pm 4.82$ | 40.01 |

Table 5.9: FLOW9 efficiencies *vs.* residence time in seconds for unbuffered pH7 sources. All $MnO_2$ samples were batch 8810-02. Runs 3&4 were in the presence of 0.25% NaCl.

of aliquots, the permeation of Thorium and Radium through a pair of columns could in principle be determined independently of CPC data.

In all the above cases, the run in question is the fastest (highest flow rate) of the series, and was therefore expected to yield the highest permeation of Radium and Thorium through the pair of columns into the filtrate. In the case of FLOW9, Runs 2&4 were respectively the faster of the two runs conducted in the absence and presence of Sodium Chloride.

Since the gamma-ray (239keV) used for monitoring the filtrates is associated with $^{212}$Pb decay, the time dependence of the activity of the sample is sensitive to the initial loading of $^{212}$Pb in addition to the loading of $^{224}$Ra and $^{228}$Th, which are determined by CPC data. However, determination of the $^{212}$Pb content of a sample ideally requires measurements to be repeated on a time scale short compared to the $10.6hr$ half-life of that isotope. Two considerations often made this impossible:

1. Those filtrates of low activity could not be counted at all in a time much less than 24 hours. This length of time was frequently necessary for the accumulation of sufficient statistics.

2. Normally, many samples were simultaneously under investigation. The requirement to obtain information from all of these often excluded the possibility of allowing a sample to remain in the system for long periods.

In general, therefore, insufficient information was collected to determine accurately the $^{212}$Pb *and* $^{224}$Ra contents of a filtrate. In most cases the data allow large, correlated, uncertainties in the loadings of these two isotopes. The $^{228}$Th loading of a sample is, by contrast, generally well determined, since its activity decays with a $2yr$ half-life, and this sets the scale of the time available for the assay of an isotope. The information obtained from filtrates is summarised in the remainder of this section. The tables presented give the permeated activities, determined by Ge(Li) measurements, in units which are the same as for Table 5.2 and Tables 5.3 to 5.9, *ie.* equivalent CPC counts per second. Permeated activities are also expressed as a percentage of source activity and the total detected activities (*ie.* filtrate plus columns) is also given as a percentage. This last quantity is a sensitive test of the measured relative efficiencies of Ge(Li) source geometries, of the Ge(Li)/CPC cross-calibration and of the relative efficiencies of $^{220}$Rn de-emanation.

The tables presented give all the information available: limits are quoted when an actual value could not be determined and are in all such cases $3\sigma$ confidence limits. Quantities determined too poorly to be meaningful are omitted from the tables.

### FLOW6, **Run 4**

| | Permeated activities | |
|---|---|---|
| | $s^{-1}$ | % |
| $^{228}$Th | 0.051 ± 0.010 | 1.4 ± 0.3 |
| $^{224}$Ra | 0.090 ± 0.130 | 2.7 ± 3.9 |
| $^{212}$Pb | 0.010 ± 0.110 | |
| Total detected activities | | |
| $^{228}$Th | 107.4 ± 6.1% | |
| $^{224}$Ra | 108.9 ± 10.9% | |

The low permeations accord with the high extractions seen in FLOW6, and no activity remains unaccounted for.

### FLOW7, **Run 4**

| | Permeated activities | |
|---|---|---|
| | $s^{-1}$ | % |
| $^{228}$Th | 1.111 ± 0.029 | 64.8 ± 2.3 |
| $^{224}$Ra | 0.189 ± 0.073 | 6.4 ± 2.5 |
| $^{212}$Pb | < 1.800 | |
| Total detected activities | | |
| $^{228}$Th | 78.6 ± 3.3% | |
| $^{224}$Ra | 101.1 ± 4.4% | |

The data imply that some Thorium remains unaccounted for, suggesting that Thorium may have been adhered to the tubing before reaching the A-column, or possibly between columns. This is not a surprising result at high pH, but if correct then it constitutes a source of systematic error when assessing Thorium extraction efficiencies.

### FLOW8, **Run 2**

|  | Permeated activities |  |
|---|---|---|
|  | $s^{-1}$ | % |
| $^{228}$Th | $0.015 \pm 0.010$ | $0.5 \pm 0.3$ |
| $^{224}$Ra | $< 0.069$ |  |
| $^{212}$Pb | $< 0.601$ |  |
| Total detected activities |  |  |
| $^{228}$Th | $103.7 \pm 2.8\%$ |  |
| $^{224}$Ra | $< 106.9\%$ |  |

Permeation of both isotopes is low, as expected at pH2, and no activity is unaccounted for.

FLOW9, **Run 2**

|  | Permeated activities |  |
|---|---|---|
|  | $s^{-1}$ | % |
| $^{228}$Th | $0.187 \pm 0.012$ | $12.1 \pm 0.8$ |
| $^{224}$Ra | $0.335 \pm 0.088$ | $13.2 \pm 3.5$ |
| $^{212}$Pb | $< 0.001$ |  |
| Total detected activities |  |  |
| $^{228}$Th | $80.6 \pm 2.8\%$ |  |
| $^{224}$Ra | $127.1 \pm 4.7\%$ |  |

Thorium has again apparently been lost, and Radium appears substantially over-represented.

FLOW9, **Run 4**

|  | Permeated activities |  |
|---|---|---|
|  | $s^{-1}$ | % |
| $^{228}$Th | $0.086 \pm 0.009$ | $38.4 \pm 4.5$ |
| $^{224}$Ra | $0.050 \pm 0.280$ | $2.9 \pm 16.0$ |
| Total detected activities |  |  |
| $^{228}$Th | $102.7 \pm 7.0\%$ |  |
| $^{224}$Ra | $89.3 \pm 18.4\%$ |  |

Substantial Thorium permeation accords with the observed extraction efficiencies and, in contrast to the similar run in the absence of Sodium Chloride, no Thorium appears to have been lost.

### 5.2.6 Summary

The extraction efficiencies obtained from FLOW3–FLOW8 are plotted *vs.* residence time $\mathcal{R}$ in Figures 5.4–5.6. Figures 5.5 and 5.6 of A-column and B-column Thorium extractions clearly show the division of the Thorium extraction results into two populations of fast and slow extractions, with FLOW5 (unbuffered pH4) as an intermediate case. The high-pH trials are seen to be slowly-extracting for Thorium whereas the low-pH trials extract rapidly. The evidence strongly suggests a transition in the behaviour of Thorium at or near pH4.

Figure 5.4 clearly shows the comparison between FLOW6 and FLOW8 Radium extractions. These two trials were conducted with the same source, the A-columns all being from the 86HX005-11 $MnO_2$ batch: they are therefore directly comparable and constitute a test of the reproducibility of the results. The points resulting from the two trials appear to lie on the same curve of extraction efficiency *vs.* residence time, suggesting that the results, at least in the case of pH2 trials, are reasonably reproducible.

There is some suggestion in the whole data set that Radium extraction in B-columns can under some conditions be suppressed by long residence times of the sources in the A-column. This has been tentatively attributed to competition for sorption between Radium and a large excess of leached Potassium. If this is correct, then the Potassium content of the resins is damaging their performance and might be expected to limit equilibrium sorption. For SNO use, a method of preparation would be required which either avoids Potassium deposition or elutes it before the resin is used.

A *caveat* to be applied to this conclusion is that it is sensitive to the estimate of the A-column $^{220}$Rn de-emanation efficiency. This was measured up to 100BVM, but the A-columns were used at over 1000BVM gas flow rate, so the required extrapolation into an unmeasured region is large. If the extrapolation under-estimated A-column $^{220}$Rn de-emanation, then the adsorbed activity on the A-column would be under-estimated, the permeation to the B-column over-estimated and the B-column extraction efficiency under-estimated. This would be most important when the A-column extracted most efficiently, when a small ($\simeq 5\%$) error in the inferred counting efficiency would lead to a very significant error in the apparent permeation. The greatest apparent Radium suppressions are consistently seen in the 1B-columns, and the 1A-columns extract with $\simeq 90\%$ efficiency. Conclusions about the extent to which Potassium competes with Radium must therefore be guarded.

The filtrate data are generally in accord with expectations based on Tables 5.6 to 5.9, suggesting that the overall accuracy of the conversions between geometries and units is reasonable. There is some suggestion of Thorium loss in the course of the neutral- and high-pH trials, probably due to plate-out at the peristaltic pump.

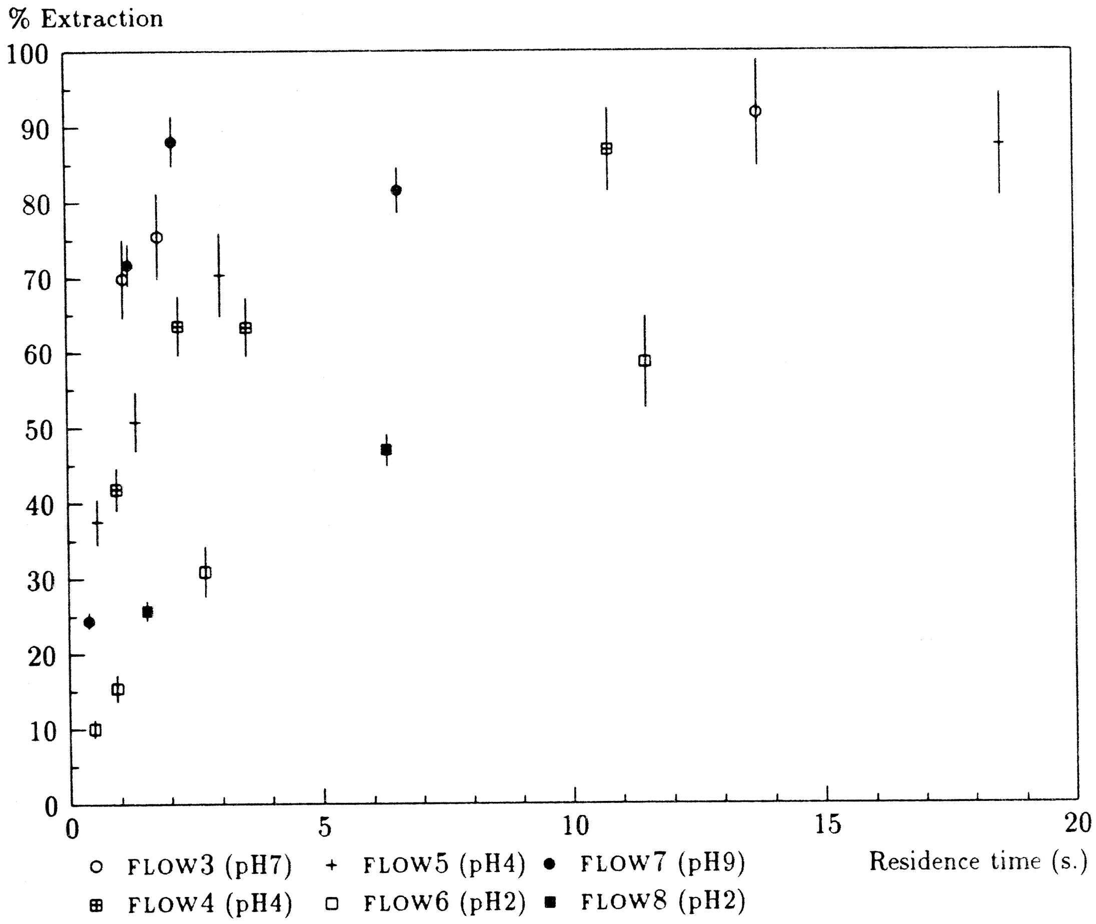

Figure 5.4: A-column Radium extraction efficiencies *vs.* Residence Time.

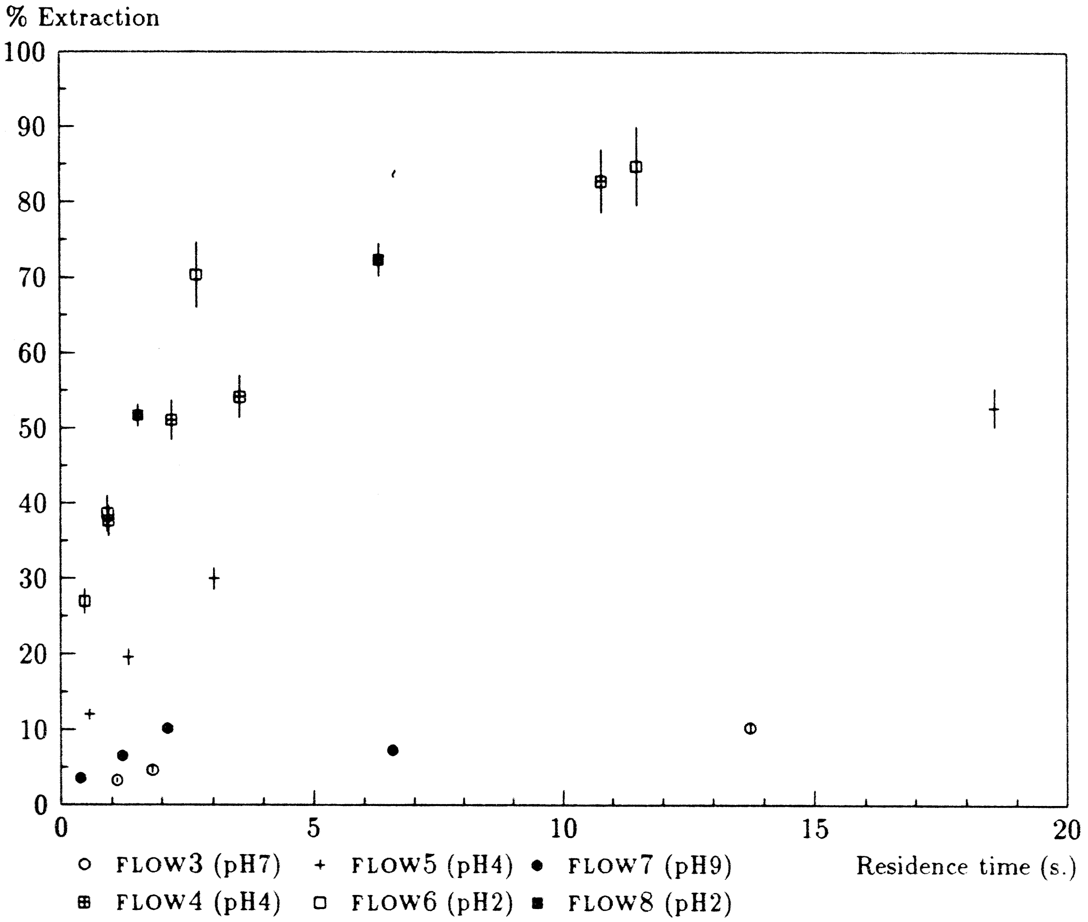

Figure 5.5: A-column Thorium extraction efficiencies *vs.* Residence Time.

## 5.3 Auxiliary experiments

In addition to the main sequence of flow rate trials presented in the previous section, several auxiliary experiments were performed using similar apparatus. The function of these experiments, AUX1 to AUX4, was to investigate phenomena related to the main FLOW trials. These were:

1. Thorium adsorption by $MnO_2$ under conditions of pH7 and residence time $\mathcal{R} \gg 200s$,
2. Radium implantation (Chapter 3), and
3. Thorium and Radium adsorption by acrylic wool

The experimental procedure used for all the auxiliary trials reported in this section was similar to that of the FLOW trials: $100cm^3$ pure water was pumped from a reservoir through

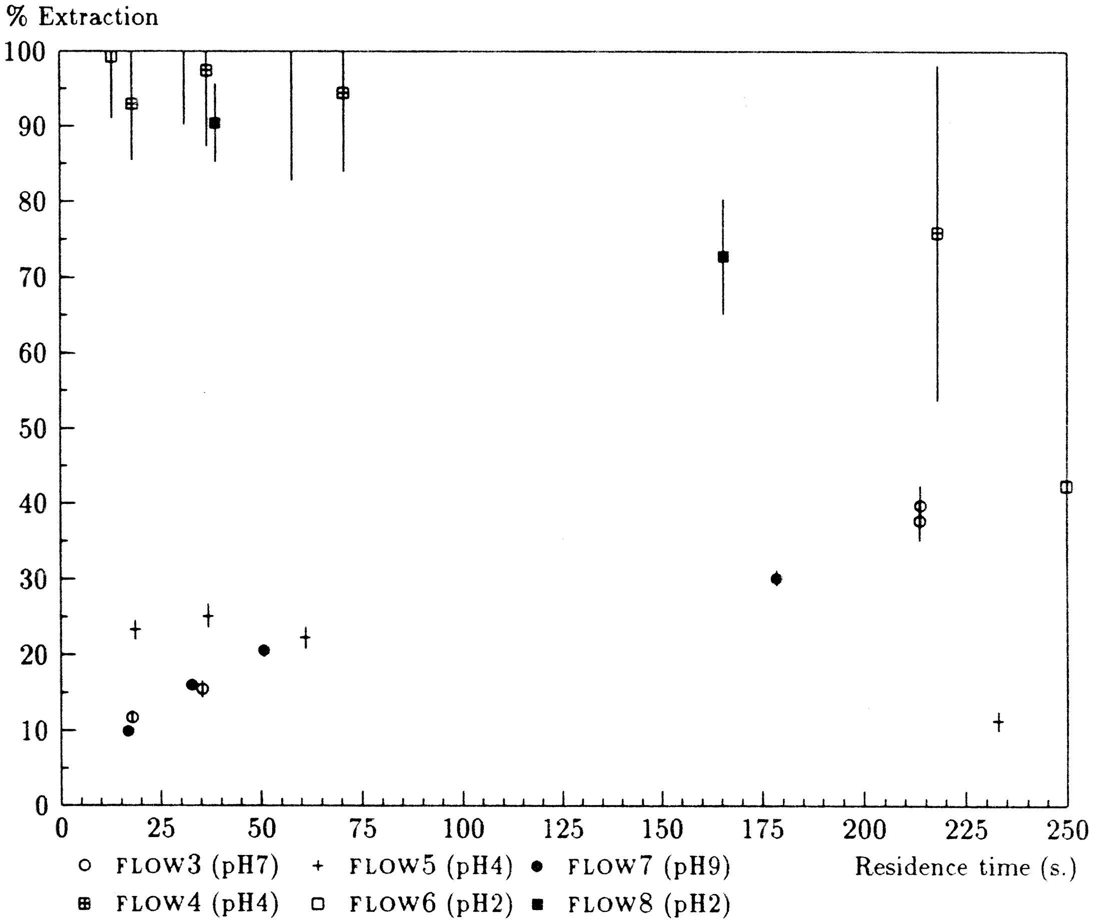

Figure 5.6: B-column Thorium extraction efficiencies *vs.* Residence Time.

the samples using a peristaltic pump, followed by $100cm^3$ $^{228}$Th-spiked solution, followed by a further $100cm^3$ pure water. $MnO_2$ samples were dried by vacuum baking.

### 5.3.1 AUX1

This experiment tested the extraction properties of $MnO_2$ at pH $\simeq 7$ given residence times $\mathcal{R}$ long compared to those typically reached in the FLOW-trial sequence.

The absorber for this experiment was a bed of $11.87g$ $MnO_2$ resin contained in a single column of the same type as the 'B-columns' of the FLOW trials, *ie.* $18.37mm$ bore and $220mm$ length. Through this was passed $100cm^3$ unbuffered pH7 $^{228}$Th-spiked solution — the same as used for FLOW3. Although the mass of resin in the column was comparable to the masses used for the FLOW trials, the flow rate of source was adjusted such that the residence time $\mathcal{R}$, defined in Section 5.2, for the extraction was $1060s$, very much longer than those reached in the FLOW trials.

The $MnO_2$ activated in this experiment was dried and then a known fraction, determined by weight, placed in a sealed polyethylene container of internal dimensions $13mm$ bore and $56mm$ height. A filtrate sample was also retained in an identical container. The initial $^{228}$Th and $^{224}$Ra loadings of the samples were compared by repeated measurements of the 240keV activity of each sample using the Ge(Li) apparatus described in Section 4.3.

An aliquot of the source used for the experiment was taken on the previous day, and a second aliquot a month later. Both were placed in polyethylene containers identical to those used in the above procedure. Their initial $^{228}$Th and $^{224}$Ra loadings were determined using the Ge(Li) apparatus. Taken together, they showed rapid plate-out of Thorium from the solution.

Taking the previous day's aliquot as reasonably representing the state of the source at the time of the experiment, a Thorium extraction of $76.6 \pm 9.1\%$ was calculated from comparison of the activities of source and column. Radium extraction was found to be consistent with 100%. The activity of the filtrate sample was too low to afford any assessment of Radium or Lead extraction, but Thorium permeation was assessed to be $21.5 \pm 9.9\%$, in good agreement with the assessment of the column's extraction efficiency. The experiment therefore demonstrates that at pH7, given sufficiently long residence time, Thorium extraction efficiencies may be obtained which are substantially greater than the $\simeq 40\%$ reached in the FLOW trials.

### 5.3.2 AUX2

This experiment looked for the Radium implantation effects introduced in Section 3.3. Two $MnO_2$–loaded columns were activated under similar conditions. The $^{220}$Rn emanated from one was measured using the CPC and the 240keV gamma radiation from the other measured using a Ge(Li). Since the CPC is sensitive to changes in the efficiency of $^{220}$Rn de-emanation, whereas gamma-counting is not (assuming only that free $^{220}$Rn does not diffuse out of the sample within its 1 minute half-life), comparing the apparent ratios of initial $^{224}$Ra to $^{228}$Th content of the two columns tests for such changes if the columns were activated identically.

|  | Mass $MnO_2$(g) | $\mathcal{R}$ (s) |
|---|---|---|
| Column# 1 | 0.507 | 2.8 |
| Column# 2 | 0.598 | 3.5 |

Table 5.10: Masses of $MnO_2$-loaded acrylic resin and residence times for the two AUX2 trials

|  | $R/T$ |
|---|---|
| Column# 1 | $1.215 \pm 0.046$ |
| Column# 2 | $1.348 \pm 0.041$ |

Table 5.11: $R/T$ ratios for the two columns activated in the AUX2 trial.

To achieve this two glass columns of 5.85$mm$ bore and 150$mm$ length (the same style as used for the 'A-columns' of the FLOW trials) were loaded with accurately known weights of $MnO_2$. Each was separately activated using the same buffered pH4 source as was used for FLOW4, according to the procedure outlined in Section 5.3. The masses of resin and the residence times for the two runs are given in Table 5.10.

Column #1 was counted several times using the Ge(Li) apparatus described in Section 4.3 and Column# 2 was similarly counted using the CPC. The $^{224}$Ra/$^{228}$Th ($R/T$) ratios of the columns are given in Table 5.11. The ratios thus determined are not very significantly different, the difference being a $2\sigma$ effect. If taken at face value, thay imply a $9.9 \pm 4.4\%$ decrease in $^{220}$Rn emanation efficiency after a time long compared to the $^{224}$Ra half-life.

Direct comparison of the ratios is not quite valid, however, because of their 25% difference in residence time $\mathcal{R}$. The effect on $R/T$ of increasing $\mathcal{R}$ from $\mathcal{R}_1$ to $\mathcal{R}_2$ depends on whether Thorium or Radium sorption is increasing faster in that region of $\mathcal{R}$. A simple calculation shows that Radium extraction would need to be increasing around three times as fast as Thorium extraction if the effect were attributed to this effect. Figures 5.4 and 5.5 show that the difference was not that large, as Radium kinetics during the FLOW4 extraction was only marginally better than Thorium. The AUX2 data therefore suggest a small Radium implantation effect which may be statistically significant.

Column #1 of this trial was one of the few $MnO_2$ samples to have the time evolution of its activity characterised by gamma-counting. The activity of 239keV gamma-rays soon after activation is indicative of the $^{212}$Pb content of the sample, so that the behaviour of Lead with respect to adsorption onto $MnO_2$ at pH4 can be determined from the data collected in the course of analysing the results of this trial. The results of activity measurements on Column #1 are presented in Figure 5.7, together with the results of the three-parameter fit to the decay series

$$^{228}\mathrm{Th} \longrightarrow {}^{224}\mathrm{Ra} \longrightarrow {}^{212}\mathrm{Pb}$$

described in Section 4.4.2. It is clear that the time variation of the activity implies a low

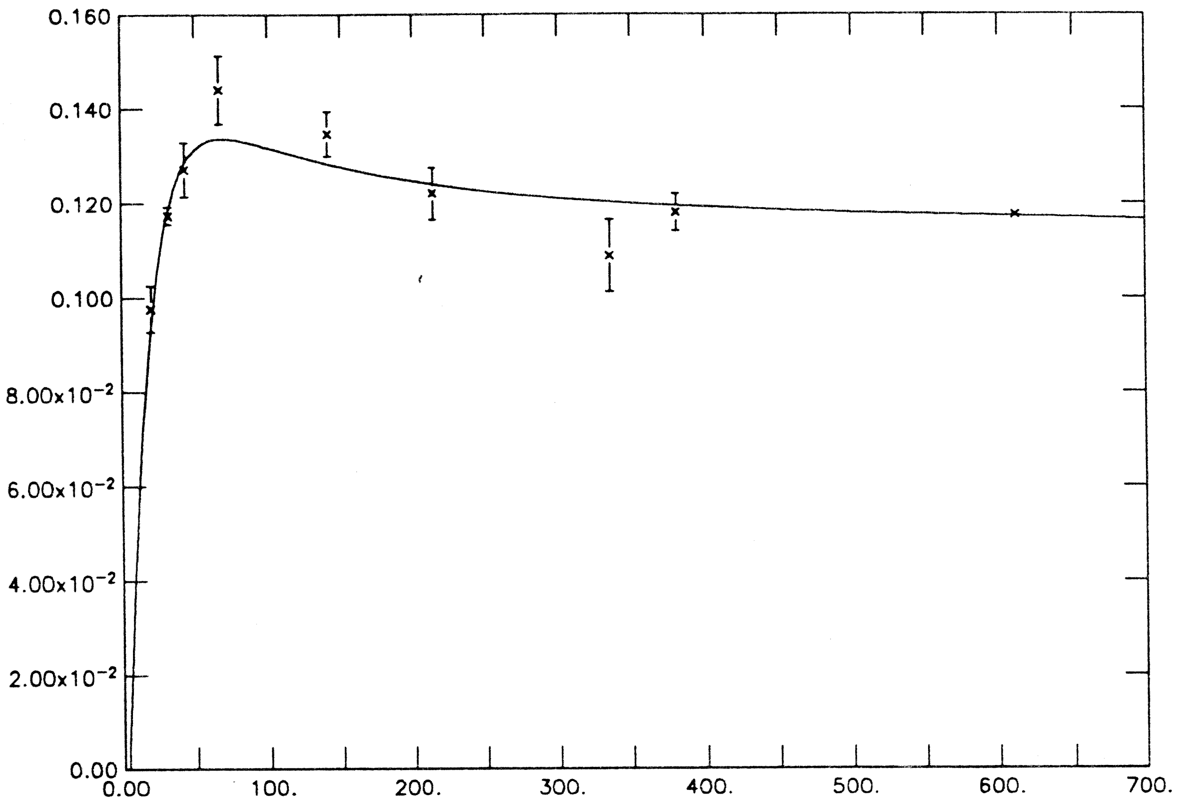

Figure 5.7: Activity *vs.* time for AUX1 Column 1. Evidence for $^{212}$Pb ingrowth is conclusive. Ordinate is counts per second and abscissa is time in hours since activation.

initial $^{212}$Pb activity. The fitted value of this quantity is $-0.037 \pm 0.025 s^{-1}$. Analysis of the available data on the time evolution of 239keV gamma-ray activity of the two aliquots taken from the AUX2 source shows no evidence of $^{212}$Pb/$^{224}$Ra disequilibrium, indicating that $^{212}$Pb remains in solution. Lead adsorption onto MnO$_2$ at pH4 is thus consistent with zero.

### 5.3.3 AUX3

In this trial, a single sample of MnO$_2$ was activated using the same unbuffered pH7 source as was used for FLOW3 and AUX1. The mass of the sample was 8.98$g$ and the residence time $\mathcal{R}$ of the source solution in the absorber bed was 31.6$s$. The experiment was thus similar to AUX1, excepting its much shorter residence time, which was comparable to those of B-columns in FLOW3.

After activation, the MnO$_2$ sample was dried and split into two parts of accurately known masses: 4.370$g$ was placed in a sealed polyethylene container of internal dimensions 13$mm$ bore and 56$mm$ height and the remaining 3.159$g$ in the column in which it was activated. (The masses of two parts of the sample sum to 16% less than the mass of the original sample:

| Sample | Thorium extraction % | Radium extraction % | $R/T$ |
|---|---|---|---|
| CPC | $7.1 \pm 2.4$ | $94 \pm 13$ | $76.0 \pm 7.3$ |
| Ge(Li) | $10.5 \pm 4.9$ | $110 \pm 15$ | $60 \pm 20$ |

Table 5.12: AUX3 extraction efficiencies of the CPC-counted and the Ge(Li)–counted $MnO_2$ samples.

the difference is due to water loss during vacuum baking). Samples of the source and filtrate were also retained in identical containers. The three samples in polyethylene containers were repeatedly counted with the Ge(Li) apparatus described in Section 4.3. The $MnO_2$ sample remaining in the column was similarly counted with the CPC. The initial activities of $^{228}$Th, $^{224}$Ra and $^{212}$Pb were thus determined for the three gamma-counted samples, and of $^{228}$Th and $^{224}$Ra for the CPC-counted sample.

Since the two $MnO_2$ samples were activated identically, a comparison of their $R/T$ ratios was made to search for Radium implantation effects. Since a source aliquot was taken at the time of the trial, a comparison of Thorium and Radium extraction efficiencies may be made with FLOW3. The extraction efficiencies for Thorium and Radium implied by the Ge(Li) and CPC data are given in Table 5.12. It is seen that Radium extraction efficiencies are consistent with 100%, as is clearly expected from FLOW3 data, and that Thorium extraction efficiencies are comparable to the 14% seen in Column 2B of FLOW3, although clearly rather lower. The difference is attributed to uncertainties in the Thorium content of the source at the time of FLOW3 and AUX3 trials: Thorium was plating out rapidly from this source and the low levels at which it was present makes its measurement in all samples prone to errors from background subtraction.

The $R/T$ ratios of the CPC and Ge(Li) samples can also be compared: they are clearly consistent within the large error on that of the gamma-counted sample, which results from the closeness of the observed count rate in that sample to the background rate. The fact that CPC data successfully fit to a decaying exponential also implies that the overall counting efficiency of the system is not a strong function of the sample's activity.

### 5.3.4 AUX4

In view of the FLOW3 result that a glass column containing only acrylic wool has a measurable affinity for Thorium at pH7, a trial was conducted to verify this result. A glass column of 5.85$mm$ bore and 150$mm$ length was loaded with 181$mg$ acrylic wool, occupying 135$mm$ of the column's length. It was activated by passing through it 100$cm^3$ of phosphate-buffered pH7 $^{228}$Th solution and two 100$cm^3$ volumes of pure water, as described in Section 5.3. A second column was treated identically, except that it contained no acrylic wool. The rate of flow was such that the residence time of source in the wool was 31.3$s$: the flow rate of source through the empty column was identical, but a residence time is not defined. The column loaded with acrylic wool was labelled Column #1 and the empty column as Column #2.

| Sample ID | Thorium extraction % | Radium extraction % |
|---|---|---|
| Col.1 | $1.14 \pm 0.17$ | $1.38 \pm 0.25$ |
| Col.2 | $< 0.15$ | $< 0.26$ |

Table 5.13: AUX4 extraction efficiencies of the woolly and empty columns.

Both columns were dried and their $^{220}$Rn emanation repeatedly counted with the CPC to determine their Thorium and Radium contents. An aliquot of the source was also taken at the time of the trial for gamma-counting.

The Thorium and Radium extraction efficiencies calculated from the activities of the source aliquot and glass columns are given in Table 5.13. Column #1 shows measurable Thorium and Radium adsorption, and is only approximately in agreement with Column 4A of the FLOW3 trial, where 4% Thorium adsorption and 1% Radium adsorption were seen. The empty glass column, Column #2, shows no evidence of any adsorption: the values given in Table 5.13 are $3\sigma$ upper limits. This result demonstrates that plate-out of Radium and Thorium onto the glass surfaces of the columns is insignificant, even in the absence of competing sorption processes onto $MnO_2$ or acrylic wool.

## 5.4 Equilibrium constants for Thorium and Radium sorption

The two parameters which characterise the behaviour of $MnO_2$ with respect to the sorption of aqueous species are the time constant for the forward reaction and the position of the equilibrium eventually obtained. The kinetics of the sorption reaction were investigated in Section 5.2 in the most directly relevant way, *ie.* using the packed-bed arrangement intended for the assay stage in the SNO water treatment cycle. The sorption kinetics are of importance because they determine the size of column needed to extract efficiently from a given flow rate of water (see Section 2.4).

The equilibrium of a sorption reaction may be characterised by a *distribution coefficient*, $k_d$, which is defined by considering a mass of absorber brought into equilibrium with an active solution. Then

$$k_d \equiv \frac{A_{abs}}{A_{soln}} \tag{5.18}$$

where $A_{abs}$ and $A_{soln}$ are *specific* activities of the absorber and aqueous phases respectively.

The importance of the distribution coefficient can be seen by considering the idealised case of a column long compared to the length necessary to obtain near-complete extraction. As water moves along such a column, there will be a net adsorption of active species onto the $MnO_2$ in those regions of the column where the rate of adsorption exceeds the rate of desorption. After a long length of column has been traversed, therefore, the solution comes into equilibrium with the absorber and the specific activities of solution and absorber are related by:

$$\frac{A_{res}}{A_{soln}} = k_d \tag{5.19}$$

where $A_{res}$ is the residual specific activity initially present at active sites on the absorber due to contamination with the active species. Hence the effluent concentration from an infinite column is given by:

$$A_{\infty} = \frac{A_{res}}{k_d} \tag{5.20}$$

This makes explicit the importance of the distribution coefficient: together with the level of contamination present in the absorber, it dictates the ultimate level of purity attainable by passing the solution through an absorbing column. An investigation of this parameter was therefore required in order to fully characterise the anticipated performance of $MnO_2$ absorbers in the SNO experiment, and to specify acceptable levels of impurities. In this section are reported experiments which attempt to obtain values of $k_d$ from Equation (5.18) for Thorium and Radium between $MnO_2$ and water.

### 5.4.1 Radium equilibration experiments

#### Experimental

The measurement of a distribution coefficient requires that known masses of solution and absorber be brought into equilibrium, and their respective activities then measured. The method used must thus contact an absorber sample with a spiked solution in a suitable vessel and allow the sorption reaction to proceed. Since the solid absorber sinks to the bottom of the vessel, agitation is clearly required in order to prevent the setting up of concentration gradients which would greatly slow the reaction. Gently agitated conical flasks were used by Phillips *et al.* [89] and Beaven *et al.* [90] in their work on the preparation and adsorption properties of a number of sorbents, including $MnO_2$.

The method adopted for bringing into equilibrium an active solution and an absorber sample was to contain the two phases in a polyethylene bottle, normally of a nominal $1l$ capacity and either square or circular cross-section, and to rotate it 'end-over-end' at 33 rpm. This was found to keep the $MnO_2$-loaded beads suspended in the volume and, since the bottles were never quite full, the liquid was easily seen to be thoroughly mixed. An apparatus was built which held two such bottles and enabled pairs of such experiments to be conducted in parallel.

All the 'shaking experiments' reported here were conducted at pH $\simeq$ 7, since this is the condition of direct relevance to the SNO experiment. The experimental procedure consisted of preparing the absorber samples, preparing the spiked solution, allowing the two to come into equilibrium, separating the two phases, preparing sources for gamma-counting and finally determining the activity of each. Each stage is specified in more detail below.

**Preparation of absorbers** At the time of the shaking experiments, it was well known that contacting $MnO_2$ beads with pure water moved the pH of the water towards alkalinity and that to minimise this effect, absorbers needed to be conditioned to the pH of the experiment. This was achieved by standing the samples (of dry mass between $0.25g$ and $2.0g$) overnight in neutral 0.1M $NaNO_3$: their pH was measured after this treatment and was in every case within 0.4pH of neutrality.

**Preparation of solutions** $^{226}$Ra-spiked solutions were prepared by addition of accurately known masses[2] of stock $^{226}$Ra solution, of specific activity $23.9kBq\,l^{-1}$ in 1.3M HCl, to $\simeq 1000g$ of $\simeq$ 0.1M Sodium Nitrate. The solutions were weighed to an accuracy of $0.1g$ before addition of the spike. The spiked solutions, whose initial pH was around 2.5, were then carefully neutralised by addition of dilute Sodium Hydroxide. The final pH's of the solutions, before addition of the absorber sample, were between 6.7 and 7.0 in every case. More precise adjustment was difficult because small added quantities of alkali gave rise to large pH changes in the neighbourhood of pH7, and an error on the acid side was preferable since it made allowance for the anticipated pH drift towards alkalinity during the equilibration.

**Equilibration** After neutralisation of the solution, the absorber sample was added and the agitation begun. The time allowed for equilibration was either 20 or 24 hours. The pH of the solution was measured after this time had elapsed in 4 of 6 cases: it was found to have drifted slightly alkaline, to between pH7.15 and pH7.45.

The results of Beaven *et al.* suggest that for many absorbers, this length of time allows a reasonably close approach to equilibrium, sufficient for a preliminary measurement of $k_d$. In particular, they find that $MnO_2$ at pH8 has achieved equilibrium within 24 hours in almost all the cases studied. In most cases equilibrium was achieved in 1 or 2 hours. Approach to equilibrium was in all cases markedly slower at pH2. Their experiments follow the time evolution of the activity in the aqueous phase by regular sampling and so gain some kinetic information. This approach requires the use of much higher activities and was not adopted here. Consequently, the closeness of approach to equilibrium could not be definitely determined, although the results obtained here, together with those of Beaven *et al.* suggest that equilibrium was at least approximately achieved.

**Phase separation** After shaking, separation of the phases was effected by slowly pumping, using a peristaltic pump, the solution through a $1\mu$ membrane filter into a clean bottle of identical type. After filtration, the $MnO_2$-loaded beads were decanted from the original vessel into a third identical bottle. In most cases, the filter accumulated a brown deposit of $MnO_2$, representing some fraction of the absorbing material: in order properly to account for the activity adsorbed onto this fraction, the filter was removed, after filtration, from its housing and placed in the same bottle as the bulk of the absorber sample. Three separate sources were therefore generated for counting by each equilibration experiment: the filtrate, the absorber and the shaking vessel,

---

[2] A syringe whose movement was controlled with a micrometer was used to decant the aliquots of stock $^{226}$Ra solution, allowing a precision of 1 part in 1600 to be obtained with the quantities used for these experiments.

corresponding to the three possible fates of the initial spike — remaining in solution, adsorption onto the $MnO_2$ and adsorption onto the container walls. Although only the water/$MnO_2$ equilibrium is of interest, a third phase — the container walls — has unavoidably been introduced into the system.

**Preparation of sources** The three sources generated by the phase separation procedure were counted using the Ge(Li) apparatus described in Section 4.3, and it was thus of the highest importance to ensure that all could be brought into comparable counting geometries. Excepting further processing, the filtrate's geometry was fixed, *ie.* a uniform distribution of activity throughout its volume, in a container of given shape. The remaining two samples had therefore to be brought into the same, or a comparable, geometry. Since Moore and Reid [96] report that strong acid elutes Radium from $MnO_2$, the absorber samples were allowed to stand in strong nitric acid overnight, a treatment which visibly removed all $MnO_2$ from the acrylic beads. The acid was then topped up to the same level as in the filtrate container. As a precaution against further sorption onto the container walls, the filtrate was also acidified. The activity on the walls of the shaking vessel could in principle have been dissolved up into the same volume of mild acid, but since the amount of such activity was expected to be small, this was not done, effectively enhancing the this component of the signal relative to the others. Finally, the screw-tops of all bottles were sealed with silicone rubber in the threads, as a precaution against outward diffusion of $^{222}Rn$ along this path.

**Counting** The 352keV gamma-ray in the decay of $^{214}Pb$ was used as a measure of the activity of each source. Each was counted twice using the Ge(Li) apparatus described in Section 4.3. The first activity measurement was made about 700-1000 hours after the creation of the source, and the second after 2300-3000 hours. These two measurements do not serve to provide a meaningful determination of the two parameters involved *viz.* the initial $^{220}Rn$ and $^{226}Ra$ contents of the source — an exact fit can always be obtained, but may yield a meaningless result such as a very high initial $^{222}Rn$ content. The procedure which was therefore adopted was to take the second measurement as definitive, and relegate the first to the status of a rough consistency check. No correction was made for the half-life of $^{226}Ra$, as the effect was at the $10^{-3}\%$ level and the accuracy of the measurements was typically $\simeq 1\%$ for the most active sources and $\geq 30\%$ for the filtrates.

Table 5.14 presents the details of the equilibration experiments which were carried out, listing the weights of $MnO_2$ and solution used, the type of container and the time for which the agitation proceeded.

### Results and analysis

The measured activities of the 352keV gamma-ray are listed for every source generated by these experiments in Table 5.15, before adjustments for detector background. The most noticeable feature of the results is that in every case, the activity in the filtrate is very small,

| Run ID | Duration<br>*hrs* | Mass Solution<br>*g* | Mass $MnO_2$<br>*/mg* | Mass spike<br>*mg* |
|---|---|---|---|---|
| EQ1 | 20 | 1000 | 955 | 1600 |
| EQ2 | 20 | 1000 | 1048 | 3200 |
| EQ3 | 24 | 1000 | 453 | 1600 |
| EQ4 | 24 | 1000 | 1957 | 1600 |
| EQ5 | 20 | 500 | 247 | 1600 |
| EQ6 | 20 | 500 | 475 | 1600 |

Table 5.14: Experimental conditions for the six equilibration experiments.

| Expt.# | Bottle | Filtrate | Solids |
|---|---|---|---|
| 1 | 0.00879±0.00072 | 0.00004±0.00035 | 0.1001±0.0013 |
| 2 | 0.00667±0.00063 | 0.00067±0.00043 | 0.1973±0.0018 |
| 3 | 0.01579±0.00076 | 0.00004±0.00042 | 0.0939±0.0012 |
| 4 | 0.00299±0.00040 | 0.00081±0.00047 | 0.0992±0.0012 |
| 5 | 0.00760±0.00046 | 0.00061±0.00033 | 0.1098±0.0014 |
| 6 | 0.00624±0.00046 | 0.00142±0.00030 | 0.11864±0.00085 |

Table 5.15: The measured 352keV gamma-ray activities, in counts per second, of each source generated by the equilibration experiments, with $1\sigma$ errors. The raw data are presented, uncorrected for background or differences of counting geometry.

indeed consistent with background[3]. The activity held on the container walls, while generally small compared to the activity held on the solid phase sorbent, is clearly non-zero.

A natural conclusion from these observations is that the equilibria for the the water/absorber and water/walls reactions lie, in both cases, far from the aqueous phase *ie.* at equilibrium, the concentration of activity in solution is very much lower than in the other, sorbed, phase. We may also conclude that the sorption reaction onto the $MnO_2$ proceeds much faster than onto the walls of the container, not a surprising result in view of the demonstrated affinity of $MnO_2$ for Radium. The low aqueous activities also demonstrate, incidentally, that a negligible amount of adsorbed activity passes the filtration stage into the filtrate, implying that the activity loss onto $< 1\mu$ particles is insignificant.

In the cases of equilibration experiments conducted in containers of the same size, intercomparison of the total detected activity was a meaningful check for unanticipated $^{226}$Ra losses. After correction for different attenuation of gamma-rays from the empty and water-filled bottles, and after background subtraction and normalisation of the amounts of added Radium, these comparisons yield mutual agreement to better than 5% for runs 1–3, and to

---

[3] Counter background in the case of runs 5&6 were higher than for the other runs.

|  | $k_d/10^5$ |
|---|---|
| EQ1 | $> 0.99$ |
| EQ2 | $> 2.15$ |
| EQ3 | $> 1.76$ |
| EQ4 | $> 0.56$ |
| EQ5 | $> 1.48$ |
| EQ6 | $> 1.42$ |

Table 5.16: 95% c.l. lower limits on $k_d$ deduced from the the Radium-$MnO_2$ equilibration experiments, assuming equilibrium.

about 10% for runs 5–6, so that no very large Radium losses are revealed.

The data may be analysed under the simplest assumption, that a close approach to equilibrium has been made. In this case the ratio

$$k_d \equiv \frac{A_{abs}}{A_{soln}}$$

may be evaluated, where $A_{abs}$ and $A_{soln}$ are the adsorbed activity and that remaining in solution, respectively, and both are *specific* activities, that is activities per unit mass, and both are by definition measured at equilibrium.

Taking account of the counter background $B$, the expression for $k_d$ becomes

$$k_d = \frac{(A_{abs} - B)}{(A_{soln} - B)} \frac{M_{soln}}{M_{abs}} \tag{5.21}$$

where the A's are now count rates of 352keV gamma-rays in the Ge(Li) apparatus, and the M's are masses of the two phases. Since the observed activities of the liquid phase are consistent with background, it is clear that only a limit may be placed on $k_d$. The probability distribution of $A_{soln} - B$ overlaps the non-physical region of negative values, so the analysis method used follows that recommended by the Particle Data Group [71]. Accordingly, the probability content of the distribution lying in the physical region was normalised to unity, and the value below which 95% of this probability lay was considered to be a 95% confidence upper limit for the parameter. This corresponded to a 95% c.l. lower limit for $k_d$, and the resulting values for each of the six equilibration experiments are given in Table 5.16.

### 5.4.2 Thorium equilibration experiments

The $k_d$ which characterises Thorium adsorption onto $MnO_2$ is at least as significant for SNO as that for Radium. Experiments similar to those described above were therefore carried out using Thorium instead of Radium. The Thorium isotope used was $^{234}$Th, the 24-day half-life daughter of $^{238}$U. It decays by $\beta^-$ emission with associated production of two strong gamma-ray lines at 63 and 92keV. The advantage of this isotope over $^{228}$Th for this work is that, since the diagnostic radiations are produced directly by $^{234}$Th decay, there is no delay while daughter isotopes come into equilibrium, as would be the case with $^{228}$Th/$^{224}$Ra.

As in the case of Radium/$MnO_2$ equilibration, active solutions were shaken with known amounts of absorber, the two phases separated and then counted. Many of the experimental details were common to the two series of experiments and will not be repeated here. In this section, whenever activities of sources are compared, they have always been extrapolated to a common reference time: this is, in each case, taken as the time at which shaking of the source/absorber mixture ceased. The procedure was made necessary by the relatively short half-life of $^{234}$Th.

### Experiments and results

**Th/$TiO_2$** Beaven *et al.* [90] have demonstrated that hydrous titanium oxide is capable of removing from solution a range of species between pH2 and pH11, although it does not show at any pH the rapid approach to equilibrium exhibited by $MnO_2$ under neutral and alkaline conditions. Two forms of $TiO_2$ were therefore shaken with $^{234}$Th solutions.

A 200$ml$ sample from 1$l$ $^{234}$Th stock solution was neutralised by careful addition of dilute Sodium Hydroxide. It was split into two 100$ml$ volumes which were made up with water to $\simeq$ 600$ml$ volume. A sample of $\simeq$ 1$g$. HTiO (hydrous titanium oxide[4] — a fine, hydrated precipitate) was added to one solution and $\simeq$ 1$g$. OXTi (coarse anhydrous grains of $TiO_2$) to the other. The solutions were shaken for 26 hours and pumped through a 1$\mu$ membrane filter. The HTiO filtrate was found to be pH7.0, whereas the OXTi filtrate had drifted to pH8.3, despite pre-conditioning of both absorbers.

The two filtrates were retained in polyethylene bottles identical to those in which the Th/$TiO_2$ shaking was carried out, and were acidified after pH measurement in order to avoid Thorium plate-out. The filters used to separate the phases were placed in the containers in which the respective samples had been shaken, together with such solids as remained in the containers. Concentrated nitric acid was added to dissolve the solids, and then diluted to a final volume of 600$ml$.

The four active sources thus generated by this trial were counted in the shielded Ge(Li) apparatus described in Section 4.3. The 92keV radiation was used to assay $^{234}$Th, being subject to slightly less background than the 63keV line.

Both varieties of $TiO_2$ absorber were found to extract Thorium from solution. Defining the extraction efficiency as the ratio

$$\frac{A_{abs}}{A_{abs} + A_{fil}}$$

it is found to be 43.1 ± 3.7% for HTiO and 26.7 ± 2.8% for OXTi, where $A_{abs}$ is the activity of the absorber and $A_{fil}$ is that of the filtrate. Summing the activities of the two sources generated by each of the two experiments, it is found that the $A_{abs} + A_{fil}$

---

[4] generously supplied by E.W. Hooper.

are equal within statistical errors, suggesting that no Thorium remains unaccounted for.

The higher apparent extraction afforded by HTiO sample is in accordance with *prima facie* expectations of the sorption kinetics, *ie.* that a more finely divided absorber of comparable mass should extract activity from solution more quickly. The experiment is subject to the criticism, however, that it is not known whether filtration to $1\mu$ is sufficient to remove from the filtrate all the fines associated with the absorber sample: the observed activity in the filtrate could be attributed to Thorium adsorbed onto particles less than $1\mu$ in size.

**Th/MnO$_2$ (#1)** Further Thorium sorption experiments were carried out using $MnO_2$ as the sorbent since an equilibration experiment could be used to investigate whether the equilibrium or kinetic properties of the Thorium sorption process were limiting Thorium sorption in the FLOW trials. Seakem $MnO_2$ also has the advantage that it is not associated with any visible amounts of fines.

Dissolved Sodium Nitrate was found to have a buffering effect on the usual tendency for $MnO_2$ samples to drive a solution alkaline. Two $^{234}$Th-activated solutions were thus made up from $200ml$ water and $100ml$ 0.5M Sodium Nitrate, before $200ml$ stock $^{234}$Th solution was carefully added to each. Both were then neutralised so that the shaken solutions were of $500cm^3$ volume, 0.1M $NaNO_3$ and pH7. Finally a $\simeq 1g$ sample of $MnO_2$ was added to each and the containers shaken for 24 hours.

After shaking, the solutions were filtered to $1\mu$ as before and the filtrates acidified after pH measurement (both were slightly alkaline). The bulk of the $MnO_2$ remained in the shaken container during filtration, but a brown colour on the filter membranes showed that some fines had been retained on them. The membranes were added to the $MnO_2$ beads, the $MnO_2$ dissolved in nitric acid and finally diluted to $500cm^3$ volume. As before, this procedure brought adsorbed Thorium into the same geometry for gamma-counting as Thorium in the filtrate.

All four active sources were counted in the shielded Ge(Li) apparatus described in Section 4.3. The amounts of activity observed in the filtrates were consistent with background and corresponded to no more than 1% of the activities of the respective absorber samples. The absorber samples themselves, however, were found to differ in activity by a factor of $\simeq 1.4$, despite the equality, to better than 1%, of the volumes of stock $^{234}$Th solution used.

Possible explanations for this result include —

1. Inhomogeneity of the stock Thorium solution,
2. Incorrect placing of a source in the Ge(Li) cave,
3. Thorium plate-out in containers used temporarily to hold the filtrates, and
4. Thorium retention on the acrylic beads after the $MnO_2$ was dissolved.

The second and third of the above possibilities were easily demonstrated not to be significant by repeating measurements and counting the temporary holding containers. The fourth possibility was tested by separating the solution from the beads and re-counting the solution: the result showed no significant change (at about 2% statistical accuracy). The tubing used during the filtration was also counted and found to be clean.

The possibility that the stock might have been inhomogeneous, or stratified, was investigated by counting two samples of known masses: they were found to differ in specific activity by a factor of 1.14. In this case, as in that of the two shaken solutions, the second sample to be decanted was the more active, which would be consistent with the settling of aggregates of hydrolysed Thorium atoms. The hypothesis of inhomogeneity is also consistent with the significantly different methods of source preparation used in this and the above $Th/TiO_2$-shaking experiment. In the $Th/TiO_2$ case, a sample was removed from the stock $^{234}$Th bottle and then neutralised, a process involving repeated addition of Sodium Hydroxide aliquots followed by vigorous shaking to mix the solution. In the second case, stock solution was poured carefully into the bottles to be shaken, so that an accurately known weight $\simeq 200g$ could be decanted into each. It is therefore reasonable to conclude that the stock $^{234}$Th solution spontaneously became inhomogeneous on standing. The measured pH of the solution was 6.0.

The low Thorium concentrations observed in the filtrate suggest that dissolved Thorium may be effectively removed from solution by $MnO_2$, given a sufficiently long contact time.

**$Th/MnO_2$ (#2)** Since the strength of Thorium solutions cannot be relied upon, and since Thorium was known to plate out of solution onto the walls of a container, a further equilibration experiment was performed to take account of these effects.

An accurately known mass ($\simeq 200g$) of stock $^{234}$Th solution was placed in a $250ml$ capacity bottle, acidified and counted in the Ge(Li) apparatus. As before, it was diluted so as to make up $500ml$ of 0.1M Sodium Nitrate solution which was finally neutralised. A $MnO_2$ sample of mass $0.99g$ was added to the solution and the mixture shaken for 17 hours. Its pH was then measured to be 7.6. The solution was filtered to $1\mu$, as before, and the filtrate acidified.

The $MnO_2$ beads were removed from the $600ml$ capacity bottle in which the equilibration occurred and placed in a 250cc capacity bottle identical to that in which the source solution had been counted prior to dilution. Concentrated nitric acid was used to dissolve the $MnO_2$ off the beads, and later diluted to $200ml$. The shielded Ge(Li) apparatus described in Section 4.3 was used to count this bottle: by comparison with the rate due to the whole shaken source, an extraction efficiency of 52.6% was deduced. The filtrate was similarly counted and found to contain $< 0.1\%$ of the source activity. A quick check discovered substantial Thorium on the walls of the shaken vessel. This was dissolved in $100ml$ nitric acid, poured into a separate $250ml$ vessel and diluted to 200*ml*. Counting as before showed that it contained 42.32 ± 0.79% of the total Thorium.

Further tests showed that the washed shaking vessel was inactive, and thus that the acid wash effectively removed adsorbed Thorium from the walls, the tubing used during filtration was inactive and that the bottle used to store the source solution for around 24 hours prior to shaking contained $\simeq 0.6\%$ of the total Thorium. The total Thorium thus accounted for is approximately 96% of the total contained in the source.

**Th/MnO$_2$ (#3)** To test the reproducibility of the previous Thorium/MnO$_2$ equilibration experiment, a further experiment identical in most respects was carried out. The same mass of MnO$_2$ was used and the final pH of the solution was 7.1.

Of the total activity measured, it was found that the solids contained 91.9 ± 1.4%, the walls of the container 6.52 ± 0.14%, and the bottle in which the source had been temporarily stored 1.53 ± 0.20%. The filtrate, as before, was found to contain no significant Thorium. The total activity observed was consistent with no Thorium loss, to within the approximately 5% accuracy with which the source activity was known.

The differences are obvious between this experiment and the previous one, in fractions of Thorium observed on the walls of the vessel and adsorbed onto the MnO$_2$. They suggest either that

1. the two samples of MnO$_2$ behave differently — they were taken from different containers of the 8810-02 production batch, or that
2. the two source solutions, taken from the same $^{234}$Th stock container at the same time, were chemically different. They were known to have different specific activities, thus conclusively demonstrating inhomogeneity in the stock solution, and if this were attributed to settling of Thorium complexes, then the more active solution would be richer in heavier aggregates.

The pronounced tendency for Thorium to plate out onto the walls of a container, demonstrated by this series of experiments, prevents any conclusions being drawn regarding the distribution coefficient $k_d$ of Thorium between water and MnO$_2$: it is not possible to assume that the aqueous and adsorbed phases are even approximately in equilibrium.

# Chapter 6

# The operation of SNO and treatment of radiogenic backgrounds

## 6.1 Prospects for the use of $MnO_2$ in SNO background measurements

### 6.1.1 Radon de-emanation from $MnO_2$

It appears from Figure 5.2 that $^{220}$Rn extraction from a $MnO_2$ column takes very low values at low BVM flow rates and may tend towards an asymptote not lower than 65%. The data are consistent with the simple model outlined in Section 5.1 and fit to the values of the parameters $\alpha, \beta$ given in Equation (5.7):

$$\begin{aligned} \alpha &= 0.7219 \pm 0.0050 \\ \beta &= 0.0411 \pm 0.0011 \end{aligned}$$

If the model of that section is used to account for the value of $\beta$, *ie.* that it is due to repeated adsorption and desorption of Radon atoms, then an estimate may be obtained of the fractional time which $^{220}$Rn atoms spend free to drift in a $MnO_2$ column which has been treated in the usual manner. We may set, according to the model,

$$\beta = \frac{\xi}{1 - f_p} \tag{6.1}$$

where $\xi$ is the fractional free time. If $f_p = 0.9$, then $\xi = 0.0041$ and $^{220}$Rn is free to drift for less than 0.5% of its time in a bed of $MnO_2$!

The use of different column sizes in the disappearance experiments has afforded a certain amount of evidence that BVM flow rate is a genuine scale variable: the two runs performed with a $0.54 cm^3$ column yield points which lie on the curve defined by runs performed with a $13 \cdot 2 cm^3$ column. This is again consistent with the simple model. On the basis of the fitted values of $\alpha, \beta$, we may use Equation (5.6) to calculate the $^{220}$Rn extraction efficiencies from columns under the conditions typically used for CPC operation, when the Ar/Me flow rate through the columns was about $1000 cm^3 min^{-1}$. The difference in calculated extraction efficiencies for large and small columns is approximately 15%, which was a significant correction.

The high value of $\alpha$, representing the escape probability of $^{220}$Rn from the $MnO_2$ bead where it was created, was unexpected. A plane $MnO_2$ surface on which $^{224}$Ra atoms lie before decay would imply $\alpha = 0.5$. If the parent atom had been implanted deeper into the surface by $^{228}$Th decay, then $\alpha < 0.5$ would be expected. That $\alpha$ is so high may be connected with surface roughness of the $MnO_2$ or with scattering of the recoiling daughter. It is easily seen, in the extreme case, that a $^{224}$Ra atom at the tip of a needle-shaped structure has a chance > 50% of decaying to a free Radon atom. Similarly, a Radium atom lying on a thin 'wall' of $MnO_2$ (only a few atoms thick) could have an enhanced chance of producing a free daughter if the daughter's recoil range is greater than the wall's thickness. If scattering of the recoiling daughter is significant, then it could only enhance the escape probability of an inwards-directed decay product.

A rough surface is a reasonable assumption in view of the fact that $MnO_2$ is known to have a favoured direction of crystal growth and furthermore that the hydrated form is expected to have a very disorganised surface.

### 6.1.2 The kinetics of Thorium and Radium sorption onto $MnO_2$

**Radium** Figure 5.4 collects together the Radium sorption data from the FLOW trials. It is the most important collection of results in the present work. The principal conclusions which may be drawn from it are:

- The high-pH trials (FLOW3 at pH7 and FLOW7 at pH9) show Radium extraction which, it is probably safe to conclude, is around 90% by $\mathcal{R} = 5s$. The possibility exists that cleaner $MnO_2$ could increase this figure. These are clearly the experiments of most relevance to SNO, which will operate at pH7.

- In a clearly distinct class are FLOW6 and FLOW8, both at pH2. The much slower kinetics exhibited by these runs suggest that at low pH, the equilibrium constant for the sorption process has shifted away from the adsorbed phase, as expected on the basis of Moore's demonstration that acid conditions elute Radium from $MnO_2$.

- There is some suggestion in the data that FLOW4 Radium extraction (buffered pH4) is slower than FLOW3 and FLOW7. If true, this would suggest a small pH dependence of Radium extraction even at pH4-7. A small difference between buffered and unbuffered pH4 measurements might then also be expected (FLOW4 and FLOW5), but any such difference is too small to be readily apparent in the data.

From this data we may estimate a suitable residence time in a $MnO_2$ bed which will give reasonably efficient extraction. If an efficiency not less than 80% is required, then a cautious estimate of the required residence time is 3*s*, to be implemented in SNO. This corresponds to a flow rate of 20BVM, which is high by the standards of commercial ion exchange plants, which are required to deliver essentially quantitative extraction. Here it is required only to assay the stream, rather than to purify it in the same process.

**Thorium** The prospects for Thorium monitoring using $MnO_2$-loaded beads are clearly much poorer than for Radium. The results of the FLOW trials imply unambiguously that Thorium extraction at near-neutral pH is relatively slow. Figures 5.5 and 5.6 summarise the information, and a number of points may be noted:

- The A-Column data show that, even at pH2, the Thorium extraction kinetics are inferior to Radium. A clear pH-dependence is apparent in Figure 5.5, with the pH2 runs being fastest and pH7&9 slowest. The reasons for the FLOW5 runs forming an intermediate case were discussed in Section 5.2. There is in addition some indication in Figure 5.5 that FLOW4 is rather slower than the pH2 runs, showing a continued pH dependence below pH4.

  In view of the known chemical properties of Thorium — its tendency to hydrolyse and even polymerise in near-neutral solutions — it is natural to identify the active, low-pH form of Thorium with a partially-hydrolysed, charged species and the inactive, high-pH form with the fully-hydrolysed, uncharged form. The extent of hydrolysis of the active form is not established, although the fact that Thorium extraction at pH2 is nearly as efficient as Radium at pH7 suggests that Thorium at pH2 has a mean charge of around +2, in agreement with the findings of Cotton and Wilkinson [73].

- The FLOW7 Columns 2A&3A, drawn from a different production batch to the other samples, show Thorium extraction which is anomalously high in comparison with Columns 1A&4A. Their Radium extractions may also be high. These data, together with observations reported in Section 3.2 concerning the water content of resin samples, make it clear that the manufacturing process is not reproducible, and that this can have a real effect on the sorption properties of the resin.

- The FLOW5 (unbuffered pH4) data shed some light on the response of Thorium to changes of pH caused by contact with the resins. That the FLOW5 extraction is slower than FLOW4 has been accounted for, and it demonstrates that Thorium responds quite quickly to pH change, at least in the case of increasing pH. The same effect can also be seen in the FLOW5 B-column data, Figure 5.6, in the clear suppression of Thorium extraction as residence time in the A-column increases.

### 6.1.3 Equilibria of the sorption reactions

Manganese Dioxide and Titanium Dioxide have both been shown to act as sorbents for Thorium, and $MnO_2$ has been shown to be capable of giving good extraction, although poor reproducibility. It is clear that a full investigation of Thorium sorption would require much more careful control of the chemical condition of the solution at neutral pH. An investigation under acid conditions, say around pH3 or 4, would be much easier but of less relevance to SNO. An important consequence of Thorium's tendency to plate out of solutions is that, presumably, dissolved Thorium in SNO would deposit onto any available surface, including the pipework of the water recirculation system, thus rendering it unavailable for assay by water sampling.

The complete extraction of Thorium from solution observed in the $MnO_2$ equilibration experiments suggests that the limited extraction observed in FLOW3 (pH7) is not limited by the equilibrium constant for the reaction

$$\mathrm{Th_{(aq)}} \rightleftharpoons \mathrm{Th_{(ads)}}$$

*ie.* that Thorium does not necessarily have a very different equilibrium constant to Radium for adsorption onto $MnO_2$. We may thus tentatively conclude either that the kinetics of the above reaction are very much poorer than is the case for Radium, or that the Thorium extractions measured in the FLOW trials were limited by the rate of a (slow) reaction of the form

$$\mathrm{Th_{(inactive)}} \longrightarrow \mathrm{Th_{(active)}} \tag{6.2}$$

where 'inactive' refers to a form of Thorium not readily extracted onto $MnO_2$ and 'active' indicates the converse. As above, the inactive form may be tentatively identified with the fully-hydrolysed species and the active form with a charged species. This in no way conflicts with the observation above that Thorium reacts quickly to an increase in pH, by hydrolysing, as Reaction (6.2) is the reverse of that reaction. Indeed, the two statements are consistent with the known fact that Reaction (6.2) is displaced far to the left at neutral pH.

It is also clear that Thorium at neutral pH is a very difficult species to work with. Its tendency to form inhomogeneous solutions suggests that even at low concentrations it may aggregate and settle out of solution, from which it would follow that the chemical state of a Thorium solution may vary with time. The aging of Thorium solutions has, in fact, been demonstrated by Hietanen and Sillén [76] and appears in their data to be more pronounced at the lowest Thorium concentration they used, 0.25mM. The experience gained with Thorium under neutral pH conditions reinforces the conclusion reached above that the behaviour of Thorium in the SNO detector will not be known until the detector is in operation.

### 6.1.4 Other properties of $MnO_2$–loaded beads

As noted previously, the pH of a solution which comes into contact with the $MnO_2$ resins, unless effectively buffered, is increased. This is attributed to the injection of $K^+$ into solution, and is not surprising in view of the known Potassium content of the resins. Injection by an absorber in SNO of any ions into the water stream is undesirable since, at best, it imposes an additional load on the polisher. It has a further drawback in that it also prevents the absorber being used as a final stage in the water polisher plant in the event that the conventional polisher does not give sufficiently high rejection of a particularly important species, such as Radium. Similar considerations apply to any absorber — the species it injects into the stream must be investigated as well as its efficiency for removal of selected species. The injection by the resins of fine particles into the stream was also demonstrated. This behaviour would be most undesirable in SNO and if $MnO_2$ is to be used, must be prevented.

### 6.1.5 The use of $MnO_2$–loaded beads in SNO

This section brings together the results reported in Chapter 5, together with the background-monitoring requirements developed in Chapter 2, to model the way in which packed $MnO_2$ beds might be used in SNO. The results of Chapter 4 are relevant only in that they demonstrate the feasibility, and reasonable efficiency, of $^{220}$Rn-counting. The purpose of such a model is to investigate the optimum conditions of use.

An individual $MnO_2$–loaded cartridge undergoes two processes — it is first exposed to the outlet stream of the detector, when it is activated, and then to a gas stream for counting of the de-emanated Radon. There are a number of variables in this process:

1. The water flow rate, which influences the efficiency of Radium extraction, by the results of Section 5.2.
2. The gas flow rate, which influences the efficiency of Radon de-emanation, by the results of Section 5.1 and its detection efficiency in the proportional chamber.
3. The sample volume which, with the above two factors, influences both the Radium extraction efficiency and the Radon de-emanation efficiency.
4. The proportional counter's sensitive volume, which influences the Radon detection efficiency, *via* its residence time in the sensitive volume.
5. The time for which the sample is exposed to the water flow, which determines the number of Radium atoms collected in the sample.
6. The time for which it is exposed to the gas stream, which determines the number of Radium atoms decaying to potentially detectable Radon atoms.

The first stage of the process may be modelled by setting up the equation for Radium accumulation by a column in the water flow:

$$\frac{dN}{dt} = \eta_a C F_w - \lambda N \tag{6.3}$$

which has the solution

$$N_a = \frac{\eta_a C F_w}{\lambda} [1 - \exp(-\lambda t_a)] \tag{6.4}$$

In these equations $F_w$ is the water flow rate, $\lambda$ the decay constant of $^{224}$Ra, $\eta_a$ the efficiency for adsorption of Radium, $C$ the concentration of dissolved activity and $N_a$ the number of adsorbed atoms after time $t_a$.

The second stage may be modelled by an expression for the number of detected Radium atoms (irrespective of the method of detection) after a time $t_d$,

$$\begin{aligned} N_d &= N_a \eta_d [1 - \exp(-\lambda t_d)] \\ &= \frac{\eta_a \eta_d C F_w}{\lambda} [1 - \exp(-\lambda t_a)] [1 - \exp(-\lambda t_d)] \qquad (6.5) \end{aligned}$$

in which $\eta_d$ is the overall detection efficiency for a Radium decay. It has been assumed that a negligible interval elapses between extraction and counting, *ie.* that the problem of quickly drying large volumes of resin is solved, for example by using a microwave oven.

Were the aim of the assay and counting procedure to gain as accurate a measure of the activity in the outlet stream as possible, then the column would be left in stream for a long period, to come into equilibrium, and then counted for a long period, to allow all the adsorbed Radium atoms to decay. At both these stages, however, it is clear that returns diminish after a time similar to a $^{224}$Ra half-life: in the first case, the sample activity is hardly changing and in the second, very few Radium atoms remain to be detected. In both cases, therefore, it is clear that the sample should be changed after this time. Simply maximising the number of counts obtained from a sample is not an appropriate metric for the effectiveness of the procedure.

A better metric would be the rate at which detected Radium atoms were removed from the detector, averaged over the time for collection plus the time for counting. This can be seen as maximising the rate at which information is obtained. It also allows real-time monitoring of the detector, a requirement stated in Section 2.5, whereas pursuit of the highest possible statistical accuracy does not. Applying this criterion to the problem of determining suitable extraction and counting times amounts to maximising $N_d/T$ where $T = t_a + t_d$. The unsurprising result is that the maximum occurs at $t_a = t_d = T/2$, which is valid irrespective of the values of $\eta_a$ and $\eta_d$.

Substituting these values into Equation (6.5) yields for the averaged rate of accumulation of detected events

$$R_d^* = \frac{N_d}{T} = \frac{\eta_a \eta_d C F_w}{\lambda} \frac{[1 - \exp(-\lambda T/2)]^2}{T} \qquad (6.6)$$

in which form it is clear that there is an optimum time $T$ for the extraction/count cycle. By numerically solving $\partial R_d^* / \partial T = 0$, the non-trivial solution is found to be $\lambda T \simeq 2.512$ so that the whole cycle should last $2.512 t_{1/2} / \ln 2 = 3.624 t_{1/2}$.

Expressions for $\eta_a$ and $\eta_d$ are now required. The proportional counter to be used in SNO has a $50l$ volume[1]; if it is assumed to be 100% efficient throughout this volume $V_d$ then, from Equation (5.6),

$$\eta_d = \alpha\beta \frac{F_g}{V_r} \tau \left[ 1 - \exp\left( -\frac{V_r}{\beta F_g \tau} \right) \right] \left[ 1 - \exp\left( -\frac{V_d}{F_g \tau} \right) \right] \qquad (6.7)$$

in which $F_g$ is the gas flow rate through the cartridge, $V_r$ the resin volume, $\alpha$ and $\beta$ are defined in Section 5.1 and $\tau$ is the exponential time constant for Radon decay. For given

---

[1] It is a Time Projection Chamber with cartesian geometry, in contrast to the CPC.

resin and detector volumes there must be an optimum gas flow rate, but it is obviously not expressible in closed form.

To obtain $\eta_a$ as a function of $\mathcal{R}$, and hence of water flow rate and resin volume, the data of Figure 5.4 must be modelled by an analytic expression:

$$\eta_a = \left[1 - \exp\left(-\frac{V_r}{F_w \tau_{ex}}\right)\right] \tag{6.8}$$

in which $\tau_{ex}$ is the time constant associated with the extraction of Radium by $MnO_2$ at pH7.

Equation (6.8) states that the Radium extraction efficiency of a $MnO_2$ column is related to residence time through an exponential time constant. Modelling the data of Section 5.2 with such exponentials, or with any functional form, has hitherto been avoided: the limited number of points available, their limited accuracy (in many cases) and the uncertain influence of Thorium plate-out suggest that the data could not really test such a model, although it is a very reasonable one. For the purposes of this calculation *only*, an estimate of $\tau_{ex}$ was calculated under the assumption that the limiting adsorption is essentially 100% — approximately true for Radium. The FLOW3 and FLOW7 Radium data were amalgamated for this purpose as there is no reason to believe in a pH-dependence of Radium sorption in the pH7–9 range. (Burgess [85] gives $pK_1$ values for the alkaline earth metals, and the trend clearly shows that no formation of Radium Hydroxide is likely except under extremely alkaline conditions). A non-linear least squares fit (using MINUIT) to the data yields $\tau_{ex} = 1.063 \pm 0.015s$ . The data were not weighted by their respective standard deviations, as it is clear from Figure 5.4 that they do not lie on the same curve. The quoted error on $\tau_{ex}$ thus derives from the scatter of the points.

The variables in Equations (6.7) and (6.8) are the resin sample volume, the water flow rate during the extraction stage and the gas flow rate during the counting stage. The product $\eta_a \eta_d F_w$ in Equation (6.5) was maximised with respect to these variables, completing the solution for the optimum conditions of use of $MnO_2$ in SNO. MINUIT was again used for this purpose.

For $\tau_{ex} = 1.063 \pm 0.015s$ and $F_w < 150 l\, min^{-1}$ the solution is

$$\begin{aligned} V_r &= 2.83 l \\ F_w &= 150.0 l\, min^{-1} \\ F_g &= 35.1 l\, min^{-1} \end{aligned}$$

It can be seen that the highest possible $F_w$ has been selected *ie.* the statistical accuracy obtainable is limited by the flow rate at which the water can be re-circulated. This is a consequence of the fast kinetics of Radium sorption by $MnO_2$. $F_g$ is surprisingly low at well under 20BVM, but still yields a residence time in the detector of under two half-lives. Clearly a compromise is reached between de-emanation efficiency and detection efficiency. The detected activity of the $MnO_2$ sample at commencement of counting may be calculated and is $18.0d^{-1}$ .

Repeating the optimisation using a very conservative $\tau_{ex} = 4.0s$ changes the optimum operating conditions to

$$V_r = 6.57l$$
$$F_w = 150.0l\,min^{-1}$$
$$F_g = 56.9l\,min^{-1}$$

and so does not alter the conclusion that $R_d^*$ is limited by the capability of the water recycling plant. The initial detected activity is in this case $7.7d^{-1}$ . It can be seen how good extraction kinetics increase the available signal by decreasing the required resin volume and so increasing the achievable Radon detection efficiency.

## 6.2 The experimental programme for SNO

Of the three principal reaction mechanisms (electron scattering and the neutral and charged currents) available to solar neutrinos in SNO, the electron scattering reaction gives rise to the most easily distinguished events. It has been demonstrated by the Kamiokande detector that the forward-peaked distribution of electron trajectories can be used to resolve these events from an isotropic background. The separation of neutral current disintegration events from charged current absorption events will present a much greater difficulty if discrete neutron detectors cannot be implemented.

In the absence of discrete neutron detectors, the Čerenkov signal due to NC events is an energetically broad, isotropic peak resulting from Compton scattering of capture gamma-rays. The CC signal is only weakly anisotropic — the directional asymmetry is two-to-one backward-to-forward. The peak is again energetically broad. The sum of these two signals, after subtraction of the ES spectrum, is therefore weakly anisotropic and is superimposed on an isotropic background.

As currently envisaged, the experimental programme to be carried out with the SNO detector consists of three phases. Phase 1 will be a light water fill of the entire detector, both inner and outer sections. During this phase, the detector will only be capable of recording the ES reaction as there is no absorption of $\nu_e$ by free protons. This phase will constitute a pilot run of the detector systems in addition to obtaining a measurement of the ES rate. The isotropic radiogenic background will also be measured and may be compared with the levels of Thorium and Radium detected in water from the inner and outer regions of the detector. This will allow a check of the Monte Carlo calculations which predict the backgrounds arising from known levels of activity.

Phase 2 of the proposed experimental programme replaces the light water in the central volume with heavy water, but without any neutron-capturing additive. In the absence of any neutron absorber, the almost pure heavy water captures about 25% of neutrons produced, a factor of three fewer than would be captured within the acrylic sphere if 0.25% NaCl were added. In this phase the CC rate would be measured with as little NC contamination as possible. The ES rate would also be observable, allowing a check for changes since the first phase.

The introduction of NaCl as a neutron absorber in the third experimental phase has two beneficial effects. Firstly it increases the neutron capture probability within the heavy water (pure $D_2O$ allows about 50% of neutrons to leak into the $H_2O$, there to be rapidly and undetectably captured) and secondly it increases the energy of the peak in the Compton electron spectrum resulting from capture gamma-rays [56]. Both effects increase the detectable NC rate.

However, it is clear that during Phase 3 it will not be possible to distinguish between CC and NC interactions in real time, event-by-event, by studying their individual PMT hit patterns alone. Determination of the isotropic NC rate and anisotropic CC rate by analysis of the overall weakly anisotropic distribution of events, superposed on a (presumably) isotropic background would be very uncertain. Instead, Phase 2 and Phase 3 data will be used in conjunction to infer a NC event rate during Phase 3. The Phase 3 ES rate, easily separable from the remainder of the signal, will be used to infer the Phase 3 CC rate, from a relation between ES and CC rates established during Phase 2. The ES rate during Phase 3 also serves as a monitor of possible changes in the neutrino flux. From the total Phase 3 non-ES event rate, it will then be possible to deduce a NC rate by subtraction of the inferred CC rate and the background, which should by that time be well understood. The accuracy with which the NC rate is thus determined seems likely to be limited by statistical accuracy.

Distributed neutron detection using NaCl, for example, suffers from the disadvantage that the method of detection is rather indirect: a neutrino interaction produces a free neutron which is captured. The resulting capture gamma-rays Compton scatter to produce fast electrons, which in turn radiate Čerenkov photons. The use of discrete neutron detectors would reduce the scope for contamination of the NC signal by restricting background processes intrinsic to the SNO detector to those which actually generate free neutrons. Backgrounds inherent in the neutron detectors are of course introduced but these, at least in principle, may be adequately suppressed by a development programme prior to their introduction into SNO. Measurements of background rates in discrete neutron detectors could be made, perhaps on an individual basis, before their installation so that the necessity for uncertain subtractions of two event rates in SNO is removed — this is their key advantage over a distributed neutron absorber.

Discrete neutron detectors thus make Phase 2 unnecessary since their signal does not interfere with the CC rate in the $D_2O$. Furthermore, if neutron detectors were installed in time for the light water fill, a good *in situ* measurement of their intrinsic background rates would be obtained, increasing confidence that the background rate during the NC measurement was well known. Discrete detectors could thus provide a clean measurement of the NC signal with little possibility of contamination by events produced by the CC or ES reactions. Provision is therefore being made in the design of the acrylic sphere for attachment points on its lower hemisphere for strings of neutron detectors, so that they could be installed at any time during the operational life of the experiment.

## 6.3 The monitoring of radiogenic backgrounds in SNO

### 6.3.1 Self-monitoring by reconstruction

The principal reason why SNO needs a capability for accurate event reconstruction is to make it possible to veto events located outside the fiducial volume. However, in addition to this function, event reconstruction capabilities would lend themselves to use as a tool for self-monitoring of background sources within the detector, which are not necessarily accessible to external measurements nor measurable before the detector is completed.

An example of such a background source would be an isolated sheet or sheets of acrylic which are dirtier than average, due to some inhomogeneity in the source material or non-reproducibility in the manufacturing process. (Quality control procedures will implemented in an attempt to minimise the risk of this). A second possibility is that mine dust or other contaminants become sealed in the joints between acrylic sheets during fabrication of the sphere. Either cause would give rise to a permanent, localised region generating more copious gamma-ray and Čerenkov light fluxes than the surrounding regions. Such an eventuality could be detected by off-line data analysis, since that region would produce more events than nearby regions. When the problem has been identified and quantified, it would be possible to make corrections for it by subtracting the excess event rate in the final data analysis.

Temporary localised regions in which the activity is anomalously high might, if they are sufficiently long-lived, also be detected. This should be regarded as a real possibility since an obvious potential cause of such an effect is the formation of eddies in the region between the acrylic and PMT spheres or outside the PMT sphere. Such a flow pattern, if it were stable and little mixed with the surrounding water, could easily accumulate leachates and act as a long-lived, localised source of activity. Its lifetime could be limited by periodic mixing with the remaining water. If recognised, then a sufficiently flexible and controllable water recirculation system could be adjusted to prevent it recurring.

### 6.3.2 Water flow pattern

Although the water flow pattern in SNO has been modelled, as noted in Section 2.4, it is not clear how applicable a simplified model will be to the real detector[2]. If an independent (of the detector) method of determining the concentration of dissolved radioisotopes is to be available, then assay of the water is necessary and, as established in Section 2.5, outlets to the extraction apparatus must be provided at the PMT sphere. For possible inhomogeneities in the dissolved activity within the PMT sphere to be detectable, then several such outlets should be provided as alternative routes to the assay plant. If such a scheme were implemented, it would provide additional information to that gained from SNO's event reconstruction capability by assaying the activity in a number of regions and so assessing the

---

[2] In particular, the light water outside the PMT sphere will contain the PMT support structure, the cabling to the PMT's and probably struts anchoring the support structure to the cavity wall. All of this will break the cylindrical symmetry assumed in simple models.

homogeneity of the dissolved activity.

A potential problem with any attempt to assay water within the PMT sphere, or anywhere in the detector, is that the very act of pumping a sample from the cavity disturbs the activity distribution which is to be measured, by disturbing the flow pattern. In a region of the cavity where the water is well mixed, flow velocities are high and conditions turbulent – the conditions expected outside the PMT sphere – this is probably not important. However, within the PMT sphere, conditions *must* be arranged such that inwards flow is avoided completely and flow patterns are laminar. Under these conditions, flow velocities at the PMT sphere are $\sim 10^{-6} ms^{-1}$: such a flow velocity is clearly easily disrupted. A sample pipe at the PMT sphere, therefore, will certainly disrupt the local flow pattern and risks suck-back of water from the outer to the inner sphere, with a consequent false measurement of the activity within the PMT sphere.

The PMT sphere will be designed, however, to offer a high impedance to water flow (see Section 2.4) as this appears to be necessary to prevent convective movements and inward flow within it. This will certainly limit any suck-back during sampling, but a natural extension of this would be to render the sphere permeable in the outward direction only, by making it impermeable except at discrete points where one-way valves could be fitted. This would prevent any suck-back during sampling and, more importantly, prevent any inward movement of water during routine operation. Free movement must, however, be allowed at at least one point, to avoid any possibility of a pressure difference building up across the PMT sphere in the event of, for example, a pump failure.

It is also worth considering the injection of a tracer into the cavity as a test of the water flow characteristics. Such a substance would be injected into the inflow in controlled amounts for a short duration. Its concentration-time profile at each of several outlets could then be studied. Its time of first arrival at the outflows from the inner sphere would test uniform radial flow and identify any stagnant regions. The distribution of residence times of water within the cavity would also be measured.

Such a tracer would clearly have to be detectable in small quantities to be valuable, and would have to satisfy a number of other requirements in addition. In view of the nature of the detector, it would absolutely have to be non-radioactive. It would have to be chemically fairly inert so as to run no risk of damaging the acrylic or other components of the detector, nor could it be UV-absorbing. A substance capable of detection by chemical methods at the *ppm* level is a possibility, but an isotopic tracer would be ideal, although requiring a mass spectrometer (not necessarily located in the mine). No attempt is known to have been made to identify suitable tracers, as it is not a critical item at this stage in the experiment's development, but if mass spectrometry were used then there is potentially a large number of possibilities among salts of medium-weight nuclei, or possibly dissolved gases such as Argon.

### 6.3.3 External monitoring of Radium and Thorium

**Radium** Radium monitoring in SNO using a $MnO_2$ sorbent seems, from the results of Chapter 5, to present little problem. It was examined in detail above. A problem which has not been mentioned hitherto is that a mechanism exists by which $MnO_2$, or any other sorbent or extraction plant, can act as a *source* of dissolved activity. Both isotopes of Radium decay to Radon and it is possible that an absorber which is loaded with Radium will release its daughter into solution. This is discussed in more detail below.

**Thorium** The monitoring of Thorium by assay external to the detector presents much more serious problems than does Radium. The known chemistry of Thorium, and the observations made in the course of this work, imply that the Thorium concentration of the outlet stream does not necessarily reflect that in the detector, since some fraction of Thorium could plate out onto the surfaces of any pipe-work with which it comes into contact, prior to assay. A substantial length of such pipe will be present if the assay stage is close to the purifier, which will be well removed from the detector. In the worst case, in which Thorium accumulates in the outlet piping, the level of Radium which it generates would eventually exceed that in the assay stream, a potential problem.

Conversely, the same chemical properties which could remove Thorium from the stream between the cavity and assay stage, might be expected to minimise the extent to which Thorium is leached, since by hypothesis it has little tendency to migrate away from a solid surface. Thorium levels in solution (measured in $Bq\,l^{-1}$) might thus be much lower than Radium levels. No work is known which establishes Thorium leaching rates from solids.

It is also clear that the chemical form of any dissolved Thorium in SNO is very hard to predict, and may be dependent on the source of the isotope and on the presence of other leached species. As noted in Section 3.1, the presence of anions can greatly enhance the solubility of Thorium, and so, presumably, its tendency to leach. Assuming that a charged species results, however, its availability for sorption onto $MnO_2$ or an ion exchange resin would correspondingly be enhanced.

Finally, the observation that Thorium will under some circumstances plate out onto relatively inert surfaces such as membrane filters [110] or acrylic wool (Section 5.2) suggests that Thorium extraction from both inlet and outlet streams might be achieved by simple filtration, although this will doubtless depend on its chemical form. A conclusion from the present work is that Thorium solutions at near-neutral pH can behave unpredictably, and it seems likely that the chemical form, and concentration, of dissolved Thorium in SNO will not be known until the detector is built.

### 6.3.4 Extraction of radioisotopes from the inlet stream

The present work has concerned the requirement to assay the outflow from the SNO cavity: $^{228}$Th and $^{224}$Ra were shown to be the isotopes which yielded information concerning troublesome gamma-ray generation in the detector. The aspect not considered was the effect of radioisotopes injected into the detector at the inflow, having permeated the polisher stage. Since it is intended to inject the purest water next to the acrylic sphere, any radioisotopes present in this stream will be damaging. A true index of the degree of damage is the the rate of events reconstructing into the heavy water resulting from an inflow containing a given specific activity of the isotope *ie.* to 'level the playing-field' between the members of a decay chain, the chain is supposed to be in secular equilibrium. The problem is not simple as competing effects are present. Short-lived species ($^{212}$Bi, $^{212}$Pb) decay in the neighbourhood of the acrylic sphere and so have a high probability of generating a background event from each decay. Longer-lived species ($^{224}$Ra, $^{228}$Th) however, decay on average further from the boundary and have a greater chance of leaving the inner $H_2O$ sphere without decaying, but their presence sustains the level of activity in the water for a longer time. The one clear conclusion is that accurate event reconstruction will benefit the detector by reducing backgrounds from this source.

The special case of Radon deserves consideration since it seems certain to permeate any conventional polisher plant and is produced, as noted above, by adsorbed Radium or by leaching into the water of the outer cavity. $^{220}$Rn leaving the cavity will probably decay to a chemically active form before reaching the final polisher stage, and so be retained, but if produced in the polisher stage this may not occur and its descendant would then reach the cavity. $^{222}$Rn is worse in this respect, as it will almost certainly reach the cavity whether it originates in the outer cavity or in the assay or polisher stages.

Clearly the rate at which Radon activity is generated by an absorber can never exceed that at which Radium activity is deposited onto it, so that the water quality can never be worsened by this process. A serious problem could arise, however, if a water purifier which is used to decontaminate $H_2O$ from the outer sphere then injects the stream into the inner cavity, as is intended.

It is also known that components of the detector emanate $^{222}$Rn, and the emanation and permeation of Radon by materials is an active subject of research by the collaboration ([91] and other reports). It is currently thought that removal of $^{222}$Rn from the water stream before injection into the cavity is essential as the levels expected to be injected onto the outer sphere are far too high to be re-cycled into the inner sphere. Vacuum de-gassing and gas bubbling are methods of Radon extraction currently under investigation.

# Appendix A

# Collected results of FLOW trials

This Appendix presents the activity data resulting from Cylindrical Proportional Chamber measurements of Manganese Dioxide samples activated in the course of FLOW trials, including FLOW1 and FLOW2 which are not reported in the main text because the CPC was not functioning correctly during early measurements on these samples. The unreliable data have been suppressed in Tables A.1 and A.2.

## A.1 Raw activity data

Tables A.1 to A.9 list the time in hours between the creation of the sample and the measurement, together with the rate of $^{220}$Rn events in the chamber.

| Column 1A | | Column 1B | |
|---|---|---|---|
| time/hrs. | rate/$s^{-1}$ | time/hrs. | rate/$s^{-1}$ |
| 554.5 | 0.1968 ± 0.0145 | 554.0 | 0.6935 ± 0.0409 |
| 696.9 | 0.1892 ± 0.0165 | 696.6 | 0.6855 ± 0.0379 |
| Column 2A | | Column 2B | |
| time/hrs. | rate/$s^{-1}$ | time/hrs. | rate/$s^{-1}$ |
| 555.6 | 0.3974 ± 0.0291 | 555.4 | 1.0889 ± 0.0604 |
| 698.0 | 0.3238 ± 0.0235 | 697.8 | 1.1134 ± 0.0558 |
| Column 3A | | Column 3B | |
| time/hrs. | rate/$s^{-1}$ | time/hrs. | rate/$s^{-1}$ |
| 573.0 | 0.1474 ± 0.0129 | 572.8 | 0.5706 ± 0.0437 |
| 717.9 | 0.1626 ± 0.0131 | 717.6 | 0.6245 ± 0.0325 |
| Column 4A | | Column 4B | |
| time/hrs. | rate/$s^{-1}$ | time/hrs. | rate/$s^{-1}$ |
| 575.0 | 0.1206 ± 0.0147 | 574.7 | 0.3773 ± 0.0302 |
| 720.0 | 0.1335 ± 0.0107 | 719.6 | 0.3886 ± 0.0246 |

Table A.1: Measurements of $^{220}$Rn event rates in the Cylindrical Proportional Chamber due to columns activated in the FLOW1 experiment.

| Column 1A | | Column 1B | |
|---|---|---|---|
| time/hrs. | rate/$s^{-1}$ | time/hrs. | rate/$s^{-1}$ |
| 339.4 | $0.2626 \pm 0.0173$ | 339.1 | $0.4656 \pm 0.0281$ |
| 505.6 | $0.1308 \pm 0.0107$ | 505.1 | $0.5175 \pm 0.0219$ |
| 601.6 | $0.0968 \pm 0.0092$ | 601.3 | $0.4366 \pm 0.0278$ |
| Column 2A | | Column 2B | |
| time/hrs. | rate/$s^{-1}$ | time/hrs. | rate/$s^{-1}$ |
| 356.9 | $0.1968 \pm 0.0126$ | 356.5 | $0.3016 \pm 0.0215$ |
| 524.6 | $0.1259 \pm 0.0093$ | 524.2 | $0.3058 \pm 0.0227$ |
| 602.2 | $0.1073 \pm 0.0093$ | 601.8 | $0.3094 \pm 0.0148$ |
| Column 3A | | Column 3B | |
| time/hrs. | rate/$s^{-1}$ | time/hrs. | rate/$s^{-1}$ |
| 359.4 | $0.1269 \pm 0.0117$ | 359.1 | $0.2840 \pm 0.0220$ |
| 603.6 | $0.0665 \pm 0.0080$ | 602.7 | $0.2324 \pm 0.0162$ |
| Column 4A | | Column 4B | |
| time/hrs. | rate/$s^{-1}$ | time/hrs. | rate/$s^{-1}$ |
| 408.6 | $0.1176 \pm 0.0101$ | 361.1 | $0.2850 \pm 0.0114$ |
| 604.5 | $0.0704 \pm 0.0079$ | 604.1 | $0.1857 \pm 0.0170$ |

Table A.2: Measurements of $^{220}$Rn event rates in the Cylindrical Proportional Chamber due to columns activated in the FLOW2 experiment.

| Column 1A | | Column 1B | |
|---|---|---|---|
| time/hrs. | rate/s$^{-1}$ | time/hrs. | rate/s$^{-1}$ |
| 23.4 | 3.9887 ± 0.1492 | 23.2 | 0.2912 ± 0.0182 |
| 172.1 | 1.6539 ± 0.0743 | 171.7 | 0.9142 ± 0.0554 |
| 311.3 | 0.7482 ± 0.0326 | 311.0 | 1.0235 ± 0.0380 |
| 599.0 | 0.4295 ± 0.0256 | 598.5 | 1.1285 ± 0.0486 |
| 671.1 | 0.4077 ± 0.0214 | 670.8 | 1.0553 ± 0.0542 |

| Column 2A | | Column 2B | |
|---|---|---|---|
| time/hrs. | rate/s$^{-1}$ | time/hrs. | rate/s$^{-1}$ |
| 23.5 | 3.3022 ± 0.1175 | 23.3 | 0.9272 ± 0.0559 |
| 172.6 | 1.1690 ± 0.0529 | 172.4 | 0.5922 ± 0.0407 |
| 312.5 | 0.5107 ± 0.0283 | 312.2 | 0.5029 ± 0.0282 |
| 600.2 | 0.1989 ± 0.0131 | 599.8 | 0.4711 ± 0.0229 |
| 672.4 | 0.1999 ± 0.0131 | 672.0 | 0.5455 ± 0.0303 |

| Column 3A | | Column 3B | |
|---|---|---|---|
| time/hrs. | rate/s$^{-1}$ | time/hrs. | rate/s$^{-1}$ |
| 24.6 | 3.0704 ± 0.1017 | 24.4 | 1.1604 ± 0.0574 |
| 173.2 | 1.0226 ± 0.0534 | 172.9 | 0.6294 ± 0.0365 |
| 315.3 | 0.4204 ± 0.0224 | 315.0 | 0.4524 ± 0.0232 |
| 601.6 | 0.1555 ± 0.0115 | 601.2 | 0.3972 ± 0.0211 |
| 673.5 | 0.1309 ± 0.0089 | 673.0 | 0.3678 ± 0.0178 |
| 770.5 | 0.1370 ± 0.0090 | 770.0 | 0.3663 ± 0.0176 |

| Column 4A | | Column 4B | |
|---|---|---|---|
| time/hrs. | rate/s$^{-1}$ | time/hrs. | rate/s$^{-1}$ |
| 25.4 | 0.0506 ± 0.0089 | 24.5 | 3.9565 ± 0.1287 |
| 173.9 | 0.1268 ± 0.0149 | 173.6 | 1.9906 ± 0.0916 |
| 316.6 | 0.1437 ± 0.0113 | 316.0 | 1.7511 ± 0.0700 |
| 603.2 | 0.1318 ± 0.0108 | 602.7 | 1.3257 ± 0.0352 |
| 675.2 | 0.1324 ± 0.0087 | 674.4 | 1.1869 ± 0.0578 |
| 771.0 | 0.1266 ± 0.0094 | 770.4 | 1.1691 ± 0.0440 |

Table A.3: Measurements of $^{220}$Rn event rates in the Cylindrical Proportional Chamber due to columns activated in the FLOW3 experiment.

| Column 1A | | Column 1B | |
|---|---|---|---|
| time/hrs. | rate/s$^{-1}$ | time/hrs. | rate/s$^{-1}$ |
| 22.4 | $5.1790 \pm 0.2079$ | 22.2 | $0.3952 \pm 0.0260$ |
| 116.0 | $5.2784 \pm 0.1713$ | 115.4 | $0.5447 \pm 0.0302$ |
| 355.1 | $4.8167 \pm 0.1636$ | 354.9 | $0.6221 \pm 0.0324$ |
| 524.0 | $4.6633 \pm 0.1251$ | 523.8 | $0.6389 \pm 0.0329$ |
| 642.6 | $4.8962 \pm 0.0954$ | 642.3 | $0.6761 \pm 0.0339$ |

| Column 2A | | Column 2B | |
|---|---|---|---|
| time/hrs. | rate/s$^{-1}$ | time/hrs. | rate/s$^{-1}$ |
| 22.7 | $3.6526 \pm 0.1427$ | 22.5 | $1.5233 \pm 0.0800$ |
| 116.8 | $3.7020 \pm 0.1245$ | 116.7 | $1.9254 \pm 0.0802$ |
| 356.0 | $3.3608 \pm 0.1189$ | 355.8 | $2.0981 \pm 0.0764$ |
| 525.6 | $3.2635 \pm 0.1045$ | 525.4 | $2.1954 \pm 0.0858$ |
| 643.0 | $2.8990 \pm 0.0988$ | 642.7 | $2.0967 \pm 0.0840$ |

| Column 3A | | Column 3B | |
|---|---|---|---|
| time/hrs. | rate/s$^{-1}$ | time/hrs. | rate/s$^{-1}$ |
| 23.6 | $3.8233 \pm 0.1460$ | 23.5 | $1.6680 \pm 0.0840$ |
| 117.7 | $3.3050 \pm 0.1176$ | 117.5 | $1.9693 \pm 0.0687$ |
| 359.5 | $3.0519 \pm 0.1314$ | 359.1 | $2.3566 \pm 0.0892$ |
| 526.6 | $2.9961 \pm 0.1003$ | 526.2 | $2.4756 \pm 0.0915$ |
| 645.8 | $2.9839 \pm 0.1003$ | 645.7 | $2.3826 \pm 0.0899$ |

| Column 4A | | Column 4B | |
|---|---|---|---|
| time/hrs. | rate/s$^{-1}$ | time/hrs. | rate/s$^{-1}$ |
| 24.9 | $2.4991 \pm 0.1037$ | 24.7 | $2.5678 \pm 0.1203$ |
| 120.0 | $2.4139 \pm 0.1014$ | 119.8 | $2.8221 \pm 0.1090$ |
| 360.4 | $2.2389 \pm 0.0972$ | 360.2 | $3.0027 \pm 0.1123$ |
| 527.6 | $2.0847 \pm 0.0841$ | 527.5 | $3.0349 \pm 0.1015$ |
| 646.3 | $2.2819 \pm 0.0883$ | 646.0 | $2.9886 \pm 0.0918$ |
| | | 646.6 | $2.7346 \pm 0.0966$ |

Table A.4: Measurements of $^{220}$Rn event rates in the Cylindrical Proportional Chamber due to columns activated in the FLOW4 experiment.

| Column 1A | | Column 1B | |
|---|---|---|---|
| time/hrs. | rate/$s^{-1}$ | time/hrs. | rate/$s^{-1}$ |
| 22.2 | 3.2403 ± 0.1041 | 20.8 | 0.0248 ± 0.0026 |
| 49.9 | 3.0912 ± 0.1020 | 49.1 | 0.0444 ± 0.0062 |
| 166.7 | 2.0320 ± 0.0752 | 165.8 | 0.0852 ± 0.0057 |
| 356.5 | 1.3302 ± 0.0471 | 355.8 | 0.1029 ± 0.0076 |
| 523.5 | 1.3196 ± 0.0447 | 522.9 | 0.1074 ± 0.0071 |

| Column 2A | | Column 2B | |
|---|---|---|---|
| time/hrs. | rate/$s^{-1}$ | time/hrs. | rate/$s^{-1}$ |
| 24.3 | 2.7108 ± 0.0955 | 22.8 | 0.7085 ± 0.0345 |
| 50.1 | 2.2291 ± 0.0872 | 49.7 | 0.6778 ± 0.0282 |
| 168.0 | 1.3905 ± 0.0483 | 166.8 | 0.4584 ± 0.0161 |
| 358.2 | 0.8024 ± 0.0189 | 357.4 | 0.3615 ± 0.0189 |
| 382.2 | 0.8459 ± 0.0360 | 381.7 | 0.3092 ± 0.0145 |
| 547.1 | 0.8083 ± 0.0261 | 523.8 | 0.3471 ± 0.0140 |
| | | 546.3 | 0.3332 ± 0.0097 |

| Column 3A | | Column 3B | |
|---|---|---|---|
| time/hrs. | rate/$s^{-1}$ | time/hrs. | rate/$s^{-1}$ |
| 24.9 | 1.8977 ± 0.0461 | 24.4 | 1.4187 ± 0.0490 |
| 45.6 | 1.6439 ± 0.0526 | 45.0 | 1.1982 ± 0.0451 |
| 168.4 | 0.9589 ± 0.0287 | 168.0 | 0.7211 ± 0.0262 |
| 383.7 | 0.5465 ± 0.0249 | 382.5 | 0.4649 ± 0.0200 |
| 525.4 | 0.4840 ± 0.0203 | 524.9 | 0.4431 ± 0.0173 |

| Column 4A | | Column 4B | |
|---|---|---|---|
| time/hrs. | rate/$s^{-1}$ | time/hrs. | rate/$s^{-1}$ |
| 25.7 | 1.3948 ± 0.0633 | 25.3 | 1.5988 ± 0.0625 |
| 46.4 | 1.2089 ± 0.0450 | 45.9 | 1.5502 ± 0.0432 |
| 169.3 | 0.6609 ± 0.0240 | 168.7 | 0.8198 ± 0.0307 |
| 384.5 | 0.3080 ± 0.0147 | 383.9 | 0.5394 ± 0.0192 |
| 548.8 | 0.3333 ± 0.0139 | 526.8 | 0.4218 ± 0.0157 |
| | | 547.3 | 0.4406 ± 0.0174 |

Table A.5: Measurements of $^{220}$Rn event rates in the Cylindrical Proportional Chamber due to columns activated in the FLOW5 experiment.

| Column 1A | | Column 1B | |
|---|---|---|---|
| time/hrs. | rate/s$^{-1}$ | time/hrs. | rate/s$^{-1}$ |
| 22.2 | $2.4379 \pm 0.0824$ | 21.7 | $1.3071 \pm 0.0468$ |
| 50.0 | $2.6817 \pm 0.0673$ | 49.4 | $1.2077 \pm 0.0455$ |
| 166.3 | $3.3806 \pm 0.0970$ | 165.8 | $0.6333 \pm 0.0230$ |
| 338.0 | $3.3098 \pm 0.1058$ | 337.1 | $0.3210 \pm 0.0140$ |
| 504.5 | $3.3455 \pm 0.1057$ | 504.0 | $0.2673 \pm 0.0115$ |
| 914.3 | $3.6702 \pm 0.1111$ | 912.5 | $0.2233 \pm 0.0104$ |

| Column 2A | | Column 2B | |
|---|---|---|---|
| time/hrs. | rate/s$^{-1}$ | time/hrs. | rate/s$^{-1}$ |
| 23.5 | $1.4759 \pm 0.0456$ | 22.9 | $2.0808 \pm 0.0660$ |
| 50.5 | $1.7906 \pm 0.0557$ | 49.8 | $1.9946 \pm 0.0558$ |
| 167.9 | $2.5267 \pm 0.0727$ | 166.9 | $1.5617 \pm 0.0512$ |
| 338.2 | $2.8459 \pm 0.0894$ | 337.7 | $1.1743 \pm 0.0448$ |
| 504.6 | $2.8983 \pm 0.0898$ | 338.6 | $1.2210 \pm 0.0468$ |
| 914.8 | $2.8422 \pm 0.0830$ | 504.2 | $1.0986 \pm 0.0430$ |
| | | 914.1 | $1.1190 \pm 0.0348$ |

| Column 3A | | Column 3B | |
|---|---|---|---|
| time/hrs. | rate/s$^{-1}$ | time/hrs. | rate/s$^{-1}$ |
| 25.1 | $0.7676 \pm 0.0336$ | 24.8 | $2.9763 \pm 0.0707$ |
| 45.4 | $0.9209 \pm 0.0325$ | 45.0 | $2.9575 \pm 0.0909$ |
| 169.4 | $1.3794 \pm 0.0397$ | 168.4 | $2.7690 \pm 0.0763$ |
| 333.5 | $1.3901 \pm 0.0508$ | 333.1 | $2.0743 \pm 0.0760$ |
| 505.1 | $1.6138 \pm 0.0521$ | 504.8 | $2.2829 \pm 0.0524$ |
| 525.3 | $1.7104 \pm 0.0536$ | 525.0 | $2.2437 \pm 0.0794$ |
| 910.7 | $1.5834 \pm 0.0516$ | 910.4 | $2.2971 \pm 0.0694$ |

| Column 4A | | Column 4B | |
|---|---|---|---|
| time/hrs. | rate/s$^{-1}$ | time/hrs. | rate/s$^{-1}$ |
| 25.4 | $0.4980 \pm 0.0271$ | 25.2 | $2.9643 \pm 0.1000$ |
| 47.2 | $0.6473 \pm 0.0238$ | 46.4 | $3.2357 \pm 0.1041$ |
| 170.2 | $0.9598 \pm 0.0336$ | 169.8 | $2.8441 \pm 0.0984$ |
| 335.3 | $0.9642 \pm 0.0329$ | 334.7 | $2.3988 \pm 0.0761$ |
| 505.8 | $1.1923 \pm 0.0452$ | 505.4 | $2.9700 \pm 0.1001$ |
| 526.0 | $1.1808 \pm 0.0503$ | 506.1 | $2.8736 \pm 0.0985$ |
| 909.3 | $1.1353 \pm 0.0399$ | 525.7 | $2.6541 \pm 0.0943$ |
| | | 908.5 | $2.7628 \pm 0.0647$ |

Table A.6: Measurements of $^{220}$Rn event rates in the Cylindrical Proportional Chamber due to columns activated in the FLOW6 experiment.

| Column 1A | | Column 1B | |
|---|---|---|---|
| time/hrs. | rate/$s^{-1}$ | time/hrs. | rate/$s^{-1}$ |
| 48.2 | $1.9878 \pm 0.0576$ | 52.7 | $0.3473 \pm 0.0136$ |
| 53.3 | $1.9252 \pm 0.0577$ | 67.8 | $0.3584 \pm 0.0165$ |
| 68.3 | $1.6523 \pm 0.0527$ | 187.4 | $0.4507 \pm 0.0159$ |
| 188.3 | $0.7023 \pm 0.0244$ | 361.7 | $0.4547 \pm 0.0160$ |
| 362.4 | $0.2768 \pm 0.0104$ | 695.2 | $0.4743 \pm 0.0163$ |
| 696.2 | $0.1533 \pm 0.0069$ | 1007.3 | $0.4521 \pm 0.0159$ |
| 1008.5 | $0.1461 \pm 0.0060$ | | |

| Column 2A | | Column 2B | |
|---|---|---|---|
| time/hrs. | rate/$s^{-1}$ | time/hrs. | rate/$s^{-1}$ |
| 49.1 | $2.0417 \pm 0.0586$ | 48.3 | $0.3356 \pm 0.0114$ |
| 69.5 | $1.8320 \pm 0.0508$ | 69.0 | $0.3562 \pm 0.0139$ |
| 167.2 | $0.9712 \pm 0.0329$ | 166.7 | $0.3399 \pm 0.0138$ |
| 363.2 | $0.3378 \pm 0.0178$ | 362.7 | $0.2942 \pm 0.0124$ |
| 699.2 | $0.2124 \pm 0.0074$ | 697.7 | $0.3256 \pm 0.0117$ |
| 1010.5 | $0.1923 \pm 0.0082$ | 1009.1 | $0.3048 \pm 0.0108$ |

| Column 3A | | Column 3B | |
|---|---|---|---|
| time/hrs. | rate/$s^{-1}$ | time/hrs. | rate/$s^{-1}$ |
| 50.5 | $1.6121 \pm 0.0499$ | 49.8 | $0.6714 \pm 0.0197$ |
| 70.1 | $1.4668 \pm 0.0459$ | 69.8 | $0.6341 \pm 0.0239$ |
| 167.8 | $0.7834 \pm 0.0318$ | 167.4 | $0.4259 \pm 0.0190$ |
| 380.9 | $0.2470 \pm 0.0130$ | 380.4 | $0.2976 \pm 0.0130$ |
| 671.3 | $0.1356 \pm 0.0088$ | 670.5 | $0.2341 \pm 0.0126$ |
| 1055.1 | $0.1258 \pm 0.0056$ | 1053.3 | $0.2527 \pm 0.0068$ |

| Column 4A | | Column 4B | |
|---|---|---|---|
| time/hrs. | rate/$s^{-1}$ | time/hrs. | rate/$s^{-1}$ |
| 51.2 | $0.6498 \pm 0.0240$ | 50.8 | $1.3460 \pm 0.0421$ |
| 68.1 | $0.5277 \pm 0.0219$ | 67.7 | $1.2060 \pm 0.0456$ |
| 189.8 | $0.2032 \pm 0.0097$ | 188.0 | $0.5789 \pm 0.0171$ |
| 383.7 | $0.1025 \pm 0.0046$ | 382.3 | $0.2479 \pm 0.0104$ |
| 673.1 | $0.0705 \pm 0.0046$ | 672.0 | $0.1667 \pm 0.0083$ |
| 1058.0 | $0.0774 \pm 0.0036$ | 1056.2 | $0.1617 \pm 0.0069$ |

Table A.7: Measurements of $^{220}$Rn event rates in the Cylindrical Proportional Chamber due to columns activated in the FLOW7 experiment.

| Column 1A | | Column 1B | |
|---|---|---|---|
| time/hrs. | rate/s$^{-1}$ | time/hrs. | rate/s$^{-1}$ |
| 25.1 | $1.8905 \pm 0.0512$ | 24.8 | $1.6449 \pm 0.0524$ |
| 51.7 | $1.9853 \pm 0.0576$ | 51.3 | $1.5151 \pm 0.0504$ |
| 361.2 | $2.8439 \pm 0.0975$ | 360.7 | $0.7234 \pm 0.0275$ |
| 867.8 | $2.6334 \pm 0.0857$ | 867.2 | $0.6546 \pm 0.0234$ |
| 1127.5 | $2.4684 \pm 0.0911$ | 1127.0 | $0.6023 \pm 0.0232$ |
| 1558.4 | $2.4778 \pm 0.0831$ | 1557.8 | $0.6062 \pm 0.0225$ |

| Column 2A | | Column 2B | |
|---|---|---|---|
| time/hrs. | rate/s$^{-1}$ | time/hrs. | rate/s$^{-1}$ |
| 26.0 | $1.0575 \pm 0.0345$ | 25.1 | $2.2575 \pm 0.0614$ |
| 51.8 | $1.3838 \pm 0.0483$ | 51.4 | $1.9437 \pm 0.0572$ |
| 362.4 | $1.8976 \pm 0.0460$ | 361.9 | $1.4980 \pm 0.0501$ |
| 867.8 | $1.8182 \pm 0.0552$ | 867.4 | $1.3281 \pm 0.0472$ |
| 1127.4 | $1.9193 \pm 0.0568$ | 1127.1 | $1.3367 \pm 0.0475$ |
| 1559.7 | $1.7041 \pm 0.0536$ | 1558.0 | $1.3752 \pm 0.0479$ |

Table A.8: Measurements of $^{220}$Rn event rates in the Cylindrical Proportional Chamber due to columns activated in the FLOW8 experiment.

| Column 1A | | Column 1B | |
|---|---|---|---|
| time/hrs. | rate/$s^{-1}$ | time/hrs. | rate/$s^{-1}$ |
| 25.7 | $2.7390 \pm 0.0809$ | 24.8 | $0.0723 \pm 0.0047$ |
| 49.9 | $2.6446 \pm 0.0796$ | 48.7 | $0.0962 \pm 0.0063$ |
| 336.1 | $1.1275 \pm 0.0434$ | 335.6 | $0.1595 \pm 0.0095$ |
| 431.3 | $1.0294 \pm 0.0364$ | 432.2 | $0.1821 \pm 0.0072$ |
| 769.0 | $0.9454 \pm 0.0329$ | 768.3 | $0.2072 \pm 0.0115$ |
| 817.9 | $0.9813 \pm 0.0406$ | 816.9 | $0.1996 \pm 0.0071$ |
| 1203.1 | $0.9201 \pm 0.0256$ | 1202.2 | $0.1946 \pm 0.0089$ |

| Column 2A | | Column 2B | |
|---|---|---|---|
| time/hrs. | rate/$s^{-1}$ | time/hrs. | rate/$s^{-1}$ |
| 26.1 | $1.7954 \pm 0.0656$ | 25.5 | $0.6282 \pm 0.0225$ |
| 50.2 | $1.7043 \pm 0.0536$ | 49.5 | $0.6954 \pm 0.0247$ |
| 338.4 | $0.7241 \pm 0.0251$ | 336.8 | $0.5212 \pm 0.0241$ |
| 432.9 | $0.6654 \pm 0.0237$ | 432.3 | $0.4592 \pm 0.0198$ |
| 818.1 | $0.5918 \pm 0.0224$ | 817.6 | $0.4869 \pm 0.0204$ |
| 1225.6 | $0.5384 \pm 0.0171$ | 1224.3 | $0.4263 \pm 0.0115$ |

| Column 3A | | Column 3B | |
|---|---|---|---|
| time/hrs. | rate/$s^{-1}$ | time/hrs. | rate/$s^{-1}$ |
| 26.7 | $1.5639 \pm 0.0514$ | 25.7 | $0.0398 \pm 0.0044$ |
| 44.2 | $1.3387 \pm 0.0452$ | 43.3 | $0.0379 \pm 0.0043$ |
| 481.5 | $0.1390 \pm 0.0089$ | 480.5 | $0.0592 \pm 0.0041$ |
| 841.8 | $0.1243 \pm 0.0124$ | 841.2 | $0.0778 \pm 0.0062$ |
| 863.0 | $0.1105 \pm 0.0056$ | 866.9 | $0.0818 \pm 0.0071$ |
| 1244.8 | $0.0969 \pm 0.0058$ | 1225.7 | $0.0696 \pm 0.0045$ |

| Column 4A | | Column 4B | |
|---|---|---|---|
| time/hrs. | rate/$s^{-1}$ | time/hrs. | rate/$s^{-1}$ |
| 27.5 | $0.8371 \pm 0.0321$ | 26.9 | $0.4354 \pm 0.0160$ |
| 45.7 | $0.7333 \pm 0.0249$ | 45.0 | $0.3488 \pm 0.0145$ |
| 482.6 | $0.0685 \pm 0.0078$ | 481.9 | $0.1050 \pm 0.0066$ |
| 865.5 | $0.0592 \pm 0.0038$ | 863.9 | $0.0867 \pm 0.0047$ |
| 1247.9 | $0.0586 \pm 0.0040$ | 1246.1 | $0.0712 \pm 0.0047$ |

Table A.9: Measurements of $^{220}$Rn event rates in the Cylindrical Proportional Chamber due to columns activated in the FLOW9 experiment.

## A.2 Fitted initial Thorium and Radium activities

Tables A.10 to A.18 give, for each sample, the least-squares-fitted values of the initial activities in the sample of $^{228}$Th and $^{224}$Ra, in units of $^{220}$Rn counts per second in the CPC, after subtraction of chamber background. The limited data available for FLOW1 and FLOW2 samples allow a fit to be obtained for any choice of data, and preclude testing of the fit (there being no degrees of freedom). The fitted activities are given for these trials in the following tables, and it can be seen that estimates of the Thorium activity may be calculated, but not meaningful estimates of the Radium activity.

| | | $^{228}$Th/s$^{-1}$ | $^{224}$Ra/s$^{-1}$ |
|---|---|---|---|
| FLOW1 | Col.1A | 0.1900 ± 0.0265 | 1.0000 ± 2.6000 |
| | Col.1B | 0.7000 ± 0.0612 | 1.2000 ± 6.5000 |
| | Col.2A | 0.2960 ± 0.0393 | 8.8000 ± 4.4000 |
| | Col.2B | 1.1550 ± 0.0901 | -2.5000 ± 9.7000 |
| | Col.3A | 0.1740 ± 0.0216 | -2.0000 ± 2.5000 |
| | Col.3B | 0.6680 ± 0.0532 | -7.1000 ± 7.3000 |
| | Col.4A | 0.1430 ± 0.0187 | -1.7000 ± 2.5000 |
| | Col.4B | 0.4050 ± 0.0403 | -1.5000 ± 5.3000 |

Table A.10: Fitted initial Thorium and Radium activities of the columns of trial FLOW1.

|  |  | $^{228}$Th/s$^{-1}$ | $^{224}$Ra/s$^{-1}$ |
|---|---|---|---|
| FLOW2 | Col.1A | $0.0771 \pm 0.0107$ | $2.8000 \pm 0.3200$ |
|  | Col.1B | $0.4950 \pm 0.0235$ | $0.2700 \pm 0.5800$ |
|  | Col.2A | $0.0973 \pm 0.0103$ | $1.7800 \pm 0.2900$ |
|  | Col.2B | $0.3160 \pm 0.0168$ | $0.1200 \pm 0.4900$ |
|  | Col.3A | $0.0574 \pm 0.0110$ | $1.2500 \pm 0.2800$ |
|  | Col.3B | $0.2280 \pm 0.0206$ | $1.2100 \pm 0.5300$ |
|  | Col.4A | $0.0590 \pm 0.0121$ | $1.5500 \pm 0.4000$ |
|  | Col.4B | $0.1720 \pm 0.0206$ | $2.1400 \pm 0.4000$ |

Table A.11: Fitted initial Thorium and Radium activities of the columns of trial FLOW2.

|  |  | $^{228}$Th/s$^{-1}$ | $^{224}$Ra/s$^{-1}$ |
|---|---|---|---|
| FLOW3 | Col.1A | $0.3940 \pm 0.0168$ | $4.8300 \pm 0.1501$ |
|  | Col.1B | $1.1310 \pm 0.0275$ | $0.1240 \pm 0.0235$ |
|  | Col.2A | $0.1781 \pm 0.0106$ | $3.9800 \pm 0.1101$ |
|  | Col.2B | $0.4910 \pm 0.0168$ | $0.9860 \pm 0.0632$ |
|  | Col.3A | $0.1246 \pm 0.0076$ | $3.6800 \pm 0.1001$ |
|  | Col.3B | $0.3790 \pm 0.0112$ | $1.3320 \pm 0.0632$ |
|  | Col.4A | $0.1386 \pm 0.0071$ | $0.0340 \pm 0.0121$ |
|  | Col.4B | $1.2780 \pm 0.0245$ | $4.5300 \pm 0.1401$ |

Table A.12: Fitted initial Thorium and Radium activities of the columns of trial FLOW3.

|  |  | $^{228}$Th/s$^{-1}$ | $^{224}$Ra/s$^{-1}$ |
|---|---|---|---|
| FLOW4 | Col.1A | $4.9070 \pm 0.0712$ | $5.3800 \pm 0.2201$ |
|  | Col.1B | $0.6670 \pm 0.0196$ | $0.3460 \pm 0.0304$ |
|  | Col.2A | $3.2100 \pm 0.0632$ | $3.9200 \pm 0.1501$ |
|  | Col.2B | $2.1930 \pm 0.0483$ | $1.4170 \pm 0.0901$ |
|  | Col.3A | $3.0240 \pm 0.0642$ | $3.9300 \pm 0.1601$ |
|  | Col.3B | $2.4460 \pm 0.0522$ | $1.4460 \pm 0.0931$ |
|  | Col.4A | $2.2300 \pm 0.0532$ | $2.5900 \pm 0.1201$ |
|  | Col.4B | $3.0000 \pm 0.0512$ | $2.5000 \pm 0.1301$ |

Table A.13: Fitted initial Thorium and Radium activities of the columns of trial FLOW4.

| | | $^{228}$Th/s$^{-1}$ | $^{224}$Ra/s$^{-1}$ |
|---|---|---|---|
| FLOW5 | Col.1A | 1.2640 ± 0.0344 | 3.7860 ± 0.0941 |
| | Col.1B | 0.1117 ± 0.0068 | 0.0098 ± 0.0059 |
| | Col.2A | 0.7200 ± 0.0168 | 3.0540 ± 0.0812 |
| | Col.2B | 0.3273 ± 0.0084 | 0.8120 ± 0.0275 |
| | Col.3A | 0.4710 ± 0.0168 | 2.2050 ± 0.0433 |
| | Col.3B | 0.4220 ± 0.0139 | 1.5770 ± 0.0423 |
| | Col.4A | 0.2890 ± 0.0121 | 1.6310 ± 0.0463 |
| | Col.4B | 0.4290 ± 0.0112 | 1.9660 ± 0.0463 |

Table A.14: Fitted initial Thorium and Radium activities of the columns of trial FLOW5.

| | | $^{228}$Th/s$^{-1}$ | $^{224}$Ra/s$^{-1}$ |
|---|---|---|---|
| FLOW6 | Col.1A | 3.5920 ± 0.0602 | 2.2470 ± 0.0742 |
| | Col.1B | 0.2368 ± 0.0087 | 1.5960 ± 0.0393 |
| | Col.2A | 2.9830 ± 0.0483 | 1.1850 ± 0.0493 |
| | Col.2B | 1.1390 ± 0.0226 | 2.3610 ± 0.0572 |
| | Col.3A | 1.6390 ± 0.0255 | 0.5930 ± 0.0324 |
| | Col.3B | 2.2950 ± 0.0344 | 3.1990 ± 0.0722 |
| | Col.4A | 1.1450 ± 0.0206 | 0.3860 ± 0.0255 |
| | Col.4B | 2.7560 ± 0.0383 | 3.1490 ± 0.0941 |

Table A.15: Fitted initial Thorium and Radium activities of the columns of trial FLOW6.

| | | $^{228}$Th/s$^{-1}$ | $^{224}$Ra/s$^{-1}$ |
|---|---|---|---|
| FLOW7 | Col.1A | 0.1447 ± 0.0067 | 2.7550 ± 0.0453 |
| | Col.1B | 0.4795 ± 0.0105 | 0.2810 ± 0.0187 |
| | Col.2A | 0.2013 ± 0.0074 | 2.9780 ± 0.0552 |
| | Col.2B | 0.3182 ± 0.0084 | 0.3590 ± 0.0149 |
| | Col.3A | 0.1303 ± 0.0068 | 2.4260 ± 0.0493 |
| | Col.3B | 0.2587 ± 0.0075 | 0.8850 ± 0.0235 |
| | Col.4A | 0.0715 ± 0.0056 | 0.8280 ± 0.0235 |
| | Col.4B | 0.1649 ± 0.0071 | 1.9470 ± 0.0423 |

Table A.16: Fitted initial Thorium and Radium activities of the columns of trial FLOW7.

|  |  | $^{228}$Th/s$^{-1}$ | $^{224}$Ra/s$^{-1}$ |
|---|---|---|---|
| FLOW8 | Col.1A | $2.6970 \pm 0.0473$ | $1.6890 \pm 0.0532$ |
|  | Col.1B | $0.6500 \pm 0.0139$ | $1.8970 \pm 0.0493$ |
|  | Col.2A | $1.9260 \pm 0.0284$ | $0.9260 \pm 0.0383$ |
|  | Col.2B | $1.4140 \pm 0.0255$ | $2.3440 \pm 0.0572$ |

Table A.17: Fitted initial Thorium and Radium activities of the columns of trial FLOW8.

|  |  | $^{228}$Th/s$^{-1}$ | $^{224}$Ra/s$^{-1}$ |
|---|---|---|---|
| FLOW9 | Col.1A | $0.9720 \pm 0.0168$ | $3.2660 \pm 0.0762$ |
|  | Col.1B | $0.1966 \pm 0.0064$ | $0.0460 \pm 0.0071$ |
|  | Col.2A | $0.5960 \pm 0.0121$ | $2.1710 \pm 0.0572$ |
|  | Col.2B | $0.4660 \pm 0.0101$ | $0.7170 \pm 0.0226$ |
|  | Col.3A | $0.1074 \pm 0.0062$ | $1.8750 \pm 0.0453$ |
|  | Col.3B | $0.0708 \pm 0.0056$ | $0.0290 \pm 0.0065$ |
|  | Col.4A | $0.0591 \pm 0.0057$ | $1.0230 \pm 0.0275$ |
|  | Col.4B | $0.0849 \pm 0.0059$ | $0.4920 \pm 0.0149$ |

Table A.18: Fitted initial Thorium and Radium activities of the columns of trial FLOW9.

# Bibliography

[1] H.H. Chen, *Solar Neutrinos and Neutrino Astronomy*, eds. Cherry, Fowler, K. Lande; AIP, 1984.

[2] H.H. Chen, *Phys. Rev. Lett.*, **55**, 1534, 1985.

[3] C. Rolfs and W. Rodney, *Cauldrons in the Cosmos*, Univ. of Chicago Press, 1988.

[4] P.D. Parker, J.N. Bahcall and W.A. Fowler *Ap. J.*, **139**, 602, 1964.

[5] J.N. Bahcall and R.A. Wolf *Ap. J.*, **139**, 622, 1964.

[6] P.D. Parker *Ap. J.*, **175**, 1972.

[7] R.E. Hardie *et al.*, *Phys. Rev. C*, **29**, 1199, 1984.

[8] J.N. Bahcall, R.K. Ulrich *Rev. Mod. Phys.* **60**, 297, 1988.

[9] N. Grenvesse *Physica Scripta* **T8**, 49, 1984.

[10] L.H. Aller in *Spectroscopy of Astrophysical Plasmas*, eds. Dalgarno & Layzer, Cambridge:CUP, 1986

[11] G. Rakavy and G. Shaviv, *Ap.J.* **148**, 803, 1967.

[12] Schwarzchild, Structure and Evolution of the Stars, Princeton N.J: Princeton University Press, 1958. ("The clearest book ever written on the subject" - J.N. Bahcall).

[13] W.F. Huebener in *Physics of the Sun*, eds. P.A. Sturrock, T.E. Holzer, D.M. Mihala, R.K. Ulrich; Dortrecht:Reidel, 1986.

[14] P.D. Parker in *Physics of the Sun*, eds. P.A. Sturrock, T.E. Holzer, D.M. Mihala, R.K. Ulrich; Dortrecht:Reidel, 1986.

[15] J.N. Bahcall, W.F. Huebener, S.H. Lubow, P.D. Parker, R.K. Ulrich *Rev. Mod. Phys.* **54**, 767, 1982.

[16] J.N. Bahcall, *Neutrino Astrophysics*, CUP, 1989.

[17] G.J. Wasserburg, F. Tera, D.A. Papanastassiou, T. Lee; *Earth Planet Sci. Lett.*, **35**, 294, 1977.

[18] I.W. Roxburgh in *The Internal Solar Angular Velocity* eds. Durney, Sofia; Dortrecht:Reidel, 1987.

[19] I.W. Roxburgh, *Solar Phys.* **100**, 21, 1985.

[20] Wolfendale *et al.* Nature(Phys.Sci.) 238, 130, 1972

[21] Davis, Evans, Radeka, Rogers in *Proc. Neutrino '72 Conf., Baltonfüred, Hungary.* Eds. Frenkel, Marx. Budapest: OMKDK Technoinform 1972.

[22] Soo Bong Kim, *PhD. thesis*, University of Pennsylvania, 1989.

[23] R. Davis, K. Lande, B.T. Cleveland, J. Ullman, J.K. Rowley in *Proc. Neutrino '88 Conf.* eds. Schneps, Kafka, Mann, Pran Nath; World Scientific, 1988.

[24] E.L. Fireman, B.T. Cleveland, R. Davis Jr. and J.K. Rowley in *Solar Neutrinos and Neutrino Astronomy, Proceedings of the Homestake Conference*, AIP:N.Y., 1984.

[25] J.N. Bahcall, B.T. Cleveland, R. Davis Jr., J.K Rowley *Ap. J. Lett.*, **292**, L79, 1985.

[26] A.I. Abazov *et al.* (SAGE collaboration) in *Proc. Neutrino '90 Conf.* Nucl. Phys. B (Proc. Suppl.) 19, 1991.

[27] T. Kirsten in *Proc. Neutrino '90 Conf.* Nucl. Phys. B (Proc. Suppl.) 19, 1991.

[28] J.N. Bahcall, K. Kubodera, S. Nozawa *Phys. Rev. D*, **38**, 1030, 1988.

[29] S. Nozawa, Y. Kohyama, T. Kaneta and K. Kubodera *J. Phys. Soc. Jpn.*, **55**, 2636, 1986.

[30] G. t'Hooft *Phys. Lett.* **B37**, 195, 1971.

[31] N.T. Taddeucci *et al. Nucl. Phys.* **A469**, 125, 1987.

[32] Y. Totsuka in *Proc. Neutrino '90 Conf.* Nucl. Phys. B (Proc. Suppl.) 19, 1991.

[33] E. Fernandez in *Proc. Neutrino '90 Conf.* Nucl. Phys. B (Proc. Suppl.) 19, 1991.

[34] T.M. Brown and C.A. Morrow, in *The Internal Solar Angular Velocity* eds. B.R. Durney, S. Sofia; Dortrecht:Reidel, 1987.

[35] Duvall, Harvey and Pomerantz *Nature*, **321**, 500, 1986.

[36] T.M. Brown and C.A. Morrow, *Ap. J. Lett.* **314**, L21, 1987.

[37] M.J. Newman in *Physics of the Sun*, eds. P.A. Sturrock, T.E. Holzer, D.M. Mihala, R.K. Ulrich; Dortrecht:Reidel, 1986.

[38] F.W.W. Dilke and D.O. Gough *Nature*, **240**, 262, 1972.

[39] H.C. Spruit in *The Internal Solar Angular Velocity* eds. B.R. Durney, S. Sofia; Dortrecht:Reidel 1987.

[40] J.N. Bahcall, N.A. Bahcall and R.K. Ulrich *Astrophys.Lett.*, **2**, 91, 1968.

[41] Winkler and Newman *Ap. J.*, **236**, 201, 1980.

[42] Winkler and Newman *Ap. J.*, **238**, 311, 1980.

[43] Winkler and Newman *Space Sci. Rev.*, **27**, 261, 1980.

[44] B. Pontecorvo *Sov. JETP*, **26**, 984, 1968.

[45] V. Gribov and B. Pontecorvo *Phys. Lett.*, **28B**, 493, 1969.

[46] J.N. Bahcall and S.C. Frautschi *Phys. Lett.* **29B**, 623, 1969.

[47] L. Wolfenstein *Phys. Rev. D*, **17**, 2369, 1978.

[48] S.P. Rosen and J.M. Gelb *Phys. Rev. D*, **34**, 969, 1986.

[49] J.N. Bahcall, J.M. Gelb and S.P. Rosen *Phys. Rev. D*, **35**, 2976, 1987.

[50] A.S. Davydov *Quantum Mechanics*, Pergamon Press, 1965. p. 394.

[51] *Table of Isotopes, 7th edition* eds. C.M. Lederer and V.S. Shirley, Wiley, 1978.

[52] W.H. Press, B.P. Flannery, S.A. Teukolsky and W.T. Vetterling, *Numerical Recipes — The art of scientific computing (2nd ed.)*, CUP, 1989.

[53] P.R. Bevington. *Data Reduction and Error Analysis for the Physical Sciences.*, McGraw-Hill, 1969.

[54] Kelly and Uberall *Phys. Rev. Lett.*, **16**, 145, 1966.

[55] Sudbury Neutrino Observatory Proposal, SNO-87-12, 1987.

[56] *Scientific and Technical Description of the Mark II SNO Detector* eds. E. Beier and D. Sinclair, SNO-89-15, 1989

[57] M.A. Lone, R.A. Leavitt and D.A. Harrison, *Atomic and Nucl. Data Tables*, **26**, 511, 1981.

[58] Jackson, *Classical Electrodynamics*, Wiley, 1962.

[59] R.C. Mobley and R.A. Laubenstein *Phys. Rev.*, **80**, 309, 1950.

[60] M.L. Rustgi and N.L. Pandey*Phys. Rev.*, **C40**, 1581, 1989.

[61] Hargrave and Paterson, *Solar Neutrino Neutral Current Detection Methods in SNO*, SNO-STR-88-60, 1988.

[62] T.K. Gaisser and T. Stanev in *Solar Neutrinos and Neutrino Astronomy, Proceedings of the Homestake Conference*, AIP:N.Y., 1984.

[63] Y. Birenbaum, S. Kahane and R. Moreh, *Phys. Rev. C*, **32**, 1825, 1985.

[64] D. Sinclair, private communication.

[65] P.T. Trent, SNO-STR-91-038, 1991.

[66] C. Waltham, private communication.

[67] W.T. Eadie, D. Drijard, F.E. James, M. Roos and B. Sadoulet, *Statistical Methods in Experimental Physics*, North-Holland, 1971.

[68] S. Baker and R.D. Cousins, *Nucl. Instr. Meth. Phys. Res.*, **221**, 437, 1984.

[69] Nelder and Mead, *Comp J.*, **7**, 308, 1965.

[70] Fletcher, *Comp. J.*, **13**, 317, 1970.

[71] Particle Data Group, *Phys. Lett. B*, **239**, 1, 1990.

[72] K.S. Hirata, T. Kajita, K. Kifune, *et al. Phys. Rev. Lett.*, **63**, 16, 1989.

[73] *Cotton and Wilkinson*, *Advanced Inorganic Chemistry*, Wiley, 1967.

[74] *The Radiochemical Manual*, Radiochemical Centre, Amersham.

[75] B. Allard in *Actinides in perspective*, ed. N.M. Edelstein, Pergamon Press, 1982.

[76] Hietanen and Sillén *Acta Chem. Scand.*, **22**, 270, 1968.

[77] N.B. Milić *Acta Chem. Scand.*, **25**, 2494, 1971.

[78] G.R. Choppin and J. Rydberg, *Nuclear chemistry, theory and applications*, Pergamon Press, 1980

[79] R.M. Gershey and D.R. Green in *Radionuclides: a tool for oceanography*, eds. J.C. Guary, P. Guegueniat and R.J. Pentreath, Elsevier, 1988.

[80] D.J. Cardin, S.A. Cotton, M. Greenand J.A. Labinger *Organometallic compounds of the Lanthanides, Actindides and early transition metals*

[81] L.I. Katzin and D.C. Sonnenberger in *The chemistry of the actinide elements*, eds. Katz, Seaborg and Morss, 2nd ed., Chapman & Hall, 1986.

[82] S. Ahrland in *The chemistry of the actinide elements*, eds. Katz, Seaborg and Morss, 2nd ed., Chapman & Hall, 1986.

[83] A. Fratiello, R.E. Lee and R.E. Schuster *Inorg. Chem.*, **9**, 391, 1970.

[84] J. Burgess, *Metal ions in solution*, Ellis-Horwood, 1978.

[85] J. Burgess, *Ions in solution*, Ellis-Horwood, 1988.

[86] M. Traube, *Plutonium*, Warsaw, 1964.

[87] W. Stumm and J.J. Morgan, *Aquatic Chemistry,* Wiley-Interscience, 1970.

[88] E.W. Hooper, B.A.Phillips, S.P. Dagnell and N.P. Monckton, *An assessment of the application of inorganic ion exchangers to the treatment of intermediate level wastes,* AERE-R 11088, HMSO, 1984.

[89] B.A. Phillips, E.W. Hooper, S.P. Dagnall and N.P. Monckton, *Study of the behaviour of inorganic ion exchangers in the treatment of medium-active effluents. Part 1: Preliminary experimental work on absorber preparation and performance*, AERE-G 2872, UKAEA, 1984.

[90] G.W. Beaven, J.E. Cross and E.W. Hooper, *Study of the behaviour of inorganic ion exchangers in the treatment of medium active effluents. Part 4: Further studies on absorber performance*, AERE-G 4381, UKAEA, 1988.

[91] M.-Q. Liu, H. Lee, I. Fallas, A. McDonald, *Radon emanation from stainless steel,* SNO-STR-90-75, 1990.

[92] R. Aveyard and D.A. Haydon, *An introduction to the principles of surface chemistry,* CUP, 1973.

[93] D. Nicholson and N.G. Parsonage, *Computer simulation and the statistical mechanics of adsorption,* Academic Press, 1982.

[94] *Adsorption from solution at the solid-liquid interface,* eds. G.D. Parfitt and C.H. Rochester, Academic Press, 1983.

[95] A.W. Adamson, *The physical chemistry of surfaces,* Interscience, 1960.

[96] W.S. Moore and D.F. Reid, *J. Geophys. Res.*, **78**, 880, 1973.

[97] W.S. Moore, *Deep Sea Res.*, **23**, 647, 1976.

[98] N. Yamagata and K. Iwashima, *Nature*, **200**, 52, 1963.

[99] E. Ebler and W. Bender, *Z. Anorg. Allgem. Chem.*, **84**, 77, 1913.

[100] E. Ebler and W. Bender, *Angen. Chem.*, **28I**, 25, 1915.

[101] W.S. Moore and L.M. Cook, *Nature*, **253**, 262, 1975.

[102] T.A. Littlefield and N. Thorley *Atomic and nuclear physics*, van Nostrand, 1963.

[103] C. Bigliocca, F. Girardi, J. Pauly, E. Sabbioni, S. Meloni and A. Provasoli *Anal. Chem.* **39**, 1634, 1967.

[104] *Encyclopedia of chemical technology*, 2nd ed., Vol. 2, ed. Kirk-Othmer, 1966.

[105] L.N. Ushenko and N.A. Skorik *Russ. J. Inorg. Chem.*, **17**, 1533, 1972.

[106] T.K. Kuo and J. Pantaleone, *Phys. Rev. D*, **35**, 3432, 1987.

[107] D.D. Clayton *Principles of stellar evolution and nucleosynthesis*, Univ. of Chicago Press, 1983.

[108] G.W. Grime and F. Watt, *Nucl. Instr. Meth.*, **B50**, 197, 1990.

[109] G.W. Grime, M. Dawson, M.Marsh, I.C. McArthur and F. Watt, *Nucl. Instr. Meth.*, **B54**, 52, 1991.

[110] D. Sinclair, private communication.

[111] E. Schatzman in *Solar Neutrinos and Neutrino Astronomy, Proceedings of the Homestake Conference*, AIP:N.Y., 1984.